eXPRESS Polymer Letters Vol.5, No.4 (2011) 283
Available online at www.expresspolymlett.com
DOI: 10.3144/expresspolymlett.2011.28

Editorial corner – a personal view
Investigating thermal degradation kinetics of polymers: Does it have practical significance?

A.S. Luyt[*]

Department of Chemistry, University of the Free State (Qwaqwa Campus), Private Bag X13, Phuthaditjhaba, South Africa

Menczel and Prime, in an introduction to a section describing thermal degradation kinetics of polymers by using thermogravimetric analysis, state that kinetic information is crucial for evaluating the times and temperatures associated with the processing, service lifetimes, and storage of materials [Thermal Analysis of Polymers – Fundamentals and Applications, ISBN 978-0-471-76917-0]. As most of us know, these kinds of kinetic analysis may be divided into isothermal and non-isothermal methods, of which the most controversial, but also most used, is the non-isothermal method. This method is based on a relationship between heating rate, extent of conversion and temperature, and there are a number of models derived over the past 40–50 years that may be used to calculate activation energies, preexponential factors, lifetime estimates, etc.

If different models are applied to the same set of data, different kinetic parameters may be obtained. The reliability of these parameters depends very much on the actual processes occurring during the thermal degradation of a polymer, and the assumptions made when applying these models. During the four years of existence of this journal only two papers were published on the thermal degradation kinetics of different polymers obtained through TGA analysis at different heating rates [Express Polymer Letters, **1**, 208–216 (2007); Express Polymer Letters, **2**, 133–146 (2008)], but I think they are very good papers that provide more information on the polymer degradation mechanisms than just cranking data through complex mathematical procedures.

I recently assisted someone in the submission of a manuscript describing the degradation kinetics of a novel polyester prepared in their laboratories. One of the reviewers commented that the TGA community is addicted to these complex analyses of their data and fitting to models, and that this sort of analysis does not give any real insight into what is really happening.

It seems as if there are different viewpoints on the usefulness of non-isothermal degradation kinetic investigations, especially on polymers. How realistic are the estimated lifetimes determined from kinetic analyses on the very small samples normally used for TGA analysis? How applicable are these data to larger polymer samples used in real life? Whatever the answer may be, I think that degradation kinetic analysis serves a purpose, even if it is only to compare the thermal behaviour of newly synthesised polymers with that of known polymers, or the influence of (especially nano-sized) additives on the thermal behaviour of selected polymers. Eventually this information will add to the bigger picture painted through the efforts of all polymer scientists.

Prof. Dr. Adriaan Stephanus Luyt
Member of International Advisory Board

[*]Corresponding author, e-mail: LuytAS@qwa.ufs.ac.za

eXPRESS Polymer Letters Vol.5, No.4 (2011) 284–294
Available online at www.expresspolymlett.com
DOI: 10.3144/expresspolymlett.2011.29

Synthesis and characterization of novel poly(butylene succinate-*co*-2-methyl-1,3-propylene succinate)s

C.-H. Chen, C.-S. Yang, M. Chen, Y.-C. Shih, H.-S. Hsu, S.-F. Lu*

Department of Materials and Optoelectronic Science, National Sun Yat-sen University, Kaohsiung 80424, Taiwan, Republic of China

Received 5 September 2010; accepted in revised form 4 November 2010

Abstract. Poly(butylene succinate) (PBSu), poly(2-methyl-1,3-propylene succinate) (PMPSu), and PBSu-rich copolyesters were synthesized using an effective catalyst, titanium tetraisopropoxide. Measurements of intrinsic viscosity (1.20–1.28 dl/g) and gel permeation chromatography demonstrated the success of the preparation of polyesters with high molecular weights. The compositions of the copolyesters were determined in three approaches from ^{1}H and ^{13}C NMR (nuclear magnetic resonance) analyses, and good agreement between the results was obtained. The distributions of the comonomers were found to be random from the spectra of carbonyl carbon. Their thermal properties were elucidated using a differential scanning calorimeter and a thermogravimetric analyzer. No marked difference exists among the thermal stabilities of these polyesters. However, the window between the glass transition and the melting temperatures becomes narrower with the increase in the concentration of 2-methyl-1,3-propylene succinate in the copolymers. Additionally, the cold crystallization ability decreases considerably. Finally, PMPSu is an amorphous homopolymer. Wide-angle X-ray diffractograms of isothermally crystallized copolyesters also follow the same trend.

Keywords: *polymer synthesis, copolyesters, NMR, thermal properties, WAXS*

1. Introduction

Biodegradable materials can be degraded to CO_2, CH_4, H_2O, or other natural substances by the action of enzymes and microorganisms. They offer viable solutions to solve environmental pollution caused by the worldwide disposal of used synthetic polymers in the last several decades. Among biodegradable polymers, aliphatic polyesters have received considerable attention [1]. Poly(butylene succinate) (PBSu) is a chemosynthetic polyester with a relatively high melting temperature ($T_m \approx 113°C$) and favorable mechanical properties, which are comparable with those of such widely used polymers as polyethylene and polypropylene [2]. Moreover, owing to the excellent processability of PBSu, it can be processed using conventional equipment.

In general, the degree of crystallinity, spherulite size and lamellar structure of aliphatic polyesters affect their biodegradation rates, because biodegradation initially occurs in the amorphous regions [3, 4]. The crystalline structure [5–9], and crystallization and melting behavior [10–18] of PBSu have been investigated extensively. PBSu has a relatively low biodegradation rate because of its high crystallization rate and high crystallinity. To promote the physical properties, extend the application field, and increase the biodegradability of PBSu, numerous approaches have been used, such as physical blending, copolymerization, or formation of composites. With respect to copolymers, the degradation rates of PBSu can be increased by incorporating small amounts of various diols [19–24] or

*Corresponding author, e-mail: mingchen@mail.nsysu.edu.tw

diacids [24–28]; this is basically attributed to the reduced crystallinity.

Unlike PBSu, poly(propylene succinate) (PPSu) has an odd number of carbon atoms in the backbone. PPSu has gained increasing attention, because it has a higher biodegradation rate [29–32]. Papageorgiou and Bikiaris [33] have synthesized a series of poly(butylene succinate-*co*-propylene succinate)s (PBPSu) and have reported that the tensile strength and Young's modulus were very low and almost identical to those of the neat PPSu for PPSu–rich copolymers (50–90 mol%). The decrease in the crystallinity of copolymers was attributed to the reduction in length of homopolymer sequences and the occurrence of defects. These copolyesters with a low degree of crystallinity and slower crystallization rate exhibited a higher biodegradation rate than PBSu. Recently, Chen *et al.* [34] also synthesized and characterized a series of PBSu-rich PBPSu copolyesters by combining PBSu with a high melting point and PPSu with high biodegradability. They also reported that incorporating propylene succinate units to PBSu not only narrows the window between the glass transition temperature (T_g) and T_m, but also retards the cold crystallization ability, thereby lowering the crystallinity to a considerable extent.

In contrast with the high cost and the limited availability of 1,3-propanediol, 2-methyl-1,3-propanediol (MPD) became commercially available in the early 1990s. It is well recognized that the linearity and conformation of polymer backbone have a significant effect on the crystallization behavior of the polymer. The methyl group which MPD introduces into the polymer side chain helps to inhibit the crystallization of polyester resins [35–39]. The effects of MPD monomer on the physical properties of unsaturated [40–43] and isophthalate-based polyesters have been studied [44]. No prior investigation of succinate involving MPD could be found in the literature. Furthermore, methyl substituent in the diol of PBSu-based biodegradable polyesters has not been probed.

In this work, PBSu, poly(2-methyl-1,3-propylene succinate) (PMPSu), and PBSu-rich copolyesters [poly(butylene succinate-*co*-2-methyl-1,3-propylene succinate), PBMPSu] with high molecular weight were synthesized. They were characterized by ^{1}H and ^{13}C Nuclear Magnetic Resonance (NMR) spectrometer, differential scanning calorimeter (DSC), thermogravimetric analyzer (TGA) and wide-angle X-ray diffractometer (WAXD). ^{13}C NMR spectra were analyzed to evaluate the composition and the distribution of butylene succinate (BS) units and 2-methyl-1,3-propylene succinate (MS) units. The purpose of the present study is to examine the effect of methyl substituent on the cold crystallization of quenched polymers.

2. Experimental

2.1. Materials

1,4-Butanediol (BD) (Acros, 99%, Waltham, MA, USA), MPD (Aldrich, 99%, Louis, MO, USA) and succinic acid (SA) (Acros, 99%) were used without purification. Titanium tetraisopropoxide (TTP) (Acros, 98+%) was used as received. Other solvents in the analysis were also used without purification.

2.2. Synthesis

PBSu, PMPSu and PBSu-rich copolyesters were synthesized via a two-step esterification reaction in the melt. The reactor was a 1 l stainless flask that was equipped with a magnetic agitator, an electric heater, a nitrogen inlet and outlet, a drain, a water cooling system and a condenser. The reaction mixture was charged into the reactor with a diols:diacid molar ratio of 1:1. TTP was used as a catalyst with a concentration of 0.1 mol% based on the amount of

Table 1. Intrinsic viscosity, molecular weight, and thermal properties of synthesized polyesters

Sample code	η [dl/g]	$\bar{M}_n$ [10^4 g/mol]	$\bar{M}_w$ [10^4 g/mol]	PDI[a]	T_g [°C]	T_{cc} [°C]	T_m [°C]
PBSu	1.27	3.0	7.4	2.5	–41.1	–15.5	113.1
PBMPSu 95/5	1.23	2.7	7.3	2.7	–39.9	–3.0	107.4
PBMPSu 90/10	1.20	2.4	5.2	2.2	–38.3	–0.3	102.5
PBMPSu 80/20	1.28	3.1	9.7	3.1	–37.8	12.2	91.6
PBMPSu 50/50	1.28	3.1	9.1	2.9	–33.1	–	50.2[b]
PMPSu	1.24	4.0	12.0	3.0	–30.9	–	–

[a]Polydispersity index

[b]Specimen was kept at room temperature for more than 3 days

diacid used. The first column of Table 1 shows the sample codes of copolyesters (PBMPSu), with the numerical values representing the feed ratios of the diols (BD/MPD). As an example, the synthesis of copolyester (PBMPSu 50/50) with equal amounts of diols is described as follows.

The reaction mixture of BD (45 g; 0.5 mol), MPD (45 g; 0.5 mol), SA (118 g; 1 mol), and the TTP catalyst (0.283 g; 1.0 mmol) was charged into the polycondensation reactor. The mixture was purged with nitrogen and heated with an electrical heater that was placed around the reactor. The temperature of the reactor was raised to 150°C to melt the acid component completely. Thereafter, the temperature was gradually increased to 190°C at 10°C/h. The water byproduct formed during the first stage was collected using a condenser. The condenser was kept at 100°C by an electrical heater for the separation of water from the monomers. The volume of water collected was 80 mol% of the theoretical value. In the second stage of the reaction, the pressure was slowly reduced to below 1 Torr (1 Torr = 133 Pa) and the temperature was increased to 220°C after 3 h of reaction. This condition was maintained for about 20 h to enable further the reactions of polycondensation and transesterification until the torque of magnetic agitator reached 80% of the meter to read. The synthesized polyester was dissolved in chloroform and precipitated into ten times the amount of vigorously stirred ice-cooled methanol. Then, the precipitate was filtered, washed with methanol and dried at reduced pressure condition at room temperature (*RT*). The other three copolyesters (PBMPSu 95/5, PBMPSu 90/10, and PBMPSu 80/20) as well as PBSu and PMPSu homopolymers were synthesized by the same procedures. Ivory white, pale brown or transparent polyesters were finally obtained.

2.3. Measurement of molecular weights

Gel permeation chromatography (GPC) was performed at 40°C using a Waters GPC-150CV and a Waters hexafluoroisopropanol (HFIP) column (Milford, MA, USA). The flow rate of the eluent, HFIP, was 1.0 ml/min. The number average ($\overline{M}_n$) and weight average ($\overline{M}_w$) molecular weights of each polyester were calculated using a calibration curve, which was obtained using eight poly(methyl methacrylate) standards having low polydispersity indices.

Purified polyester samples were dissolved in 60/40 w/w phenol/1,1,2,2-tetrachloroethane solution. The solution viscosities of the polyesters at 30°C were measured using an Ubbelohde viscometer. The intrinsic viscosity, (η), of each polyester was determined from measurements at five solution concentrations.

2.4. NMR analyses

NMR spectra of *d*-chloroform solutions were recorded with tetramethylsilane as the reference standard using a Varian UNITY INOVA-500 NMR (Santa Clara, CA, USA) at 295.5 K. ^{1}H NMR spectra were analyzed to determine the compositions of the copolyesters. To perform quantitative ^{13}C NMR measurement, it is important to take into account the difference of spin-lattice relaxation time among different carbons. ^{13}C NMR was conducted using a 30-s pulse cycle [34] to determine both the composition and the ester sequence distribution in these copolyesters.

2.5. Measurement of thermal properties

Compressed films with a thickness of around 0.2 mm were made and then dried in vacuum overnight at *RT* before use. A specimen with a diameter of 6 mm and a weight of around 4 mg was cut from a film and sealed in an aluminum pan. The thermal properties of the polyesters were analyzed using a Perkin-Elmer Pyris 1 DSC (Waltham, MA, USA), equipped with a refrigerating system (Pyris Intracooler 2P). DSC was calibrated with deionized water and indium and was also calibrated using the heat of fusion of indium. The specimen was heated at a rate of 20°C/min to 50°C above its T_m, which was held for 5 min to eliminate the thermal history. Subsequently, the specimen was quenched with liquid nitrogen, and then heated at a rate of 10°C/min to above its T_m. The T_g, cold crystallization temperature (T_{cc}) and T_m were detected during the heating process.

2.6. Measuring thermal stability

Thermal experiments were performed using a TA 2050 TGA (New Castle, DE, USA). Nitrogen gas was the purge gas with a flow rate of 50 ml/min. A

specimen lighter than 10 mg was heated at a rate of 10°C/min from *RT* to 800°C. Weight loss curves and their derivatives were obtained to compare the relative thermal stabilities of the synthesized polyesters.

2.7. WAXD measurements

Specimens with a thickness of around 0.5 mm, following completely isothermal crystallization at *RT* (room temperature) or at a temperature of 10–12°C below their respective T_m values, were prepared using a heating stage (Linkam THMS-600) (Tadworth, Surrey, UK). X-ray diffractograms were obtained using a Siemens D5000 diffractometer (Bruker AXS Inc., Madison, WI, USA) with Ni-filtered Cu K_α radiation ($\lambda = 0.1542$ nm, 40 kV, 30 mA) at a scanning rate of 1°/min. Measurements were made at *RT*.

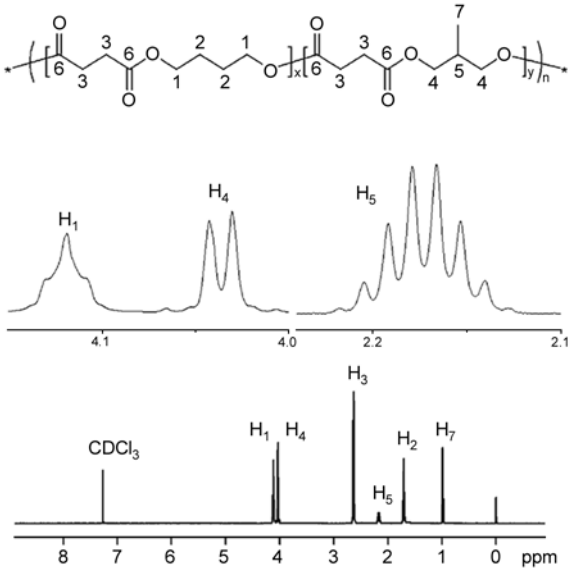

Figure 1. ^{1}H NMR spectrum of PBMPSu 50/50 and peak assignments

3. Results and discussion

3.1. Molecular weights and distribution

The intrinsic viscosities of these polyesters ranged from 1.20 to 1.28 dl/g, as listed in column 2 of Table 1. $\overline{M}_n$ and $\overline{M}_w$ values of these polyesters were between $2.4 \cdot 10^4$ and $4.0 \cdot 10^4$ g/mol and between $5.2 \cdot 10^4$ and $1.2 \cdot 10^5$ g/mol, respectively, and their polydispersity indices (PDI) ranged from 2.2 to 3.1, as shown in columns 3–5 of Table 1. These wide PDI values may be due to the transesterification at 220°C for about 20 h. In this work, PBSu, PMPSu, and PBMPSu copolyesters were synthesized using an effective catalyst, TTP, without the addition of any heat stabilizer. The molecular weights of these synthesized polyesters are high enough. Therefore, they could be made into films for the subsequent works.

3.2. Copolyester composition and sequence distribution

Figure 1 displays the ^{1}H NMR spectrum of PBMPSu 50/50 copolymer and the peak assignments. The two chemical shifts at 4.09–4.15 and 1.68–1.74 ppm are associated with the methylene protons α (H_1) and β (H_2) bonded to the ester oxygen in the BS units. The chemical shift of the protons of the succinic moiety (H_3) appears at 2.61–2.66 ppm, while those of the H_4, H_5 and H_7 protons derived from the MPD monomer are at 4.01–4.06 ppm (methylene, doublet), 2.12–2.22 ppm (methine, octet) and 0.97–1.01 ppm (methyl, doublet, not shown here), respectively. The composition of this copolyester was evaluated from the relative integration areas of the proton peaks of BS and MS units. The mole percent ratio of BS/MS in PBMPSu 50/50 was 50.0/50.0, as presented in the third column of Table 2. Rows 1–3 of the same column show the compositions of the other copolymers. An expanded view of the proton peaks is presented in the inset spectra in Figure 1. H_1, H_4 and H_5 appear as triplet, doublet and octet, respectively.

Figure 2 shows the ^{13}C NMR spectrum of PBMPSu 50/50. For BS units, the chemical shifts of the carbons α and β bonded to the ester oxygen are located at 64.05–64.20 (C_1) and 25.10–25.20 (C_2) ppm, respectively. The three chemical shifts at 65.85–66.00 (C_4), 32.27–32.37 (C_5) and 13.69–13.77 (C_7) ppm are associated with carbons derived from the MPD monomer. The chemical shifts of the ethylene carbons and the carbonyl carbons of the succinic moiety are at 28.86–29.00 (C_3) and 172.06–172.28 (C_6) ppm, respectively. The composition was determined from the relative integration areas of the C_1 and C_4 peaks. The mole percent ratio of BS/MS in PBMPSu 50/50 was 49.6/50.4, as presented in the fourth column of Table 2. The compositions of the other three copolymers are tabulated in rows 1–3 of the same column.

A close-up view of the ^{13}C NMR spectrum of PBMPSu 50/50 shows that the carbonyl carbons

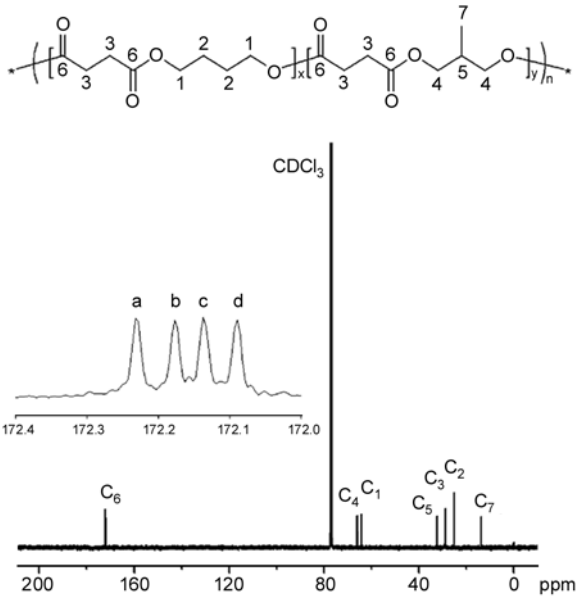

Figure 2. ^{13}C NMR spectrum of PBMPSu 50/50 and peak assignments

(C_6) are split into four peaks, as shown in the inset spectrum in Figure 2. The peak C_{6a} is assigned to the carbonyl carbons with butylene groups on both sides of the succinic ester, abbreviated as BSB. The assigned C_{6b}, C_{6c}, and C_{6d} peaks represent the carbonyl carbons of the BSM-B side, BSM-M side, and MSM structures, respectively (where B denotes the BD unit, S represents the succinate unit, and M is the MPD unit). Figure 3 presents the expanded spectra of the carbonyl carbons of all synthesized polyesters. It is obvious that the slight variation in chemical shifts of these split peaks is caused by the difference among the chemical environment; therefore, the integration areas can be employed to characterize the chemical microstructures of these copolyesters.

The total areas of C_{6a}, C_{6b}, C_{6c}, and C_{6d} peaks were normalized to unity for each copolyester, and the percentage values of each peak area are presented in columns 5–8 of Table 2 under the subtitles of BSB, BSM-B side, BSM-M, side and MSM. Two peaks (C_{6b} and C_{6c}) of equal intensity were observed from the unequivalent carbonyl carbons in the mixed diester sequence BSM. Three possible triad sequences, BSB, BSM, and MSM, of copolyesters were then evaluated from the normalized areas, and tabulated in columns 9–11 of the Table 2. In the case of PBMPSu 50/50, *P*(BSB), *P*(BSM), and *P*(MSM) were 25.0, 50.2 and 24.8 mol%, respectively, as presented in the fourth row of Table 2. The

Table 2. Composition, probabilities of triads, randomness factor (β), and the average number sequence lengths (L_n) of synthesized copolyesters

Sample code	Composition			Normalized peak areas of the carbonyl carbons [%]				Triad sequence probabilities [%]			Composition	β	L_{nBS}	L_{nMS}
	Feed ratio BD/MPD	^{1}H NMR BS/MS	^{13}C NMR BS/MS[a]	BSB	BSM-B	BSM-M	MSM	*P*(BSB)	*P*(BSM)	*P*(MSM)	^{13}C NMR BS/MS[b]			
PBMPSu 95/5	95/5	93.5/6.5	95.3/4.7	84.6	8.7	6.7	0.0	84.6	15.4	0.0	92.3/7.7	1.08	12.0	1.0
PBMPSu 90/10	90/10	89.2/10.8	86.4/13.6	78.0	12.2	9.8	0.0	78.0	22.0	0.0	89.0/11.0	1.12	8.1	1.0
PBMPSu 80/20	80/20	78.8/21.2	75.7/24.3	59.6	17.5	16.7	6.2	59.6	34.2	6.2	76.7/23.3	0.96	4.5	1.4
PBMPSu 50/50	50/50	50.0/50.0	49.6/50.4	25.0	25.2	25.0	24.8	25.0	50.2	24.8	50.1/49.9	1.00	2.0	2.0

[a]Estimated from diol carbons α bonded to the ester oxygen

[b]Estimated from the split carbonyl carbons

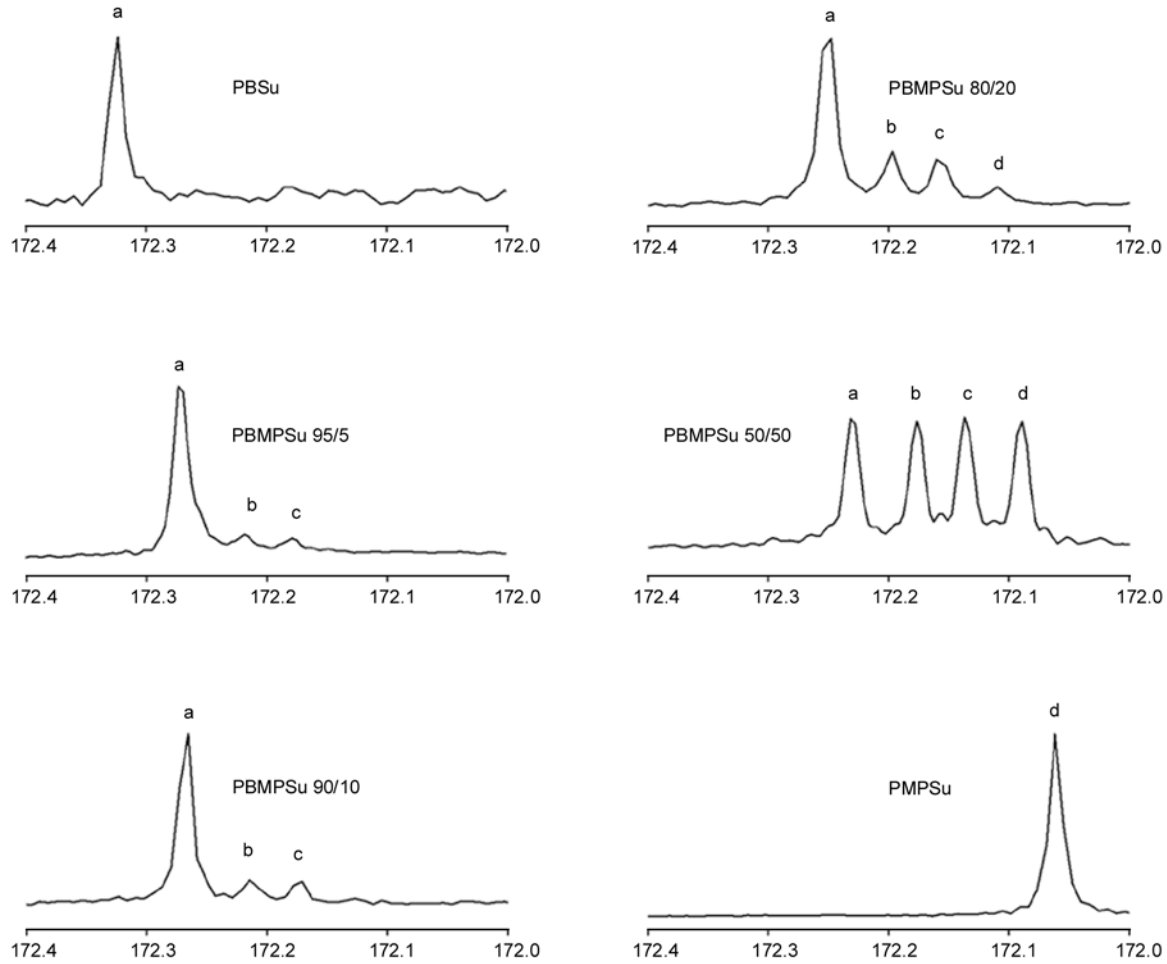

Figure 3. Enlarged ^{13}C NMR spectra of the carbonyl carbons (C_6) in the succinate units of all synthesized polyesters

BS% and MS% of copolyesters are given by Equations (1) and (2):

$$\mathrm{BS\%} = P_{\mathrm{BS}} = P(\mathrm{BSB}) + \frac{P(\mathrm{BSM})}{2} \tag{1}$$

$$\mathrm{MS\%} = P_{\mathrm{MS}} = P(\mathrm{MSM}) + \frac{P(\mathrm{BSM})}{2} \tag{2}$$

where P_{BS} and P_{MS} are the molar fractions of BS and MS units, respectively. This copolyester had 50.1 mol% BS units and 49.9 mol% MS units. Column 12 of Table 2 displays the mole percent ratio of BS/MS of the other copolyesters. The agreement of composition among these three methods is good in this study, as shown in Table 2.

The randomness B of the copolymer [34, 45–49] is given by $B = P(\mathrm{BSM})/(2P_{\mathrm{BS}} \cdot P_{\mathrm{MS}})$. Copolyesters synthesized by polycondensation have usually been considered to have a random distribution. This expectation is due to the relatively equal reactivity of the comonomers and the random transesterification during the polycondensation process. For total randomness of a copolymer, B is one. The calculated B values of PBMPSu 95/5, 90/10, 80/20, and 50/50 were 1.08, 1.12, 0.96, and 1.00, respectively, as presented in column 13 of Table 2. The distribution of BS and MS units in these copolyesters can be regarded as random. The reactivities of BD and MPD with SA can be assumed to not differ by much. The average number sequence lengths [33, 45, 48–50] of BS and MS units are $L_{\mathrm{nBS}} = 2P_{\mathrm{BS}}/P(\mathrm{BSM})$ and $L_{\mathrm{nMS}} = 2P_{\mathrm{MS}}/P(\mathrm{BSM})$, respectively. In the case of PBMPSu 50/50, both values were 2.0. These values are tabulated in the last two columns of Table 2. The values of L_{nBS} for PBMPSu 95/5, 90/10, and 80/20 were 12.0, 8.1, and 4.5, respectively. The L_{nBS} value decreases as the amount of MS unit increases along the polymer chain.

3.3. Thermal properties

Figure 4 shows DSC heating curves of quenched polyesters. PBSu has the lowest T_g at –41.1°C. T_g value gradually increases as the moiety of the MS units increases. It ranges from –41.1 to –30.9°C, as listed in column 6 in Table 1. The copolyesters had intermediate T_g between those of the parent homopolyesters. Such a T_g increment is attributed to a decrease in the chain flexibility by incorporating MS units. All of these copolyesters exhibited a single T_g rather than two T_gs, for possible blocks of PBSu and PMPSu. Moreover, all of these copolyesters had *B* (randomness parameter) values of about 1.0, which were obtained from the ^{13}C NMR analysis (Table 2). These results demonstrate that the comonomer placement in these copolymers was essentially random. The T_g value of PBMPSu is slightly higher than that of the corresponding PBPSu [34]. However, the T_g value of PMPSu is 0.4°C less than that of PPSu [34]. This contradictory result may be due to the difference in molecular weight. It seems that the methyl substituted effect on the T_g value is not obvious.

A cold crystallization peak was observed for PBSu and PBSu-rich PBMPSu copolyesters, as presented in Figure 4. The peak temperature of cold crystallization (T_{cc}) occurs at –15.5°C for PBSu, and this peak is sharper and earlier than those of the other three copolyesters, suggesting that the cold crystallization rate of the PBSu homopolymer markedly exceeds that of the other copolyesters. For PBMPSu 95/5, 90/10, and 80/20, T_{cc} moves from –3.0, through –0.3 to 12.2°C (see the penultimate column in Table 1) and the corresponding peak becomes lower and broader, as shown in Figure 4. These T_{cc} values are 4~6°C higher than those of the corresponding PBPSu [34]. No cold crystallization is revealed by the curves of PBMPSu 50/50 and PMPSu. Clearly, incorporating minor MS units into PBSu reduced the cold crystallization rate of quenched specimens. Accordingly, the intensity of the melting peak fell and the corresponding T_m declined from 113.1 to 91.6°C, as indicated in the final column of Table 1. The enthalpy of melting (ΔH_m) was evaluated and the degree of crystallinity was calculated by dividing ΔH_m by 210 J/g [16]. The degrees of crystallinity were 35.0% for PBSu, 32.8% for PBMPSu 95/5, 28.1% for PBMPSu 90/10, and 25.0% for PBMPSu 80/20. These values were only 0.3% less than the degrees of crystallinity of the corresponding PBPSu 95/5 and 90/10 copolymers.

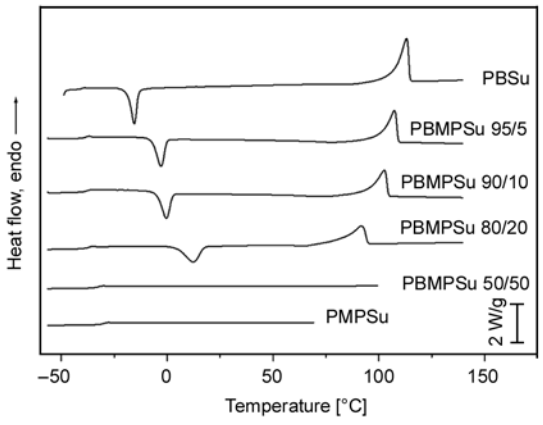

Figure 4. DSC thermograms of quenched polyesters at a heating rate of 10°C/min

Comparing the values of T_{cc} and T_m between PBMPSu and PBPSu [34], the results indicate that the effect of methyl substitution on the T_m value is little. The reason is due to the melting−recrystallization−remelting behavior [11, 12, 15, 17] of PBSu-rich copolymers during the heating process. In the case of PBMPSu 50/50, the T_m value was 50.2°C, when the specimen was maintained at *RT* for more than three days. No melting phenomenon was detected for PMPSu homopolymer even after holding at different subzero temperatures for a long period. On the contrary, PPSu had a melting temperature at 55.6°C [34]. The effect of methyl substitution on retarding crystallization becomes more evident for neat PMPSu.

3.4. Thermal stability

Figure 5 plots the weight loss curves as functions of temperature for all of the polyesters used in this investigation in flowing nitrogen at a heating rate of 10°C/min. For brevity, the derivative curves of weight loss have not been shown here. At temperatures below 240°C, these specimens appear to be stable; they exhibit detectable weight loss only above 242°C (defined as T_{start} from the derivative curve of weight loss). $T_{loss2\%}$ is denoted as the temperature at a weight loss of 2% from the weight loss curve, and T_{max} represents the temperature with the greatest slope from the weight loss curve. The average values of T_{start}, $T_{loss2\%}$, and T_{max} were 244.4±1.8, 298.8±3.9, and 404.5ºC±5.4°C, respectively. These polyesters exhibited no significant difference or

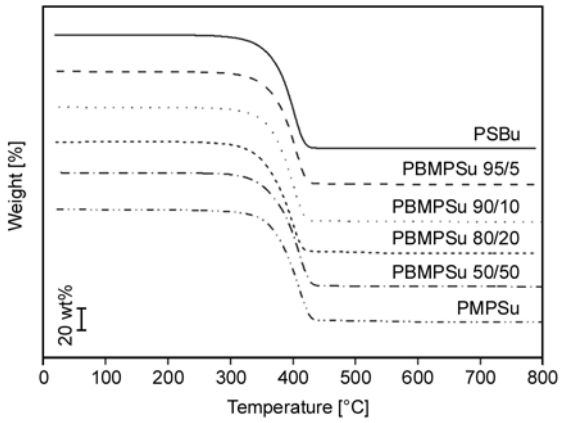

Figure 5. Thermogravimetric traces of polyesters at a heating rate of 10°C/min under nitrogen

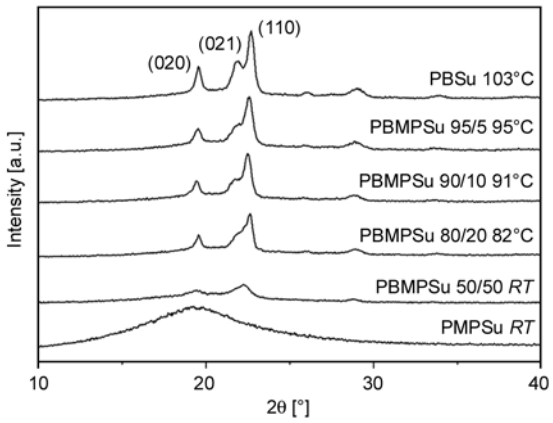

Figure 6. WAXD patterns from polyesters crystallized at the indicated temperatures

trend in these three temperature parameters because they degraded via the same cyclization degradation mechanism around the succinate groups. Similar results have been reported for the other series of aliphatic copolyesters [23, 34, 45, 49]. The values of $T_{loss2\%}$ are well above 220ºC, the temperature of the last step of synthesis. It can be assumed that no appreciable thermal degradation occurred during polycondensation; therefore, there is no demand to use a heat stabilizer during the synthesis of these polyesters. For PMPSu, the values of T_{start} and $T_{loss2\%}$ were 243.3 and 293.4°C, respectively, which were ~8°C lower than those of PPSu [34]. It may be due to the reason that PMPSu is an amorphous polymer.

3.5. Wide angle X-ray diffraction patterns

Figure 6 displays WAXD patterns of PBSu, PMPSu, and PBSu-rich PBMPSu copolyesters that were isothermally crystallized at 10–12°C below their respective T_m values. The unit cell of the crystalline PBSu α form is monoclinic [5–9], and the diffraction peaks from the (020) and (110) planes are detected at $2\theta \approx 19.6$ and 22.7°, respectively. All PBSu-rich copolyesters have diffraction peaks of the PBSu α form, revealing only one crystalline form. As the proportion of the MS units increases, the intensity of the diffraction peaks from the (020) and (110) planes becomes weaker and the width at half−maximum peak increases gradually. The mean crystal sizes L_{hkl}, perpendicular to the (*hkl*) plane, can be estimated with the familiar Scherrer equation, as follows [51]:

$$L_{hkl} = \frac{K\lambda}{\beta_0 \cos\theta} \tag{3}$$

where β_0 is the breath at half-maximum peak corrected for instrumental broadening and K denotes the Scherrer factor. L_{hkl} was strongly dependent on the peak broadening (β_0). However, the numerical values obtained from Equation (3) are not accurate because of the prevalence of lattice distortions. Figure 6 shows that the sizes or the lamellar thickness of the crystals declines with increasing the MS amounts, indicating less crystalline order in copolymers. PMPSu shows amorphous scattering. The results of the WAXD patterns and DSC heating curves reveal that incorporation of MS units into PBSu markedly inhibit the crystallization behavior of the resultant polymers.

4. Conclusions

PBMPSu copolyesters were synthesized in a random sequence, as evidenced by a single T_g and a randomness value of around 1.0. Their intrinsic viscosities (1.20–1.28 dl/g) and the relative molecular weights are high enough to demonstrate that the synthesis of these polyesters was successful even without the use of stabilizers, and that they can be cast into films without complications. The compositions of the copolyesters were evaluated from three methods based on the relative areas of the proton peaks under BS and MS units, the carbon peaks α bonded to the ester oxygen, and the split peaks of carbonyl carbons. The results of these three approaches are in good agreement. The incorporation of MS units to PBSu not only narrows the window between T_g and T_m, but also retards the cold crystallization ability, thereby lowering the degree of crystallinity to a considerable extent. Comparing

with PBPSu copolyesters, this retarding is more efficient in PBMPSu copolyesters, which have methyl substituents on the main chain. The WAXD patterns of melt-crystallized specimens also indicate that the incorporation of MS units into PBSu markedly inhibits the crystallinity of the resultant copolymer, and becomes amorphous for PMPSu. However, the thermal stability of these polyesters does not vary markedly.

Acknowledgements

The authors would like to thank Mr. C.L. Lin at Chung Shan Institute of Science and Technology for his help in the GPC experiments. The financial support of the National Science Council (Grant NSC 97-2221-E-110-033) is also acknowledged.

References

[1] Mochizuki M., Hirami M.: Structural effects on the biodegradation of aliphatic polyesters. Polymers for Advanced Technologies, **8**, 203–209 (1997).
DOI: 10.1002/(SICI)1099-1581(199704)8:4<203::AID-PAT627>3.0.CO;2-3

[2] Ishioka R., Kitakuni E., Ichikawa Y.: Aliphatic polyesters: 'Bionolle'. in 'Biopolymers' (eds.: Doi Y., Steinbüchel A.) Wiley, Weinheim, Vol 4, 275–297 (2002).
DOI: 10.1002/3527600035.bpol4010

[3] Kumagai Y., Kanesawa Y., Doi Y.: Enzymatic degradation of microbial poly(3-hydroxybutyrate) films. Makromolecular Chemistry and Physics, **193**, 53–57 (1992).
DOI: 10.1002/macp.1992.021930105

[4] Abe H., Doi Y., Aoki H., Akehata T.: Solid-state structures and enzymatic degradabilities for melt-crystallized films of copolymers of (R)-3-hydroxybutyric acid with different hydroxyalkanoic acids. Macromolecules, **31**, 1791–1797 (1998).
DOI: 10.1021/ma971559v

[5] Ichikawa Y., Kondo H., Igarashi Y., Noguchi K., Okuyama K., Washiyama J.: Corrigendum to 'Crystal structures of α and β forms of poly(tetramethylene succinate)'. Polymer, **42**, 847 (2001).
DOI: 10.1016/S0032-3861(00)00390-6

[6] Ichikawa Y., Suzski J., Washiyama J., Moteki Y., Noguchi K., Okuyama K.: Strain-induced crystal modification in poly(tetramethylene succinate). Polymer, **35**, 3338–3339 (1994).
DOI: 10.1016/0032-3861(94)90144-9

[7] Ichikawa Y., Suzski J., Washiyama J., Moteki Y., Noguchi K., Okuyama K.: Crystal transition mechanisms in poly(tetramethylene succinate). Polymer Journal, **27**, 1230–1238 (1995).
DOI: 10.1295/polymj.27.1230

[8] Ihn K. J., Yoo E. S., Im S. S.: Structure and morphology of poly(tetramethylene succinate) crystals. Macromolecules, **28**, 2460–2464 (1995).
DOI: 10.1021/ma00111a045

[9] Ichikawa Y., Kondo H., Igarashi Y., Noguchi K., Okuyama K., Washiyama J.: Crystal structures of α and β forms of poly(tetramethylene succinate). Polymer, **41**, 4719–4727 (2000).
DOI: 10.1016/S0032-3861(99)00659-X

[10] Miyata T., Masuko T.: Crystallization behaviour of poly(tetramethylene succinate). Polymer, **39**, 1399–1404 (1998).
DOI: 10.1016/S0032-3861(97)00418-7

[11] Yoo E. S., Im S. S.: Melting behavior of poly(butylene succinate) during heating scan by DSC. Journal of Polymer Science Part B: Polymer Physics, **37**, 1357–1366 (1999).
DOI: 10.1002/(SICI)1099-0488(19990701)37:13<1357::AID-POLB2>3.0.CO;2-Q

[12] Yasuniwa M., Satou T.: Multiple melting behavior of poly(butylene succinate). I. Thermal analysis of melt-crystallized samples. Journal of Polymer Science Part B: Polymer Physics, **40**, 2411–2420 (2002).
DOI: 10.1002/polb.10298

[13] Qiu Z. B., Komura M., Ikehara T., Nishi T.: DSC and TMDSC study of melting behaviour of poly(butylene succinate) and poly(ethylene succinate). Polymer, **44**, 7781–7785 (2003).
DOI: 10.1016/j.polymer.2003.10.045

[14] Qiu Z., Fujinami S., Komura M., Nakajima K., Ikehara T., Nishi T.: Nonisothermal crystallization kinetics of poly(butylene succinate) and poly(ethylene succinate). Polymer Journal, **36**, 642–646 (2004).
DOI: 10.1295/polymj.36.642

[15] Yasuniwa M., Tsubakihara S., Satou T., Iura K.: Multiple melting behavior of poly(butylene succinate). II. Thermal analysis of isothermal crystallization and melting process. Journal of Polymer Science Part B: Polymer Physics, **43**, 2039–2047 (2005).
DOI: 10.1002/polb.20499

[16] Papageorgiou G. Z., Bikiaris D. N.: Crystallization and melting behavior of three biodegradable poly(alkylene succinates). A comparative study. Polymer, **46**, 12081–12092 (2005).
DOI: 10.1016/j.polymer.2005.10.073

[17] Wang X. H., Zhou J. J., Li L.: Multiple melting behavior of poly(butylene succinate). European Polymer Journal, **43**, 3163–3170 (2007).
DOI: 10.1016/j.eurpolymj.2007.05.013

[18] Papageorgiou G. Z., Achilias D. S., Bikiaris D. N.: Crystallization kinetics of biodegradable poly(butylene succinate) under isothermal and non-isothermal conditions. Macromolecular Chemistry and Physics, **208**, 1250–1264 (2007).
DOI: 10.1002/macp.200700084

[19] Mochizuki M., Mukai K., Yamada K., Ichise N., Murase S., Iwaya Y.: Structural effects upon enzymatic hydrolysis of poly(butylene succinate-*co*-ethylene succinate)s. Macromolecules, **30**, 7403–7407 (1997). DOI: 10.1021/ma970036k

[20] Yoo Y. T., Ko M. S., Han S. B., Kim T. Y., Im S., Kim D. K.: Degradation and physical properties of aliphatic copolyesters derived from mixed diols. Polymer Journal, **30**, 538–545 (1998). DOI: 10.1295/polymj.30.538

[21] Gan Z., Abe H., Doi Y.: Crystallization, melting, and enzymatic degradation of biodegradable poly(butylene succinate-*co*-14 mol ethylene succinate) copolyester. Biomacromolecules, **2**, 313–321 (2001). DOI: 10.1021/bm0056557

[22] Gan Z., Abe H., Kurokawa H., Doi Y.: Solid-state microstructures, thermal properties, and crystallization of biodegradable poly(butylene succinate) (PBS) and its copolyesters. Biomacromolecules, **2**, 605–613 (2001). DOI: 10.1021/bm015535e

[23] Cao A., Okamura T., Nakayama K., Inoue Y., Masuda T.: Studies on syntheses and physical properties of biodegradable aliphatic poly(butylene succinate-*co*-ethylene succinate)s and poly(butylene succinate-*co*-diethylene glycol succinate)s. Polymer Degradation and Stability, **78**, 107–117 (2002). DOI: 10.1016/S0141-3910(02)00124-6

[24] Zhu C. Y., Zhang Z. G., Liu Q. P., Wang Z. P., Jin J.: Synthesis and biodegradation of aliphatic polyesters from dicarboxylic acids and diols. Journal of Applied Polymer Science, **90**, 982–990 (2003). DOI: 10.1002/app.12722

[25] Montaudo G., Rizzarelli P.: Synthesis and enzymatic degradation of aliphatic copolyesters. Polymer Degradation and Stability, **70**, 305–314 (2000). DOI: 10.1016/S0141-3910(00)00139-7

[26] Ahn B. D., Kim S. H., Kim Y. H., Yang J. S.: Synthesis and characterization of the biodegradable copolymers from succinic acid and adipic acid with 1,4-butanediol. Journal of Applied Polymer Science, **82**, 2808–2826 (2001). DOI: 10.1002/app.2135

[27] Nikolic M. S., Djonlagic J.: Synthesis and characterization of the biodegradable poly(butylene succinate-*co*-butylene adipate)s. Polymer Degradation and Stability, **74**, 263–270 (2001). DOI: 10.1016/S0141-3910(01)00156-2

[28] Tserki V., Matzinos P., Pavlidou E., Vachliotis D., Panayiotou C.: Biodegradable aliphatic polyesters. Part I. Properties and biodegradation of poly(butylene succinate-*co*-butylene adipate). Polymer Degradation and Stability, **91**, 367–376 (2006). DOI: 10.1016/j.polymdegradstab.2005.04.035

[29] Carothers W. H., Arvin J. A.: Studies on polymerization and ring formation. II. Poly-esters. Journal of the American Chemical Society, **51**, 2560–2570 (1929). DOI: 10.1021/ja01383a042

[30] Ranucci E., Liu Y., Lindblad M. S., Albertsson A-C.: New biodegradable polymers from renewable sources. High molecular weight poly(ester carbonate)s from succinic acid and 1,3-propanediol. Macromolecular Rapid Communications, **21**, 680–684 (2000). DOI: 10.1002/1521-3927(20000601)21:10<680::AID-MARC680>3.0.CO;2-Y

[31] Liu Y., Ranucci E., Lindblad M. S., Albertsson A. C.: New biodegradable polymers from renewable sources: Polyester-carbonates based on 1,3-propylene-*co*-1,4-cyclohexanedimethylene succinate. Journal of Polymer Science Part A: Polymer Chemistry, **39**, 2508–2519 (2001). DOI: 10.1002/pola.1227

[32] Bikiaris D. N., Papageorgiou G. Z., Achilias D. S., Pavlidou E., Stergiou A.: Miscibility and enzymatic degradation studies of poly(ε-caprolactone)/poly(propylene succinate) blends. European Polymer Journal, **43**, 2491–2503 (2007). DOI: 10.1016/j.eurpolymj.2007.03.051

[33] Papageorgiou G. Z., Bikiaris D. N.: Synthesis, cocrystallization, and enzymatic degradation of novel poly (butylene-*co*-propylene succinate) copolymers. Biomacromolecules, **8**, 2437–2449 (2007). DOI: 10.1021/bm0703113

[34] Chen C-H., Peng J-S., Chen M., Lu H-Y., Tsai C-J., Yang C-S.: Synthesis and characterization of poly(butylene succinate) and its copolyesters containing minor amounts of propylene succinate. Colloid and Polymer Science, **288**, 731–738 (2010). DOI: 10.1007/s00396-010-2187-9

[35] Sullivan C. J., Dehm D. C., Reich E. E., Dillon M. E.: Polyester resins based upon 2-methyl-1,3-propanediol. Journal of Coatings Technology, **62**, 37–45 (1990).

[36] Bello P., Bello A., Riande E.: Conformational characteristics and crystalline order in poly(2-methyl-1,3-propane glycol terephthalate). Macromolecules, **32**, 8197–8203 (1999). DOI: 10.1021/ma990485f

[37] Nalampang K., Johnson A. F.: Kinetics of polyesterification: modelling and simulation of unsaturated polyester synthesis involving 2-methyl-1,3-propanediol. Polymer, **44**, 6103–6109 (2003). DOI: 10.1016/S0032-3861(03)00552-4

[38] Suh J., Spruiell J. E., Schwartz S. A.: Melt spinning and drawing of 2-methyl-1,3-propanediol-substituted poly(ethylene terephthalate). Journal of Applied Polymer Science, **88**, 2598–2606 (2003). DOI: 10.1002/app.11871

[39] Lewis C. L., Spruiell J. E.: Crystallization of 2-methyl-1,3-propanediol substituted poly(ethylene terephthalate). I. Thermal behavior and isothermal crystallization. Journal of Applied Polymer Science, **100**, 2592–2603 (2006). DOI: 10.1002/app.22786

[40] Huang Y-J., Jiang W-C.: Effects of chemical composition and structure of unsaturated polyester resins on the miscibility, cured sample morphology and mechanical properties for styrene/unsaturated polyester/low-profile additive ternary systems. 1: Miscibility and cured sample morphology. Polymer, **39**, 6631–6641 (1998).
DOI: 10.1016/S0032-3861(98)00164-5

[41] Huang Y. J., Chen L. D.: Effects of chemical composition and structure of unsaturated polyester resins on the miscibility, cured sample morphology and mechanical properties of styrene/unsaturated polyester/low-profile additive ternary systems: 2. Mechanical properties. Polymer, **39**, 7049–7059 (1998).
DOI: 10.1016/S0032-3861(98)00165-7

[42] Kharas G. B., Kamenetsky M., Simantirakis J., Beinlich K. C., Rizzo A-M. T., Caywood G. A., Watson K.: Synthesis and characterization of fumarate-based polyesters for use in bioresorbable bone cement composites. Journal of Applied Polymer Science, **66**, 1123–1137 (1997).
DOI: 10.1002/(SICI)1097-4628(19971107)66:6<1123::AID-APP13>3.0.CO;2-2

[43] Kharas G. B., Villaseñor G., Diener C. A., Baugh M., McColough K., Mikach S., Scola A., Whitesell J., Watson K.: Synthesis and characterization of fumarate copolyesters for use in bioresorbable bone cement compositions. Journal of Macromolecular Science Part A: Pure and Applied Chemistry, **43**, 855–863 (2006).
DOI: 10.1080/10601320600653582

[44] Diakoumakos C. D., Jones F. N.: Studies on the chemical, physical and mechanical properties of high-solids clearcoats prepared from hydroxyl-terminated isophthalate-based oligoesters and a melamine resin. Surface and Coatings Technology, **140**, 183–194 (2001).
DOI: 10.1016/S0257-8972(01)01047-7

[45] Chen C-H., Lu H-Y., Chen M., Peng J-S., Tsai C-J., Yang C-S.: Synthesis and characterization of poly(ethylene succinate) and its copolyesters containing minor amounts of butylene succinate. Journal of Applied Polymer Science, **111**, 1433–1439 (2009).
DOI: 10.1002/app.29035

[46] Yamadera R., Murano M.: The determination of randomness in copolyesters by high resolution nuclear magnetic resonance. Journal of Polymer Science Part A-1: Polymer Chemistry, **5**, 2259–2268 (1967).
DOI: 10.1002/pol.1967.150050905

[47] Newmark R. A.: Sequence distribution in polyethylene/tetramethylene terephthalate copolyesters by ^{13}C-NMR. Journal of Polymer Science: Polymer Chemistry, **18**, 559–563 (1980).
DOI: 10.1002/pol.1980.170180216

[48] Ko C-Y., Chen M., Wang H-C., Tseng I-M.: Sequence distribution, crystallization and melting behavior of poly(ethylene terephthalate-*co*-trimethylene terephthalate) copolyesters. Polymer, **46**, 8752–8762 (2005).
DOI: 10.1016/j.polymer.2005.01.107

[49] Tsai C-J., Chang W-C., Chen C-H., Lu H-Y., Chen M.: Synthesis and characterization of polyesters derived from succinic acid, ethylene glycol and 1,3-propanediol. European Polymer Journal, **44**, 2339–2347 (2008).
DOI: 10.1016/j.eurpolymj.2008.05.002

[50] Backson S. C. E., Kenwright A. M., Richards R. W.: A ^{13}C n.m.r. study of transesterification in mixtures of poly(ethylene terephthalate) and poly(butylene terephthalate). Polymer, **36**, 1991–1998 (1995).
DOI: 10.1016/0032-3861(95)91443-B

[51] Alexander L. E.: X-ray diffraction methods in polymer science. Huntington, New York (1969).

eXPRESS Polymer Letters Vol.5, No.4 (2011) 295–307
Available online at www.expresspolymlett.com
DOI: 10.3144/expresspolymlett.2011.30

Processing and characterization of halloysite nanotubes filled polypropylene nanocomposites based on a masterbatch route: effect of halloysites treatment on structural and mechanical properties

K. Prashantha[1,2*], *M. F. Lacrampe*[1,2], *P. Krawczak*[1,2]

[1]Univ. Lille Nord de France, F-59500 Lille, France
[2]Ecole des Mines de Douai, Polymers and Composites Technology and Mechanical Engineering Department, 941 rue Charles Bourseul, BP 10838, F-59508 Douai Cedex, France

Received 25 June 2010; accepted in revised form 4 November 2010

Abstract. Halloysites/polypropylene nanocomposites with different nanotubes contents were prepared by diluting a masterbatch containing 30 wt.% halloysites with polypropylene (PP). Unmodified (HNTs) and quaternary ammonium salt treated (QM-HNTs) halloysite nanotubes were used. Both degree of crystallinity and crystallization temperature increase upon addition of halloysites into PP, thus indicating a potential nucleation effect induced by the nanotubes. An homogeneous distribution and dispersion of nanotubes was observed throughout the PP matrix, with a slightly better dispersion in the case of modified QM-HNTs compared to unmodified HNTs. Mechanical tests in tension, bending and notched impact demonstrated that strength and modulus of the nanocomposites significantly increase with addition of halloysites without significant loss of ductility. An halloysite content of 6 wt.% appears as an optimum. Modified halloysites (QM-HNTs) lead to globally better performances due to strong interfacial interaction between the polymer matrix and the nanotubes.

Keywords: *nanocomposites, polypropylene, halloysite nanotubes, masterbatch*

1. Introduction

Polymer nanocomposites are new class of materials that are filled with nanofillers, and which usually exhibit exceptionally superior thermomechanical performance and physical properties at much lower filler loadings compared to conventional polymer composites [1–3]. Improvements in mechanical properties, such as stiffness and toughness, dimensional stability, electrical, barrier and thermal properties as well as fire retardant enhancements, with respect to the bulk polymer, are usually observed [1–3]. The interfacial interactions and the degree of dispersion of fillers in polymer matrix are key issues in determining the final performance of polymer nanocomposites [4–7].

Polypropylene (PP) is an important commercial plastic widely used to produce household goods and automotive parts due to its well-balanced physical and mechanical properties and easy processability at a relatively low cost. The application of PP in various industrial sectors can be further expanded once its mechanical performances have been highly upgraded. Therefore, PP has been a popular matrix used in association with all kinds of nanofillers such as carbon nanotubes (CNTs) [8–12], layered silicates (clays such as montmorillonite (MMT)

*Corresponding author, e-mail: kalappa.prashantha@mines-douai.fr

etc.,) [13–15] and nanoparticles such as silica, graphite and calcium carbonate [16–19], even though the nanofiller dispersion is challenging in that case and often remains an issue.

Halloysite nanotubes (HNTs) have recently become the subject of research attention as a new type of additive for enhancing the mechanical, thermal and fire-retardant performance of polymers [20–32]. Halloysite is mainly composed of aluminosilicate and has a predominantly hollow tubular structure with the chemical composition $Al_2(OH)_4Si_2O_5(2H_2O)$. It is a weathering product of volcanic rocks of rhyolitic up to granitic composition and occurs in great deposits. Common halloysites can be found in form of fine, tubular structures with a length of 300~ 1500 nm, and with inner and outer diameters of 15–100 nm and 40–120 nm, respectively [33].

Even if the usage of a silica based, natural occurring nanotube as reinforcing material for polymers is still new, halloysite nanotubes are considered as the ideal materials for preparing polymer composites due to the fact that halloysites are rigid materials and that unique crystal structure of HNTs resembles that of carbon nanotubes (CNTs) in terms of aspect ratio. Compared with other nanoparticles such as fumed silica, montmorillonite, and carbon nanotubes, halloysite nanotubes are more easily dispersed in polymer matrix by shearing due to their rod-like geometry and limited intertubular contact area [33]. Chemically, HNTs are recognized for their relatively lower hydroxyl density on their outer surfaces compared with fumed silica and other layered silicates such as montmorillonite [21]. Therefore, the aggregation induced by the intertubular hydrogen bonding is susceptible to the shearing force. In fact, morphology study for many polymer/HNTs composites has shown single-tube dispersed halloysites in the matrix [34]. Halloysite nanotubes are readily obtainable, are much cheaper than other nanofillers such as carbon nanotubes and they are biocompatible [35]. In addition, only traces of heavy metals were detected, much lower than standards of the restriction of harmful substances of the European Union. Consequently it can be concluded that halloysite nanotubes (HNTs) are a type of 'green', unique and promising reinforcing material for thermoplastics [33].

Polypropylene does not have any polar groups that could interact with the halloysites. This usually results in poor level of dispersion of the halloysites in the PP matrix and a poor interfacial bonding between the filler surface and the PP matrix. This also limits the advantages of incorporation of the halloysites into the PP matrix. To overcome this problem, strategies such as compatabilization between fillers and PP have been reported, including the use of benzothiazole sulfide grafted polypropylene [31]. Pre-treatment of fillers with coupling agents is also well documented [28, 32]. Furthermore, surface modification of fillers also provides good wetting and bonding with polymers.

Most common methods used for the production of polymer nanocomposites, are melt mixing, solution casting and in situ polymerization [36]. Among them, melt mixing is a most desirable method as it combines high shear with simplicity. Furthermore, it is free of solvents and contaminants and the required equipment for efficient manufacturing of large amounts of nanocomposites is already available in the plastics industry. In all the techniques mentioned above, a homogeneous dispersion and good interfacial adhesion are crucial for the successful preparation of nanocomposites [36–37]. Additionally, recent advancement in the usage of pre-elaborated masterbatches, usually containing 10–30 wt.% nanofillers, facilitates both the processing and the formulation development and eliminates the dispersion and handling difficulties. A recent comprehensive study highlights the benefits and results obtained by dilution of commercially available carbon nanotube filled PP masterbatches [9]. However, whereas few reports are available in the literature, which examine the mechanical and structural properties of melt processed halloysite filled PP nanocomposites [28–32], no reports are available to our knowledge on detailed investigations on the properties of nanocomposites prepared via dilution of halloysite filled PP masterbatches. Moreover, distribution of masterbatch and subsequent dispersion of nanotubes in the polymer matrix after processing needs to be ascertained.

As a consequence, the present work aims at comparing the properties of as received halloysite nanotubes (HNTs)/PP and quaternary ammonium salt treated halloysite nanotubes (QM-HNTs)/PP nanocomposites produced with varying nanotube content by diluting a commercial available masterbatch in a twin screw extruder. The structure, morphology

and mechanical properties (in tension, bending and impact) of the prepared nanocomposites were characterized.

2. Experimental section

2.1. Materials

The materials used in this study are two commercially available polypropylene based masterbatches (Pleximer™ PP grade, Natural Nano Inc, USA) containing 30 wt.% halloysite nanotubes: one unspecified quaternary ammonium salt treated halloysites (QM-HNTs) filled polypropylene and one unmodified halloysites (HNTs) filled polypropylene. Halloysites used in the masterbatch were mainly of tubular structure with a diameter smaller than 100 nm and lengths typically ranging from about 500 nanometers to over 1.2 microns with a density of 250 kg/m^3. The dilution matrix was made of homopolymer PP granules (FB 027 grade, Polychim, France) with a melt flow index of 12 g/10 min at 190°C.

2.2. Preparation of nanocomposites

Unmodified halloysite nanotubes (HNTs)/PP and quaternary ammonium salt treated halloysite nanotubes (QM-HNTs)/PP nanocomposites were produced by extrusion process by mixing homo PP granules with the commercial 'Pleximer' masterbatch containing 30 wt.% of halloysites. The dilution was carried out in a co-rotating twin screw extruder (Clextral BC 45, Clextral, France) at a screw speed of 50 rpm. The temperatures setting from the hopper to the die was 180/190/200/210°C. During melt extrusion ventilation was kept on to remove trapped air in composites. After pelletizing, the nanocomposite granules were dried for 5 hours at 80°C before injection-molding. Dried pellets were injection-molded (KM80-160E injection molding machine, KraussMaffei, Germany) into standard test specimen for tensile, impact, flexural and dynamic mechanical analysis. The temperature profile setting ranged from 200 to 215°C and the mold temperature was kept at 25°C. The holding pressure and screw rotation speed were 300 bar and 100 rpm, respectively with a throughput of 50 cm^3/s. The final nanocomposites bearing 2, 4, 6 and 8 wt.% fillers in the PP matrix were fabricated and as a reference, neat PP was also similarly extruded and injection-molded for mechanical and dynamic mechanical studies.

2.3. Structural and morphological characterization

Samples for scanning electron microscopy (SEM) were prepared by coating a thin layer of carbon onto the nanocomposite samples. Electron microscopy imaging of the nanocomposites was performed under high vacuum with a SEM instrument (S-4300SE/N, Hitachi, Japan) operating at 5 kV.

For transmission electron microscopy (TEM), ultrathin sections were cut at ambient temperature with a microtome (Leica Reichert FCS, Leica Microsystems GmbH, Germany) and collected on a 300 mesh copper grid. Thickness of the ultrathin sections was 125 nm. They were examined with a TEM (LEO 922) operated at 120 kV and the micrographs were taken using an energy filter in zero loss mode for an optimal contrast of the nanotubes.

Differential scanning calorimetry (DSC 7, Perkin-Elmer, USA,) was performed under nitrogen atmosphere. The sample was heated from 35 to 200°C at a heating rate of 10°C/min, held at 210°C for 5 min to eliminate any previous thermal history, and then cooled to 35°C at a cooling rate of 10°C/min. The samples were kept at this temperature for another 5 min and heated again to 200°C at a heating rate of 10°C/min. On the basis of the recorded DSC thermograms, melting temperature (T_m), crystallization temperature (T_c), heat of fusion (ΔH_m) and relative degree of crystallinity (X_c) were determined. X_c was calculated from the DSC crystallization curves with Equation (1):

$$X_c = \frac{\Delta H_m}{\Delta H_m^\circ (1 - w_t)} \tag{1}$$

where ΔH_m is the specific melting heat or heat of fusion, calculated by integrating the area under the crystallization peak, ΔH_m° is the theoretical specific melting heat of 100% crystalline isotactic PP, which is taken as 209 J/g [38], and w_t is the weight fraction of nanotubes.

2.4. Dynamic mechanical analysis

Dynamic mechanical properties were measured with a DMA (DMA +150, MetraviB, France) operating in the tensile mode at a frequency of 10 Hz.

The strain amplitude was 20 μm and the static force was 1 N as per the reported procedure elsewhere [39]. Data were collected from –50°C temperature to 120°C at a scanning rate of 3°C/min. DMA specimens were cut from injection-molded impact bar samples in the form of rectangular bars of nominal dimensions: 4 (±0.2) mm × 10 (±0.5) mm × 30 mm. A minimum of 3 specimens of each composition were tested.

Dynamic mechanical analysis (DMA) is generally being used to study relaxation in polymers. An analysis of the storage modulus (E'), loss modulus (E''), and loss factor (tanδ) curves is very useful in evaluating the performance of samples under stress and temperature. It is well known that the tanδ vs. temperature curve of PP exhibits three relaxations localized in the vicinity of −80°C (γ), 10°C (β) and 100°C (α) [40]. In the present work, the study was focused on the β-relaxation of PP that corresponds to the glass-rubber transition of the amorphous portions and the temperature of the maximum tanδ peak is assigned to the glass transition temperature (T_g).

2.5. Mechanical characterization

Mechanical performance of all compounded materials was evaluated from injection-molded specimens. Tensile properties of the molded dogbone specimens were tested using a tensile machine (Model 1185, Instron, USA) at a crosshead rate of 20 mm/min at 25°C (50% relative humidity) according to the ISO 527 standard. The tensile strength, modulus and elongation at break of the PP and its nanocomposite samples could be directly obtained from the recorded stress–strain curves. Flexural properties of the nanocomposites were determined by three point bending tests as per ISO 178 standard at a thickness to span length ratio of 1:16 at a crosshead rate of 2 mm/min. Notched Charpy impact tests were carried out as per ISO 179-1 standard by using a pendulum impact machine (Model 5101, Zwick, Germany). The Charpy impact tests were performed on single-notched specimens at room temperature. All the reported values were calculated as averages over five specimens for each composition.

3. Result and discussions

3.1. Structural and morphological characterization

3.1.1. Nanotube dispersion

Scanning electron miscroscopy (SEM) and transmission electron microscopic (TEM) analysis were conducted on cryofractured nanocomposite samples in order to investigate the nanotube dispersion and interfacial features in nanocomposites. Figure 1a shows typical SEM micrograph of 6 wt.% HNTs filled nanocomposites. The nanotube distribution appears to be uniform across the specimen. Smaller agglomerates remain however, which are smeared out and well penetrated into the PP matrix (marked as 'A' in Figure 1a). This observation is further supported by TEM micrographs (Figure 2a), which confirm that melt-compounding grants fairly homogeneous dispersion of the HNTs within the polymer matrix with occasionally micron-sized aggregates scattered within a matrix of neat polypropylene (marked as 'A' in Figure 2a). Existence of agglomerates indicates insufficient interactions between HNTs and PP matrix. The microstructure of the nanocomposites is substantially changed after incorporation of 6 wt.% functionalized halloysites (PP/QM-HNTs) into PP matrix as shown in Figures 1b and 2b. The aggregates previously observed for the nanocomposites containing non-modified halloysites (Figure 2a) are less or no more present

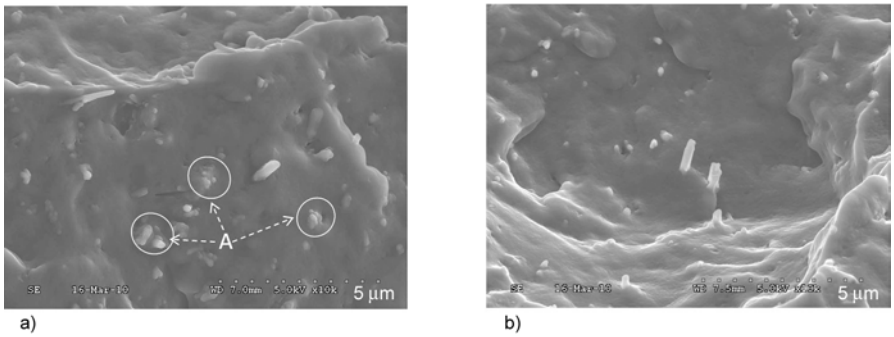

Figure 1. Scanning electron microscopic images of 6 wt.% nanotube filled PP/HNT (a) and PP/ QM-HNT (b) nanocomposites – A : aggregates of nanotubes

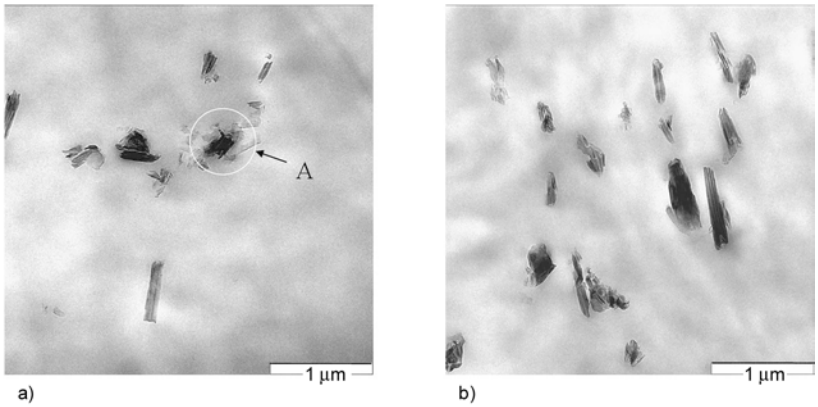

Figure 2. Transmission electron microscopic images of 6 wt.% nanotube filled PP/HNT (a) and PP/QM-HNT (b) nanocomposites – A : aggregates of nanotubes

in modified halloysites filled nanocomposites. The improved dispersion of QM-HNT in PP may be explained by the fact that functional groups brought by quaternary ammonium salt present on the surface of halloysites decreases their surface free energy and hinders nanotube/nanotube interaction, thereby breaking up the aggregates during the extrusion process, and further improves the interface between fillers and the PP matrix. Besides, significant differences are also observed when considering the amount of individual nanotubes dispersed in the matrix, which is higher in the case of QM-HNTs. Overall microscopic analysis indicates that halloysite nanotubes are distributed and dispersed quite homogenously throughout the PP matrix with a good adhesion between nanotubes and PP, a slightly better dispersion being however noticed when QM-HNTs were used as filler.

3.1.2. Crystallinity

As the matrix crystallinity may have an influence on mechanical properties of nanocomposites, non-isothermal DSC experiment was also carried out. Figure 3 shows the crystallization curves obtained during cooling of the PP/HNTs (Figure 3a) and PP/QM-HNTs (Figure 3b) nanocomposites at different nanotube loadings. Relative degree of crystallinity (X_c) values of the various nanocomposites are reported in Table 1. The crystallization behaviour of polypropylene is affected by the addition of

Table 1. Crystallization temperature (T_c), melting temperature (T_m), heat of fusion (ΔH_m) and degree of crystallinity (X_c) values for PP/HNT and PP/QM-HNT nanocomposites

Material	T_m [°C]	T_c [°C]	ΔH_m [J/g]	X_c [%]
PP	163.2	105.7	85.90	41.1
PP + 2 wt.% HNT	163.5	117.6	90.07	44.0
PP + 4 wt.% HNT	163.4	117.2	92.10	45.9
PP + 6 wt.% HNT	163.3	116.3	90.41	46.0
PP + 8 wt.% HNT	163.4	116.7	88.72	45.2
PP + 2 wt.% QM-HNT	163.3	116.6	93.25	45.5
PP + 4 wt.% QM-HNT	163.7	116.5	94.74	47.2
PP + 6 wt.% QM-HNT	163.2	117.5	94.85	48.3
PP + 8 wt.% QM-HNT	163.3	117.4	90.98	47.3

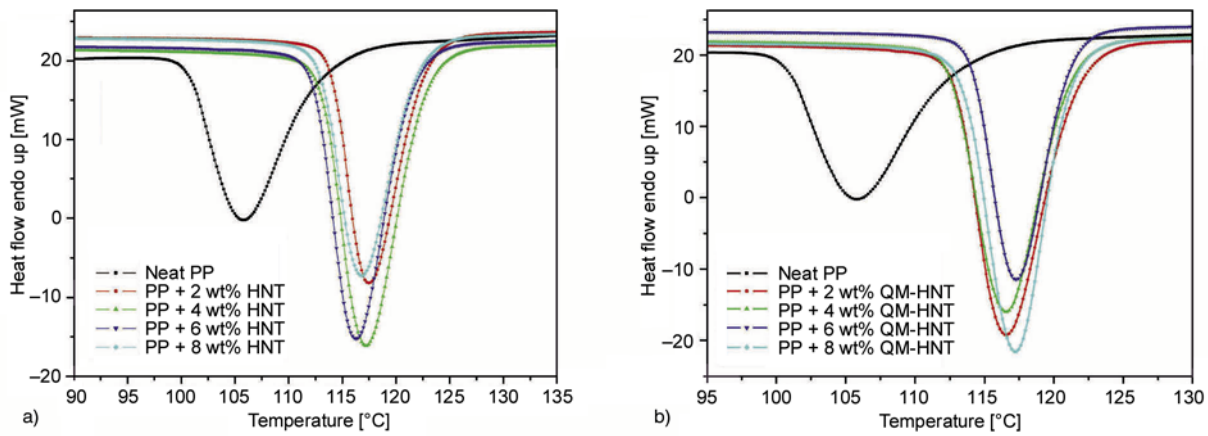

Figure 3. DSC cooling thermograms of the PP/HNT (a) and PP/QM-HNT (b) nanocomposites at different nanotube loadings

halloysite nanotube. The crystallinity (X_c) of PP/HNTs increased from 41.1% up to 45%±1% and 46.6%±1.6% after adding HNTs and QM-HNTs, respectively. The increase is maximum and reaches in relative values, compared to neat PP, +12% (respectively +17.6%) at an halloysite content of 6 wt.%. These results further indicate that halloysites may act as nucleation sites for the crystallization of polypropylene and accelerate the crystallization process in PP matrix by increasing the growth rate of spherulite [41]. The spherulite size may also reduce upon addition of HNTs. Significantly higher crystallinity and lower spherulite size may partly contribute to the enhancement of mechanical properties (increase in modulus and strength) of the nanocomposites (see section 3.4). However, decrease in percentage crystallinity was observed for 8 wt.% halloysite filled nanocomposites. This may be ascribed to the fact that, dispersions of halloysites become poor at relatively higher halloysite content and this hinders the increase of crystallinity in the nanocomposites.

3.2. Thermal properties

Crystallization temperature (T_c) and melting temperature (T_m) values of the various nanocomposites are also reported in Table 1. Compared to neat PP, no significant change is observed in the melting point T_m of polypropylene nanocomposites, which is logical as halloysites are mineral fillers. On the contrary, the addition of halloysite nanotubes to the polypropylene matrix induces an increase in crystallization temperature T_c by more than 10°C. The crystallization peak appears at 105.7°C for the PP matrix and shifts to higher temperatures as the amount of nanotube increases, confirming that halloysites nanotubes act as nucleating agents. Similar behavior has been reported previously in literature for other polypropylene based nanocomposites (with CNTs or MMT) [42–43]. There is no clear or significant dependence of T_c on halloysite nanotube amount. The crystallization peak also appears to be narrower in the case of all nanocomposites.

3.3. Dynamic mechanical properties.

The dynamic mechanical properties of PP and its nanocomposites, with unmodified and modified halloysite nanotubes, are represented in Figures 4 and 5. Figure 4 shows the dynamic storage modulus as a function of temperature for PP and its nanocomposites. The results clearly indicate that, storage modulus (E') of all nanocomposites (modified and unmodified) is higher than that of neat PP. Storage modulus of PP increases with increasing halloysites content, which is due to the reinforcement effect and restrictions in the chain mobility. This means that the incorporation of halloysites into PP matrix remarkably enhances stiffness and load bearing capability of the material. Furthermore, increase in storage modulus for the nanocomposites bearing modified halloysites i.e. PP/QM-HNTs (Figure 4b) is much higher than that of nanocomposites bearing as received halloysites i.e. PP/HNTs (Figure 4a). The rate of increase of storage modulus with increase in QM-HNTs content in the matrix is more pronounced than that of PP/HNTs references. This illustrates the more efficient stiffening/reinforcement effect of QM-HNTs. The increase in the modulus confirms the formation of highly dispersed nanocomposites with improved interfacial interactions

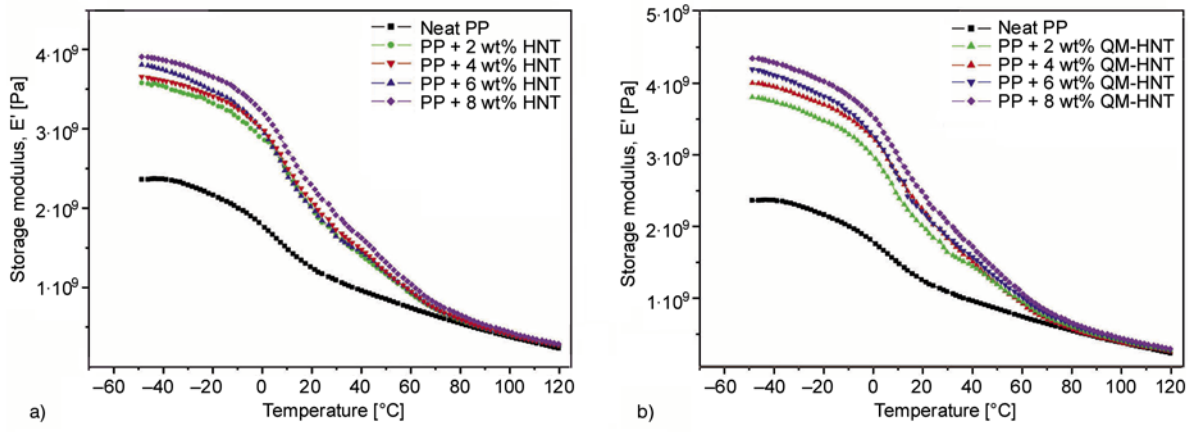

Figure 4. Storage modulus (E') with temperature sweep as a function of nanotube content for PP/HNT (a) and PP/QM-HNT (b) nanocomposites

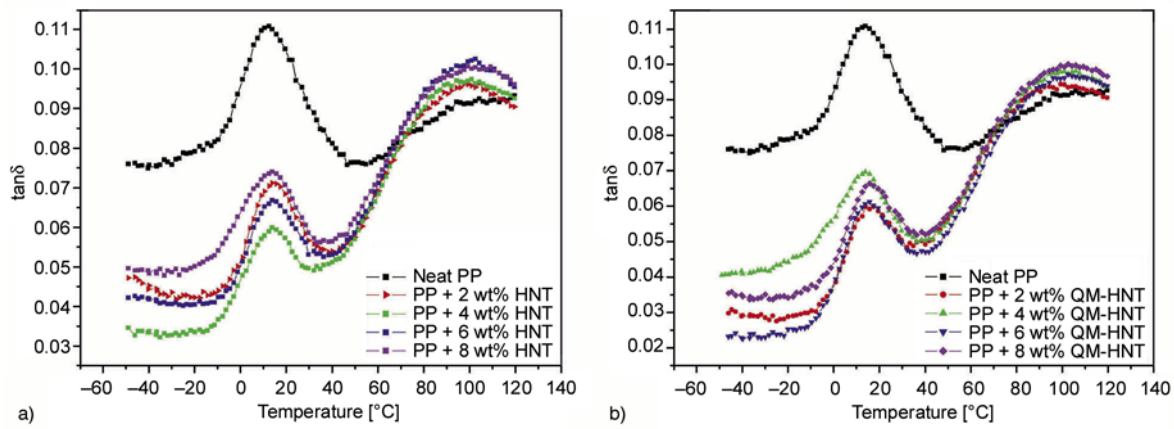

Figure 5. Tanδ with temperature sweep as a function of nanotube content for PP/HNT (a) and PP/QM-HNT (b) nanocomposites

Table 2. Glass transition temperature (T_g) and tanδ of PP/HNTs and PP/QM-HNTs nanocomposites

Material	T_g [°C]	tanδ at peak
PP	12.5	0.107
PP + 2 wt.% HNT	13.9	0.076
PP + 4 wt.% HNT	13.8	0.060
PP + 6 wt.% HNT	12.5	0.066
PP + 8 wt.% HNT	13.8	0.067
PP + 2 wt.% QM-HNT	15.6	0.060
PP + 4 wt.% QM-HNT	15.7	0.069
PP + 6 wt.% QM-HNT	13.8	0.061
PP + 8 wt.% QM-HNT	13.9	0.066

between nanotubes and matrix as evidenced by the microscopy analysis.

Figure 5 illustrates the effect of halloysite nanotubes on the loss factor (tanδ) for PP nanocomposites. The glass transition temperatures T_g of prepared nanocomposites, derived from log tanδ–T curves (temperature at peak tanδ), are slightly higher than that of neat PP in general (except 6 wt.% HNT nanocomposites, which showed a T_g value similar to PP) (Table 2). All QM-HNTs filled nanocomposites showed T_g values, higher than neat PP and PP/HNTs nanocomposites (Table 2). It is well known that the T_g of a polymer depends on the mobility of the chain segment of the macromolecules in the polymer matrix. If the molecular chain is restricted, motion or relaxation of the chain segment becomes difficult at the original glass transition temperature and becomes easy at higher temperature [44]. Therefore, the increase in T_g values may be related to the degree of nanotubes homogeneous dispersion in the polymer matrix and the interactions between the filler and polymer, which is consistent with the reported literature on PP/clay [44].

3.4. Mechanical properties

3.4.1. Tensile properties

The effect of both untreated and treated halloysite nanotubes on the tensile properties of PP is depicted in Figure 6. It is evident that with the incorporation of HNTs, tensile strength (determined as the maximum of the stress-strain curve, i.e. the yield stress)

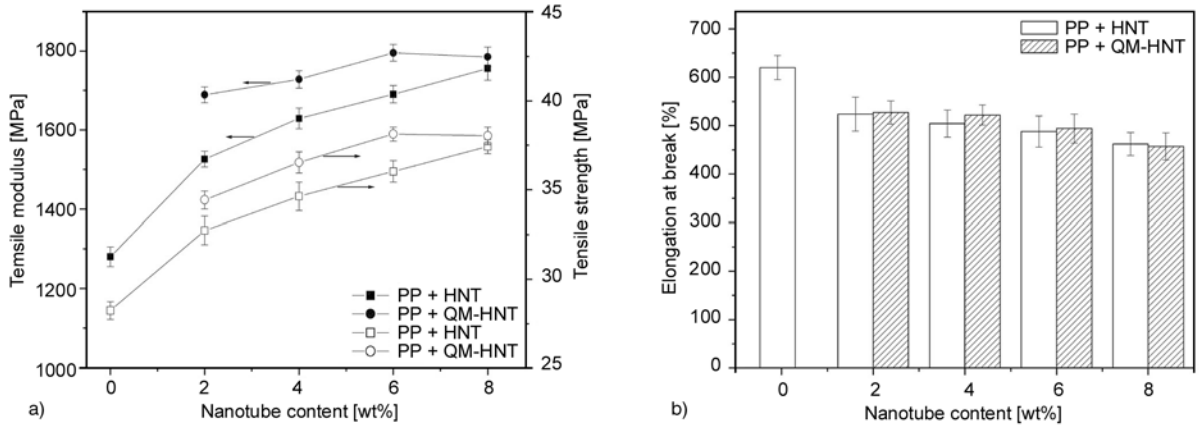

Figure 6. Tensile properties (a) and elongation at break (b) of PP/HNT and PP/QM-HNT nanocomposites

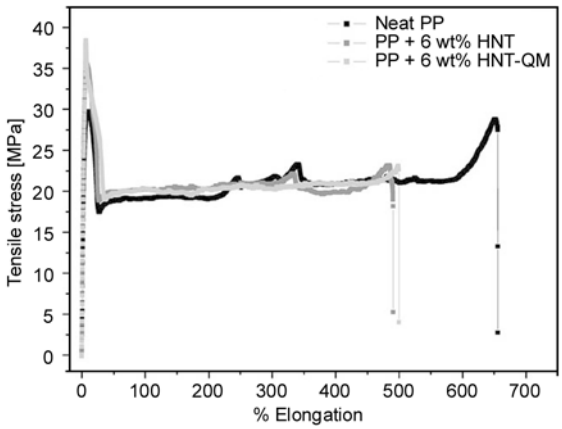

Figure 7. The typical tensile stress-starin curves of PP/HNT and PP/QM-HNT nanocomposites

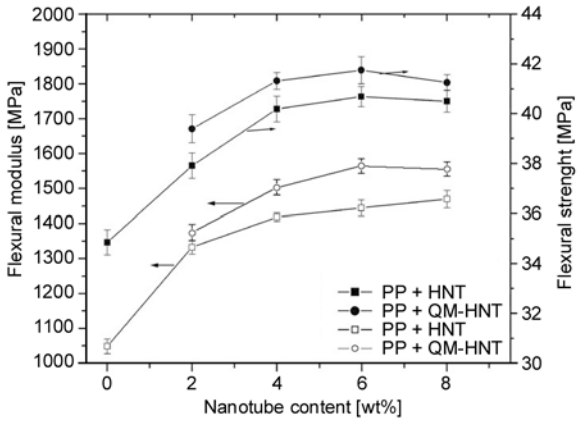

Figure 8. Flexural properties of PP/HNT and PP/QM-HNT nanocomposites.

and tensile modulus (Figure 6a) of PP gradullay increase with increase in nanotube content with a slight reduction (–15 to –25%) in the elongation at break (Figure 6b), indicating the reinforcing benefits of halloysites within PP matrix. The percentage increase ranges from 19 to 37% for Young's modulus and from 15 to 32.5 % for yield stress, depending on HNT concentration. In case of modified halloysites (QM-HNTs), this increase ranges from 32 to 40% for Young's modulus and from 22 to 35% for yield stress, a plateau being achieved at a nanotubes content of 6 wt.%. The typical tensile stress–strain curves of nanocomposite samples at optimized halloysite content i.e. at 6 wt.% halloysites is shown in Figure 7.

Overall results indicate that the improvement range of the mechanical properties, compared to neat PP, is larger for PP/QM-HNTs than for PP/HNTs nanocomposites. These results suggest that the utilization of surface modified nanotubes is essential to achieve higher strength and stiffness at very low nanofiller concentrations. Increase in tensile strength and modulus in PP/QM-HNTs nanocomposites without much loss in ductility (i.e. elongation at break) may be explained by better dispersion of the nanotubes within the matrix as well as improved inter-tubular and interfacial interactions between the QM-HNTs and PP matrix. Similar trends have been reported by Pasbakhsh *et al*. for ethylene propylene diene monomer/modified halloysite nanocomposites [45].

3.4.2. Bending properties

To further assess the reinforcing efficiency of halloysites, flexural properties of the modified and unmodified halloysite nanotubes filled PP nanocomposites were also investigated (Figure 8). It appears that addition of halloysite nanotubes leads to an improvement in the flexural modulus and strength of PP. As shown in Figure 7, the maximum percentage increase is about 43% for bending modulus and 16% for bending strength in case of as received halloysites (HNTs), whereas it reaches again slightly higher values, about 49% for bending modulus and 20% for bending strength, in case of modified halloysites. A nanotube content of 6 wt.% appear to be an optimal value as flexural properties tend to reach a plateau above this value (and sometimes even decrease). Decrease in flexural properties at higher loadings (i.e. 8 wt.% QM-HNTs) is due to the fact that overloadings of halloysites leads to agglomeration of nanotubes, such micron-sized aggregates acting as weak points and failure initiation sites. Similar observations have been reported by Liu *et al*. [46], for halloysites filled epoxy nanocomposites.

3.4.3. Impact properties

The effect of halloysite loadings on the notched Charpy impact strength of PP/HNTs and PP/QM-HNTs nanocomposite is shown in Figure 9. It can be seen that the impact strength of all nanocomposites irrespective of filler type increases with increase in nanotube content. The maximum increase, reaching 70 , was here again found at 6 wt.% nanotube loadings. Further addition of halloysite nanotubes reduces the impact strength of nanocomposites. The decrease in impact strength at higher halloysite loadings (i.e. at 8 wt.%) is due to the fact that the increase in nanotubes content leads to the formation

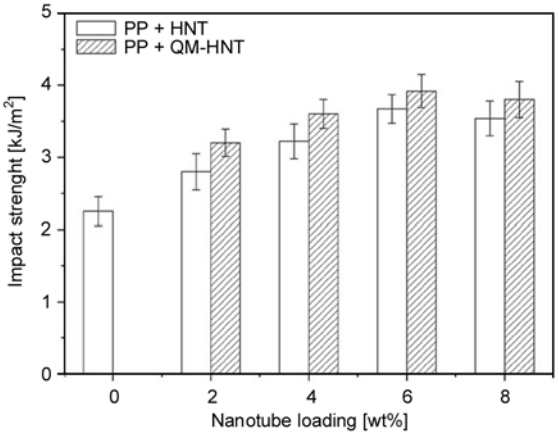

Figure 9. Notched Charpy properties of PP/HNT and PP/QM-HNT nanocomposites

of aggregates, which acts as a stress concentrator in the sample, which intiates a brittle failure. Increase in impact strength for the PP/HNTs is due to the intrinsic toughening properties of the halloysites [23]. Impact strength of notched PP/QM-HNTs samples showed slightly better resistance than that of PP/HNT samples (Figure 9). This is attributed to the fact that modifier on the surface of halloysites promotes the efficient interfacial shear stress transfer between PP and halloysites. A better interfacial interaction could lead to improvement of impact strength with high absorption energy during impact deformation. Figure 10 illustrates the fractured surface of high energy consumed i.e. 6 wt.% filled PP/HNT and PP/QM-HNTs nanocomposites. Nanotube pullout (marked 'A') and nanotube breakage (marked 'B') may be clearly seen for PP/HNTs nanocomposites (Figure 10a). In case of PP/QM-HNT nanocomposites, in addition to nanotube pullout and breakage, nanotube bridging (marked 'C') seems to be another possible toughening factor (Figure 10b). Also, higher impact energy for PP/QM-HNTs nanocomposites is due to the better dispersion and distribution of modified nanotubes in the matrix. In addition, large aspect ratio of nanotubes would cause complex matrix-filler interaction during nanotube bridging, breaking and pullout, which probably promotes the local plastic deformation of matrix [47].

3.4.4. Comparison of halloysites reinforcement potential with other nanofillers

It is also worth comparing the reinforcement potential of halloysites with other nanofillers, such as carbon nanotubes (e.g. MWNT [9]) or layered silicates (e.g. MMT clay [48, 49]) melt-compounded with PP using similar processing conditions. Table 3 shows the percentage variations of mechanical properties of PP nanocomposites containing similar amounts (2 or 4 wt.%) of MWNTs, MMT and QM-HNTs compared to neat PP matrix. The order of magnitude of the increase in moduli and strengths observed in tension, bending and notched Charpy impact is globally the same for the three nanofillers. However, whereas the elongation at break decreases drastically by –75% for carbon nanotubes and by about –80% for montmorillonite, it remains almost unaltered for halloysites (property loss less than 20%). It is also worth noting that, compared to montmorillonite, halloysite nanotubes yield a significantly higher increase in impact resistance, the percentage variation being even higher when the nanofiller weight content tends to reach its optimum value. Table 3 thus compares the percentage variations of mechanical properties of PP nanocomposites containing different nanofillers at their optimum loadings, which is 2 wt.% for MWNT/PP, 4 wt.% for MMT/PP, 6 wt.% for QM-HNTs/PP. Halloysites clearly provide the best reinforcement potential compared with carbon nanotubes and montmorillonite. Whereas the same (if not higher)

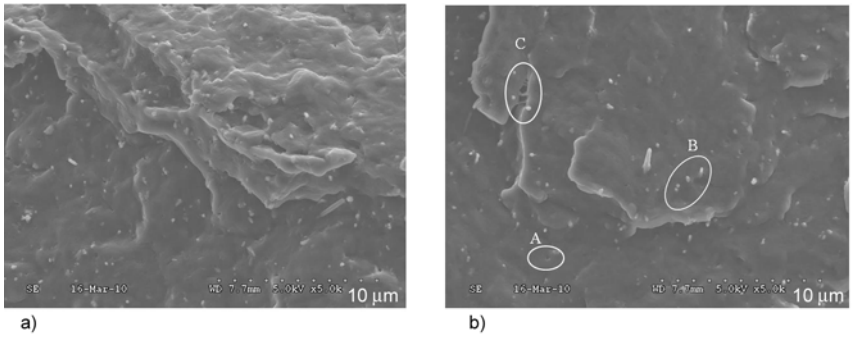

Figure 10. Fracture surface of notched Charpy impact tested samples for 6 wt.% nanotube filled PP/HNT (a) and PP/QM-HNT (b) nanocomposites – A: nanotube pullout ; B: nanotube breakage ; C: nanotube bridging

Table 3. Percentage variations of mechanical properties of nanocomposites containing MWNT, MMT and HNTs nanofillers (compared with neat PP matrix)

Mechanical properties		Property percentage variation (compared with neat PP matrix) of nanocomposites containing same amounts of fillers					Property percentage variation at optimum loading* (compared with neat PP matrix)		
		2 wt.% MWNT/PP [9]	2 wt.% MMT/PP [48, 49]	2 wt.% QM-HNT/PP	4 wt.% MMT/PP [48, 49]	4 wt.% QM-HNT/PP	2 wt.% MWNT/PP [9]	4 wt.% MMT/PP [48, 49]	6 wt.% QM-HNT/PP
Tensile	Modulus	+35%	+33%	+32%	+47%	+35%	+35%	+47%	+40%
	Strength (yield stress)	+26%	+11%	+22%	+12%	+29%	+26%	+12%	+35%
	Elongation at break	–75%	–79%	–15%	–83%	–18%	–75%	–83%	–21%
Bending	Modulus	+ 47%	+45%	+30%	+46%	+44%	+ 47%	+46%	+48%
	Strength (max. stress)	+23%	+29%	+17%	+28%	+20%	+23%	+28%	+23%
Charpy impact	Notched	+37%	+24%	+37%	+28%	+60%	+37%	+28%	+77%

*Optimum loading is 2 wt.% for MWNT/PP, 4 wt.% for MMT/PP, 6 wt.% for QM-HNT/PP

percentage increases of moduli and strength in tension and bending are noticed for the three nanofillers, halloysites are characterized by almost no reduction (–21% only) of the elongation at break and a huge (+77%) percentage increase in impact strength.

These results may be explained by the fact that carbon nanotubes have a tendency to form agglomerates in the composites. Similarly montmorillonite clay suffers from a lack of formation of an exfoliated clay network structure and a mere dispersion of tactoids in the PP matrix. These tactoids and agglomerates usually act as crack initiation sites leading to sudden failure of the material. Comparatively, halloysite nanotubes are less prone to form agglomerates. Additionally, halloysites are discrete nanofillers with no or little surface charge and therefore, halloysite nanotubes may not require the intercalation and exfoliation process, as required by nanoclay fillers (33). These results indicate an obvious advantage in using halloysite over clays or carbon nanotubes, as filler for polymer composites.

4. Conclusions

Natural nanotubes (halloysites) filled polypropylene nanocomposites were successfully prepared by an industrially benign masterbatch dilution technique using high shear extrusion process followed by injection molding.

The influence of addition of both unmodified halloysite nanotubes (HNTs) and quaternary ammonium salt modified halloysite nanotubes (QM-HNTs) on structural and mechanical and properties of polypropylene (PP) nanocomposites was investigated for different halloysites weight contents. Differential scanning calorimetry showed that both degree of crystallinity and crystallization temperature increase upon addition of halloysites into PP, thus indicating a potential nucleation effect induced by the nanotubes. Scanning and transmission electron microscopy highlighted an homogeneous distribution and dispersion of nanotubes throughout the PP matrix, with a slightly better dispersion in the case of QM-HNTs compared to HNTs. Dynamic mechanical analysis evidenced a slight increase in glass transition temperature as well as an improvement in storage modulus with the incorporation of halloysites, more important for QM-HNTs than for HNTs. Mechanical tests demonstrated that strength and modulus of the nanocomposites significantly increase with addition of halloysites without significant loss of ductility. A halloysite content of 6 wt.% appears to be optimum as mechanical properties in tension, bending and impact tend to reach a plateau or even to decrease above this value. Quarternary ammonium salt modified halloysites (QM-HNTs) lead to globally better performances, which has been ascribed to the synergistic effects of surface modified nanotubes and well dispersed nanotubes on a nano-scale in the PP matrix, and in a lesser extent to the increase in the crystallinity.

Acknowledgements

The authors are grateful to the Nord-Pas-de-Calais Region and to the European Community (FEDER) for having partly funded the DMA equipment in the frame of the International Campus on Safety and Intermodality in Transportation (CISIT).

References

[1] Alexandre M., Dubois P.: Polymer-layered silicate nanocomposites: Preparation, properties and uses of a new class of materials. Material Science and Engineering: Review, **28**, 1–63 (2000).
DOI: 10.1016/S0927-796X(00)00012-7

[2] Prashantha K., Soulestin J., Lacrampe M. F., Krawczak P.: Present status and key challenges of carbon nanotubes reinforced polyolefins: A review on nanocomposites manufacturing and performance issues. Polymers and Polymer Composites, **17**, 205–245 (2009).

[3] Shi Z., Gao X., Song D., Zhou Y., Yan D.: Preparation of poly(ε-caprolactone) grafted titanate nanotubes. Polymer, **48**, 7516–7522 (2007).
DOI: 10.1016/j.polymer.2007.10.037

[4] Laine R. M., Choi J. W., Lee I.: Organic-inorganic nanocomposites with completely defined interfacial interactions. Advanced Materials, **13**, 800–803 (2001).
DOI: 10.1002/1521-4095(200106)13:11<800::AID-ADMA800>3.0.CO;2-G

[5] Rong M. Z., Zhang M. Q., Pan S. L., Lehmann B., Friedrich K.: Analysis of the interfacial interactions in polypropylene/silica nanocomposites. Polymer International, **53**, 176–183 (2004).
DOI: 10.1002/pi.1307

[6] Kelnar I., Khunova V., Kotek J., Kaprálková L.: Effect of clay treatment on structure and mechanical behavior of elastomer-containing polyamide 6 nanocomposite. Polymer, **48**, 5332–5339 (2007).
DOI: 10.1016/j.polymer.2007.06.062

[7] Lim J. S., Noda I., Im S. S.: Effect of hydrogen bonding on the crystallization behavior of poly(3-hydroxybutyrate-co-3-hydroxyhexanoate)/silica hybrid composites. Polymer, **48**, 2745–2754 (2007).
DOI: 10.1016/j.polymer.2007.03.034

[8] Bao S. P., Tjong S. C.: Mechanical behaviors of polypropylene/carbon nanotube nanocomposites: The effects of loading rate and temperature. Material Science and Engineering: A, **485**, 508–516 (2008).
DOI: 10.1016/j.msea.2007.08.050

[9] Prashantha K., Soulestin J., Lacrampe M. F., Krawczak P., Dupin G., Claes M.: Masterbatch-based multiwalled carbon nanotube filled polypropylene nanocomposites: Assessment of rheological and mechanical properties. Composites Science and Technology, **69**, 1756–1763 (2009).
DOI: 10.1016/j.compscitech.2008.10.005

[10] Prashantha K., Soulestin J., Lacrampe M. F., Krawczak P., Dupin G., Claes M.: Taguchi analysis of shrinkage and warpage of injection-moulded polypropylene/multiwall carbon nanotubes nanocomposites. Express Polymer Letters, **3**, 630–638 (2009).
DOI: 10.3144/expresspolymlett.2009.79

[11] Zhang H., Zhang Z.: Impact behaviour of polypropylene filled with multi-walled carbon nanotubes. European Polymer Journal, **43**, 3197–3207 (2007).
DOI: 10.1016/j.eurpolymj.2007.05.010

[12] López Manchado M. A., Valentini L., Biagiotti J., Kenny J. M.: Thermal and mechanical properties of single-walled carbon nanotubes–polypropylene composites prepared by melt processing. Carbon, **43**, 1499–1505 (2005).
DOI: 10.1016/j.carbon.2005.01.031

[13] Hári J., Dominkovics Z., Fekete E., Pukánszky B.: Kinetics of structure formation in PP/layered silicate nanocomposites. Express Polymer Letters, **3**, 692–702 (2009).
DOI: 10.3144/expresspolymlett.2009.87

[14] Chinellato A. C., Vidotti S. E., Hu G-H., Pessan L. A.: Compatibilizing effect of acrylic acid modified polypropylene on the morphology and permeability properties of polypropylene/organoclay nanocomposites. Composites Science and Technology, **70**, 458–465 (2010).
DOI: 10.1016/j.compscitech.2009.11.020

[15] Betega de Paiva L., Morales A. R., Ribeiro Guimarães T.: Structural and optical properties of polypropylene–montmorillonite nanocomposites. Materials Science and Engineering: A, **447**, 261–265 (2007).
DOI: 10.1016/j.msea.2006.10.066

[16] Papageorgiou G. Z., Achilias D. S., Bikiaris D. N., Karayannidis G. P.: Crystallization kinetics and nucleation activity of filler in polypropylene/surface-treated SiO_2 nanocomposites. Thermochimica Acta, **427**, 117–128 (2005).
DOI: 10.1016/j.tca.2004.09.001

[17] Mubarak Y. A., Abbadi F. O., Tobgy A. H.: Effect of iron oxide nanoparticles on the morphological properties of isotactic polypropylene. Journal of Applied Polymer Science, **115**, 3423–3433 (2010).
DOI: 10.1002/app.31374

[18] Causin V., Marega C., Marigo A., Ferrara G., Ferraro A.: Morphological and structural characterization of polypropylene/conductive graphite nanocomposites. European Polymer Journal, **42**, 3153–3161 (2006).
DOI: 10.1016/j.eurpolymj.2006.08.017

[19] Yang K., Yang Q., Li G., Sun Y., Feng D.: Morphology and mechanical properties of polypropylene/calcium carbonate nanocomposites. Materials Letters, **60**, 805–809 (2006).
DOI: 10.1016/j.matlet.2005.10.020

[20] Guo B., Lei Y., Chen F., Liu X., Du M., Jia D.: Styrene–butadiene rubber/halloysite nanotubes nanocomposites modified by methacrylic acid. Applied Surface Science, **255**, 2715–2722 (2008).
DOI: 10.1016/j.apsusc.2008.07.188

[21] Liu M., Guo B., Zou Q., Du M., Jia D.: Interactions between halloysite nanotubes and 2,5-bis(2-benzoxazolyl) thiophene and their effects on reinforcement of polypropylene/halloysite nanocomposites. Nanotechnology, **19**, 205709 (2008).
DOI: 10.1088/0957-4484/19/20/205709

[22] Ye Y., Chen H., Wu J., Ye L.: High impact strength epoxy nanocomposites with natural nanotubes. Polymer, **48**, 6426–6433 (2007).
DOI: 10.1016/j.polymer.2007.08.035

[23] Deng S., Zhang J., Ye L., Wu J.: Toughening epoxies with halloysite nanotubes. Polymer, **49**, 5119–5127 (2008).
DOI: 10.1016/j.polymer.2008.09.027

[24] Marney D. C. O., Russell L. J., Wu D. Y., Nguyen T., Cramm D., Rigopoulos N., Wright N., Greaves M.: The suitability of halloysite nanotubes as a fire retardant for nylon 6. Polymer Degradation and Stability, **93**, 1971–1978 (2008).
DOI: 10.1016/j.polymdegradstab.2008.06.018

[25] Ismail H., Pasbakhsh P., Fauzi M. N. A., Abu Bakar A.: Morphological, thermal and tensile properties of halloysite nanotubes filled ethylene propylene diene monomer (EPDM) nanocomposites. Polymer Testing, **27**, 841–850 (2008).
DOI: 10.1016/j.polymertesting.2008.06.007

[26] Hedicke-Höchstötter K., Lim G. T., Altstädt V.: Novel polyamide nanocomposites based on silicate nanotubes of the mineral halloysite. Composites Science and Technology, **69**, 330–334 (2009).
DOI: 10.1016/j.compscitech.2008.10.011

[27] Du M., Guo B., Lei Y., Liu M., Jia D.: Carboxylated butadiene–styrene rubber/halloysite nanotube nanocomposites: Interfacial interaction and performance. Polymer, **49**, 4871–4876 (2008).
DOI: 10.1016/j.polymer.2008.08.042

[28] Ning N-Y., Yin Q-J., Luo F., Zhang Q., Du R., Fu Q.: Crystallization behavior and mechanical properties of polypropylene/halloysite composites. Polymer, **48**, 7374–7384 (2007).
DOI: 10.1016/j.polymer.2007.10.005

[29] Du M., Guo B., Jia D.: Thermal stability and flame retardant effects of halloysite nanotubes on poly(propylene). European Polymer Journal, **42**, 1362–1369 (2006).
DOI: 10.1016/j.eurpolymj.2005.12.006

[30] Liu M., Guo B., Du M., Chen F., Jia D.: Halloysite nanotubes as a novel β-nucleating agent for isotactic polypropylene. Polymer, **50**, 3022–3030 (2009).
DOI: 10.1016/j.polymer.2009.04.052

[31] Liu M., Guo B., Lei Y., Du M., Jia D.: Benzothiazole sulfide compatibilized polypropylene/halloysite nanotubes composites. Applied Surface Science, **255**, 4961–4969 (2009).
DOI: 10.1016/j.apsusc.2008.12.044

[32] Du M., Guo B., Lei Y., Jia D.: Thermal decomposition and oxidation ageing behaviour of polypropylene/halloysite nanotube nanocomposites. Polymers and Polymer Composites, **15**, 321–328 (2007).

[33] Du M., Guo B., Jia D.: Newly emerging applications of halloysite nanotubes: A review. Polymer International, **59**, 574–582 (2010).
DOI: 10.1002/pi.2754

[34] Liu M. X., Guo B. C., Du M. L, Cai X. J., Jia D. M.: Properties of halloysite nanotube-epoxy resin hybrids and the interfacial reactions in the systems. Nanotechnology, **18**, 455703 (2007).
DOI: 10.1088/0957-4484/18/45/455703

[35] Vergaro V., Abdullayev E., Lvov Y. M., Zeitoun A., Cingolani R., Rinaldi R., Leporatti St.: Cytocompatibility and uptake of halloysite clay nanotubes. Biomacromolecules, **11**, 820–826 (2010).
DOI: 10.1021/bm9014446

[36] Grossiord N., Loos J., Regev O., Koning C. E.: Toolbox for dispersing carbon nanotubes into polymers to get conductive nanocomposites. Chemistry and Materials, **18**, 1089–1099 (2006).
DOI: 10.1021/cm051881h

[37] Andrews R., Jacques D., Minot M., Rantell T.: Fabrication of carbon multiwall nanotube/polymer composites by shear mixing. Macromolecular Materials and Engineering, **287**, 395–403 (2002).
DOI: 10.1002/1439-2054(20020601)287:6<395::AID-MAME395>3.0.CO;2-S

[38] Jang G-S., Cho W-J., Ha C-S.: Crystallization behavior of polypropylene with or without sodium benzoate as a nucleating agent. Journal of Polymer Science Part B: Polymer Physics, **39**, 1001–1016 (2001).
DOI: 10.1002/polb.1077

[39] Luyt A. S., Dramićanin M. D., Antić Ž., Djoković V.: Morphology, mechanical and thermal properties of composites of polypropylene and nanostructured wollastonite filler. Polymer Testing, **28**, 348–356 (2009).
DOI: 10.1016/j.polymertesting.2009.01.010

[40] Wang L., Sheng J.: Preparation and properties of polypropylene/org-attapulgite nanocomposites. Polymer, **46**, 6243–6249 (2005).
DOI: 10.1016/j.polymer.2005.05.067

[41] Du M., Gio B., Wan J., Zou Q., Jia D.: Effects of halloysites nanotubes on kinetics and activation energy of non isothermal crystallization of polypropylene. Journal of Polymer Research, **17**, 109–118 (2010).
DOI: 10.1007/s10965-009-9296-5

[42] Logakis E., Pollatos E., Pandis Ch., Peoglos V., Zuburtikudis I., Delides C. G., Vatalis A., Gjoka M., Syskakis E., Viras K., Pissis P.: Structure–property relationships in isotactic polypropylene/multi-walled carbon nanotubes nanocomposites. Composites Science and Technology, **70**, 328–335 (2010).
DOI: 10.1016/j.compscitech.2009.10.023

[43] Krump H., Luyt A. S., Hudec I.: Effect of different modified clays on the thermal and physical properties of polypropylene-montmorillonite nanocomposites. Materials Letters, **60**, 2877–2880 (2006).
DOI: 10.1016/j.matlet.2006.02.006

[44] Zhang Y-Q., Lee J-H.,. Rhee J. M., Rhee K. Y.: Polypropylene–clay nanocomposites prepared by in situ grafting-intercalating in melt. Composites Science and Technology, **64**, 1383–1389 (2004).
DOI: 10.1016/j.compscitech.2003.10.014

[45] Pasbakhsh P., Ismail H., Fauzi M. N. A., Abu Bakar A.: EPDM/modified halloysite nanocomposites. Applied Clay Science, **48**, 405–413 (2010).
DOI: 10.1016/j.clay.2010.01.015

[46] Liu M., Guo B., Du M., Lei Y., Jia D.: Natural inorganic nanotubes reinforced epoxy resin nanocomposites. Journal of Polymer Research, **15**, 205–212 (2008).
DOI: 10.1007/s10965-007-9160-4

[47] Ajayan P. M., Schadler L. S., Giannaris C., Rubio A.: Single-walled carbon nanotube–polymer composites: Strength and weakness. Advanced Materials, **12**, 750–753 (2000).
DOI: 10.1002/(SICI)1521-4095(200005)12:10<750::AID-ADMA750>3.0.CO;2-6

[48] Rothe B.: Influence of clay addition and processing variables on the properties of injection-moulded thermoplastic nanocomposites (in French). Master Thesis, École des Mines de Douai, France (2005).

[49] Fourdrin S., Soulestin J., Lafranche E., Lacrampe M-F., Krawczak P.: Dimensional accuracy and stability of polypropylene-clay nanocomposites injectionmouldings. in 'PPS-23, The Polymer Processing Society 23rd Annual Meeting, Salvador, Brasil' CD-ROM P03-040 (2007).

eXPRESS Polymer Letters Vol.5, No.4 (2011) 308–317
Available online at www.expresspolymlett.com
DOI: 10.3144/expresspolymlett.2011.31

Fabrication of electrospun polyacrylonitrile ion-exchange membranes for application in lysozym

H. T. Chiu[1*], *J. M. Lin*[1], *T. H. Cheng*[2], *S. Y. Chou*[2]

[1]Department of Materials Science and Engineering National Taiwan University of Science and Technology, No.43, Keelung Rd., Section 4, Taipei, Taiwan
[2]Department of Products, Taiwan Textile Research Institute, No. 6, Chengtian Rd., Tucheng City, Taipei County 23674, Taiwan

Received 18 August 2010; accepted in revised form 7 November 2010

Abstract. Ion exchange (IEX) chromatography is commonly used in separation and purification systems. However, micropore blockage within its resin structure can easily lead to a reduction in the effectiveness of purification. To tackle this problem, we adopted the concept of membrane separation by combining electrospinning techniques with rapid alkaline hydrolysis to prepare a weak acid IEX nanofibrous membrane (AEA-COOH), consisting of polyethyleneterephthalate (PET) meltblown fabric as a supporting layer, with upper and lower IEX layers consisting of polyacrylonitrile (PAN) nanofibrous membranes. To determine the characteristics of the AEA-COOH membrane, we used the commercial product Sartobind® C IEX membrane as the standard of comparison. Results showed that the base weight and thickness of AEA-COOH were 33 and 64%, relative to Sartobind® C membrane. The thermo-degradable temperature of AEA-COOH membrane (320°C) was far higher than that of Sartobind® C (115°C), indicating high thermal stability. Finally, comparisons between the lysozyme adsorption rates and capacity of various IEX membranes confirmed that AEA-COOH was lighter, thinner, faster, possessing higher protein adsorption efficiency than Sartobind® C membrane.

Keywords: *polymer membranes, electrospun, nanofiber, ion-exchange, lysozymes adsorption*

1. Introduction

A conventional ion exchange resin usually has a gel or granular structure, composed of styrene or acrylic material [1]. However, micropore structures within the resin result in lower molecular adsorption/desorption rates, due to diffusion distance. With an increase in the pace of processing, the volume of adsorbed molecules increased, and an increase in the frequency of its application rapidly decreased the efficiency of its ion exchange capability, to the point where it was suitable only for smaller molecules. In addition, micropores in traditional resins are easily blocked, which reduces the effectiveness of purification and decreases the regeneration response rate. Furthermore, the resin itself is vulnerable to damage due to pressure [2–3]. To tackle the above problems, the fiber structure of the ion exchange filters has undergone significant development in recent years. Compared to resins of other types of gel or granular structure, fiber structured resins are simple to use, thanks to their large surface area, and possess high adsorption capacity, fast ion exchange and regeneration rate, as well as other unique features [4–6]. It is widely used in dyes, precious metals, protein pharmaceuticals and other high value-added materials during the enrichment and purification; it is also used in wastewater and gas decontamination processes. The potential benefits and value to researchers cannot be overlooked [7–11].

*Corresponding author, e-mail: hchiu@mail.ntust.edu.tw

According to previous studies [12–18], electrospinning is the only direct, efficient, and continuous method for producing polymer nanofibers showing the most promise and greatest efficiency. Hundreds of polymer nanofibers of various kinds have been developed using electrospinning. Electrospinning polymer processing systems deliver polymer solutions to a spin feeder, to form liquid droplets. With the application of a high voltage charge, the electrical charge within the polymer mutually excludes and overcomes the surface tension of the solution. The surface of the droplets spray a charged liquid column, which, under the continuous effect of the electric field, quickly spiral downward to form a lashing extension. The resulting nanofiber is a thousand times thinner than fibers manufactured using normal micro-spinning technology. As the process continues, the solvent in the solution rapidly evaporates. Finally, non-woven membranes of nanometer fiber diameter are collected in the collector plate beneath. By electrospinning, fibers with a diameter between a few dozen to several hundred nanometers could be manufactured. When compared to traditional fibers (diameter of 50 microns) under the same volumetric conditions, these fibers had a smaller diameter pore aperture, more densely interconnected pores and increased porosity. In addition, the specific surface area of nanofibers is approximately 100 times that of normal fibers. Thus, nanofiber membrane filters, when compared to traditional filters, have a higher throughput, lower loss, lower energy consumption, shorter transmission distance, higher adsorption, faster reaction, as well as other advantages [19–21].

Polyacrylonitrile (PAN) possesses high mechanical strength thanks to the strong hydrogen bonding of its molecular structure. It also exhibits strong chemical resistance, excellent acid-proof alkalinity, resistance to sunlight, a diminished susceptibility to humidity, and low cost [22–23]. Thus, it has caught the attention of many researchers, in the past 10 years. It is widely used in the preparation of microfiltration (MF), ultrafiltration (UF) and hollow fiber membranes [24–26]. In addition, PAN molecular chains carry a cyano group, which can be modified. It is hydrolysable and can be adjusted to achieve functionality in a number of applications. If part of the hydrolysis process could be performed with carboxyl functional groups (–COOH) in a solution, it could quickly adsorb metal ions, lysozymes, and other molecules. Its unique features include high absorption capacity, fast absorption speed, and good dynamic performance. It is an excellent material for use in the purification of heavy metal wastewater and lysozymes [27–30].

In this study, we first used electrospinning technology to prepare PAN/PET/PAN nanofiber composite membrane. The nanofiber was stacked into a 3D reticular fiber structure through cross laying. This gave the membrane a high specific surface area, higher porosity (>80%), and micron size membrane pores. With the use of alkaline hydrolysis techniques, high-density carboxyl groups appeared on the surface of PAN nanofibers. This prepared the nanofiber membrane for weak acid ion exchange. During the exchange of ions through the nanofiber membrane shortened the distance in molecular diffusion, thereby accelerating the rate of ion exchange and improving adsorption capacity. Scanning electron microscopy, porosity analysis, and Toluidine Blue O (TBO) functional groups detector were used to analyze micro-porous PAN/PET/PAN structure, patterns, pore size, distribution, and density of nanofiber composite membrane and its functional groups. Finally, the nanofiber composite membrane was compared to commercial product Sartobind® C membrane in order to further explore the different ion exchange membranes in the lysozyme adsorption.

2. Experiments

2.1. Materials

Polyacrylonitrile (PAN) yarn (M_w = 120 000, containing 93% acrylonitrile and 7% vinylacetate) and dimethylacetamide (DMAc) were purchased from Fortune Industries Inc (Tao-Yuan, Taiwan) and I-Chang Chemical Co., Ltd (Taipei, Taiwan), respectively. Sodium hydroxide (NaOH) was from J.T. Baker. Lysozyme and Toluidine Blue O (TBO) were from Sigma. The reagents and solvents were of analytical grade and used without further purification.

2.2. Electrospinning of polyacrylonitrile

Electrospinning device was purchased from Jyi Goang Enterprise Co., Ltd. (Taipei, Taiwan). PAN yarn was dissolved in DMAc at a concentration of 15% (w/v). PAN/DMAc solution was loaded into a

syringe and delivered to the tip of a 21-gauge stainless steel nozzle with a syringe pump. The nozzle was connected to a power supply and charged to 26.5 kV. The electrospinning mats were collected on nonwoven PET (basis weight 15 g/m^2) and wrapped on a grounded steel sheet. The distance between the tip of the nozzle and the substrate was 15.8 cm, the flow rate was 1ml/h, and the collector rotation rate was 24 cm/s. The nozzle was moving along the y-axis (20 cm), and the frequency was 12 times/min.

2.3. Introduction of anionic moieties into PAN nanofiber membranes

Electrospun PAN nanofiber mats were chemically activated by substituting the nitrile groups with anion carboxylic acid groups as an ion exchange material. First, PAN nanofiber mats were alkaline hydrolyzed by immersion in various concentrations (1N, 2N, 3N) of sodium hydroxide stirred (150 rpm) at different temperatures (25–85°C) for 0–40 min. They were washed out with deionized water until no change in pH was apparent. Finally, the carboxylated electrospun PAN nanofiber mat was treated with 0.1M HCl, followed by drying in an oven, at 60°C.

2.4. Characterization of fabrics

The morphology and diameter of electrospun PAN nanofiber mats before and after the introduction of the ion-exchange groups were observed using a scanning electron microscope (SEM, JEOL, and JSM 6510). All samples were sputter-coated with Pt.

Thermogravimetric analysis (TGA) was conducted with TGA Q50 from TA Instruments at a heating rate of 20°C/min under nitrogen. To characterize the crystallinity of the fibers, wide-angle X-ray diffraction (WAXD, SIEMENS, and D5005) patterns of PAN nanofiber membranes under various alkaline hydrolysis conditions were obtained using an X-ray goniometer operating at 40 kV and 30 mA with a scanning speed of 1°/min.

The distribution of pore size and the mean pore size of electrospun PAN nanofiber mats were determined with a measuring instrument (Perm-Porometer, PMI, USA). The porosity and the specific surface area were measured with fully automatic density analyzer (AccuPyc 1330 Pycnometer) and BET apparatus (Micrometritics, ASPS 2000), respectively.

2.5. Adsorption behavior [31–32]

Subsequent to alkaline hydrolysis, the concentration of carboxyl group on the surface of the PAN nanofiber was measured using Toluidine Blue O (TBO) dye. We placed the modified PAN nanofiber membrane in 2 ml 1mM TBO dyeing agent (dissolved in 1 mM NaOH solution, pH = 10), at room temperature for 6 hours. It was cleaned several times with de-ionized water. This was followed by additional cleaning of the membrane using 0.1 mM NaOH to remove TBO dye adsorbed on the surface of the membrane. Then, 2 ml of 50% acetic acid solution was added to remove the TBO dye of carboxyl ionic bond. Finally, UV spectrum absorption was set to a wavelength of 633 nm for quantitative analysis. Using TBO/COOH = 1:1, the number of carboxyl groups on the membrane surface was calculated. Under lysozyme adsorption conditions, in various time frames, at 298 K, with stirring speed of 150 rpm, the lysozyme initial concentration was 0.5 mg/ml (in 20 mM glycine buffer (pH 9)), and the 595 nm absorbance wavelength was measured using Bio-Rad lysozyme concentration analysis. By using the standard concentration curve of lysozyme, the adsorption capacity of lysozyme nanofiber could be obtained.

3. Results and discussion

3.1. Polyacrylonitrile (PAN) nanofiber membranes

This study combines electrospinning nanofibers with rapid alkaline hydrolysis technology, to develop an ion-exchange nanofiber membrane with high

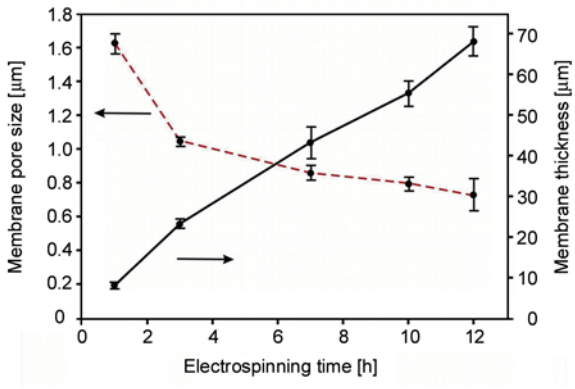

Figure 1. Effect of electrospinning duration on pore size and thickness of PAN nanofiber membranes

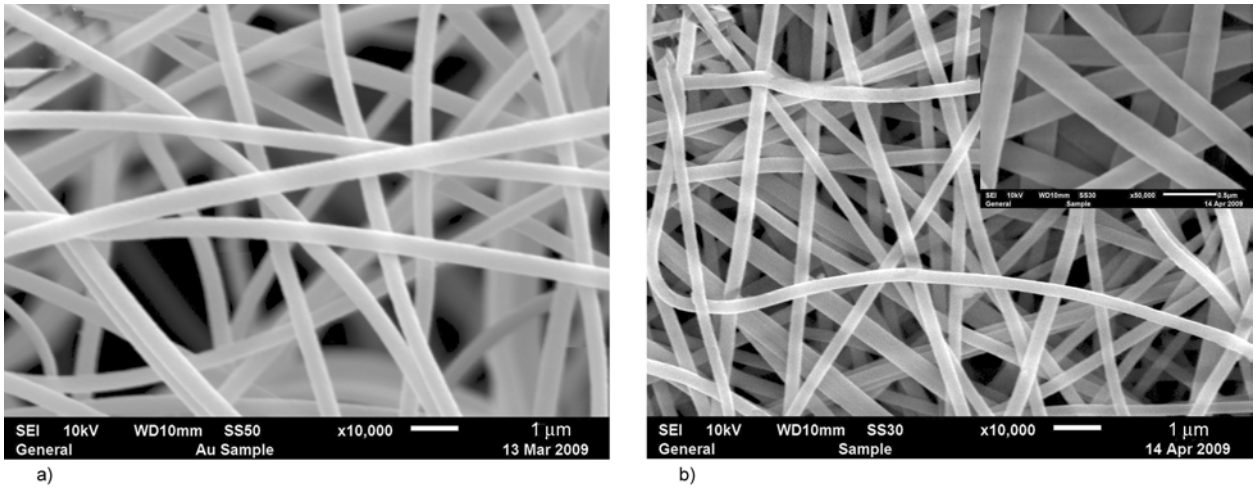

Figure 2. SEM images of electrospun fibers of polyacrylonitrile: (a) electrospinning a PAN nanofiber mat; (b) compacting the mat to increase the volume density of fibers. The insert shows the morphology of nanofibers at a magnification of 50 000.

surface area and high porosity. Figure 1 shows the relationship between the duration of electrospinning and the thickness and average pore size of the electrospun PAN nanofiber membrane. These results indicated that the thickness of nanofiber membrane increased linearly and proportionally to increases in electrospinning duration. Conversely, the average pore diameter declined rapidly over time within the 1–3 h of the spinning time frame, whereupon it was stabilized. The duration of the electrospinning had no significant effect on the pore size of membranes. SEM photos in Figure 2 show electrospun PAN membrane with a loose structure comprising a mat of network of cross-laid nanofibers, with large diametric pores between the fibers. After the heat pressing process, the structure of the membrane increased in density, with an increased in the concentration and distribution of pores. Figure 2b illustrates that variations in the diameter distribution of the PAN nanofiber was uniform, with the average diameter falling between 200–250 nm. Therefore, we selected a PAN nanofiber membrane (thickness: 55.26±2.87 µm, an average pore size: 0.79±0.04 µm), electrospun over a 10 hr period, to serve as the basis for ion-exchange membrane.

3.2. Alkaline hydrolysis of polyacrylonitrile (PAN) nanofiber membranes

Partial hydrolysis is one of the most commonly used methods for PAN-based membranes in the substitution of nitrile groups (–C≡N) with carboxylic acid groups (–COOH) subject to base conditions. The chemical mechanism of alkali hydrolysis reaction is described in detail by Wang *et al.* [27] We used NaOH to quickly and easily alkaline hydrolyze –C≡N bond on the surface of the PAN nanofiber, converting it into COOH functional groups. Figure 3 shows the effects of alkaline hydrolysis on the surface density of COOH PAN nanofibers. Under conditions of fixed alkalization time (10 min) and temperature (25, 40, 55, 70, 85°C), the density of COOH increased, following an increase in the concentration of alkaline hydrolyzed NaOH. The trend of increasing became clear as the temperature of the alkalization increased. When the concentration of NaOH had reached 3N, the COOH density on the PAN nanofiber surface showed the most significant increase.

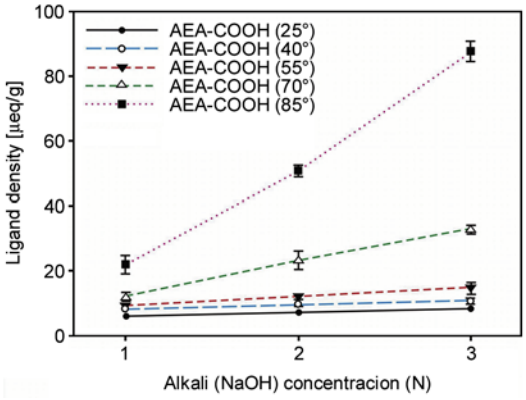

Figure 3. Effect of alkali (NaOH) concentration (N) on carboxylic acid ligand density of AEA-COOH composite membranes

Figure 4 shows the effect of NaOH alkaline hydrolysis temperature on COOH density of the surface of

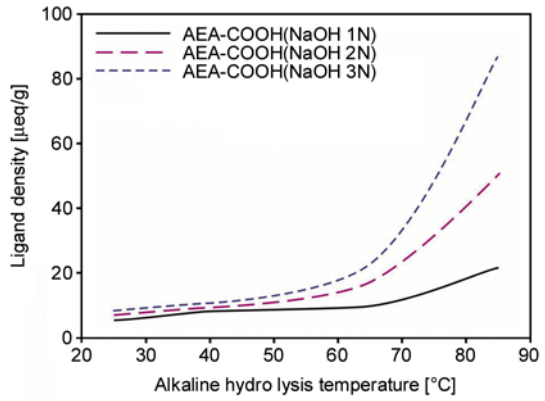

Figure 4. Effect of alkaline hydrolysis temperature on carboxylic acid ligand density of AEA-COOH composite membranes

PAN nanofiber. Under conditions of fixed alkalization time (10 min) and concentration (1N, 2N, 3N), COOH density following an increase in temperature to above 60°C in the alkaline hydrolyzed NaOH. Particularly with a high concentration of NaOH lye, the rate of increase became even more apparent. In addition, the curves in Figure 4 show a critical alkaline hydrolysis temperature in AEA-COOH composite nanofiber membrane. When that temperature was below 60°C, this had little effect on the density of the functional group, but when it increased to above 60°C, COOH the density increased exponentially as a function of temperature.

By TBO dye test analysis, the set COOH density in commercial standard Sartobind® C membrane was determined to be 135.1 μeq/g. Figure 5 shows the effect of NaOH alkaline hydrolysis duration on the COOH density of the PAN nanofiber surface. Under fixed alkalization temperature (85°C) and concentration (3N), when alkaline hydrolysis time for AEA-COOH composite nanofiber membrane was less than 13 minutes, the COOH group density was less than Sartobind® C. However, with a further increase in alkaline hydrolysis duration, PAN nanofiber surface density of COOH groups rapidly increased after 35 minutes. The density of the ionic group was 3.3 times that of the commercial product. After alkaline hydrolysis had continued for more than 60 minutes, the COOH density decreased rapidly to about 1.9 μeq/g. This was due to an overreaction in the hydrolysis reaction, resulting in alkali-soluble conditions in PAN nanofiber (data not shown). Thus, under appropriate reaction conditions, and as the need arose, the density of the functional group AEA-COOH composite nanofiber membrane was modified in order to adjust the duration of alkaline hydrolysis. Yet if Sartobind® C membranes were processed through phase separation, their functional group density could not be adjusted for time, and its operating flexibility was thus limited.

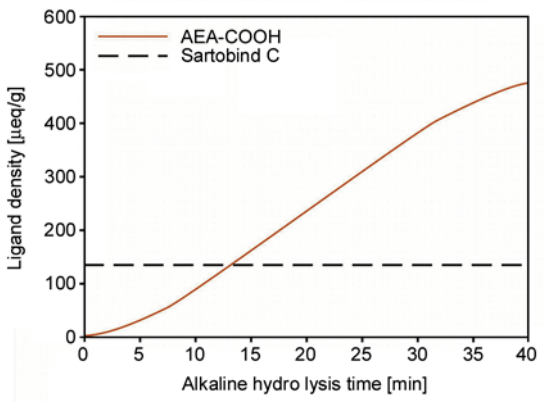

Figure 5. Effect of alkaline hydrolysis time on carboxylic acid ligand density in AEA-COOH composite membranes

3.3. Physical properties of different ion-exchange membranes

Different SEM microstructures of ion exchange membrane are shown in Figure 6. Due to the phase separation process, the surface of the Sartobind® C membrane had an uneven pore distribution; most of the surface area of the membranes was occupied by polymer. Observed by a SEM cross-section view, the Sartobind® C membrane was found to possess an asymmetric structure, which increased its liquid circulation. In this study, the weak acid ion exchange membrane was prepared by electrospinning of PAN nanofiber membrane using NaOH alkaline hydrolysis. Under conditions of fixed alkalization temperature (85°C), concentration (3N), and time (35 min), the membranes were able to maintain the integrity of its nanofiber structure; its surface pore distribution was uniform and dense. With PET serving as an intermediate substrate, it was synthesized into a PAN-PET-PAN (AEA-COOH) asymmetric membrane structure.

Results from PMI pore data test on different membranes showed the relationship between pore distribution [%] and size [μm], as shown in Figure 7. The data confirmed that the pore size distribution on commercial product Sartobind® C membranes was very broad, and its distribution ranged widely from 0.5 to 2.5 μm. The PAN-PET, PAN-PET-PAN ion-

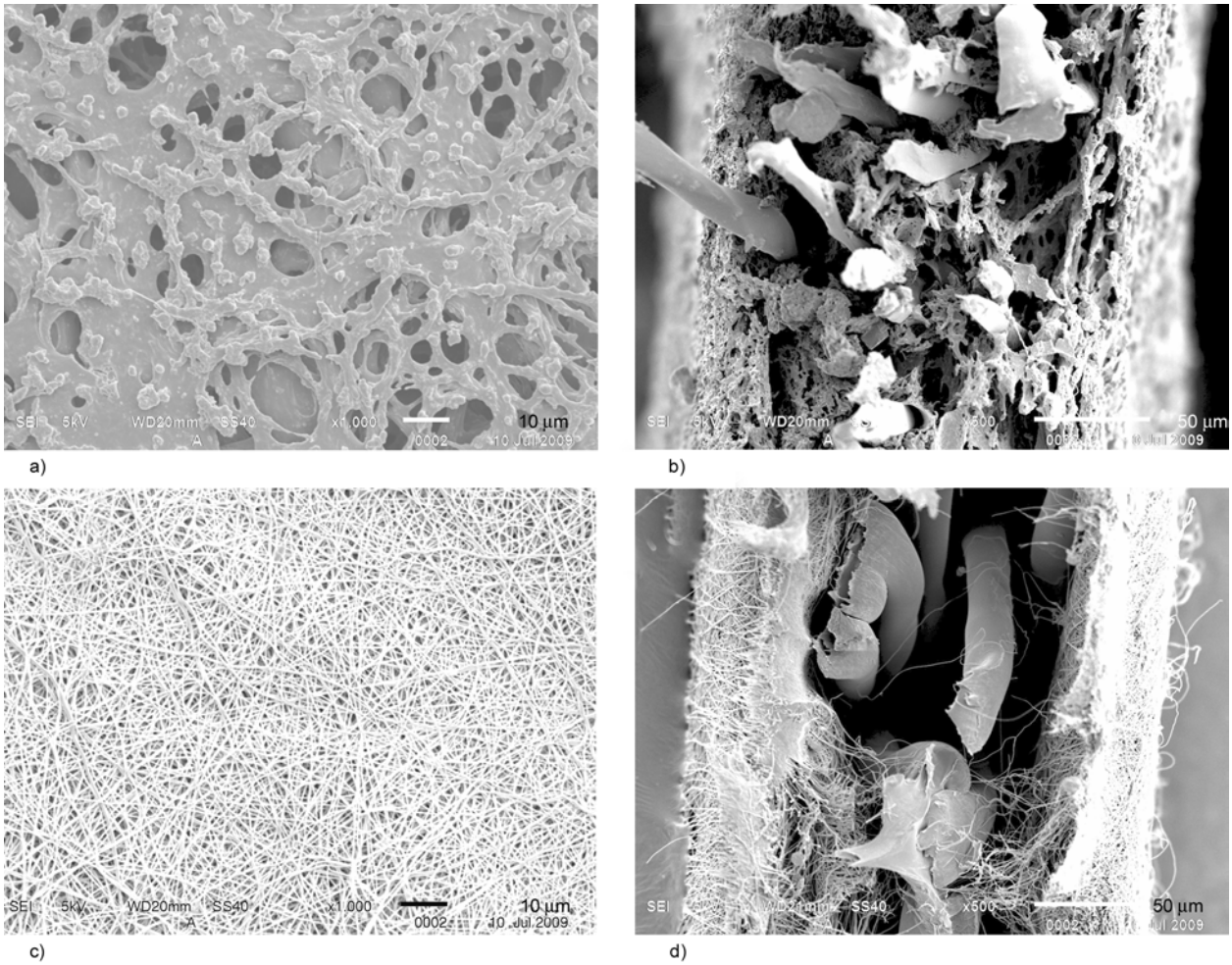

Figure 6. SEM micrographs of ion-exchange membranes. (a) and (b) are surface and cross-sectional images of Sartorius weak acidic cation exchanger (Sartobind® C). (c) and (d) are surface and cross-sectional SEM images of electrospun polyacrylonitrile composite membrane hydrolyzed with NaOH (AEA-COOH).

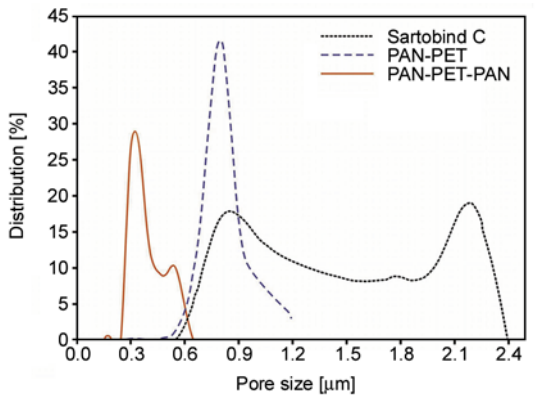

Figure 7. Pore size distribution [%] of different ion-exchange membranes

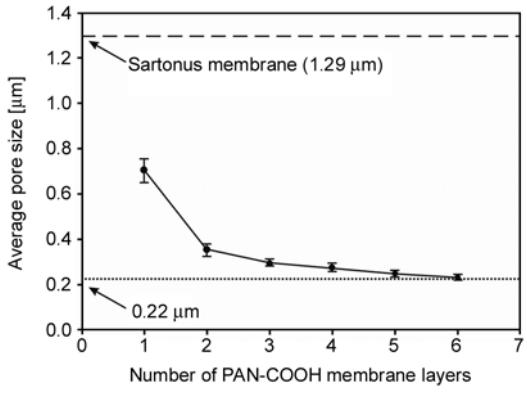

Figure 8. The relationship between average pore size and number of PAN-COOH membrane layers

exchange composite membranes, with their cross-laid, densely packed nanofiber mesh pattern, had a more concentrated arrangement of their pore size and distribution than Sartobind® C membrane.

Figure 8 shows the relationship between the number of PAN-COOH membrane layers and its average pore size; it was similar to control group Sartobind® C membrane in its average pore size of 1.29±0.04 µm. A single PAN-COOH layer combined with PET composite membrane had an average pore size of 0.70±0.05 µm. However, following an increase in the number of PAN-COOH layers,

the average pole diameter quickly declined. When the membrane was in the form of PAN-PET-PAN (PAN-COOH layer number was 2), with an average pore size of 0.36±0.03 μm (less than 0.45 μm); the membrane was capable of micro-filtration. A further increase in the number of layers generated little additional change in the margin of decrease of average pore diameter. However, when the membrane was PAN3-PET-PAN3 (number of PAN-COOH layer was 6), the average pore size was approximately 0.22 μm; the membrane was capable of bacteria filtration. Integrating together all the results from the above experiment showed that, in terms of biotechnology and food purification applications, commercial product Sartobind® C membrane was only capable of ion exchange; its discharged solution still required sterilization, filtration, and other steps in order to complete the purification process. In this study, the capabilities of AEA-COOH nanofiber membrane functional included adsorption, micro-filtration, and bacteria filtration. It could also filter out bacteria and small particles during ion exchange, which reduced the subsequent processing steps and overall purification time.

Table 1 show a comparison between various physical properties of the ion exchange membranes. The result indicated that AEA-COOH membrane's base weight and thickness were approximately 33% and 64% that of Sartobind® C membrane, respectively. In addition, it was discovered, using a BET true density meter, that the AEA-COOH membrane specific surface area (6.1768 m^2/g) was 7 times greater than that of Sartobind® C membrane (0.8873 m^2/g); the ionic base group density was 3.3 times higher, and its porosity (84.4%) was also higher than Sartobind® C membrane (73.4%). These result confirmed that ion exchange membrane formed by PAN nanofibers, was lighter and thinner, with a faster absorption rate and higher volume of liquid circulation than that of Sartobind® C membrane.

Thermal stability analysis of different membranes (e.g. Figure 9 below) showed that the unmodified PAN nanofiber membrane started to thermally decompose at temperatures of about 330°C; thermogravimetric loss increased as temperature increased. However, when the temperature increased to over 450°C, the percentage of thermogravimetric loss was nearly 50%, which then stabilized with no further evidence of loss. That was because the PAN fibers had started carbonizing into carbon fiber. Additionally, it was also found (as shown in Figure 9) that PAN-COOH membrane, after it had already gone through the alkaline hydrolysis process, had a thermal decomposition pattern similar to that of unmodified PAN (its thermal decomposition temperature was about 320°C or so), confirming that it remained under appropriate conditional control. An alkaline hydrolysis reaction took place on the surface of PAN nanofiber membrane where it formed COOH functional groups, without destroying its internal bond, and the mechanical strength of the nanofibers was thereby maintained. Finally, the data showed that thermal stability of Sartobind® C membrane was not high. As the temperature increased, cracks in its structure (thermal decomposition temperature was approximately 115°C) occurred constantly, confirming that Sartobind® C was not suitable for high temperature operations. Neither was it able to perform high temperature sterilization, and its usage repetition was not high. Sartobind® C membrane was therefore limited in its application.

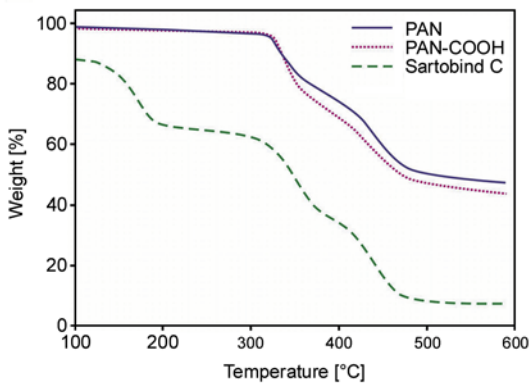

Figure 9. Thermogravimetric analysis of PAN, PAN-COOH, and Sartobind® C membranes

The morphology of the various nanofibrous membranes was examined by wide-angle X-ray diffraction (WXRD) as shown in Figure 10. The unmodi-

Table 1. Physical properties of different ion-exchange membranes

Membranes	Basis weight [g/m^2]	Thickness [μm]	BET surface area [m^2/g]	Porosity [%]	Ligand capacity [μeq/g]
Sartobind® C	128.04	261.2±7.6	0.8873	73.4	135.1
AEA-COOH	42.44	167.1±5.6	6.1768	84.4	439.8

PET: thickness 86.7 μm, basis weight 15 g/m^2

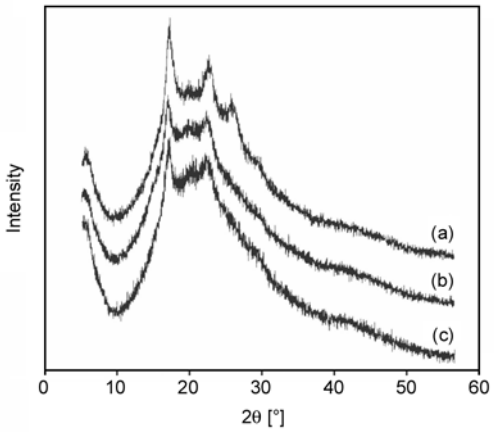

Figure 10. Wide-angle X-ray diffraction patterns of PAN nanofiber membranes at different alkaline hydrolysis conditions. (a) electrospun PAN nanofiber mat; (b) PAN-COOH at the alkaline hydrolysis condition of 85°C, 3N, 10 imn; (c) PAN-COOH at the alkaline hydrolysis condition of 85°C, 3N, 30 imn

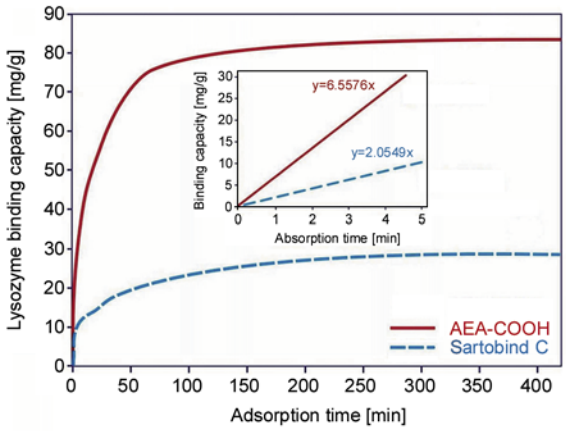

Figure 11. Lysozyme adsorption capacity on the (—)AEA-COOH and (– –) Sartobind® C. Temperature: 298 K; shaking rate: 150 rpm; adsorption solution: 0.5 mg/ml lysozyme in 20 mM glycine buffer (pH 9). The insert shows the initial linear adsorption rate.

fied PAN membrane exhibited three diffraction peaks at 17, 23, and 26°, which correspond to the crystalline structure of linear PAN. The diffractogram also showed peaks at 17 and 23° for PAN-COOH nanofibrous membranes under different alkaline hydrolysis conditions. The diffraction peak at 26º disappeared and only a minor decrease of relative intensity was observed when the PAN nanofibrous mat was modified with NaOH to substitute the nitrile groups with anion carboxylic acid groups, indicating minor interference of the crystalline formation for PAN-COOH. Combining TGA thermal stability data in Figure 9 with XRD results in Figure 10, this study confirmed that the rapid alkaline hydrolysis process only formed COOH functional groups on the surface of the PAN nanofiber membrane while under appropriate conditional control; the process did not cause any damage to its main structure. Thus, the PAN nanofiber membrane maintained a certain degree of mechanical integrity while simultaneously maintaining high-density ion functional groups.

3.4. Adsorption behavior of different ion-exchange membranes

Figure 11 shows comparisons of ion exchange membranes and their lysozyme adsorption volume. The results indicated that, using unit weight of membrane as a benchmark, under the adsorption conditions set with temperature of 298 K, stirring speed of 150 rpm, and lysozyme initial concentration of 0.5 mg/ml (in 20 mM glycine buffer (pH 9)), the maximum lysozyme adsorption capacity of Sartobind® C membrane was 28.6 mg/g. The AEA-COOH membrane was 83.2 mg/g, or about 2.9 times that of the commercial product. Under condition of fixed lysozyme concentration and adsorption time, comparison could be made on the adsorption rate among different ion exchange membranes, due to its initial linear absorption characteristic. Results of the experiment showed that the adsorption rate of AEA-COOH> Sartobind® C. Nanofiber structure based ion exchange membrane had an adsorption time 3.2 times faster than that of the commercial product.

4. Conclusions

This study combines electrospinning and alkali hydrolysis processes to create a weak acid ion exchange membrane possessing high surface functional group density, high porosity, and 3D nanofiber structure. The membrane facilitated an increase in lysozyme adsorption, improved fluid throughput, reduced pressure loss, enhanced overall efficiency of lysozyme purification, increased membrane life span, and reduced the cost of the adsorption membrane. Therefore, compared with the commercially available ion exchange membranes, the AEA-COOH nanofiber membrane was lighter and thinner, with a high adsorption capacity. It also had other unique characteristics such as low-pressure

drop and rapid adsorption rate. Its functional group density adjusted to changes in the duration of basic hydrolysis. It simultaneously possessed capabilities such as adsorption, micro-filtration, and bacteria filtration functions. During ion exchange, it can also filter out bacteria and small particles in order to reduce subsequent processing steps and overall purification time.

References

[1] An H., Shin C., Chase G. G.: Ion exchanger using electrospun polystyrene nanofibers. Journal of Membrane Science, **283**, 84–87 (2006).
DOI: 10.1016/j.memsci.2006.06.014

[2] Dominguez L., Benak K. R., Economy J.: Design of high efficiency polymeric cation exchange fibers. Polymers for Advanced Technologies, **12**, 197–205 (2001).
DOI: 10.1002/pat.125

[3] Kariduraganavar M. Y., Nagarale R. K., Kittur A. A., Kulkarni S. S.: Ion-exchange membranes: Preparative methods for electrodialysis and fuel cell applications. Desalination, **197**, 225–246 (2006).
DOI: 10.1016/j.desal.2006.01.019

[4] Kumar A., Gurian P. L., Bucciarelli-Tieger R. H., Mitchell-Blackwood J.: Iron oxide – Coated fibrous sorbents for arsenic removal. Journal of the American Water Works Association, **100**, 151–164 (2008).

[5] Greenleaf J. E., SenGupta A. K.: Environmentally benign hardness removal using ion-exchange fibers and snowmelt. Environmental Science and Technology, **40**, 370–376 (2006).
DOI: 10.1021/es051702x

[6] Ma Z., Lan Z., Matsuura T., Ramakrishna S.: Electrospun polyethersulfone affinity membrane: Membrane preparation and performance evaluation. Journal of Chromatography B, **877**, 3686–3694 (2009).
DOI: 10.1016/j.jchromb.2009.09.019

[7] Ding Z. J., Qi L., Ye J. Z.: Research on preparation of sheath-core bicomponent composite ion exchange fibers and absorption properties to metal ion. Macromolecular Research, **16**, 21–30 (2008).

[8] Stanelle R. D., Straut C. M., Marcus R. K.: Nylon-6 capillary-channeled polymer fibers as a stationary phase for the mixed-mode ion exchange/reversed-phase chromatography separation of proteins. Journal of Chromatographic Science, **45**, 415–421 (2007).

[9] Greenleaf J. E., Lin J-C., Sengupta A. K.: Two novel applications of ion exchange fibers: Arsenic removal and chemical-free softening of hard water. Environmental Progress, **25**, 300–311 (2006).
DOI: 10.1002/ep.10163

[10] Matsumoto H., Wakamatsu Y., Minagawa M., Tanioka A.: Preparation of ion-exchange fiber fabrics by electrospray deposition. Journal of Colloid and Interface Science, **293**, 143–150 (2006).
DOI: 10.1016/j.jcis.2005.06.022

[11] Wakamatsu Y., Matsumoto H., Minagawa M., Tanioka A.: Effect of ion-exchange nanofiber fabrics on water splitting in bipolar membrane. Journal of Colloid and Interface Science, **300**, 442–445 (2006).
DOI: 10.1016/j.jcis.2006.03.077

[12] Park S. A., Park K., Yoon H., Son J. G., Min T., Kim G-H.: Apparatus for preparing electrospun nanofibers: Designing an electrospinning process for nanofiber fabrication. Polymer International, **56**, 1361–1366 (2007).
DOI: 10.1002/pi.2345

[13] Barhate R. S., Ramakrishna S.: Nanofibrous filtering media: Filtration problems and solutions from tiny materials. Journal of Membrane Science, **296**, 1–8 (2007).
DOI: 10.1016/j.memsci.2007.03.038

[14] Teo W. E., Ramakrishna S.: A review on electrospinning design and nanofibre assemblies. Nanotechnology, **17**, 89–106 (2006).
DOI: 10.1088/0957-4484/17/14/R01

[15] Subbiah T., Bhat G. S., Tock R. W., Parameswaran S., Ramkumar S. S.: Electrospinning of nanofibers. Journal of Applied Polymer Science, **96**, 557–569 (2005).
DOI: 10.1002/app.21481

[16] Huang Z-M., Zhang Y-Z., Kotaki M., Ramakrishna S.: A review on polymer nanofibers by electrospinning and their applications in nanocomposites. Composites Science and Technology, **63**, 2223–2253 (2003).
DOI: 10.1016/S0266-3538(03)00178-7

[17] Frenot A., Chronakis I. S.: Polymer nanofibers assembled by electrospinning. Current Opinion in Colloid and Interface Science, **8**, 64–75 (2003).
DOI: 10.1016/S1359-0294(03)00004-9

[18] Ma Z., Ramakrishna S.: Electrospun regenerated cellulose nanofiber affinity membrane functionalized with protein A/G for IgG purification. Journal of Membrane Science, **319**, 23–28 (2008).
DOI: 10.1016/j.memsci.2008.03.045

[19] Dhanalakshmi M., Jog J. P.: Preparation and characterization of electrospun fibers of Nylon 11. Express Polymer Letters, **2**, 540–545 (2008).
DOI: 10.3144/expresspolymlett.2008.65

[20] Demir M. M.: Investigation on glassy skin formation of porous polystyrene fibers electrospun from DMF. Express Polymer Letters, **4**, 2–8 (2010).
DOI: 10.3144/expresspolymlett.2010.2

[21] Jayakumar R., Prabaharan M., Nair S. V., Tamura H.: Novel chitin and chitosan nanofibers in biomedical applications. Biotechnology Advances, **28**, 142–150 (2010).
DOI: 10.1016/j.biotechadv.2009.11.001

[22] Heikkliä P., Harlin A.: Electrospinning of polyacrylonitrile (PAN) solution: Effect of conductive additive and filler on the process. Express Polymer Letters, **3**, 437–445 (2009).
DOI: 10.3144/expresspolymlett.2009.53

[23] Chang Z. J., Zhao X., Zhang Q. H., Chen D. J.: Nanofibre-assisted alignment of carbon nanotubes in macroscopic polymer matrix via a scaffold-based method. Express Polymer Letters, **4**, 47–53 (2010). DOI: 10.3144/expresspolymlett.2010.8

[24] Li S-F., Chen J-P., Wu W-T.: Electrospun polyacrylonitrile nanofibrous membranes for lipase immobilization. Journal of Molecular Catalysis B: Enzimatic, **47**, 117–124 (2007). DOI: 10.1016/j.molcatb.2007.04.010

[25] Wang T., Kumar S.: Electrospinning of polyacrylonitrile nanofibers. Journal of Applied Polymer Science, **102**, 1023–1029 (2006). DOI: 10.1002/app.24123

[26] Yoon K., Kim K., Wang X., Fang D., Hsiao B. S., Chu B.: High flux ultrafiltration membranes based on electrospun nanofibrous PAN scaffolds and chitosan coating. Polymer, **47**, 2434–2441 (2006). DOI: 10.1016/j.polymer.2006.01.042

[27] Wang Z-G., Wan L-S., Xu Z-K.: Surface engineerings of polyacrylonitrile-based asymmetric membranes towards biomedical applications: An overview. Journal of Membrane Science, **304**, 8–23 (2007). DOI: 10.1016/j.memsci.2007.05.012

[28] Shunkevich A. A., Akulich Z. I., Mediak G. V., Soldatov V. S.: Acid-base properties of ion exchangers. III. Anion exchangers on the basis of polyacrylonitrile fiber. Reactive and Functional Polymers, **63**, 27–34 (2005). DOI: 10.1016/j.reactfunctpolym.2005.02.002

[29] Dai Z-W., Nie F-Q., Xu Z-K.: Acrylonitrile-based copolymer membranes containing reactive groups: Fabrication dual-layer biomimetic membranes by the immobilization of biomacromolecules. Journal of Membrane Science, **264**, 20–26 (2005). DOI: 10.1016/j.memsci.2005.04.022

[30] Yang M-C., Lin W-C.: Surface modification and blood compatibility of polyacrylonitrile membrane with immobilized chitosan-heparin conjugate. Journal of Polymer Research, **9**, 201–206 (2002). DOI: 10.1023/A:1021347810130

[31] Lin W-C., Liu T-Y., Yang M-C.: Hemocompatibility of polyacrylonitrile dialysis membrane immobilized with chitosan and heparin conjugate. Biomaterials, **25**, 1947–1957 (2004). DOI: 10.1016/j.biomaterials.2003.08.027

[32] Sasai Y., Matsuzaki N., Kondo S-I., Kuzuya M.: Introduction of carboxyl group onto polystyrene surface using plasma techniques. Surface and Coatings Technology, **202**, 5724–5727 (2008). DOI: 10.1016/j.surfcoat.2008.06.085

eXPRESS Polymer Letters Vol.5, No.4 (2011) 318–326
Available online at www.expresspolymlett.com
DOI: 10.3144/expresspolymlett.2011.32

Synthesis and characterization of poly(vinylchloride) type macrophotoinitiator comprising side-chain thioxanthone via click chemistry

H. Akat[*], *M. Ozkan*

Ege University, Faculty of Science, Department of Chemistry, Bornova, Izmir, 35100, Turkey

Received 24 August 2010; accepted in revised form 7 November 2010

Abstract. Nowadays, the use of macromolecular photoinitiators provides for a good compatibility of the initiator in the formulation. Moreover, the migration of the initiator to the surface of the material is prevented, which results in low-odor and non-toxic coatings. In the present study, it has been demonstrated that polyvinylchloride macrophotoinitiator (PVC-TX) containing side chain thioxanthone (2%) moieties were successfully prepared by 'click chemistry'. For this purpose, propargyl thioxanthone and polyvinylchloride with side chain azide moieties were reacted in *N*,*N*-dimethylformamide for 24 hours at 25°C in order to give corresponding macrophotoinitiator. The synthesized polymer was characterized by ^{1}H-NMR (nuclear magnetic resonance), UV (ultraviolet) and fluorescence spectroscopies and water based gel permeation chromatography. Obtained macrophotoinitiator has similar absorption characteristics compared to parent thioxanthone. Its capabilities to act as initiator for the photopolymerization of methacrylic acid, methyl methacrylate, *N*-vinyl pyrrolidone and styrene in various solvents in the absence and presence of triethylamine media were also examined.

Keywords: *polymer synthesis, molecular engineering, macrophotoinitiator, photopolymerization, click chemistry, thioxanthone*

1. Introduction

During the last 25 years, there has been growing interest in UV-light initiated photo polymerization. Due to the advantages of macromolecules in comparison to low molecular weight analogues, significant developments are described in the synthesis of macrophotoinitiator. These developments can be arranged as energy saving, low volatility, very short cure time and higher activity [1–3].

Types of free radical photoinitiators can be divided into two classes, according to their radical generation mechanisms, namely cleavage-type (Type I) (benzoin ether, acylphosphine oxides) initiators undergo a very rapid bond cleavage after absorption of a photon on the other hand, type II initiators form relatively long-lived excited triplet states capable of undergoing hydrogen-abstraction or electron-transfer reactions with co-initiator molecules that are deliberately added to the monomer containing system [4]. Among these photoinitiators, thioxanthone (TX) derivatives have recently received interest because of their characteristic absorption of near UV range [5–12]. They have been introduced in processes such as printing inks, dental materials, surface coating, microelectronics, nanocoatings and photoresists [13–17].

Thioxanthone type photoinitiators that proceed via a hydrogen abstraction mechanism are exemplified by combination of TX and a hydrogen donor such as amine or alcohol. The radical derived from the donor can initiate the polymerization. For hydrogen abstraction type photoinitiators, activity of pho-

[*]Corresponding author, e-mail: hakan.akat@ege.edu.tr

toinitiating is designated by polymeric coil including substituent. Activity of polymeric photoinitiators is higher than lower molecular weight analogs because these have more effective excitement mechanism.

The 'click'-type reactions, mainly hold up as by Huisgen 1,3-dipolar azide-alkyne [18], [3 + 2], or have attracted much attention due to their important features including high yields, high tolerance of functional groups and selectivity [19]. Huisgen 1,3-dipolar cycloaddition occurs between an alkyne and an organic azide to give triazole ring. The reactions can be performed under mild experimental conditions when catalyzed by copper (I). The development and the application of click chemistry in polymer and material science have recently been studied extensively [20–26].

Macrophotoinitiators including chromophoric groups either in the main chain or used as pendant groups can be prepared in two ways by click reaction: The first way; we can synthesize and polymerize monomers with photoreactive groups and the second way is to introduce photoreactive groups onto polymer chains.

Polyvinylchloride (PVC) is a low-cost and weather-resistant polymer. The irradiation behavior of PVC has been investigated in detail [27]. PVC is known to be sensitive to UV irradiation. Wypych *et al.* [28] used FT-IR of original and derivative products of photodegradation for identification of photoproducts and they have demonstrated that hydrogen abstraction leads to one of two possible radicals on PVC. In this connection, taking the advantage of this feature of PVC, we have synthesized a new macrophotoinitiator which the incorporation of TX moiety onto pendant position of PVC is accomplished by click reaction. It is demonstrated that macrophotoinitiator can initiate the polymerization of various monomers without the use of extra hydrogen donor such as amines.

2. Experimental

2.1. Materials

Styrene (S, 99%, Product no: 240869, Aldrich, USA), *N*-vinyl2-pyrrolidone (NVP, 99%, Product no: V3409. Aldrich, USA), methyl methacrylate (MMA, 99%, Product no: W400201, Aldrich, USA) were distilled under reduced pressure before use. Tetrahydrofuran (THF, 99.8%, Product no: MFCD00005356, Acros Organics, Germany) was dried and distilled over benzophenone-Na. Other solvents were purified by conventional procedures. Triethylamine (TEA, 98%, Product no: T0886, Sigma-Aldrich, USA), dichloromethane (99.9%, Product no: 650463, HPLC grade, Aldrich, USA) was distilled from calcium hydride (CaH_2). Dimethylformamide (DMF, +99%, Product no: D4551, Aldrich, USA), dimethyl sulphoxide (DMSO, 99%, Product no: D2650, Aldrich, USA), 1,1,1-tris-(hydroxymethyl)-propantriacrylate (TPTA, 95%, Product no:16445, Alfa Aesar, Germany), acrylamide (AA, 99%, Product no: 800830, Merck, Germany), anhydrous magnesium sulfate (99%, Product no: M7506, Sigma-Aldrich, USA), 2,2′-bipyridyl (99%, Product no: 14453, Aldrich, USA), methylethyl ketone (99%, Product no: 360473, Sigma-Aldrich, USA), cyclohexanone (CYCLOHEX 99%, Product no: 398241, Sigma-Aldrich, USA), diethylether (98%, Product no: 296082, Sigma-Aldrich, USA), copper (I) bromide (97.0%, Product no: MFCD00010969, Acros Organics, Germany), sodium azide (NaN_3, 99.5%, Product no: MFCD00003536, Acros Organics, Germany), methanol (99%, Product no: MFCD00004595, Acros Organics, Germany), thiosalicylic acid (97%, Product no: T33200 Sigma-Aldrich, USA), propargyl bromide (80 volume % in toluene, Product no: 81831, Fluka, USA) and phenol (99%, Product no: P3653, Sigma-Aldrich, USA), were used as received. PVC (Mn: 41000, PDI: 2.17) was supplied by PETKIM (Product no: S23) co., Turkey.

2.2. Instrumentation

^{1}H-NMR spectra were recorded on Varian AS-400 spectrometers in deuterated chloroform ($CDCl_3$) with $Si(CH_3)_4$ as internal standard, FT-IR spectra were recorded on a Perkin Elmer FTIR Spectrum One-B spectrometer. UV spectra were recorded on a Shimadzu UV-1601 spectrometer. Differential scanning calorimetry (DSC) was performed on a Perkin Elmer Diamond DSC. Molecular weights and polydispersities of the linear polymers were determined by gel-permeation chromatography (GPC) using a Viscotek GPCmax auto sampler system consisting of a pump, three ViscoGEL GPC columns (G2000HHR, G3000HHR and G4000HHR), a Viscotek UV detector and a Viscotek differential refractive index (RI) detector with THF as eluent at a flow rate of 1.0 ml/min at 30°C. Both detectors

were calibrated with polystyrene standards having narrow molecular weight distribution and so the quoted molecular weights of the polymers are expressed in terms of polystyrene equivalents. Data were analyzed using Viscotek OmniSEC Omni-01 software. For water soluble polymers, gel permeation chromatography measurements were performed at room temperature with a setup consisting of a pump (HP 1050), a refractive index detector (HP 1047 A), and three high resolution Waters columns (AQ3.0, AQ4.0 and AQ5.0). The effective molecular weight ranges were 1000–60 000, 10 000–400,000 and 50 000–4 000 000, respectively. Water was used as eluent at a flow rate of 0.5 ml/min at room temperature. Data analyses were performed with HP Chemstation Software. Elemental analysis of polymers was done with a LECO CHNS 932 elemental analyzer according to ASTM D5291-96.

Fluorescence measurements were carried out using a Perkin Elmer Model LS-50 spectrophotometer. All measurements were made at 90 – position and slit widths for excitation and emission were both kept at 15 nm. Thermal gravimetric analysis (TGA) was performed on Perkin-Elmer Diamond TA/TGA with a heating rate of 10°C min under nitrogen flow.

2.3. Photo-DSC

Photo-DSC was conducted on a modified Perkin Elmer Diamond DSC equipped with a home-made aluminum cylinder. UV light (320–500 nm) was applied by a light guide (OmniCure Series 2000) with a light intensity of 18.40 mW/cm^2 measured by DeltaOhm model HD-9021 radiometer at the level of the surface of the cured samples ([PVC-TX] = $4.14 \cdot 10^{-4}$ mol l^{-1}; [TPTA] = 8 mol l^{-1}; [TEA] = 3.9 mol l^{-1}; in DMSO). The mass of the samples was 8.0 mg, and the measurements were carried out in an isothermal mode at 30°C under a nitrogen flow of 20 ml·min^{-1}. The reaction heat liberated in the polymerization was directly proportional to the number of acrylate reacted in the system. By integrating the area under the exothermic peak, the conversion of the acrylate groups (C) or the extent of the reaction was determined according to Equation (1):

$$C = \frac{\Delta H_t}{\Delta H_0^{theory}} \quad (1)$$

where ΔH_t is the reaction heat evolved at time t, and ΔH_0^{theory} is the theoretical heat for complete conversion. ΔH_0^{theory} = 19.2 kcal·mol^{-1} for an acrylate bond [29]. The rate of polymerization (R_p) is directly related to the heat flow (dH/dt) by Equation (2):

$$R_p = \frac{dC}{dt} = \frac{\frac{dH}{dt}}{\Delta H_0^{theory}} \quad (2)$$

2.4. Synthesis of Azide Functional Polyvinylchloride (PVC-N3)

PVC (1.000 g, 0.024 mmol) was dissolved in *N*,*N*-dimethylformamide (20 ml), NaN_3 (0.021 g, 0.322 mmol; chlorine group's 2%) was added. The resulting solution was allowed to stir at 25°C overnight and precipitated into methanol/water mixture (1/1 by volume). Copolymer compositions of polymer were determined using Elemental analysis. The mole fractions of PVC (98%) and PVC-TX (2%) were calculated accordingly. ^{1}H-NMR (DMSO): δ 4.5–4.35 (b, 2H), 2.4–2.2 (b, 4H). FTIR %T (cm^{-1}): 2968–2910 (–CH_2), 2108 (–N_3), 834 (C–Cl).

2.5. Synthesis of 2-hydroxythioxanthone

The synthesis of 2-hydroxythioxanthone (TX-OH) was conducted according to the literature [30]. The crude products were recrystallized from 1,4-dioxane/water (v/v 80:20).

2.6. Synthesis of 2-(prop-2-yn-1-yloxy)-9*H*-thioxanthen-9-one

A mixture of propargyl bromide (0.165 g, 1.300 mmol), potassium carbonate (0.162 g, 1.2 mmol), and TX-OH (0.228 g, 1.000 mmol) was stirred in deoxygenated and dry acetone (5 ml) at 60°C for 4 h. The reaction mixture was evaporated to dryness; the crude product was obtained as a yellow solid. Yield: 0.17 g. ^{1}H-NMR (DMSO): δ) 8.87–7.28 (b, 7H), 5.0–4.94 (s, 2H) 2.51 (s, 1H) FTIR %T (cm^{-1}): 3254 (H–C≡C–), 2131 (–C≡C–), 1709 (C=O), 1024 (C–O),

2.7. Synthesis of polyvinylchloride with thioxanthone side groups

In a flask, above obtained PVC-N_3 (0,410 g), 2-(prop-2-yn-1-yloxy)-9*H*-thioxanthen-9-one (TX-Pg) (0.100 g 0.396 mmol), copper (I) bromide

(0,113 g, 0.792 mmol), 2,2′-bipyridine (0.247 g, 1.584 mmol), and dry DMF (5 ml) were added. The flask was capped with a septum and purged with dry nitrogen for 10 min. The mixture was stirred overnight at ambient temperature. After removing the catalyst by EDTA, functionalized polymer was precipitated in methanol (200 ml), filtered and dried under vacuum. ^{1}H-NMR (DMSO): δ) 8.87–7.28 (b, 7H), 7.96 (s 1H), 4.5–4.35 (b, 2H), 4.96 (s, 2H) 2.4–2.2 (b, 4H) FTIR %T (cm^{-1}): 2968–2910 (–CH_2), 1712 (C=O), 1091 (C–O),

2.8. Photopolymerization

Appropriate solutions of monomers (10 mmol) in dimethylsuphoxide (0,5 ml), sensitizer (PVC-TX; $4.16\cdot10^{-3}$ mmol) and triethyl amine (TEA; $1.6\cdot10^{-3}$ mmol) were added to Pyrex tubes and degassed with nitrogen before irradiation. The tubes were irradiated at room temperature in a merry-go-round type photoreactor equipped with 15 Phillips lamps and emitting light nominally at 350 nm. Light intensity was 1.04 mW/cm^2 as measured by DeltaOhm model HD-9021 radiometer. At the end of given time, polymers were poured into cold methanol, filtered, dried, and weighted. Conversions were determined gravimetrically.

2.9. Photocuring

Solution of PVC-TX ($4.14\cdot10^{-4}$ mol·l^{-1}) and PVC $4.14\cdot10^{-4}$ mol·l^{-1}) in DMSO were added to Pyrex tubes the samples were irradiated for 2 hours from a photo reactor consisting of 15 Phillips lamps.

3. Results and discussion

In our study, we synthesized polyvinylchloride containing side-chain thioxanthone moieties (PVC-TX) is based on 'click' chemistry strategy. Evidence for the occurrence of the click reactions was obtained from ^{1}H-NMR, UV and fluorescence spectroscopy.

We have first synthesized azide functionalized PVC (PVC-N_3). So chlorine groups were converted to azide groups with the use of sodium azide. Approximately 2% of chlorine units were replaced with azides as estimated by elemental analysis (38.93% C, 4.53% H, 1.2% N, 55.34% Cl). From the ^{1}H-NMR spectrum of the PVC-N_3, the N_3–C***H***–(CH_2)– and Cl–C***H***–(CH_2)– protons are observed as multiple peaks at 4.5 ppm. Additionally, N_3–CH–(C***H***$_2$)– and

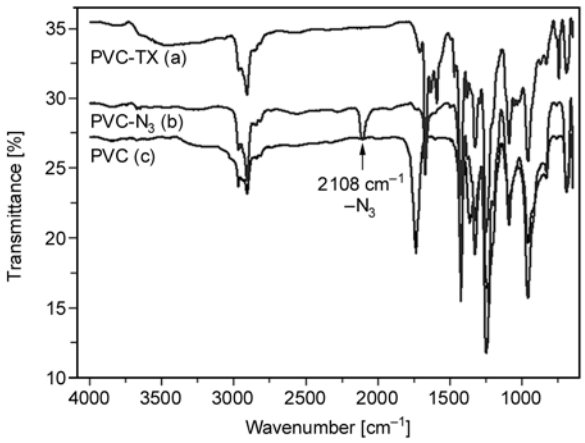

Figure 1. Infrared spectra of (a) PVC-TX, (b) PVC-N_3 and (c) PVC-TX

Cl–CH–(C***H***$_2$)– protons were detectable as broad signal between 2.21 and 2.42 ppm. The structure of PVC-N_3 was further supported by the observationof the azide-stretching band at 2108 cm^{-1} in the FT-IR spectrum of PVC-N_3 presented in Figure 1.

The chemical structure of PVC-TX was confirmed by FT-IR, ^{1}H-NMR and elemental analysis (37,6% C, 4,14% H, 1,22% N, 0,91% S, 0,89% O, 55,24% Cl) The characteristic absorptions of TX-Pg appeared 3254, 2131, 1709, 1632, 1580, 1473,1436,1350, 1210, 1024, 825, 752, 687 cm^{-1} The Click functionality, propargyl group was evidenced by characteristic bands of H–C≡C– and –C≡C-appeared at 3250 and 2131 cm^{-1}, respectively (Figure 2). The ^{1}H-NMR spectrum of PVC-TX showed two new signals. One

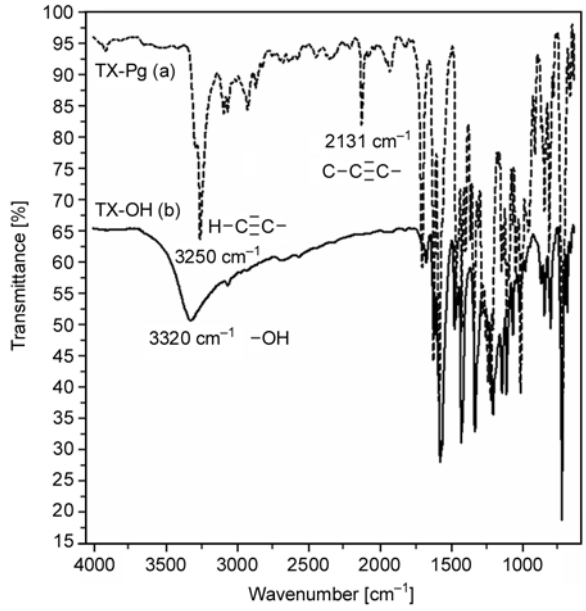

Figure 2. Infrared spectra of (a) TX-Pg and (b) TX-OH

of them is a singlet 7.96 ppm and second one is 4.96 ppm which are assigned to N–C***H***=C– and –C***H***$_2$ (propargyl) respectively. The peaks between 7.43 and 8.57 ppm, characteristic for aromatic protons of thioxanthone appeared in PVC-TX. The appearance of the peak belonging to –C*H* proton of the triazole ring at 7.96 ppm is a typical indication for the successful completion of the click reaction. The FT-IR spectra (Figure 1 and 2) also confirm quantitative reaction, as the azide-stretching band at around 2108 cm^{-1} disappears completely and a new carbonyl and aromatic bands at 1709 cm^{-1} appears respectively.

Photophysical characteristics of the obtained PVC-TX were investigated by UV and fluorescence spectroscopy. As can be seen from Figure 3, PVC-TX, TX-OH and TX-Pg displays characteristic absorption of thioxanthone in 340–400 nm range while PVC-N_3 did not. Compared with the maximum of absorption of TX-OH, the observed slight shift may be attributed to the addition of conjugated bounds in the molecules. The extinction coefficient of PVC-TX (62 300 l/(mol·cm)) was much higher than that of TX-OH (17 000 l/(mol·cm)) and TX-Pg (20 000 l/(mol·cm)) at maximum wavelength (395 nm). Compared with the maximum of absorption of TX-OH, the observed slight shift may be attributed to the addition of conjugated bounds in the molecules. The extinction coefficient of PVC-TX (62 300 l/(mol·cm)) was much higher than that of TX-OH (17 000 l/(mol·cm)) and TX-Pg (20 000 l/(mol·cm)) at maximum wavelength (395 nm). Using these values we assumed that

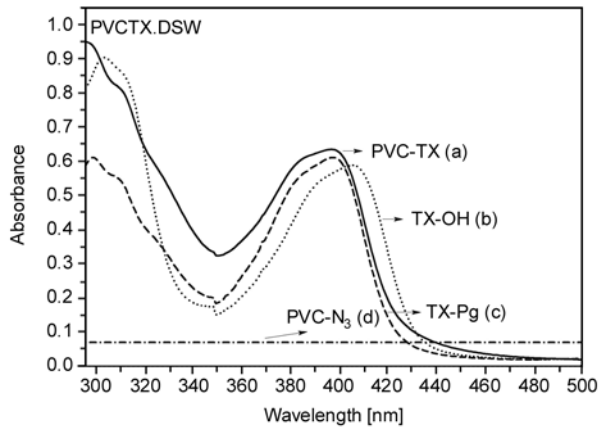

Figure 3. Absorption spectra of (a) PVC-TX (2%), (b) PVC-N_3, (c) TX-OH, and (d) TX-Pg in DMF. The concentrations are 1·10^{-5} M in terms of thioxanthone moieties.

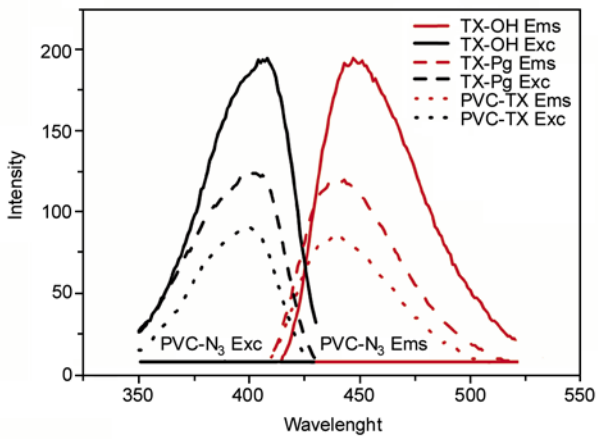

Figure 4. Emission spectra of PVC-TX (2%), TX-Pg, PVC-N_3 and TX-OH in DMF; (λ_{exc}) 380 nm. The concentrations are 2·10^{-5} M in terms of thioxanthone moieties.

every PVC chain contains three TX molecules. This result was also consistent with FT-IR calculation.

Fluorescence spectra of PVC-TX may also provide further evidence for the efficiency of the modification process and information on the nature of the excited states involved. As can be seen from Figure 4, excitation and emission fluorescence spectra of TX-OH, TX-Pg and PVC-TX, which obtained click reaction in DMF, are quite similar. It's clear that when we look at the spectrum, we see a connection between absorption and emission. As expected, this relation between emission and absorption looks like a mirror image and it's so similar with pure thioxanthone. When there is side-chain thioxanthone bound polymer in the environment, the intensities are lower than usual. No excitation and emission fluorescence spectra are obtained for PVC-N_3. It is also seen that variation of fluorescence is a bit different for TX-OH, TX-Pg and PVC-TX in spectrum. This could be due to several reasons. One of them is quenching which may be caused by a number of species in the environment. Secondly, it is considered that the addition of propargyl group can reduce the observed fluorescence intensity. Also, halogen groups in the polymer are thought to decrease the intensity of fluorescence. When we look at the structures, we can say that π Orbital C≡C moiety interacts with n-nonbonding orbitals on oxygen in TX. Because of this interaction fluorescence intensity of TX-Pg can be quenched efficiently atom containing compounds usually known as electron donors. With addition of the triazol

group to PVC, electron distribution has been changed. Consequently, expected quantum yield is smaller than TX-OH.

Moreover, because of changing substituent, the molecule geometry in the excited state can be different from that of in the ground state. Relation between emission and absorption looks like a mirror image. This situation shows that the ground state geometry preserves itself in the excited state. With respect to absorbance peaks, fluorescence peaks shifted longer wavelength. This state is excepted result of the Stokes rule [31].

When we investigate the TX-structures, we can see that hydrogen groups substitute with propargyl and triazole groups. This can be attributed to electronic energy levels of the system have been varied in part.

Some polymeric systems can be used as bimolecular photoinitiators when they used with hydrogen donors. And these polymeric systems carry side-chain TX groups. And also, these hydrogen donors are so similar with low molecular weight TXs structures. PVC-TX was used as a macrophotoinitiator for the polymerization of various monomers in the presence of triethylamine (TEA) as hydrogen donor.

For comparison, we have done several experiments either in the presence or absence of TEA. As it can be seen Table 1 and 2, PVC-TX is also an efficient photoinitiator in the absence of a co-initiator but it should be pointed out that the presence of an amine such as TEA is important for more effective photoreduction and photopolymerization. Surprisingly, PVC-TX can self initiate the free radical polymerization of various monomers in the absence traditional hydrogen donors. We also checked the photoinitiating ability of neat PVC in the presence of TEA but this media did not start the photopolymerization. Consequently, it seems that PVC-TX has the ability to generate photoinitiating species itself without commercial amines.

There are so many solvents tested in our trials and dimetylsulphoxide (DMSO) is the most appropriate among these solvents for the photopolymerization (Table 2). Obviously, the situation seems to be complex and two effects are combined. First, PVC-TX dissolves in DMSO better than it dissolves in other solvents. Second, although radical polymerizations are not sensitive to the polarity of the solvent [32–33], triplet-state lifetime of photoinitiators which involve electron transfer such as TX species, may depend on some polarity effects. The electron transfer mechanism of TX has been extensively investigated by spectroscopic and laser flash photolysis techniques in the literature [34–35].

We also used PVC-TX to test the polymerization ability of the other monomer such as styrene. When there is TEA in the environment, polymerization of styrene cannot initiated by PVC-TX. Although aromatic carbonyl/amine combinations represent an

Table 2. Effect of solvent on the photopolymerization of methyl methacrylate with PVC-TX at room temperature

Solvent	Conversion [%]	M_n [g/mol]	M_w/M_n
DMSO	49	19 500	2.0
DMF	31	19 300	2.0
CYCLOHEX	22	22 200	2.3
MEK	16	17 380	2.2
THF	27	19 800	2.3

[MMA] = 10 mol·l^{-1}; [PVC-TX] = 4.16·10^{-4} mol·l^{-1}; [TEA] = 16·10^{-4} mol·l^{-1}, irradiation time = 2 h

Table 1. Photoinitiated free radical polymerization of various monomers with macrophotoinitiator in DMSO

Monomer	PVC-TX [mol·l^{-1}]	TEA [mol·l^{-1}]	Conversion [%]	Mn [g/mol]	M_w/M_n
MA	4.16·10^{-4}	16·10^{-4}	54	80 877[b]	2.16
MA	4.16·10^{-4}	–	21	116 950[b]	1.90
MMA	4.16·10^{-4}	16·10^{-4}	49	19 500	1.98
MMA	4.16·10^{-4}	–	18	125 000	2.70
MMA	–	–	4	296 500	1.92
MMA[a]	4.16·10^{-4}	16·10^{-4}	No conversion	–	–
NVP	4.16·10^{-4}	16·10^{-4}	26	101 200[b]	1.95
NVP	4.16·10^{-4}	–	1.2	131 500[b]	2.10
S	4.16·10^{-4}	16·10^{-4}	No conversion	–	–

[a]Neat PVC (4.16·10^{-4} mol/l) was used instead of PVC-TX
[b]calculated by water based GPC
irradiation time = 2 h

effective photoinitiator system for the polymerization of (meth)acrylates, they seem to be less reactive toward styrene monomers because of the high quenching rate of the monomer and the low reactivity of R-amino radicals with styrene [36].

We also studied the efficiency of the PVC-TX in the photo-curing of formulations. And these formulations include multifunctional monomers (1,1,1-tris-(hydroxymethyl)-propan-triacrylate, (TPTA). In Figure 5, we showed photo-DSC exotherms using PVC-TX, TEA TPTA under the polychromatic light. With using the knowledge derived from the Figure 5, we see that the Figure 6 displays a plot of the conversion vs. irradiation time. This 'conversion-time' kinetics curve indicates two stages; at first stage there is a rapid stage followed by a slow stage. At the second stage, the diffusion of the components becomes more difficult by the gelation and vitrification of the polymerization of tri-functional acrylate.

We have also investigated thermal stability of PVC-TX by thermo gravimetric analyzer. In this connection, we irradiate (UV light) PVC and PVC-TX for 2 hours after then we plotted TGA curves of neat PVC, PVC-TX, photo-cured polyvinylchloride (PVC-PC) and photo-cured polyvinylchloride bearing thioxanthone (PVC-TX-PC). The first stage of PVC curve begins at 200°C (T_0) and ends at 375°C with a peak temperature at 300°C. This corresponds to a weight loss of 63%, which is attributed to the elimination of HCl molecules leaving behind longer polyene chains. The second stage of degradation begins at 375°C and ends at 500°C with a peak temperature of 465°C. Thermal degradation of the polyene sequences occurs during this stage yielding volatile aromatic and aliphatic compounds by the intramolecular cyclisation of the conjugated sequences.

The TGA curves are presented in Figure 7. It should be noted that first step degradation temperatures for PVC, PVC-TX, PVC-PC and PVC-TX-PC are similar. Compared with polymers (PVC and PVC-TX), photocured polymers (PVC-PC and PVC-TX-PC) have more thermal stability due to crosslinking. According to data obtained from TGA studies, it is clear that the char yield of the photocured polymers is enhanced when compared with not photocured ones. Despite a high char yield of PVC-TX in comparison with other PVC, another noticeable feature is that the degradation of the photo-cured PVC-TX seems to be similar to the degradation profile of PVC, PVC-PC and PVC-TX. Also compared with PVC, PVC-TX is less degradable due to three reasons. Firstly, PVC-TX has TX moieties, which is higher molecular weight instead of 2% Cl. Secondly, aromatic groups are situated in the structure. Finally, PVC-TX is crosslinked with photocuring.

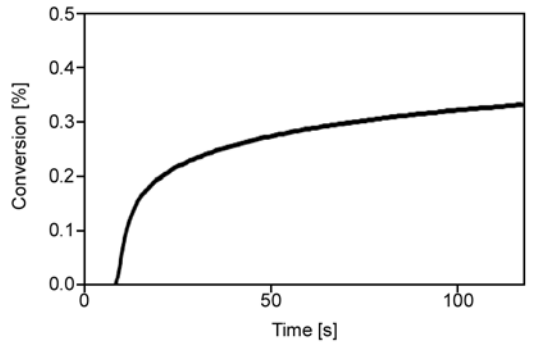

Figure 5. Conversion vs irradiation time for polymerization of TPTA in the presence of TEA and PVC-TX (2%) macrophotoinitiator, cured at 30°C by UV light with an intensity of 18.40 mW/cm^2

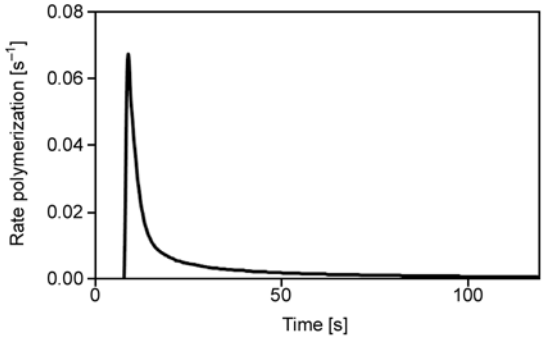

Figure 6. Photo-DSC profile for polymerization of TPTA in the presence of TEA and PVC-TX (2%) macrophotoinitiator, cured at 30°C by UV light with an intensity of 18.40 mW/cm^2

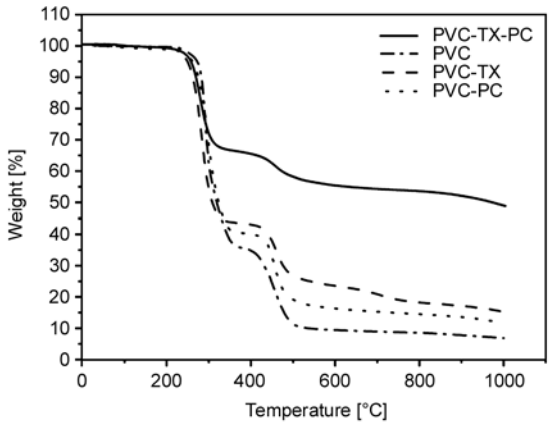

Figure 7. TGA curves of PVC-TX and PVC after and before uv curing

This state has been reflected all stages of thermal degradation.

4. Conclusions

In conclusion, we have successfully synthesized [3 + 2] click reactions for the synthesis of PVC bearing side-chain TX photoactive groups. One of the consequences of the synthesis macrophotoinitatior is that such modification causes a dramatic change in PVC chemistry. The obtained polymeric photoinitiators were shown to efficiently initiate the free radical polymerization of mono- and multifunctional monomers via hydrogen abstraction type mechanism without the use of extra hydrogen donor such as amines. Secondly, the capability of PVC-TX acts, as type II photoinitiator in the absence of hydrogen donor is interesting and worthwhile for the industrial applications.

Acknowledgements

The authors thank Prof. Yusuf Yagci for photo DSC experiments.

References

[1] Corrales T., Catalina F., Peinado C., Allen N. S.: Free radical macrophotoinitiators: An overview on recent advances. Journal of Photochemistry and Photobiology A: Chemistry, **159**, 103–114 (2003). DOI: 10.1016/S1010-6030(03)00175-8

[2] Jiang X., Yin J.: Dendritic macrophotoinitiator containing thioxanthone and coinitiator amine. Macromolecules, **37**, 7850–7853 (2004). DOI: 10.1021/ma0488360

[3] Jiang X., Xu H., Yin J.: Copolymeric dendritic macrophotoinitiators. Polymer, **46**, 11079–11084 (2005). DOI: 10.1016/j.polymer.2005.09.014

[4] Aydin M., Arsu N., Yagci Y., Jockusch S., Turro N. J.: Mechanistic study of photoinitiated free radical polymerization using thioxanthone thioacetic acid as one-component type II photoinitiator. Macromolecules, **38**, 4133–4138 (2005). DOI: 10.1021/ma047560t

[5] Jiang X., Yin J.: Copolymeric photoinitiators containing in-chain thioxanthone and coinitiator amine for photopolymerization. Journal of Applied Polymer Science, **94**, 2395–2400 (2004). DOI: 10.1002/app.21178

[6] Jiang X., Luo J., Yin J.: A novel amphipathic polymeric thioxanthone photoinitiator. Polymer, **50**, 37–41 (2009). DOI: 10.1016/j.polymer.2008.10.038

[7] Gacal B., Akat H., Balta D. K., Arsu N., Yagci Y.: Synthesis and characterization of polymeric thioxanthone photoinitatiors via double click reactions. Macromolecules, **41**, 2401–2405 (2008). DOI: 10.1021/ma702502h

[8] Wen Y. N., Jiang X. S., Liu R., Yin J.: Amphipathic hyperbranched polymeric thioxanthone photoinitiators (ahptxs): Synthesis, characterization and photoinitiated polymerization. Polymer, **50**, 3917–3923 (2009). DOI: 10.1016/j.polymer.2009.06.065

[9] Yagcı Y., Jockusch S., Turro N. J.: Photoinitiated polymerization: Advances, challenges, and opportunities. Macromolecules, **43**, 6245–6260 (2010). DOI: 10.1021/ma1007545

[10] Wen Y., Jiang X., Yin J.: Polymeric Michler's ketone photoinitiator containing coinitiator amine. Polymer Engineering and Science, **49**, 1608–1615 (2009). DOI: 10.1002/pen.21335

[11] Temel G., Arsu N., Yagci Y.: Polymeric side chain thioxanthone photoinitiator for free radical polymerization. Polymer Bulletin, **57**, 51–56 (2006). DOI: 10.1007/s00289-006-0538-y

[12] Temel G., Arsu N.: One-pot synthesis of water-soluble polymeric photoinitiator via thioxanthonation and sulfonation process. Journal of Photochemistry and Photobiology A: Chemistry, **202**, 63–66 (2009). DOI: 10.1016/j.jphotochem.2008.11.012

[13] Nese A., Sen S., Tasdelen M. A., Nugay N., Yagci Y.: Clay-PMMA nanocomposites by photoinitiated radical polymerization using intercalated phenacyl pyridinium salt initiators. Macromolecular Chemistry and Physics, **207**, 820–826 (2006). DOI: 10.1002/macp.200500511

[14] Oral A., Tasdelen M. A., Demirel A. L., Yagci Y.: Poly(cyclohexene oxide)/clay nanocomposites by photoinitiated cationic polymerization via activated monomer mechanism. Journal of Polymer Science Part A: Polymer Chemistry, **47**, 5328–5335 (2009). DOI: 10.1002/pola.23581

[15] Tasdelen M. A., Kreutzer J., Yagci Y.: In situ synthesis of polymer/clay nanocomposites by living and controlled/living polymerization. Macromolecular Chemistry and Physics, **211**, 279–285 (2010). DOI: 10.1002/macp.200900590

[16] Tasdelen M. A., Kumbaraci V., Jockusch S., Turro N. J., Talinli N., Yagci Y.: Photoacid generation by stepwise two-photon absorption: Photoinitiated cationic polymerization of cyclohexene oxide by using benzodioxinone in the presence of iodonium salt. Macromolecules, **41**, 295–297 (2008). DOI: 10.1021/ma7023649

[17] Roffey C.: Photogeneration of reactive species for UV-curing. Wiley, Sussex (1997).

[18] Padwa A.: 1,3-dipolar cycloaddition chemistry. Wiley, New York (1984).

[19] Rostovtsev V. V., Green G., Fokin V. V., Sharpless K. B.: A stepwise huisgen cycloaddition process: copper(I)-catalyzed regioselective 'ligation' of azides and terminal alkynes. Angewandte Chemie International Edition, **41**, 2596–2599 (2002).
DOI: 10.1002/1521-3773(20020715)41:14<2596::AID-ANIE2596>3.0.CO;2-4

[20] Tasdelen M. A., Van Camp W., Goethals E., Dubois P., Du Prez F., Yagci Y.: Polytetrahydrofuran/clay nanocomposites by *in situ* polymerization and 'click' chemistry processes. Macromolecules, **41**, 6035–6040 (2008).
DOI: 10.1021/ma801149x

[21] Oral A., Tasdelen M. A., Demirel A. L., Yagci Y.: Poly(methyl methacrylate)/clay nanocomposites by photoinitiated free radical polymerization using intercalated monomer. Polymer, **50**, 3905–3910 (2009).
DOI: 10.1016/j.polymer.2009.06.020

[22] Opsteen J. A., van Hest J. C. M.: Modular synthesis of block copolymers via cycloaddition of terminal azide and alkyne functionalized polymers. Chemical Communications, **1**, 57–59 (2005).
DOI: 10.1039/b412930j

[23] Lutz J-F.: 1,3-dipolar cycloadditions of azides and alkynes: a universal ligation tool in polymer and materials science. Angewandte Chemie International Edition, **46**, 1018–1025 (2007).
DOI: 10.1002/anie.200604050

[24] Binder W. H., Sachsenhofer R.: 'Click' chemistry in polymer and materials science. Macromolecular Rapid Communications, **28**, 15–54 (2007).
DOI: 10.1002/marc.200600625

[25] Ergin M., Kiskan B., Gacal B., Yagci Y.: Thermally curable polystyrene via click chemistry. Macromolecules, **40**, 4724–4727 (2007).
DOI: 10.1021/ma070549j

[26] Fournier D., Hoogenboom R., Schubert U. S.: Clicking polymers: A straightforward approach to novel macromolecular architectures. Chemical Society Reviews, **36**, 1369–1380 (2007).
DOI: 10.1039/b700809k

[27] Bowmer T. N., Hellman M. Y., Vroom W. I.: Radiation crosslinking of poly(vinyl-chloride) with trimethylolpropanetrimethacrylate. 2. Dependence on radiation-dose and blend composition. Journal of Applied Polymer Science, **28**, 2082–2092 (1983).
DOI: 10.1002/app.1983.070280620

[28] Wypych G.: PVC degradation and stabilization, ChemTec Publishing, Ontario (2008).

[29] Brandrup J., Immergut E. H.: Polymer handbook, Wiley, New York (1975).

[30] Catalina F., Tercero J. M., Peinado C., Saster R., Mateo J. L.: Photochemistry and photopolymerization study on 2-acetoxy and methyl-2-acetoxy derivatives of thioxanthone as photoinitiators. Journal of Photochemistry and Photobiology A: Chemistry, **50**, 249–258 (1989).
DOI: 10.1016/1010-6030(89)85019-1

[31] Lakowicz J. R.: Princples of fluorescence spectroscopy. Kluwer, New York (1999).

[32] Binder W. H., Kluger C.: Combining ring-opening metathesis polymerization (romp) with sharpless-type 'click' reactions: An easy method for the preparation of side chain functionalized poly(oxynorbornenes). Macromolecules, **37**, 9321–9330 (2004).
DOI: 10.1021/ma0480087

[33] Allen N. S., Catalina F., Green P. N., Green W. A.: Photochemistry of thioxanthones–IV. Spectroscopic and flash photolysis study on novel *n*-propoxy and methyl, *n*-propoxy derivatives. European Polymer Journal, **22**, 793–799 (1986).
DOI: 10.1016/0014-3057(86)90018-2

[34] Amirzadeh G., Schnabel W.: On the photoinitiation of free radical polymerization-laser flash photolysis investigations on thioxanthone derivatives. Macromolecular Chemistry and Physics, **182**, 2821–2825 (1981).
DOI: 10.1002/macp.1981.021821027

[35] Yates S. F., Schuster G. B.: Photoreduction of triplet thioxanthone by amines- Charge-transfer generates radicals that initiate polymerization of olefins. Journal of Organic Chemistry, **49**, 3349–3356 (1984).
DOI: 10.1021/jo00192a019

[36] Pappas S. P.: Photoinitiated radical polymerization. Journal of Radiation Curing, **14**, 6–10 (1987).

eXPRESS Polymer Letters Vol.5, No.4 (2011) 327–341
Available online at www.expresspolymlett.com
DOI: 10.3144/expresspolymlett.2011.33

Evidence of intra-chain phase separation in molten short-chain branched polyethylene

*F. J. Stadler**

Chonbuk National University, School of Semiconductor and Chemical Engineering, 664-14, 1-ga Deokjin-dong, Deokjin-gu, Jeonju, Jeonbuk, 561-756, Republic of Korea

Received 9 September 2010; accepted in revised form 8 November 2010

Abstract. Intramolecular phase separation is usually associated with block-copolymers, but the same phenomenon is also obtainable by random-copolymers. In this article, evidence of intramolecular phase separation is reported for a linear octadecene-ethene copolymer, which shows an evolving 'yield point' at a long time and low frequency. This is attributed to a partial phase separation of the long short-chain branches. In creep recovery, this behavior is evident as increasing elastic steady-state creep recovery compliance J_e^0. In contrast to 'normal' block-copolymers, this special polymer has an increase in phase separation with temperature, which is caused by the chemical composition and the short chain segments in the side chain domain, leading to a high surface fraction.

Keywords: *rheology, phase separation, linear low density polyethylene, time-temperature superposition*

1. Introduction

The question whether two polymers can be blended together is one of the oldest in the history of polymer science, which primarily comes from the question of whether the usual endothermic heat of mixing and the very small combinatorial entropy of mixing make a phase separation thermodynamically favorable. The usual case is the immiscibility of two polymers [1, 2]. Although polyolefins (e.g. polyethylene and polypropylene) are very similar in their molecular structure, they are known to be immiscible [3]. Also blends of polyethylene and ethylene-/α-olefin copolymers are known to be phase separating under certain conditions, which highlights the fact that rather small chemical differences can already lead to phase separation, although it is reported to be rather weak [4–8]. While two polymers in a blend have to be mixed physically, it is also possible to link them together chemically to form di- or multiblock copolymers. On a nano scale, this also leads to phase separation, whose size naturally is determined by the molar masses of the individual blocks [9, 10]. This effect differs from blending in the way that it only involves one species of polymers; hence, it is an intrachain phase separation as opposed to a normal (interchain) phase separation. Kossuth *et al.* [11] published an overview of the rheological behavior classified by their terminal behavior in the angular frequency dependent storage modulus $G'(\omega)$. In general, the better ordered, the lower the terminal slope of $G'(\omega)$. Cubic phases – the maximum ordered state – don't flow at all, while a disordered state leads to a pattern very similar to a normal polymer melt [12]. Recently, Park *et al.* [13] established that such behavior can also be observed in ethylene/octene-block-ethylene/octene-copolymers, whose blocks differ distinctly in comonomer concentration. This shows that even small chemical differences suffice to create a biphasic structure. However, they didn't give the block

*Corresponding author, e-mail: fjstadler@jbnu.ac.kr

length in their paper, as it cannot be determined due to the synthesis method.

Such block-copolymers are usually thermorheologically complex [9, 14, 15]. The group of Bates [9, 10], for example, found that below the order-disorder transition temperature, i.e., in the ordered state, the sample behaves like a gel and thermorheologically simple, while in the disordered state, a clear thermorheological complexity is found. The higher the temperature, the less pronounced the long-term relaxation process and, thus, the more similar is the data to a single-phase polymer melt.

Recently, it was also proven that pure ethylene-/α-olefin copolymers with very long comonomers (C26) can be phase separating in the solid state, if their comonomer content is sufficiently high [16]. This effect is different from the previous cases, because it only involves one type of chain and, furthermore, occurs on random copolymers. Hence, it is an effect that occurs only on a short length scale, as shown by the fact that the length of the comonomers used were 18 and 26 carbons. Thus, the second phase has to encompass only the maximum of 24 terminal carbons; realistically, 16–20 carbons. This effect had a small trace in X-ray diffraction, which points to a weak side chain crystallization [17, 18]. However, it was shown that the samples showing this phase behavior in the solid state [16] did not show it in the melt state, as the samples behaved like normal linear low density polyethylenes (LLDPEs), being only special because of their higher flow activation energy E_a, which is the consequence of the side-chain content s_c of the comonomer [19, 20].

Phase separation in the melt is usually visible by traces of the interfacial tension [21] and different temperature dependencies of the individual blend components and the interfacial processes [22, 23]. Hence, if other techniques don't show any trace, e.g., because of too low differences in the electron density in X-ray scattering, rheological behavior can provide a valuable aid to the characterization of phase separation.

Recently, molecular dynamics studies revealed that samples with significant levels of short-chain branching indeed tend to form separate phases, which affirms above observations [24, 25].

The thermorheological complexity of single phase melts was not often investigated until about 10 years ago. This is in part the consequence of its rare occurrence in commercially available products before the introduction of long-chain branched metallocene catalyzed polyethylene (LCB-mPE) in the market, and also caused by the fact that thermorheological complexity is not easy to detect in the double logarithmic plot of the complex modulus $G'(\omega)$ and $G''(\omega)$, especially, if only a relatively small frequency and temperature range is covered [24–26]. Also, the thermorheological complexity can be partially masked by a broad molar mass distribution (*MMD*), which causes the different relaxation processes to be smeared out [26]. Low density polyethylene (LDPE), for example, has a thermorheological complexity, which can be eliminated by an arbitrary modulus shift, whose origin remains to be determined [26–28]. Currently, it can only be said that the modulus shift b_T for low density polyethylene (LDPE) follows an Arrhenius-temperature dependence which is 3–4 times stronger than expected from the density difference. The physical origin of this behavior is totally illusive at the moment, but different from LCB-mPE, because, unlike for LCB-mPE, the shape of $\delta(\omega)$ is not temperature dependent for LDPE [27, 28]. Only recently, viable analysis schemes for thermorheological complexity have become available [26, 27, 29–32]. The thermorheological complexity of long-chain branched metallocene PE leads to an increase of the activation energy towards longer relaxation times/lower relaxation strengths [29–31]. A similar effect was also found for long-chain branched polypropylenes (PP) and flouropolymers [27, 28, 32, 33]. The base of these methods is to determine the activation energy locally, i.e. at a given frequency, relaxation time, modulus, or relaxation strength, or to find out which quantity reacts insensitive to the thermorheological complexity, e.g., $\delta(\omega)$ is insensitive to the thermorheological complexity in LDPE and can, thus, be used for determining the 'real' activation energy [27, 28]. If no long-chain branching is present, any single phase melt shows thermorheological simplicity, i.e., the fulfillment of the tTS-principle (time-temperature superposition).

This article attempts to answer the question of whether the phase separation observed in the solid state for special ethylene-/α-olefin copolymers can also be observed in the melt, where side-chain crystallization cannot be the driving force.

2. Materials and methods

2.1. Materials

The mLLDPE F18G is a linear ethene-octadecene copolymer, synthesized by B. Arikan (University Hamburg, Prof. Kaminsky) using the catalyst [Ph2C(2,7-di-^{tert}BuFlu)(Cp)]$ZrCl_2$/MAO (University Hamburg, Hamburg, Germany). The synthesis of similar products was previously described [34, 35]. The product was stabilized with 0.5 wt.% Irganox 1010 and 0.5 wt.% Irgafos 168 (Ciba, Basel, Switzerland). L4 and C4 were commercial grades and were used as is [19].

2.2. Molecular characterization

The comonomer content of sample F18G (cf. Table 1) was measured by solution NMR using the WALTZ-16-program [16]. For L4, melt-state NMR was used [36, 37].

Molar mass measurements were carried out by means of a high temperature size exclusion chromatograph (Waters, 150C) equipped with refractive index (RI) and infra-red (IR) (PolyChar, IR4) detectors. All measurements were performed at 140°C using 1,2,4-trichlorobenzene (TCB, Sigma-Aldrich, Schnelldorf, Germany) as the solvent. The high temperature size exclusion chromatograph (*SEC*) was coupled with a multi-angle laser light scattering (MALLS) apparatus (Wyatt, DAWN EOS). Details of the experimental SEC-MALLS set-up and the measuring conditions were previously published elsewhere [38].

The thermal behavior was measured on samples of about 10 mg by differential scanning calorimetry (DSC) (TA Instruments, DSC 2920) using the maximum of the melting peak at a heating rate of 10 K/min for the determination of the melting point.

2.3. Rheology

Samples were hot pressed into 25 mm diameter disks with 1 mm height at 180°C in vacuum for 5 min [38].

The shear rheological tests were carried out with a Bohlin Gemini air bearing and a TA Instruments AR-G2 magnetic bearing rheometer. Dynamic-mechanical tests were carried out in the frequency range between 628 and 0.01 s^{-1} in the linear viscoelastic regime with a stress $\hat{\tau}$ between 10 and 50 Pa, which yielded identical results in the complete frequency range. Hence, the linear viscoelastic range extends to at least this value, which corresponds to $\gamma_0 \approx 5\%$ at $\omega = 0.01$ s^{-1}. Using higher strains will lead to a deviation mainly at low frequencies (cf. Figure 8). Creep and creep recovery tests were also performed in the linear viscoelastic regime with stresses between 2 and 20 Pa.

The zero shear-rate viscosity η_0 was determined from the creep compliance, which can be deconvoluted as $J(t') = J_0 + \psi(t') + t'/\eta_0$. As $J_0 + \psi(t') =$ constant ($\rightarrow J_e^0$) for $t \rightarrow \infty$, obtaining η_0 is possible as soon as $J_0 + \psi(t') << t/\eta_0$. This is independent of the condition for the stationarity in the creep recovery test $J_0 + \psi(t') = c = J_e^0$ (for creep time $t_0 \rightarrow \infty$ and shear stress $\tau \rightarrow 0$). Hence, obtaining η_0 is possible after significantly shorter creep times than J_e^0.The exact definitions of the quantities discussed here are given in previous publications [29, 39].

All tests were performed in a nitrogen atmosphere between 110 and 230°C. A frequency sweep (a dynamic mechanical test, in which the angular frequency is varied) in the beginning and at the end of the measurements of each sample was performed, to prove that no thermal degradation took place during the test. A maximum deviation of ±5% between those two tests was considered to be acceptable. Also, a repetition of the test at 130°C was performed after all tests above 190°C to ensure the reversibility of the effect.

Relaxation spectra were calculated from the data using the method of Stadler and coworkers [40, 41].

3. Results

3.1. SEC-MALLS

Figure 1 shows the SEC-MALLS-data for the metallocene catalyzed linear low density polyethylenes (mLLDPE) L4 and F18G. The molar mass peak of F18G is slightly higher in M_{LS}, which is also reflected in the higher molar mass of F18G (cf. Table 1). It is obvious that both materials have a similar, and narrow, molar mass distribution of $M_w/M_n = 2$. F18G seems to be even a little bit narrower in molar mass distribution than L4. C4 is broader in molar mass distribution, which is why it will be mainly discussed with respect to its thermorheological behavior.

The *SEC-MALLS*-data of both materials show no deviation from the linear reference within the accuracy of the experiment, which points to the fact that

Table 1. Rheological and molecular characteristics

#	M_w [kg/mol]	M_w/M_n [–]	Comonomer	n_c [mol%]	w_c [wt.%]	T_m [°C]	η_0 (T = 150°C) [Pa·s]	η_0/η_0^{lin} [–]
F18G	140	1.9	octadecene	4.4	29.3	ca. 75	9 100	0.30
L4	114	2.0	butene	6.8	12.7	95 [42]	14 000	1.03
C4	216	3.0	–	0.0	0.0	134 [42]	113 000	0.78

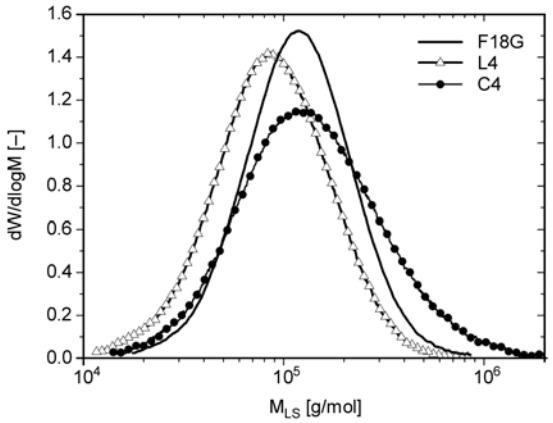

Figure 1. Molar mass distribution of C4, L4, and F18G

neither material contains any long-chain branching (see Ref. [43] for an in-depth discussion of the question of how long-chain branching can be detected in PE).

Table 1 shows the molecular characteristics of the samples characterized. For all samples in this article no long-chain branching was found.

3.2. DSC

The DSC-traces of the samples are given in Figure 2. While the mHDPE C4 and mLLDPE L4 show the expected traces of a narrow melting peak, F18G shows a broad peak, which can be described as roughly bimodal. This indicates fundamental differences in the crystalline structure. This structure was discussed by Pérez *et al.* [43], who found very similar DSC-traces for their sample. Based on their

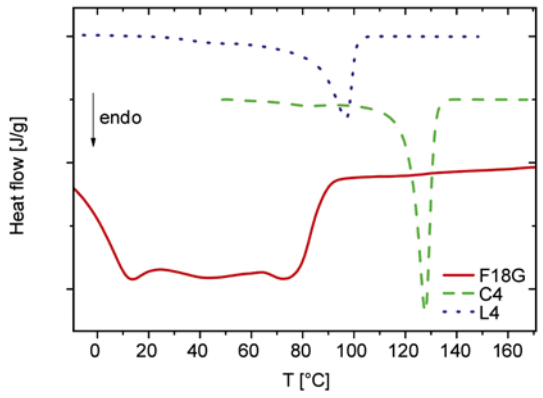

Figure 2. DSC-traces of C4, L4, and F18G (heating, q = 20 K/min)

results, they concluded that the octadecene side-chains do not crystallize themselves separately, which is in accordance with Piel *et al.* [16], who didn't find side-chain crystallization by DMTA. However, it is clear from the DSC-traces that the hexadecane side chains (formed by the octadecene) have to be somehow included into the main crystallites, which then leads to distorted low melting crystallites. The lower end of the melting area around 10°C roughly corresponds to the melting point of pentadecane, which means that probably the short-chain branches are located in higher concentrations (i.e. domains) locally and, thus, form some distorted crystals with some main chains in it.

Furthermore, it is obvious that the melting temperature of L4 is significantly higher than T_m of F18G despite the fact that L4 contains approximately 70% more comonomer (in mol%).

Although solid-state properties are not the main focus of the article, these findings already demonstrate that F18G is a special material despite the fact that it is only an LLDPE with longer comonomer.

3.3. Rheology

3.3.1. Zero shear-rate viscosity η_0

The first question needing to be answered is whether F18G is long-chain branched, as this would make the interpretation of the results significantly more complicated. However, the presence of sizable amounts of long-chain branches can also be safely excluded as the reaction conditions, under which F18G was synthesized inhibit the formation of long-chain branches [36]. Also the value of the zero shear-rate viscosity η_0 of about 9100 Pa·s (at 150°C) and the molar mass M_w of 140 kg/mol make the presence of a small amount of LCBs very unlikely, as the expected zero shear-rate viscosity η_0^{lin} at 140 kg/mol is 30 000 Pa·s [38]. Hence, the zero shear-rate viscosity increase factor η_0/η_0^{lin} is 0.3, i.e. F18G is under the η_0-M_w-relation for HDPE, which would mean that it is either of a different molecular structure (this is not the case, as the exact synthesis conditions and the NMR spectra clearly indicate it

is an LLDPE) or highly branched (which can be excluded from *SEC-MALLS* and the synthesis conditions [36]). For LCB-mPEs, values of η_0/η_0^{lin} between 2 and 1000 are usually found [35, 36, 44–48]. Only for a very low molecular LCB-mHDPE (M_w = 28 kg/mol) an $\eta_0/\eta_0^{lin} < 1$ was found [49].

Hence, it can be concluded that the standard indicator of long-chain branching, the zero shear-rate viscosity increase factor η_0/η_0^{lin}, is not in accordance with conventional polymers, but it definitely does not point to long-chain branching. Also, *SEC-MALLS* suggests a linear structure.

The zero shear-rate viscosity increase factor η_0/η_0^{lin} of below 1 might be a consequence of the significant amount (4.5 mol%) of the rather long comonomer octadecene. This is in accordance with Wang *et al.* [50], who found a significant decrease of η_0 for longer poly-α-olefins in comparison to PE. However, it remains puzzling why the sample F26F [51] has almost the same weight comonomer content w_c (having fewer but longer butacosene (C24) side chains) yet obeys the η_0-M_w-correlation of HDPE [38].

Because an explanation requires the full presentation of the rheological behavior of F18G, it is moved to the discussion section.

3.3.2. Elastic behavior

Figure 3 shows the creep and creep recovery data of F18G. While the creep compliances $J(t')$ with t_0 = 415 and 4150 s agree very well, it becomes immediately obvious that the terminal value of the recoverable compliance $J_r(t)$, the elastic recovery compliance J_e, is very much dependent on the creep time t_0 (and also on the creep stress σ_0, which was not investigated here, as all creep experiments were carried out in the linear viscoelastic regime) [52]. The elastic recovery compliance J_e also exhibits a significantly higher value than comparable mLLDPEs, which have values for the steady-state elastic recovery compliance J_e^0 around 10^{-4} Pa^{-1}, i.e., J_e^0 for F18G is more than a factor of 100 higher than that found for conventional LLDPEs (e.g. L4 in Figure 3). Please note that elastic recovery compliance J_e is smaller or equal than the steady-state elastic recovery compliance J_e^0, as for the former, no proof of stationarity could be conducted. This was found to be impossible for F18G due to the long terminal relaxation times (for a conventional LLDPE the terminal regime is reached after around 100 s for this molar mass (cf. L4 in Figure 3) [29, 52].

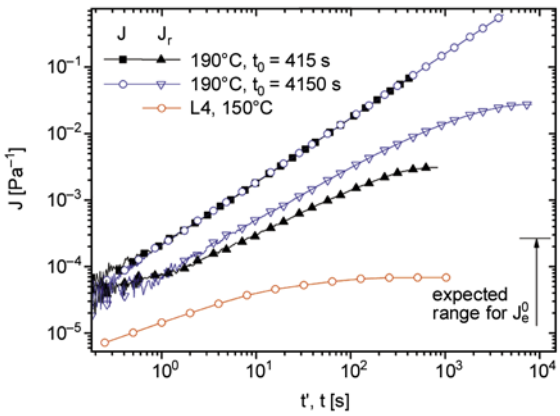

Figure 3. Creep and creep recovery compliance at 190°C for different creep times in the instationary regime. The linear and stationary creep recovery data of L4 is given in this figure for comparison [55].

The fact that only about 3% of the deformation induced by a creep deformation for t_0 = 4150 s recoverable (Figure 3), illustrates that this anomalous behavior is not the consequence of a network, as in that case the viscous part of the deformation (about 97%) would be much smaller in comparison to the elastic part (ideally 0%) [53]. In single-phase melts besides cross-linking, only a high molecular component is known to be able to elevate J_e to a level above 10^{-2} Pa^{-1} [46, 54].

However, the presence of such a high molecular component in F18G can be excluded, as such a high molecular component would certainly be detected by *SEC-MALLS*, which reacts very sensitively towards high molecular components even in very small concentrations.

3.3.3. Viscoelastic and thermorheological properties

When looking at dynamic-mechanical data, for unshifted storage moduli $G'(\omega)$, the data at different temperatures seem to converge to a common curve for $\omega < 0.03$ s^{-1} being indicated as the dashed line in Figure 4. This line has a slope of about 1, which is the terminal slope of $G''(\omega)$, but not of $G'(\omega)$. Surprisingly, this line is almost temperature independent. The curves do not fall perfectly on the dashed line because of a small temperature dependence (the data at 230°C is right of the line, while the data at 110°C is left of it). It is not possible to find reliable shift factors, as this bend in the data, being an

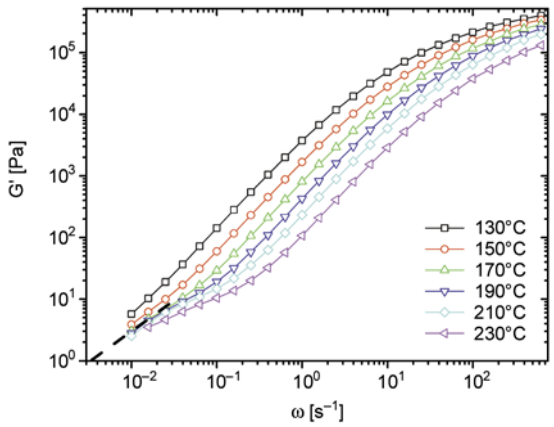

Figure 4. Storage moduli $G'(\omega)$ of F18G

additional relaxation mode, is only partially covered by the dynamic-mechanical test.

When shifting the data obtained for F18G between 130 and 230°C a pseudo-master curve can be constructed for $G'(a_T \cdot \omega)$ and $G''(a_T \cdot \omega) > 30$ Pa (Figure 5). The crossover frequency ωc is around 40 s^{-1}, which corresponds very nicely to the scaling law between the characteristic relaxation time λ (= $1/\omega_c$) that has been previously established for HDPE [38]. However, it also becomes immediately obvious that the moduli of F18G are lower than, e.g., for the LLDPE L4. The difference between L4 and F18G lies in G_N^0 and in ω_c ($\rightarrow M_w$) becomes obvious when shifting the data of L4 to the crossover frequency ω_c ($a_T = 0.5$) and modulus G_c ($b_T = 0.38$) of F18G (thick lines in Figure 5a). Both datasets almost perfectly agree for $a_T \cdot \omega > 0.07$ s^{-1}. Hence, the two materials differ in the plateau modulus G_N^0 by a factor of ≈ 2.5. Because of the comonomer content of almost w_c = 30 wt.%, this is in accordance with previous findings [56]. It is actually quite surprising that the scaling of the characteristic relaxation time λ is fulfilled in the same way as HDPE despite the differences in chemical structure and G_N^0 [56].

Self-evidently, it is not suggested to use the modulus shift (b_T) as an analytical tool. The shifted data of L4 instead provides excellent evidence that the shape of the rheological data of F18G coincides very well with L4 for $G'(a_T \cdot \omega)$ and $G''(a_T \cdot \omega) >$ 30 Pa. The conclusion is that the relaxation behavior in this regime is unaffected, while the entanglement network is slightly looser (lower G_N^0). The shift factor $a_T = 0.5$ for L4 used for this comparison is exactly the shift factor expected from the scaling law with molar mass M_w for the characteristic relaxation times established earlier for HDPE [38], which already indicates that the material doesn't behave the way expected from chemical composition, as, according to Chen *et al.* [56], a correction of the HDPE-scaling law has to be used. This discussion is given in detail in the conclusions section concerning the deviation from the η_0-M_w-relation

Figure 5b shows that the elastic compliance $J'(a_T \cdot \omega) > 0.07$ s^{-1}) of F18G is higher than that for L4, but this is a consequence of the lower plateau modulus G_N^0. This gives the opportunity to estimate the J_e^0 of this material, which should be the steady-state elastic recovery compliance J_e^0 of L4 divided by b_T, i.e. $7 \cdot 10^{-5}$ $Pa^{-1}/0.38 = 1.8 \cdot 10^{-4}$ Pa^{-1} (according to the theory of rubber elasticity $J_e^0 = f \cdot G_N^0$, where f is a factor ≥ 2.5 and dependent on molar mass distribution and molecular architecture) [12]. But as Figure 5b shows, the upturn for $J'(a_T \cdot \omega <$ 0.07 s^{-1}) is so significant that the real J_e^0 is significantly above that value (cf. Figure 3). A normal LLDPE with the same comonomers content would show a behavior similar to the data of L4, shifted to

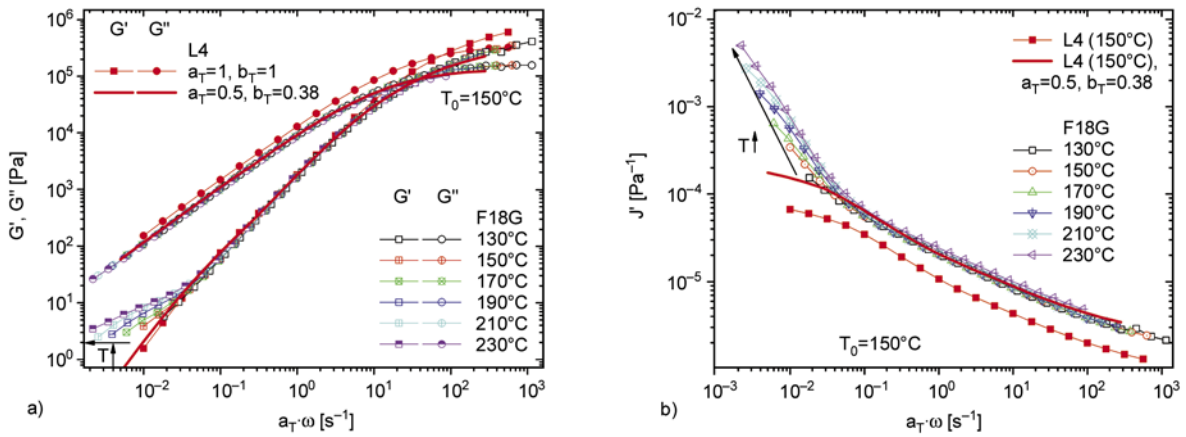

Figure 5. Pseudo-mastercurves of F18G in comparison to Butene-LLDPE L4. a) $G'(a_T \times \omega)$ and $G''(a_T \times \omega)$, b) $J'(a_T \times \omega)$

the data of F18G using the same shift factors as already applied in Figure 5a ($a_T = 0.5$, $b_T = 0.38$).

Figure 5 shows clearly that $G''(a_T \cdot \omega)$ is thermorheologically simple within the experimental accuracy, while $G'(a_T \cdot \omega)$ (and, thus, also $J'(a_T \cdot \omega)$) show a divergence below about $a_T \cdot \omega = 0.07$ s^{-1}. The upturn for $J'(a_T \cdot \omega < 0.07$ s$^{-1})$ is highly temperature dependent, such that it is no longer possible to call it a thermorheologically simple material.

Interestingly, the trend of the thermorheological complexity is exactly opposite to what is expected. Block-copolymers usually exhibit the largest thermorheological complexity at the lowest temperature, while F18G shows the largest deviations at the highest temperature [9, 14, 15]. Possible reasons for this behavior will be discussed later.

The relaxation spectra calculated according to the method of Stadler and Bailly [40, 41] given in Figure 6 lead to a highlighting of thermorheological complexity. It is obvious that the spectra of F18G can be divided into two distinctly different regimes. Above $H = 6$ Pa, the spectrum looks like a typical example of a thermorheologically simple LLDPE, such as L4, also given in Figure 6a. Below 6 Pa, a clear second process is present, which has almost no temperature dependence, as the spectra around $\tau = 100$ s are almost temperature independent.

An evaluation using the analysis method to determine the activation energy spectrum $E_a(H)$ [31] clearly confirms this qualitative observation quantitatively (Figure 6b). The activation energy $E_a(H)$ is constant (±2 kJ/mol) at the value of 39 kJ/mol published previously for this material for $H > 6$ Pa [19]. This behavior of $E_a(H)$ = constant is typically found for all thermorheologically simple fluids like normal linear LLDPE and HDPE (the data of mHDPE C4 [31] are also plotted in Figure 5b). Below this threshold, a very low and error-afflicted activation energy of around 5 kJ/mol is found. This is a very strong effect, which has not been reported previously. LCB-mPE also show a thermorheological complexity; however, their activation energy increases, i.e., the opposite effect is observed.

Figure 6 shows the values of the recoverable compliances J_e after different creep times and elastic compliances J' at different angular frequencies of F18G at different temperatures. For a better comparability the time of the creep test divided by the shift factor t_0/a_T was set to be constant for all temperatures, i.e., the preceding creep tests were longer at low T and shorter at high T. Essentially the same was done for the frequencies at which the elastic compliances were determined ($1/(\omega \cdot a_T)$ = constant). $J'(1/(\omega \cdot a_T) = 10$ s) shows almost constant values; only the highest temperatures show a slightly higher elasticity. A constant value is the behavior expected for a conventional LLDPE. This finding makes sense, as $\omega \cdot a_T = 0.1$ s^{-1} (c.f. Figure 4b) is the threshold between the normal LLDPE and the abnormal behavior of F18G at lower frequencies $\omega \cdot a_T$. At $\omega \cdot a_T = 0.01$ s^{-1}, there is a complete change in behavior: $J'(\omega \cdot a_T = 0.01$ s$^{-1})$ increases by a factor of 2 between 150 and 230°C. The creep recovery tests with preceding creep times of $t_0/a_T = 1000$ and 10 000 s are significantly higher in J_e. When looking at the slope of $J_e(T)$, it becomes obvious that the effect is smaller for these longer times than for $1/(\omega \cdot a_T) = 10$ s, which corresponds to the time scale of the process causing the abnormal behavior (cf. Figure 5a). Because of the choice of $\omega \cdot a_T = 0.01$ s^{-1}, the position on the absolute time scale at which this process is probed depends on the temperature (the

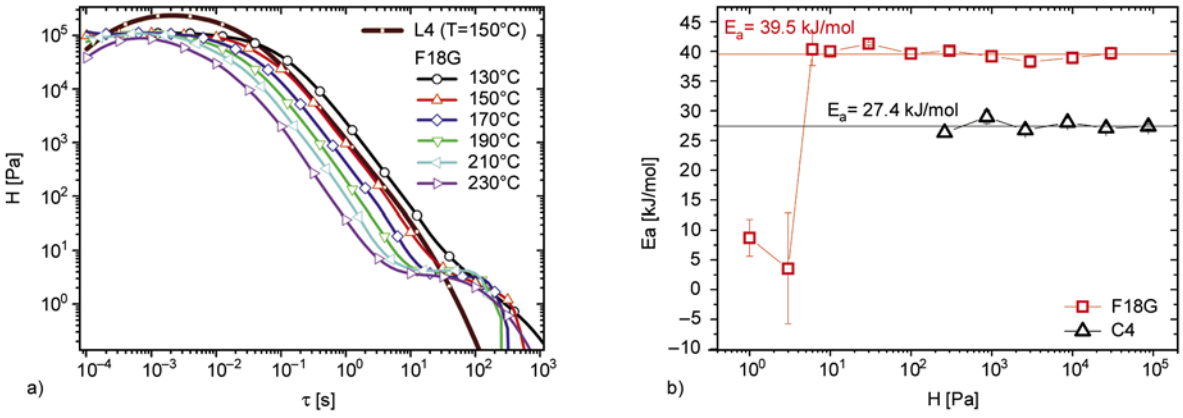

Figure 6. a) Relaxation spectra of F18G in comparison to Butene-LLDPE L4, b) activation energy spectrum

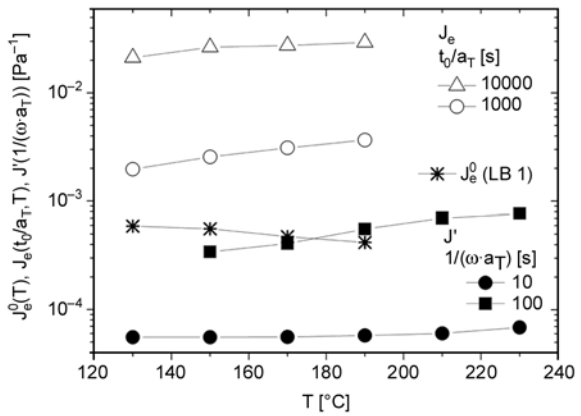

Figure 7. Recoverable compliances J_e after different creep times and elastic compliances J' at different angular frequencies of F18G as a function of temperature T in comparison to LCB-mLLDPE LB1 [29]

shift factors $a_T(T)$ are the shift factors valid for $H > 6$). When the probing time is significantly larger than the characteristic time of this process, the differences are less pronounced than at the time of the process ($1/(\omega \cdot a_T) = 100$ s).

One might argue that this dependence of J_e on the temperature is the same as the $J_e^0(T)$ dependence observed for LCB-mPE [29]. However, the temperature dependence of J_e^0 for LCB-mPE is exactly opposite to $J_e(T)$ for F18G (cf. ✳ in Figure 7 for the data of LCB-mLLDPE LB 1 [29]). Hence, these two types of thermorheological complexity have a different physical basis.

4. Discussion

4.1. Artifact?

Of course, the first question a careful reader of this article would ask is, whether the unusual behavior of F18G could be an experimental artifact. To the author's mind, the following artifacts would be conceivable:

1. At low moduli, δ of some rheometers tends to become artificially large (which would produce exactly the same effect as shown)
2. Degradation of the sample
3. Remaining unincorporated comonomer

The error in δ (1.) can be excluded, because two different rheometers with different setups were used, which were both tested to deliver the expected results with respect to $\delta(\omega)$ for similar materials (e.g., L4, but also many more [29, 52]). Furthermore, the creep recovery compliance $J_r(t)$ also shows this qualitative effect (for a quantitative comparison it would have to be proven that J_e is indeed J_e^0) [57, 58]. It is highly unlikely that a problem with the rheometer setups used would produce the same results consistently for two different rheometers and two different test modes.

The thermal degradation of the sample (2.) can be excluded for several reasons. Firstly, a frequency sweep measurement was performed as a first test, and then the identical test was performed again after all other tests, so that any difference in molecular structure could have been spotted with that test. Secondly, tests have shown that the catalyst produces polymers that are very thermally stable (a product with slightly less comonomer but otherwise identical synthesis conditions was found to be stable for more than 1.5 weeks at 150°C). Thirdly, a test at 130°C was performed before and after the test at 230°C. Both tests at 130°C were identical within the usual reproducibility intervals of ±5%, even though the data at 230°C measured between the different runs at 130°C with the same sample is distinctly different. This points to the physical nature of the effect. It was also tested whether the domain/phase structure can be distorted by heavy shear. It is possible to reduce the higher elasticity to a certain degree, although not completely, by significantly increasing the shear amplitude (Figure 8). Such shear susceptibility would be totally atypical of a chemical network.

It is, however, similar to effects found for block-copolymer melts [59], where the rheological response can be changed by several decades for samples forming well-ordered cubic structures. The changes

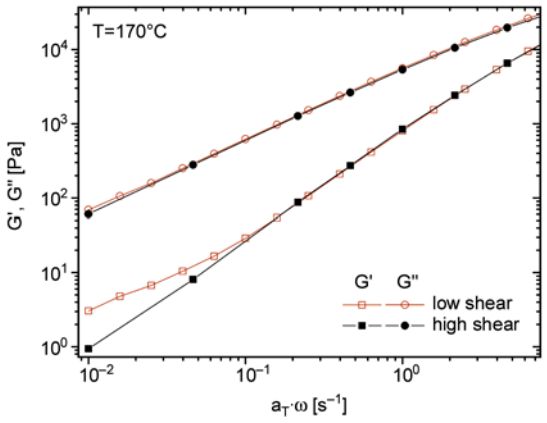

Figure 8. Comparison of the dynamic moduli of F18G at 170°C under low shear deformation ($\gamma_0 < 5\%$, open symbols) and high shear deformation ($\gamma_0(\omega = 0.01$ s$^{-1}) \approx 80\%$, filled symbols)

given in Figure 8 for F18G are rather small in comparison, but that is not surprising considering that this material can achieve a much lower degree of order than regular diblock copolymers.

The question of the remaining unincorporated octadecene (3.) cannot be answered purely by rheology. *GPC-MALLS* did not show any significant amounts of a low molecular substance, which could cause that effect. Furthermore, it was found that heptadecane, which is very similar to the octadecene, has a tendency to evaporate quickly at 150°C [38]. Typically, a significant loss of heptadecane (30%) was observed after 5 minutes. This was accompanied by a strong waxy smell in the laboratory, which lasted several hours. One can easily imagine that when keeping a sample of F18G in the rheometer for 6 days at 150°C, which was the longest measurement for this sample, no unincorporated octadecene would be left after that time. If the effect were caused by unincorporated octadecene, the behavior would change with time, but that was not the case here. Hence, a significant effect of unincorporated octadecene can be excluded.

Summarizing this section, experimental artifacts can be excluded, so that the observed effects must be due to a material property, which is discussed in the following.

4.2. Origin of the unusual behavior

4.2.1. Phase separation

The question is, if F18G is not long-chain branched, has a high molecular component, or is cross-linked, what is the origin of the thermorheological complexity?

Piel *et al.* [16] found that a high amount of long comonomers can lead to side-chain crystallization, being observable by both DSC and DMTA; in other words, the long comonomers tend to form a separate phase from the backbone in the solid state. For an octadecene-copolymers, (C18) this effect was found to be significantly smaller than for hexacosene-copolymers (C26), and barely observable for F18F (8C18 in Piel *et al.* [16]), the sample with the highest octadecene content in their study. The highest comonomer contents were around 3 mol%. The higher comonomer content of F18G of n_c = 4.5 mol% will foster the phase separation even more, leading to a more phase separated structure. In the melt, neither F18F nor F26F both with about 3 mol% comonomer content and octadecene and the longer hexacosene as comonomer, respectively, showed this abnormal behavior [19].

The reason why F26F and F18F show a phase separation in the solid state, although none can be detected in the melt, can only be that the driving forces for the phase separation are the crystallization kinetics. The thermodynamic explanation is that the methyl groups at the SCB- and chain ends cannot crystallize. This was proven by the synthesis of 'exact LLDPEs' [60], which have their short-chain branches at a defined position. In comparison to normal LLDPEs of the same comonomer content, their melting point is significantly higher and the crystallization peaks are narrower, i.e., the crystallites are more homogeneous and better built. This is a clear indicator that the SCB-ends are the moieties reducing the normal crystallization, because they do not fit in the crystal lattice. The consequence is that they stick out of the crystallites, thus, aligning them to some degree. This makes a secondary crystallization easier, which of course corresponds to a phase separation [16].

When crystallization driving forces are missing, e.g., in the melt, the phase separation becomes significantly less likely, and, therefore, needs more other driving forces to make it happen, e.g., a chemical difference. The high concentration of the SCBs in F18G increases the probability of different SCB-ends meeting each other, thus, forming a separate phase or domain (cf. Figure 9). Heindl *et al.* [24] recently suggested this type of behavior based on

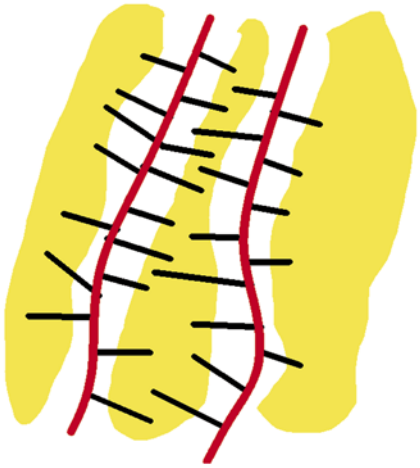

Figure 9. Sketch of the phase separated structure. Thick red lines: main chain, short, black lines: hexadecene side chains, yellow area: side chain phase

their molecular dynamics simulations. The phase boundaries of these intermolecular phase separated polymers are not very sharp, as the molecule bridges the phase boundary, hence, they can be rather considered as domains [24]. However, the rheological behavior indicates that the driving forces for the phase separation are strong enough to distinctly modify the rheological properties. On one hand, they lower the zero shear-rate viscosity η_0 by a factor of 3, but this is a consequence of the lower G_N^0; the characteristic relaxation time λ is unaffected. On the other hand, they introduce a relaxation mode into the polymer, which is very slow and differs in thermorheological behavior from that of the main chain.

4.2.2. Effect of phase separation on zero shear-rate viscosity

Finding a definite answer to the question why zero shear-rate viscosity, characteristic relaxation times, and plateau modulus do not follow the same scaling laws upon the introduction of the SCBs is not easy. The fact that F26F and F18G have almost the same weight comonomer content (around 30 wt.%) but very different η0/η0lin means that the comonomer content alone cannot be made responsible for the differences. This also shows the limitations of the approach by Chen *et al.* [56] explaining the effect of comonomer on the rheological behavior, as their scaling laws don't apply to F18G. This alone suggests that F18G differs from conventional mLLDPEs.

When assuming a phase separation, several effects occur. On one hand, the entanglement network is loosened (see also Chen *et al.* [56]). A comparison with F26F suggests that the effect on G_N^0 (and thus M_e) is almost identical, i.e., M_e(F18G) ≈ 850 kPa as opposed to 1973 kPa for L4. Hence, the entanglement network thinning is exactly as expected from the molecular data.

On the other hand, the characteristic relaxation time (e.g. the inverse crossover frequency) is almost unaffected by the comonomer content. According to Figure 5a, the crossover frequencies of L4 and F18G differ by factor 0.5, which is the ratio expected from looking at the molar masses M_w (without taking any comonomer effect into account). A comparison with Chen *et al.* [56] on the contrary would suggest a significantly higher factor, because the entanglement relaxation time τ_e should longer by factor ≈ 50 than L4. The experimental data of F18G (the ω_c-ratio of L4 and F18G is 0.5 as expected from the M_w-ratio), however, suggests that τe is unaffected by the comonomers, while Chen *et al.* [56] suggest an increase.

This difference is quite puzzling, but can be rationalized the following way. The comonomers don't contribute to the entanglement network and, hence, the fact that they are in another phase doesn't influence the entanglement network. The 'slowing down' of the entanglement motion by the hexadecane side chains, however, does not occur and, therefore, τ_e is unaffected. In other words, the material behaves just like HDPE with respect to the characteristic relaxation time λ or $1/\omega_c$. Because, η_0 is proportional to the product of G_N^0 and the terminal relaxation time (or $1/\omega_c$), a lowering of the plateau modulus by factor 3, which (in contrast to single phase LLDPEs) is not balanced by a lowering of ω_c by the same factor, the zero shear-rate viscosity η_0 is decreased to 30% of its expected value.

This decrease is predicted, when taking Chen *et al.* [56] into account. Based on the higher monomer molar mass, they predict that τ_e of F18G should be higher by factor 50, which when taking the exponent of 3.6 into account, is a factor of 3 with respect to ω_c.

4.2.3. Effect of the side chains on the low frequency properties

Looking at the hexadecane side chains as separate entities is not cogent, as an unperturbed octadecene chain would have a main relaxation time in the range of around $5 \cdot 10^{-10}$ s (calculated from the assumption that the plateau modulus G_N^0 of PE is around 2 MPa and the zero shear-rate viscosity η_0 of pure octadecene is around 1 mPa·s at 150°C [38]). Even when assuming that the incorporation of octadecene as side chains leads to a significant lengthening of the main relaxation time, it is very unlikely that its characteristic relaxation time is shifted by 10 to 11 orders of magnitude, from $5 \cdot 10^{-10}$ s to about 5 s ($\omega \approx 0.02$ s^{-1}). Also, this would not explain the low E_a of this process. Van Ruymbeke *et al.* [61] and Kapnistos *et al.* [62] found that pom-poms and combs with unentangled arms do not significantly affect the arms; i.e., the molecules behave like linear chains with a slightly lengthened

relaxation time scale. Chen *et al.* [56] found the same for LLDPE. Thus, the extra relaxation mode cannot be caused by the main relaxation time of the hexadecane side chains.

As the hexadecane-side chains (C_{16}) are certainly unentangled (the entanglement molar mass of PE is reported to be around 1000 g/mol = 70 CH_2 [63]), they do not lend themselves to acting as long-chain branches. The rheological response would also look distinctly different in this case, and the activation energy would be significantly higher in the terminal regime.

A high molecular component would also not lead to a thermorheological complexity, as long as the chemical structure is not changing distinctly as a function of molar mass, which would be also very unlikely from a reaction kinetics point-of-view. Furthermore, it would have been detected by *SEC-MALLS*.

The most likely explanation is that the long-time relaxation mode is caused by the presence of intramolecular phase separation, as samples with sizable amounts of long short-chain branches are known to tend to phase separate, which is a consequence of the immiscibility of ethene-*a*-olefin copolymers of different side-chain contents [7, 8]. That is, the long short-chain branches behave as though independent, trying to separate themselves from their own backbone, thus leading to a separate phase, which can crystallize separately as well, if they are long enough [16].

This conclusion is supported by the previous finding that the steady-state elastic recovery compliances J_e^0 of mLLDPEs with long comonomers are significantly higher than for short comonomers [51]. The higher J_e^0 can be interpreted as the influence of the long side chains leading to a very weak intra-chain phase separation – the same effect as for F18G but significantly weaker.

5. Possible reason for the different temperature dependence of the thermorheological complexity

When comparing the chemical structures of F18G to the block-copolymers characterized in detail frequently, three important differences become obvious:

– F18G is a random copolymer with relatively long side chains, which are, however, distinctly below the entanglement molar mass M_e (less than 25%). The block copolymers, characterized so far, are much higher in their block length than the side chains of F18G.
– F18G is a random copolymer, which can be considered to be a comb with short arms, block-copolymers typically contain only one A- and one B-block.
– The chemical difference in F18G is very small. Effectively, the main chemical difference is the CH_3-endgroup. Block-copolymers, however, typically contain two distinctly different comonomers, e.g. styrene and butadiene. However, also polymers with small chemical differences, e.g. the ethylene/octene-block octene might exhibit a clear phase separation although not as well ordered.

These three differences in chemical structure mean that

– The driving forces for phase separation are lower for F18G than for most block copolymers characterized so far, because the chemical difference is very small.
– The polymer does not contain an A- and a B-block, but an A-main chain and, on weight average, approximately 160 B-blocks as side chains, which is less than 16 C each. Most probably the separated domain does not involve the complete side chain but only the 'outer' half.

The direct consequence is that the sample contains only a weakly separated structure, which, however, has a very high surface area and many chains crossing the surface. Hence, the sample has some similarities with a surfactant. Self-evidently, the small B-domains will coalesce and, thus, form larger domains or phases.

One striking feature of sample F18G in comparison to the block copolymers characterized so far is that the temperature dependence is inverse to the other samples. When we consider the differences in chemical structure, it becomes obvious that the different behavior must originate from the small chemical difference and the short blocks, i.e., the high surface area.

The most logical conclusion is the following. At low temperature, the side chains are less able to form a separate phase, because the solubility in the A-phase is low. So there is a sharp interface, which only slightly coalesces and the B-domains are

small. When increasing the temperature, the miscibility increases. This has two effects. The degree of phase separation becomes smaller, but on the other hand the higher miscibility increases the thickness of the interface.

The rheological data has clearly demonstrated that the second effect is stronger. Because previously characterized block-copolymers had significantly larger blocks, this effect is not observed as the concentrations of chains passing through the surface is not as high as for F18G.

6. Conclusions

This article has shown evidence of a very unusual behavior of the special mLLDPE F18G. At low frequencies a clear secondary process becomes obvious, which is essentially unchanged by temperature, making it stronger at high temperatures. This leads to a decrease of the activation energy E_a as a function of relaxation strength H below $H = 6$ Pa. Also an increase of the elastic recovery compliance J_e with increasing T was found. Both effects are opposite to the typical behavior of long-chain branched PE, and it was, therefore, concluded that long-chain branches are not responsible for this behavior.

The sample F18G indeed shows a weak phase separation leading to a novel kind of thermorheological complexity, previously unknown for single phase melts. However, it is quite similar to the order/disorder transition for diblock copolymers [9].

The driving forces for this phase separation are the difference in chemical potential between CH_3– and –CH_2– groups and the large length and high molar fraction of the octadecene (i.e., the hexadecane side chains).

The fact that a special comonomer, as well as a relatively high concentration of that comonomer, is needed to cause this effect, and furthermore, that it is relatively weak, constitute the proffered explanation as to why it has not been discovered previously. The high interface and the weak chemical differences lead to an inversion of the usual temperature dependence found in block copolymers.

Acknowledgements

The author would like to thank the German Research Foundation and the Sanhak Industry-University Cooperation Fund for financial support. The synthesis of F18G is acknowledged to Dr. B. Arikan-Conley, group of Prof. Dr. W. Kaminsky (University Hamburg, Germany). Also the input from Prof. Dr. H. Münstedt, Dr. J. Resch, Dr. J. Kaschta, and Mrs. I. Herzer (Friedrich-Alexander University Erlangen-Nürnberg, Germany) concerning the measurements and their interpretation provided a valuable base for this article.

References

[1] Ferry J. D.: Viscoelastic properties of polymers. John Wiley and Sons, New York (1980).

[2] Sperling L. H.: Introduction to polymer science. Wiley, New York (2006).

[3] Rajasekaran J. J., Curro J. G., Honeycutt J. D.: Theory for the phase behavior of polyolefin blends: Application to the polyethylene/isotactic polypropylene blend. Macromolecules, **28**, 6843–6853 (1995). DOI: 10.1021/ma00124a020

[4] Tashiro K., Stein R. S., Hsu S. L.: Cocrystallization and phase segregation of polyethylene blends. 1. Thermal and vibrational spectroscopic study by utilizing the deuteration technique. Macromolecules, **25**, 1801–1808 (1992). DOI: 10.1021/ma00032a029

[5] Bousmina M.: Effect of interfacial tension on linear viscoelastic behavior of immiscible polymer blends. Rheologica Acta, **38**, 251–254 (1999). DOI: 10.1007/s003970050175

[6] Fan Z. G. J., Williams M. C., Choi P.: A molecular dynamics study of the effects of branching characteristics of LDPE on its miscibility with HDPE. Polymer, **43**, 1497–1502 (2002). DOI: 10.1016/S0032-3861(01)00730-3

[7] Godehardt R., Rudolph S., Lebek W., Goerlitz S., Adhikari R., Allert E., Giesemann J., Michler G. H.: Morphology and micromechanical behavior of blends of ethene/1-hexene copolymers. Journal of Macromolecular Science: Physics, **38**, 817–835 (1999).

[8] Adhikari R., Godehardt R., Lebek W., Frangov S., Michler G. H., Radusch H-J., Calleja F. J. B.: Morphology and micromechanical properties of ethylene/1-octene copolymers and their blends with high density polyethylene. Polymers for Advanced Technologies, **16**, 156–166 (2005). DOI: 10.1002/pat.578

[9] Bates F. S., Rosedale J. H., Fredrickson G. H.: Fluctuation effects in a symmetric diblock copolymer near the order-disorder transition. Journal of Chemical Physics, **92**, 6255–6270 (1990). DOI: 10.1063/1.458350

[10] Almdal K., Bates F. S., Mortensen K.: Order, disorder, and fluctuation effects in an asymmetric poly(ethylene-propylene)-poly(ethylethylene) diblock copolymer. Journal of Chemical Physics, **96**, 9122–9132 (1992).
DOI: 10.1063/1.462221

[11] Kossuth M. B., Morse D. C., Bates F. S.: Viscoelastic behavior of cubic phases in block copolymer melts. Journal of Rheology, **43**, 167–196 (1999).
DOI: 10.1122/1.550981

[12] Dealy J., Larson R. G.: Structure and rheology of molten polymers – From structure to flow behavior and back again. Munich, Hanser (2006).

[13] Park H. E., Dealy J., Marchand G. R., Wang J., Li S., Register R. A.: Rheology and structure of molten, olefin multiblock copolymers. Macromolecules, **43**, 6789–6799 (2010).
DOI: 10.1021/ma1012122

[14] Gaur U., Wunderlich B.: Study of microphase separation in block co-polymers of styrene and alpha-methylstyrene in the glass-transition region using quantitative thermal-analysis. Macromolecules, **13**, 1618–1625 (1980).

[15] Leibler L.: Theory of microphase separation in block copolymers. Macromolecules, **13**, 1602–1617 (1980).
DOI: 10.1021/ma60078a047

[16] Piel C., Starck P., Seppälä J. V., Kaminsky W.: Thermal and mechanical analysis of metallocene-catalyzed ethene–α-olefin copolymers: The influence of the length and number of the crystallizing side chains. Journal of Polymer Science Part A: Polymer Chemistry, **44**, 1600–1612 (2006).
DOI: 10.1002/pola.21265

[17] Stadler F. J., Takahashi T., Yonetake K.: Lattice sizes, crystallinities, and spacing between amorphous chains – characterization of ethene-/α-olefin copolymers with various comonomers and comonomer contents measured by wide angle X-ray scattering. e-Polymers, no.40 (2009).

[18] Stadler F. J., Takahashi T., Yonetake K.: Crystal lattice of ethene-/α-olefin copolymers with various long comonomers (C8-C26) measured by wide angle X-ray diffraction. Macromolecular Chemistry and Physics, in press (2011).

[19] Stadler F. J., Takahashi T., Yonetake K.: Crystallite dimensions – characterization of ethene-/α-olefin copolymers with various comonomers and comonomer contents measured by small- and wide angle X-ray scattering. e-Polymers, no.41 (2009).

[20] Kessner U., Kaschta J., Stadler F. J., Le Duff C. S., Drooghaag X., Münstedt H.: Thermorheological behavior of various short- and long-chain branched polyethylenes and their correlations with the molecular structure. Macromolecules, **43**, 7341–7350 (2010).
DOI: 10.1021/ma100705f

[21] Palierne J. F.: Linear rheology of viscoelastic emulsions with interfacial tension. Rheologica Acta, **29**, 204–214 (1990).
DOI: 10.1007/BF01331356

[22] Handge U. A., Okamoto K., Münstedt H.: Recoverable deformation and morphology after uniaxial elongation of a polystyrene/linear low density polyethylene blend. Rheologica Acta, **46**, 1197–1209 (2007).
DOI: 10.1007/s00397-007-0208-5

[23] Heindl M., Sommer M. K., Münstedt H.: Morphology development in polystyrene/polyethylene blends during uniaxial elongational flow. Rheologica Acta, **44**, 55–70 (2004).
DOI: 10.1007/s00397-004-0372-9

[24] Capodagli J., Lakes R.: Isothermal viscoelastic properties of PMMA and LDPE over 11 decades of frequency and time: a test of time–temperature superposition. Rheologica Acta, **47**, 777–786 (2008).
DOI: 10.1007/s00397-008-0287-y

[25] Carella J. M., Gotro J. T., Graessley W. W.: Thermorheological effects of long-chain branching in entangled polymer melts. Macromolecules, **19**, 659–667 (1986).
DOI: 10.1021/ma00157a031

[26] Laun H. M.: Orientation of macromolecules and elastic deformations in polymer melts. Influence of molecular structure on the reptation of molecules. Progress in Colloid Polymer Science, **75**, 111–139 (1987).
DOI: 10.1007/BFb0109414

[27] Keßner U., Kaschta J., Münstedt H.: Determination of method-invariant activation energies of long-chain branched low-density polyethylenes. Journal of Rheology, **53**, 1001–1016 (2009).
DOI: 10.1122/1.3124682

[28] Keßner U., Münstedt H.: Thermorheology as a method to analyze long-chain branched polyethylenes. Polymer, **51**, 507–513 (2009).
DOI: 10.1016/j.polymer.2009.11.005

[29] Resch J. A., Stadler F. J., Kaschta J., Münstedt H.: Temperature dependence of the linear steady-state shear compliance of linear and long-chain branched polyethylenes. Macromolecules, **42**, 5676–5683 (2009).
DOI: 10.1021/ma9008719

[30] Wood-Adams P. M., Costeux S.: Thermorheological behavior of polyethylene: Effects of microstructure and long chain branching. Macromolecules, **34**, 6281–6290 (2001).
DOI: 10.1021/ma0017034

[31] Stadler F. J., Kaschta J., Münstedt H.: Thermorheological behavior of various long-chain branched polyethylenes. Macromolecules, **41**, 1328–1333 (2008).
DOI: 10.1021/ma702367a

[32] Stadler F. J., Arikan B., Kaschta J., Rulhoff S., Kaminsky W.: Long-chain branch formation in syndiotactic polypropene induced by vinyl chloride. Macromolecular Chemistry and Physics, **211**, 1472–1481 (2010).
DOI: 10.1002/macp.200900688

[33] Stange J., Wächter S., Kaspar H., Münstedt H.: Linear rheological properties of the semi-fluorinated copolymer tetrafluoroethylene-hexafluoropropylene-vinylidenfluoride (THV) with controlled amounts of long-chain branching. Macromolecules, **40**, 2409–2416 (2007).
DOI: 10.1021/ma0626867

[34] Kaminsky W., Piel C., Scharlach K.: Polymerization of ethene and longer chained olefins by metallocene catalysis. Macromolecular Symposia, **226**, 25–34 (2005).
DOI: 10.1002/masy.200550803

[35] Piel C., Stadler F. J., Kaschta J., Rulhoff S., Münstedt H., Kaminsky W.: Structure-property relationships of linear and long-chain branched metallocene high-density polyethylenes characterized by shear rheology and SEC-MALLS. Macromolecular Chemistry and Physics, **207**, 26–38 (2006).
DOI: 10.1002/macp.200500321

[36] Stadler F. J., Piel C., Klimke K., Kaschta J., Parkinson M., Wilhelm M., Kaminsky W., Münstedt H.: Influence of type and content of various comonomers on long-chain branching of ethene/α-olefin copolymers. Macromolecules, **39**, 1474–1482 (2006).
DOI: 10.1021/ma0514018

[37] Klimke K., Parkinson M., Piel C., Kaminsky W., Spiess H-W., Wilhelm M.: Optimisation and application of polyolefin branch quantification by melt-state ^{13}C NMR spectroscopy. Macromolecular Chemistry and Physics, **207**, 382–395 (2006).
DOI: 10.1002/macp.200500422

[38] Stadler F. J., Piel C., Kaschta J., Rulhoff S., Kaminsky W., Münstedt H.: Dependence of the zero shear-rate viscosity and the viscosity function of linear high-density polyethylenes on the mass-average molar mass and polydispersity. Rheologica Acta, **45**, 755–764 (2006).
DOI: 10.1007/s00397-005-0042-6

[39] Gabriel C., Kaschta J., Münstedt H.: Influence of molecular structure on rheological properties of polyethylenes I. Creep recovery measurements in shear. Rheologica Acta, **37**, 7–20 (1998).
DOI: 10.1007/s003970050086

[40] Stadler F. J., Bailly C.: A new method for the calculation of continuous relaxation spectra from dynamic-mechanical data. Rheologica Acta, **48**, 33–49 (2009).
DOI: 10.1007/s00397-008-0303-2

[41] Stadler F. J.: Effect of incomplete datasets on the calculation of continuous relaxation spectra from dynamic-mechanical data. Rheologica Acta, **49**, 1041–1057 (2010).
DOI: 10.1007/s00397-010-0479-0

[42] Stadler F. J., Kaschta J., Münstedt H.: Dynamic-mechanical behavior of polyethylenes and ethene-/α-olefin-copolymers. Part I. α′-relaxation. Polymer, **46**, 10311–10320 (2005).
DOI: 10.1016/j.polymer.2005.07.099

[43] Pérez E., Benavente R., Quijada R., Narváez A., Galland G. B.: Structure characterization of copolymers of ethylene and 1-octadecene. Journal of Polymer Science Part B: Polymer Physics, **38**, 1440–1448 (2000).
DOI: 10.1002/(SICI)1099-0488(20000601)38:11<1440::AID-POLB40>3.0.CO;2-O

[44] Wood-Adams P. M., Dealy J. M., deGroot A. W., Redwine O. D.: Effect of molecular structure on the linear viscoelastic behavior of polyethylene. Macromolecules, **33**, 7489–7499 (2000).
DOI: 10.1021/ma991533z

[45] Stadler F. J., Piel C., Kaminsky W., Münstedt H.: Rheological characterization of long-chain branched polyethylenes and comparison with classical analytical methods. Macromolecular Symposia, **236**, 209–218 (2006).
DOI: 10.1002/masy.200690057

[46] Gabriel C., Münstedt H.: Influence of long-chain branches in polyethylenes on linear viscoelastic flow properties in shear. Rheologica Acta, **41**, 232–244 (2002).
DOI: 10.1007/s00397-001-0219-6

[47] Gabriel C., Kokko E., Löfgren B., Seppälä J., Münstedt H.: Analytical and rheological characterization of long-chain branched metallocene-catalyzed ethylene homopolymers. Polymer, **43**, 6383–6390 (2002).
DOI: 10.1016/S0032-3861(02)00564-5

[48] He C., Costeux S., Wood-Adams P.: A technique to infer structural information for low level long chain branched polyethylenes. Macromolecules, **45**, 3747–3754 (2004).
DOI: 10.1016/j.polymer.2004.03.085

[49] Arikan B., Stadler F. J., Kaschta J., Münstedt H., Kaminsky W.: Synthesis and characterization of novel ethene-*graft*-ethene/propene copolymers. Macromolecular Rapid Communications, **28**, 1472–1478 (2007).
DOI: 10.1002/marc.200700161

[50] Wang J-S., Knox J. R., Porter R. S.: Steady-state and dynamic rheology of poly(1-olefin) melts. Polymer, **16**, 1709–1719 (1978).
DOI: 10.1002/pol.1978.180161001

[51] Stadler F. J., Münstedt H.: Terminal viscous and elastic properties of linear ethene/α-olefin copolymers. Journal of Rheology, **52**, 697–712 (2008).
DOI: 10.1122/1.2892039

[52] Wolff F., Resch J. A., Kaschta J., Münstedt H.: Comparison of viscous and elastic properties of polyolefin melts in shear and elongation. Rheologica Acta, **49**, 95–103 (2010).
DOI: 10.1007/s00397-009-0396-2

[53] Schmidt M., Münstedt H.: On the elastic properties of model suspensions as investigated by creep recovery measurements in shear. Rheologica Acta, **41**, 205–210 (2002).
DOI: 10.1007/s003970100206

[54] Plazek D. J., Echeverria I.: Don't cry for me Charlie Brown, or with compliance comes comprehension. Journal of Rheology, **44**, 831–841 (2000). DOI: 10.1122/1.551117

[55] Gabriel C.: Einfluss der molekularen Struktur auf das viskoelastische Verhalten von Polyethylenschmelzen. Shaker-Verlag, Aachen (2001).

[56] Chen X., Stadler F. J., Münstedt H., Larson R. G.: Method for obtaining tube model parameters for commercial ethene/α-olefin copolymers. Journal of Rheology, **54**, 393–406 (2010). DOI: 10.1122/1.3305721

[57] Kaschta J., Schwarzl F. R.: Calculation of discrete retardation spectra from creep data: 1. Method. Rheologica Acta, **33**, 517–529 (1994). DOI: 10.1007/BF00366336

[58] Kaschta J., Schwarzl F. R.: Calculation of discrete retardation spectra from creep data: 2. Analysis of measured creep curves. Rheologica Acta, **33**, 530–541 (1994). DOI: 10.1007/BF00366337

[59] Sebastian J. M., Graessley W. W., Register R. A.: Steady-shear rheology of block copolymer melts and concentrated solutions: Defect-mediated flow at low stresses in body-centered-cubic systems. Journal of Rheology, **46**, 863–879 (2002). DOI: 10.1122/1.1475979

[60] Rojas G., Berda E. B., Wagener K. B.: Precision polyolefin structure: Modeling polyethylene containing alkyl branches. Polymer, **49**, 2985–2995 (2008). DOI: 10.1016/j.polymer.2008.03.029

[61] van Ruymbeke E., Kapnistos M., Vlassopoulos D., Huang T. Z., Knauss D. M.: Linear melt rheology of pom-pom polystyrenes with unentangled branches. Macromolecules, **40**, 1713–1719 (2007). DOI: 10.1021/ma062487n

[62] Kapnistos M., Vlassopoulos D., Roovers J., Leal L. G.: Linear rheology of architecturally complex macromolecules: Comb polymers with linear backbones. Macromolecules, **38**, 7852–7862 (2005). DOI: 10.1021/ma050644x

[63] Fetters L. J., Lohse D. J., Graessley W. W.: Chain dimensions and entanglement spacings in dense macromolecular systems. Journal of Polymer Science Part B: Polymer Physics, **37**, 1023–1033 (1999). DOI: 10.1002/(SICI)1099-0488(19990515)37:10<1023::AID-POLB7>3.0.CO;2-T

eXPRESS Polymer Letters Vol.5, No.4 (2011) 342–361
Available online at www.expresspolymlett.com
DOI: 10.3144/expresspolymlett.2011.34

Preparations, properties and applications of chitosan based nanofibers fabricated by electrospinning

K. Sun[*], *Z. H. Li*

Deparment of chemistry, Sichuan college of education, Chendu 610041, Sichuan province, China

Received 5 September 2010; accepted in revised form 14 November 2010

Abstract. Chitosan is soluble in most acids. The protonation of the amino groups on the chitosan backbone inhibits the electrospinnability of pure chitosan. Recently, electrospinning of nanofibers based on chitosan has been widely researched and numerous nanofibers containing chitosan have been prepared by decreasing the number of the free amino groups of chitosan as the nanofibiers have enormous possibilities for better utilization in various areas. This article reviews the preparations and properties of the nanofibers which were electrospun from pure chitosan, blends of chitosan and synthetic polymers, blends of chitosan and protein, chitosan derivatives, as well as blends of chitosan and inorganic nanoparticles, respectively. The applications of the nanofibers containing chitosan such as enzyme immobilization, filtration, wound dressing, tissue engineering, drug delivery and catalysis are also summarized in detail.

Keywords: *nanomaterials, chitosan, nanofibers, electrospinning, applications*

1. Introduction

Electrospinning is a fiber-forming process by which either polymer solutions or melts are charged by high voltage to form fine jets. It was first reported by Formhals in 1934 [1]. Fiber formation by electrospinning of polymer solutions has been extensively studied in terms of voltage, tip-to-collector distance, feeding rate of polymer solution, and polymer solution properties [2–5]. These nanofibers can form nonwoven textile mats, oriented fibrous bundles and even three-dimensional structured scaffolds, all with large surface areas and high porosity [6]. These nanofibers are of considerable interest for various kinds of applications.

Chitosan, a (1–4)-linked 2-amino-2-deoxy-D-glucopyranose (Figure 1), is derived from chitin, one of the most abundant natural polysaccharides. Chitosan is well known for its nontoxic, biocompatible and biodegradable properties [7]. In addition, it has several unique properties: it is antimicrobial and inhibits the growth of a wide variety of fungi, yeasts, and bacteria, which can be beneficial for use in the field of biomedicine [8]. It can also bind toxic metal ions, which can be beneficial for use in air cleaning and water purification applications [9]. These properties arise as a result of protonation of NH_2^- groups on the chitosan backbone.

Recently, electrospun nanofibers based on chitosan have been widely researched and various nanofiber products containing chitosan have been produced by electrospinning. These nanofibers yield potential applications in various areas. This article reviews the preparations and properties of the nanofibers by electrospinning of pure chitosan, blends of chitosan and synthetic polymers, blends of chitosan and pro-

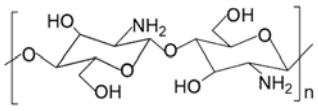

Figure 1. The molecular structure of chitosan

[*]Corresponding author, e-mail: kang-sun@163.com

tein, chitosan derivatives, as well as blends of chitosan and inorganic nanoparticles, respectively. The applications of the chitosan based nanofibers in areas such as enzyme immobilization, filtration, wound dressing, tissue engineering, drug delivery and catalysis are also summarized in detail.

2. Electrospinning of chitosan

2.1. Electrospinning of pure chitosan

Chitosan is soluble in most acids. The protonation of chitosan changes it into a polyelectrolyte in acidic solutions. The repulsive forces between ionic groups within polymer backbone that arise due to the application of a high electric field during electrospinning restrict the formation of continuous fibers and often produce beads [10], so it is difficult to fabricate pure chitosan nanofibers. An electrospun nanofibrous mat of pure chitosan was successfully prepared by Ohkawa and coworkers [11] using trifluoroacetic acid (TFA) as electrospinning solvent. TFA is a suitable spinning solvent for chitosan because the amino groups of the chitosan can form salts with TFA [12], which can effectively destroy the intermolecular interactions between the chitosan molecules and thus facilitate electrospinning. As the chitosan concentration increases, the morphology of the deposition on the collector changes from spherical beads to interconnected fibrous networks. The addition of dichloromethane (DCM) to the chitosan-TFA solution improves the homogeneity of the electrospun chitosan fibers without interconnected fibrous networks. Under optimized conditions, homogenous chitosan fibers with a mean diameter of 330 nm were prepared. Another study conducted by Ohkawa *et al.* [13] focused on optimizing the viscosity of chitosan solutions in order to decrease the average fiber diameter. It was determined that fiber diameter and polymer concentration have an inverse relationship. Sangsanoh *et al.* [14] developed electrospun chitosan nanofibers using TFA/DCM (70:30 v/v) as electrospinning solvent. The obtained fibers with average diameters of 126±20 nm were smooth without the presence of beads.

Dissolution of chitosan nanofibers by electrospinning of chitosan solution in TFA with or without DCM as the modifying cosolvent will result in the loss of the fibrous structure as soon as the membranes contact with neutral or weak basic aqueous solutions, and thus limits the further use of the membranes [15]. Dissolution occurs as a result of the high solubility in these aqueous media of $-NH_3^+CF3COO^-$ salt residues that are formed when chitosan is dissolved in TFA. Traditional neutralization with a NaOH aqueous solution only maintained partial fibrous structure. Much improvement in the neutralization method was achieved with the saturated Na_2CO_3 aqueous solution with an excess amount of Na_2CO_3(s) in the solution. The electrospun chitosan nanofibrous membranes, after neutralization in the Na_2CO_3 aqueous solution, could maintain its fibrous structure even after continuous submersion in phosphate buffer saline (pH = 7.4) or distilled water for 12 weeks. Haider and Park [16] prepared similar chitosan nanofiber mats by electrospinning. The as-spun nanofiber (~235 nm in diameter) mats which were neutralized with potassium carbonate showed good erosion stability in water and high adsorption affinity for metal ions in an aqueous solution.

Besides TFA, the second solvent that has shown to effectively produce chitosan nanofibers is concentrated acetic acid. A uniform nanofibrous mat with average fiber diameter of 130 nm was fabricated by Geng *et al.* [17] from the following optimum condition: 7% chitosan solution in aqueous 90% acetic acid solution and in the electric field of 4 kV/cm. The aqueous acetic acid concentration higher than 30% was a prerequisite for chitosan nanofiber formation, because more concentrated acetic acid in water progressively decreased the surface tension of the chitosan solution and concomitantly increased the charged density of jet without a significant effect on the solution viscosity. However, acetic acid solution of more than 90% did not dissolve enough chitosan to make a spinnable viscous concentration. Additionally, only chitosan of a molecular weight of 106 000 g/mol produced bead-free chitosan nanofibers, while low or high molecular weight chitosans of 30 000 and 398 000 g/mol did not. Average fiber diameters and size distribution decreased with increasing electric field and more bead defects appeared at 5 kV/cm or more. In addition, Vrieze *et al.* [18] attempted a range of acid aqueous solutions such as formic acid, acetic acid, lactic acid and hydrochloric acid for developing chitosan nanofibres by electrospinning. The study showed that chitosan nanofibres with a diameter of

about 70±45 nm were obtained from a concentrated acetic acid solution (90%) with a 3% chitosan concentration at an applied voltage of 2.0 kV/cm and a flow rate of 0.3 ml/h.

The problem of the high viscosity of chitosan, which limits its spinnability, is resolved through the application of an alkali treatment which hydrolyzes chitosan chains and so decreases their molecular weight [19]. Solutions of the treated chitosan in aqueous 70–90% acetic acid produce nanofibers with appropriate quality and processing stability. Decreasing the acetic acid concentration in the solvent increases the mean diameter of the nanofibers. Optimum nanofibers are achieved with chitosan which is hydrolyzed for 48 h. Such nanofibers result in a moisture regain which is 74% greater than that of treated and untreated chitosan powder. The diameter of this nanofiber, 140 nm, is strongly affected by the electrospinning conditions as well as by the concentration of the solvent. FTIR investigations prove that neither the alkali treatment nor the electrospinning process change the chemical nature of the polymer.

Pure chitosan nanofibers can be cross-linked using a method involving glutaraldehyde (GA) vapor, utilizing a Schiff base imine functionality. The study conducted by Schiffman *et al.* [20] indicated that the solubility of the chitosan mats was greatly improved after cross-linking. The as-spun medium molecular weight chitosan nanofibers have a Young's modulus of 154.9±40.0 MPa, and were highly soluble in acidic and aqueous solutions. After cross-linking, the fibers increased in diameter by an average of 161 nm, have a decreased Young's modulus of 150.8±43.6 MPa, and were insoluble in basic, acidic, and aqueous solutions. Though the extent to which GA penetrates into the chitosan fibers is currently unknown, it is evident that the cross-linking resulted in increased brittleness, a color change, and the restriction of fiber sliding. Schiff base cross-linked chitosan fibrous mats can be produced utilizing a one-step electrospinning process [21], which is 25 times faster and, therefore, more economical than the two-step vapor-cross-linking method mentioned above. These fibrous mats are insoluble in acidic, basic, and aqueous solutions for 72 h. Additionally, this improved production method results in a decreased average fiber diameter, which measures 128±40 nm.

2.2. Electrospinning of blends of chitosan and synthetic polymers

It is commonly observed when electrospinning from polymers that the formation of beads attributed to an inadequate stretch of the filaments during the whipping of the jet because of a low charge density. To overcome this defect, salts [22], ionic surfactants [23] or ionic polyelectrolytes [24] can be added into the polymer solution to improve the net charge density that enhances the whipping instability. The jet was stretched under stronger charge repulsion and at a higher speed, resulting in an exhaustion of the bead structure. Since chitosan is a linear cationic polymer, it was determined that chitosan can act like other ionic additives and reduce fiber diameter and thus producing bead free fibers [25]. Recently, the electrospun composite nanofibers have been developed using chitosan and synthetic polymers such as poly(vinyl alcohol) (PVA), poly(ethylene oxide) (PEO), poly(ethylene terpthalate) (PET), polycaprolactone (PCL), poly(lactic acid) (PLA), nylon-6 and others. These composite nanofibers are more advantageous over the electrospun nanofibers of pure chitosan, because the mechanical, biocompatible, antibacterial and other properties of the nanofibers were drastically enhanced by the addition of these polymers.

Because of its favorable properties such as nontoxicity, biocompatibility and biodegradability, PVA has been used for a variety of biomedical applications such as bone implants as a replacement for the nucleus pulposus [26] and artificial organs [27]. Because PVA has good fiber forming characteristics, many nanofibers of the blends of PVA and chitosan have been fabricated by electrospinning [28–33]. For examples, Nanofibers with average diameters between 20 and 100 nm have been prepared by electrospinning of 82.5% deacetylated chitosan (M_v = 1600 kDa) mixed with poly(vinyl alcohol) (PVA, M_w = 124–186 kDa) in 2% (v/v) aqueous acetic acid [28]. Finer fibers, fewer beaded structures and more efficient fiber formation were observed with increasing PVA contents. Chitosan/PVA nanofibers were also prepared via the electrospinning of chitosan/PVA/acrylic acid aqueous solutions at various concentrations by adjusting the concentrations of chitosan, PVA and acrylic acid [29]. The nanoporous fibers of pure chitosan could be generated by removing the PVA component in the

chitosan/PVA bicomponent fibers with NaOH aqueous solution [28, 30]. These pure chitosan nanofibers have special characteristics of excellent biocompatibility, high surface/volume ratio, and large porosity. Chitosan/PVA nanofibers can be crosslinked with heat mediated chemical crosslinking [34]. Triethylene glycol dimethacrylate (TEGDMA) was added into chitosan/PVA solution prior to spinning followed by heat-treating the as-spun mats for 2 h at 80°C. The results showed that, the nanofibers exhibited a smooth surface and regular morphology, and tensile strength of nanofibers improved with increasing of TEGDMA content.

Poly(ethylene oxide) (PEO) is also a biocompatible polymer that has been used as cartilage tissue repair [35] and wound dressing [36]. Many nanofibers of the blends of PEO and chitosan have also been fabricated by electrospinning [37–42]. For examples, Klossner *et al.* [37] fabricated defect-free nanofibers with average diameters ranging from 62±9 to 129±16 nm by electrospinning of blended solutions of chitosan and PEO in acetic acid. Their study showed that as total polymer concentration (chitosan + PEO) increased, the number of beads decreased, and as chitosan concentration increased, fiber diameter decreased. Chitosan/PEO solutions phase would separate over time, so blended solutions were able to be electrospun easily within 24 h of initially being blended. The addition of NaCl stabilized these solutions and increased the time the blended solutions could be stored before electrospinning. Bhattarai *et al.* [38] prepared nanofibers with an average fiber diameter controllable from a few microns down to ~40 nm and a narrow size distribution by electrospinning solutions containing chitosan, PEO and Triton X-100™. It was found that the matrix with a chitosan/PEO ratio of 90/10 retained excellent integrity of the fibrous structure in water. Hybrids of chitosan/PEO could be electrospun in the presence of micellar surfactant solutions [39, 40]. The presence of surfactants resulted in the formation of needle-like, smooth or beaded fibers. It was revealed that nanofibers consisted of both polymers and surfactants with concentration of the constituents differing from that in polymer solutions. Results suggest that surfactants may modulate polymer–polymer interactions thus influencing the morphology and composition of deposited nanostructures. Introduction of an ultrahigh-molecular-weight poly(ethylene oxide) (UHMWPEO) into aqueous chitosan solutions remarkably enhances the formation of chitosan nanofibrous structure and leads to much lower loading of the water soluble fiber [43]. It can be made into both extremely thin nanofibers (less than 100 nm in diameters) and large microfibers (few tens of micrometers in diameters). The excellent electrospinnability of the current formulation renders electrospinning of natural biopolymer chitosan a robust process for large-scale production of practically applicable nanofibrous structures.

Polyethylene terephthalate (PET) is a highly crystalline polymer with excellent physical, mechanical and antibacterial properties [44], and is often used in the textile and plastic industry. The polymer blends of PET and chitosan could be electrospun onto the PET micro-nonwoven mats for biomedical applications [45]. The PET/chitosan nanofibers were evenly deposited on to the surface, and the diameter of the nanofibers was in the range between 500 and 800 nm. The wettability and antibacterial activity of the PET nanofibers was significantly enhanced by the incorporation of chitosan. Lopes-da-Silva *et al.* [46] also reported the preparation and characterization of nanofibrous mats electrospun from mixed solutions of PET and chitosan. Their results indicated that the presence of chitosan increased the diameter and the size distribution of the fibers. Chitosan molecular weight and concentration affected the mechanical properties of the nanofibrous mats. Phase separation during solvent evaporation and fiber formation, taking place at varied extent depending on molecular mobility of one of the components, is suggested to explain the formation of hybrid continuous or core-sheath fibers.

Polycaprolactone (PCL) is a semi-crystalline polymer with good flexibility, it can be used as surgical sutures, fracture fixation materials and drug carrier. PCL nanofibers containing various amounts of chitosan (0, 3, 9, and 23%) were prepared [47]. Characterization of the obtained nanofibers revealed that average fiber diameter, hydrophilicity, Young's modulus, and fiber degradation were all closely correlated with the amount of chitosan in PCL nanofibers. The nanofibers are superior to PCL nanofibers in promoting bone tissue formation. Another fibrous scaffold comprising of chitosan and PCL was electrospun in a novel solvent consisting of

formic acid and acetone [48]. This study indicated that optimized combination of chitosan (1%) and PCL (8%) was in 1:3 compositions. Mohammadi *et al.* [49] also developed 3D PCL nanofibrous scaffolds containing chitosan and PVA for bone tissue engineering via a multi-jet electrospinning method.

Poly(lactic acid)(PLA) is a thermoplastic polymer made from lactic acid and has mainly been used for biodegradable products, such as plastic bags and planting cups [50]. The chitosan/PLA blend micro/nanofibers have been prepared by electrospinning in TFA [51]. It was found that the average diameter of the chitosan/PLA blend fibers became larger, and the morphology of the fibers became finer with the content of PLA increasing. Fourier transform infrared spectroscopy (FTIR) indicated that there are molecular interactions between chitosan and PLA. Chen *et al.* [52] prepared Chitosan/poly(L-lactic acid-co-ε-caprolactone) (P(LLA-CL)) blend nanofibers by electrospining using 1,1,1,3,3,3-hexafluoro-2-propanol (HFIP) and TFA as solvents. The average fiber diameter increased with increasing polymer concentration and decreasing the blend ratio of chitosan to P(LLA-CL). The porosity of chitosan/P(LLA-CL) nanofiber mats increased with increasing the weight ratio of chitosan to P(LLA-CL), while both the tensile strength and the ultimate strain increased with increasing P(LLA-CL) ratio.

Nylon-6 (polyamide-6) has good mechanical properties and thermal stability, and has earlier been used as engineering plastics. Nylon-6 nonwoven mats have been produced from solutions with formic acid (FA) by electrospinning [53]. Composite membranes of nylon-6/chitosan nanofibers with different weight ratio of nylon-6 to chitosan were fabricated by electrospinning [54]. The morphology and diameter of the nanofibers were influenced by the concentration of the solution and weight ratio of the blending component materials. This study indicated that intermolecular interactions occurred between nylon-6 and chitosan and the intermolecular interactions varied with varying chitosan content in the fibers. It was concluded that a new composite product was created and the stability of this system was attributed to strong new interactions such as hydrogen bond formation between the nylon-6 polymers and chitosan structures.

Synthetic polymers which can improve the spinnability of chitosan have a same property that the polymers can interfere with the rigid association of the chitosan molecules, and thus lead to less free amino groups on the chitosan backbone. The addition of the polymers can relieve the protonation of chitosan restricting the formation of continuous fibers. Moreover, the polymers can be conveniently electrospun to nanofibers. Except for synthetic polymers, agarose, a natural polymer which has special gelling properties resulting in various applications [55], could improve the spinnability of chitosan with TFA/DCM mixture as electrospinning solvent [56]. It was found that smooth, continuous fibers were generated at an agarose content of less than 50%. The FTIR analysis revealed a gradual shift of the absorption band in the blend fibers, suggesting the strong interaction and good compatibility between chitosan and agarose.

2.3. Electrospinning of blends of chitosan and proteins

The proteins which can be mixed with chitosan to form electrospun nanofibers have similar characteristics with the polymers mentioned above: they can be conveniently electrospun to nanofibers and can interfere with the association of the chitosan molecules. Pure electrospun collagen nanofibers have been fabricated in HFIP [57]. The nanofibrous matrix is a good candidate for biomedical applications, such as wound dressing and scaffolds for tissue engineering. To develop better biomimetic wound dressing and extracellular matrix for the tissue engineering, electrospun collagen/chitosan nanofibrous mats were developed by electrospinning using HFIP/TFA (the volume ratio of 90/10) as solvent [58]. It was found that the diameter of the spun fibers became thick with the concentration of the solution increasing and became fine with the ratio of the chitosan/collagen increasing. The intermolecular interactions in electrospun collagen/chitosan complex fibers were also studied by Chen *et al.* [59]. Their study showed that intermolecular interactions existed and varied with various chitosan contents in the fibers. These interactions make collagen and chitosan miscible at the molecular level. The mechanical properties of electrospun collagen/chitosan single fibers and fibrous membrane investigated with a nano tensile testing system and a universal materials tester, respectively, were dependent on fiber diameter and the ratio of colla-

gen to chitosan in fibers [60]. The collagen/chitosan nanofibers can be further crosslinked by glutaraldehyde (GA) vapor [61]. After crosslinking, the collagen/chitosan nanofibers do not change significantly, except for enhanced stability, neither collagen nor chitosan molecular chains could be crystallized in the course of electrospinning and crosslinking, and yielding an amorphous structure in the nanofibers. Blends of type I collagen, chitosan and PEO can be electrospun into nanofibers, which could be further crosslinked by glutaraldehyde (GA) vapor [62]. The nanofiber diameter was found to be 134±42 nm, which increased to 398±76 nm after crosslinking. The Young's modulus increased after crosslinking, however, the ultimate tensile strength, tensile strain, and water sorption capability decreased after crosslinking.

Silk fibroin (SF) is the fibrous protein that forms silkworm silk. In recent years, SF has been increasingly studied for new biomedical applications due to its biocompatibility, slow degradability, remarkable mechanical properties, low inflammatory responses, and good oxygen and water vapor permeability of the material [63, 64]. In addition, it was found that SF had a good anti-thrombogenicity and absorbability even though the polymer showed foreign body reaction [65]. Pure SF nanofibers can be made by electrospinning of SF in formic acid [66]. Similarly, SF/chitosan nanofibers can be made by electrospinning of SF/chitosan blends containing up to the chitosan content of 30% in formic acid [67]. The as-spun SF/chitosan blend nanofibers showed smaller diameter and narrower diameter distribution than pure SF nanofibers, and the diameter gradually decreased from 450 to 130 nm with the addition of chitosan in blends. Comparing with the pure SF nanofibers, the conformational change of the as-spun SF/chitosan blend nanofibers into β-sheet was faster because the chitosan with rigid backbone might synergistically promote the conformational transition of SF by an intermolecular interaction.

Zein is a 'yellowish' colored maize storage prolamine that induced great interest in a number of industrial applications such as food, food coating and food packaging, and can be easily electrospun into nanofibers [68]. Blends of zein and chitosan (up 10 wt.%) can be electrospun to yield water insoluble fiber mats with efficient biocide properties [69]. The study indicated that both components are not miscible, the presence of the chitosan phase leads to slightly enhanced glass transition temperature for the zein phase. Zein/chitosan/Poly(vinyl pyrrolidone) (PVP) composite fibrous membranes were also fabricated from aqueous ethanol solutions by electrospinning [70]. PVP was introduced to facilitate the electrospinning process. Increasing zein and PVP concentrations led to an increase in average diameters of the fibers. In order to improve stability in wet stage and mechanical properties, the composite fibrous membranes could be crosslinked by hexamethylene diisocyanate (HDI). The crosslinked membranes showed slight morphological change after immersion in water for 24 h. The tensile strength and elongation at break of the membranes were increased after crosslinking, whereas Young's modulus was decreased.

2.4. Electrospinning of chitosan derivatives

The spinnabilities are greatly improved by changing chitosan to its derivatives, because most of chitosan derivatives are soluble in water and (or) in a wide variety of common organic solvents. O-carboxymethyl chitosan (O-CMCS) is a water-soluble derivative of chitosan. It has good moisture retention, biocompatibility and antibacterial property, so it is a good biomaterial [71]. Du and Hsieh [72] synthesized O-CMCS with varying molecular weights and degrees of substitution by alkalization of chitosan, followed by carboxymethylation with monochloroacetic acid, and fabricated various O-CMCS/water-soluble polymer blend nanofibers by electrospinning. The optimal fiber formation was observed at equal mass composition of O-CMCS (89 kDa at 0.36 DS) and PVA, producing nanofibers with an average diameter of 130 nm. Heat-induced esterification (at 140°C for 30 min) produced inter-molecular covalent cross-links within and among fibers, rendering the fibrous membrane water-insoluble. Membranes containing higher CMCS carboxyl to PVA hydroxyl ratio retained better fiber morphology upon extended water exposure, indicating more favorable inter-molecular cross-links. The fibrous membranes generated with less substituted CMCS were more hydrophilic and retained a greater extent of the desirable amine functionality.

Similarly, the hybrids of N-carboxyethyl chitosan (N-CECS) and PVA could be made into nanofibers by electrospinning [73]. The electrospinning of CECS/PVA nanofibers was enabled by the ability of PVA to form an elastically deformable entanglement network based on hydrogen bonds. The average diameters of the bicomponent fibers were in the range 100–420 nm. Water-resistant nanofibrous mats were obtained by thermal crosslinking at 100°C for 10 h. Zhou *et al.* [74] prepared CECS/PVA nanofibers by electrospinning using water as solvent, The study indicated that there was strong intermolecular hydrogen bonding between the molecules of CECS and PVA. Electrospun N-CECS/polyacrylamide (PAAm) blend nanofibers have also been prepared [75].

Hexanoyl chitosan (H-CS) (Figure 2) has good blood compatibility and is anti-thrombogenic [76, 77], so it has been used for medical applications. Ultrafine H-CS fibers were successfully prepared by electrospinning of H-CS solutions in chloroform [78]. The concentration of the spinning solutions was between 4 and 14% w/v. The as-spun fibers appeared to be flat with ribbonlike morphology and average diameters in the range of 0.64–3.93 μm. The addition of an organic salt, pyridinium formate, helped to increase the conductivity of the spinning solution, which resulted in a general increase in the average diameter and a general decrease in the bead density of the resulting H-CS fibers. In addition, bead-free H-CS/polylactide blend fibres were prepared by electrospinning from solutions in chloroform with the H-CS solution content of less than or equal to 50% (w/w) [79]. Galactosylated chitosan (G-CS) (Figure 3) nanofibrous scaffold was also fabricated by electrospinning using formic acid as spinning solvent [80] for tissue engineering.

Ignatova *et al.* [81] fabricated quaternised chitosan (Q-CS)/PVA nanofibres by electrospinning of Q-CS solutions mixed with PVA. The average fibre diam-

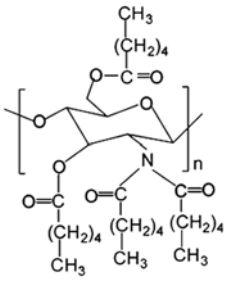

Figure 2. The molecular structure of Hexanoyl chitosan (H-CS)

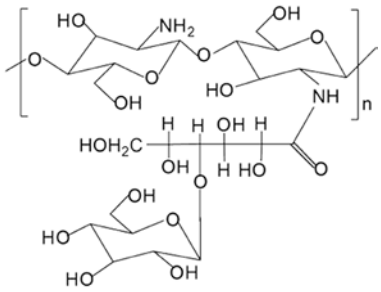

Figure 3. The molecular structure of Galactosylated chitosan (G-CS)

eter is in the range of 60–200 nm. UV irradiation of the composite electrospun nanofibrous mats containing triethylene glycol diacrylate as crosslinking agent resulted in stabilising of the nanofibres against disintegration in water or water vapours. Similarly, Q-CS/PVP nanofibres were also prepared by electrospinning [82]. The average diameter of the fibers significantly decreases from 2800 to 1500 nm with increasing the polyelectrolyte content. The Q-CS/PVP fibers can also be crosslinked by incorporation of adding photo-crosslinking additives into spinning solutions and subsequent UV irradiation to the electrospun fibers. Another quaternised chitosan, N-[(2-hydroxy-3-trimethylammonium)propyl] chitosan chloride (HTCSC), is a water-soluble derivative of chitosan, which was synthesized via the reaction between glycidyl- trimethylammonium chloride and chitosan. Defect free HTCSC/PVA blend mats were prepared by electrospinning of an aqueous solution [83]. The average fibre diameter was in the range of 200–600 nm, and decreases with increasing HTCSC content in the blends. The HTCSC/PVA nanofiber mats have a good antibacterial activity against *Staphylococcus aureus* and *Escherichia coli.*

Poly(chitosan-g-DL-lactic acid)(P(CS-g-LA)) copolymers which were produced by grafted DL-lactic acid onto chitosan were spun into submicron and/or nanofibers to fabricate scaffolds using an electro-wet-spinning technique [84]. The diameter of the fibers in different scaffolds could vary from about 100 nm to around 3 μm. The scaffolds exhibited various pore sizes ranging from about 1 μm to less than 30 μm and different porosities up to 80%. Significantly improved tensile strength and modulus for these fibrous scaffolds in their hydrated state were observed. Amino-reserved polycaprolactone-graft-chitosan (PCL-g-CS) (Figure 4) was synthe-

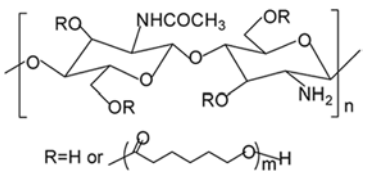

Figure 4. The molecular structure of amino-reserved polycaprolactone-graft-chitosan (PCL-g-CS)

sized by grafting ε-caprolactone oligomers onto the hydroxyl groups of CS via ring-opening polymerization by using methanesulfonic acid as solvent and catalyst [85]. PCL-g-CS exhibited good solubility in organic solvents, facilitating formation of PCL/PCL-g-CS blend nanofibers via electrospinning with the use of dimethylformamide (DMF)/ $CHCl_3$ as solvents. Owing to the enhanced cellular attachment results from cationic amino groups, it is promising that these copolymers are ideal substances for developing drug carriers and tissue engineering scaffolds. Similarly, L-lactide-g-Chitosan (LLA-g-CS) which was prepared by grafting L-lactide oligomers via ring-opening polymerization was easily made into ultrafine fibers via electrospinning due to its solubility in a broad range of organic solvents [86].

2.5. Electrospinning of blends of chitosan and inorganic nanoparticles

A biomimetic nanocomposite nanofibers of hydroxyapatite(HAp)/chitosan was prepared by combining an *in situ* co-precipitation synthesis approach with an electrospinning process [87]. A model HAp/chitosan nanocomposite with the HAp mass ratio of 30 wt% was synthesized through the co-precipitation method so as to attain homogenous dispersion of the spindle-shaped HAp nanoparticles (ca. 100× 30 nm) within the chitosan matrix. By using a small amount (10 wt%) of ultrahigh molecular weight poly(ethylene oxide) (UHMWPEO) as a fiber-forming facilitating additive, continuous HAp/chitosan nanofibers with a diameters of 214±25 nm were produced and the HAp nanoparticles with some aggregations were incorporated into the electrospun nanofibers. The crystalline nature of HAp remains and had survived the acetic acid-dominant solvent system. Similarly, Shen *et al.* [88] prepared uniform and ultrafine chitosan/PVA nanofibrous mats filled with HAp nanoparticles by electrospinning of blend solutions of HAp, chitosan and PVA. An increase in the contents of HAp nanoparticles from 0 to 0.5 wt% caused the conductivity of the blend solution to increase from 1.06 to 2.27 mS/cm, and the average diameter of the composite fibers to decrease from 59±10 to 49±10 nm. The results indicated that some particles had filled in the nanofibers whereas the others had dispersed on the surface of fibers. Similar chitosan/PVA/HAp nanofibrous biocomposite scaffolds were fabricated by Yang *et al.* [89]. The scaffolds have porous nanofibrous morphology with random fibers in the range of 100–700 nm diameters. Increase the content of HAp up to 2% increased the ultimate tensile strength and tensile modulus, but further increase HAp caused the decrease of tensile strength and tensile modulus. Another biomimetic material of HAp with electrospun chitosan/PVA nanofibrous scaffolds was prepared by using chitosan/PVA electrospun membranes as organic matrix, and HAp was formed in supersaturated $CaCl_2$ and KH_2PO_4 solution [90]. It was found that addition of poly (acrylic acid) (PAA) to the mineral solution and use of matrix with N-carboxyethyl chitosan (N-CECS) promoted mineral growth and distribution of HAp.

A fairly uniform silver nanoparticles (AgNPs)/chitosan/PEO ultrafine fibers were prepared by electrospinning of chitosan/PEO solutions containing Ag/chitosan colloids by means of *in situ* chemical reduction of Ag ions [91]. The AgNPs were evenly distributed in chitosan/PEO ultrafine fibers with the size less than 5 nm. The existence of Ag–O bond in the composite ultrafine fibers led to the tight combination between Ag and chitosan. Penchev *et al.* [92] prepared Hybrid nanofibers from chitosan or CECS, AgNPs and PEO by electrospinning using formic acid as solvent. AgNPs were synthesized *in situ* in the spinning solution. The results showed that AgNPs are uniformly dispersed in the nanofibers. The surface of the nanofibers was enriched in chitosan and 15 wt% of the incorporated AgNPs were on the fiber surface. Similar AgNPs/chitosan/PVA nanofiber mats [93] and AgNPs/chitosan/gelatin nanofibers [94] were also fabricated.

Montmorillonite (MMT) has good dispersion properties, can be widely used in macromolecular industry as an additive. Chitosan/MMT nanocomposites have been prepared for adsorption [95] and drug release [96] due to the unique properties of MMT. Submicron fibers of the composites of PVA, chi-

tosan oligosaccharide (COS) and MMT were prepared using electrospinning method with aqueous solutions [97]. The PVA/COS ratio and MMT concentration play important roles in nanofiber mat properties. The exfoliated MMT layers were well-distributed within nanofibers. It was also found that the mechanical property and thermal stability were increased with COS and MMT contents.

Another interesting nanomaterial is multiwalled carbon nanotubes (MWCNTs). MWCNTs grafted by chitosan (MWCNTs-g-CS) could disperse well in poly(vinyl alcohol) (PVA) aqueous solution with 2% (v/v) acetic acid solution. The solution containing PVA and MWCNTs-g-CS could be electrospun to nanofibers [98]. It was found that the electrospinning process did not severely alter the electron hybridization of carbon atoms within the nanotube framework. Moreover, these nanofibers showed a novel sheath–core structure, the outer and inner diameters of these sheath–core nanofibers were about 200 and 100 nm, respectively. The electrospun nanofiber mats displayed faster electron transfer kinetics and better electrochemical properties than its cast film, which justified further applications in biological areas.

Other nanofibers electrospun of blends of chitosan and inorganic nanoparticles are not discussed in detail here, such as titanium dioxide (TiO_2) nanoparticles/chitosan/PVA electrosun nanofibers exhibiting antibacterial activities against *Staphylococcus aureus* and *Escherichia coli* [99], palladium nanoparticles/chitosan grafting acrylic copolymer (PdNPs/CS-g-AA) blend electrospun nanofibrous catalyst applied to catalyze alpha-octene hydrogenation in normal temperature and pressure [100], etc. The combination of the characteristics of the inorganic nanoparticles and the features of chitosan nanofibers could lead to more products with unique properties that can fit special needs. This method may be one of the most important directions of the development of chitosan electrospinning techniques.

3. Applications of chitosan nanofibers

3.1. Enzyme immobilization:

Electrospun nanofibers have been proven to be excellent supports for enzyme immobilization because they can provide large surface area-to-volume ratios, pore sizes tailored to protein molecule dimensions, functionalized surfaces, multiple sites for interaction or attachment, and low mass-transfer limitation [101]. Huang *et al.* [30] fabricated nanofibrous membrane from mixed chitosan/PVA solution by electrospinning. The membrane was treated by removing most of PVA from the nascent one with 0.5 M NaOH aqueous solution. The stabilized chitosan nanofibrous membrane was explored as support for enzyme immobilization due to the characteristics of excellent biocompatibility, high surface/volume ratio and large porosity. Lipase from *Candida rugosa* was immobilized on the nanofibrous membrane using glutaraldehyde (GA) as coupling reagent. The lipase loading on this nanofibrous membrane was up to 63.6 mg/g and the activity retention of the immobilized lipase was 49.8% under the optimum condition. The pH and thermal stabilities of lipase were improved after it was immobilized on the membrane. In addition, the experimental results of reusability and storage stability indicated that the residual activities of the immobilized lipase were 46% after 10 cycles and 56.2% after 30 days, which were obviously higher than that of the free one.

3.2. Filtration

Nanofibers containing chitosan have the advantage of filtering material based on the high surface/volume ratio, large porosity and functionality. They can be potentially applicable in a wide variety of filtration applications ranging from water purification media to air filter media [102]. Pure chitosan nanofiber mats fabricated by electrospinning using trifluoroacetic acid (TFA) as solvent have been used for absorbing metal ions [16]. The as-spun nanofiber (~235 nm in diameter) mats which were neutralized with potassium carbonate showed good erosion stability in water and high adsorption affinity for metal ions in an aqueous solution. The adsorption data of Cu(II) and Pb(II) were fitted well with Langmuir isotherm indicating that mono-layer adsorption occurred on the nanofiber mats. The equilibrium adsorption capacities (from Langmuir isotherm data) for Cu(II) and Pb(II) were 485.44 and 263.15 mg/g, respectively. The Cu(II) adsorption data were ~6 and ~11 times higher than the previously reported highest values of chitosan microsphere (80.71 mg/g) [103] and the plain chitosan (45.20 mg/g) [104], respectively. This high adsorp-

tion capacity suggests that the chitosan electrospun nanofiber mats can be applied to filter out (or neutralize) toxic metal ions and microbes without losing their original chitosan properties such as biocompatibility, hydrophilicity, bioactivity, non-antigenicity, and non-toxicity.

Desai *et al*. [105] fabricated nanofibrous filter media by electrospinning of chitosan/PEO blend solutions onto a spunbonded non-woven polypropylene substrate. Filter media with varying fiber diameter and filter basis weight were obtained. Heavy metal binding, anti-microbial and physical filtrations efficiencies of the filter media were correlated with the surface chemistry and physical characteristics of the filter media. Filtration efficiency of the nanofiber mats was strongly related to the size of the fibers and its surface chitosan content. Hexavalent chromium binding capacities up to 35 mg /g chitosan were exhibited by the filter media along with a 2–3 log reduction in *Escherichia coli* bacteria cfu (clonal formation unit). The filter media showed high efficiencies to air and water filtration, which correlated with the fibrous media size and shape. Similar nonwoven fiber mats with fiber diameter as low as 80±35 nm for air and water filtration were also made by electrospinning high molecular weight chitosan/PEO (95:5) blends [106].

An affinity membrane made from electrospun hybrid chitosan/nylon-6 nanofibers by nucleophilic reaction of the chitosan's hydroxyl and amidocyanogen with the triazinyl chloride of Cibacron Blue F3GA (CB) ligand was used to study the purification of papain [107]. The equilibrium adsorption capacity (from Langmuir isotherm data) for papain was 93.46 mg/g affinity membrane. Fifteen layers of the composite affinity membrane were packed into a spin column to separate papain from raw material. Significant amount of the adsorbed papain (about 90.4%) was eluted by 1.0 M NaSCN at pH 9.0, and 4.8-fold purification was achieved in a single step. It is shown that this system has the potential to be developed for the industrial purification of the papain.

3.3. Wound dressing

Zhou *et al.* [74] prepared biocompatible carboxyethyl chitosan(CECS)/PVA nanofibers by electrospinning of aqueous CECS/PVA solution. The potential use of the fiber mats as scaffolding materials for skin regeneration was evaluated *in vitro* using mouse fibroblasts (L929) as reference cell lines. Indirect cytotoxicity assessment of the fiber mats indicated that the CECS/PVA electrospun mat was nontoxic to the L929 cell. Cell culture results showed that fibrous mats were good in promoting the cell attachment and proliferation. This novel electrospun matrix would be used as potential wound dressing for skin regeneration. The chitosan/ collagen/PEO nanofibrous membrane fabricated by electrospinning and then crosslinked by glutaraldehyde vapor have potential as a wound dressing for skin regeneration [62]. The membrane showed no cytotoxicity toward growth of 3T3 fibroblasts and had good *in vitro* biocompatibility. From animal studies, the membrane was better than gauze and commercial collagen sponge wound dressing in wound healing rate.

Ignatova *et al.* [81] prepared quaternised chitosan (Q-CS)/PVA nanofibres containing triethylene glycol diacrylate as crosslinking agent and which were further irradiated by UV irradiation. Microbiological screening demonstrated the antibacterial activity of the photo-crosslinked electrospun mats against Gram-positive bacteria *Staphylococcus aureus* and Gram-negative bacteria *Escherichia coli*. Similarly, Photo-crosslinked QCS/PVP electrospun mats show high antibacterial activity against the *Staphylococcus aureus* and *Escherichia coli* [82]. These obtained nanofibrous electrospun mats are promising for wound healing applications.

A wound dressing material composed of silver nanoparticles (AgNPs) and chitosan has been fabricated using a nanometer and self-assembly technology [108]. It could significantly increase the rate of wound healing. To develop a better wound dressing, fairly uniform AgNPs/chitosan/PEO ultrafine fibers were successfully prepared [91]. Evaluation of antimicrobial activities of the electrospun AgNPs/ chitosan /PEO fibrous membrane against *Escherichia coli* showed that the AgNPs in the ultrafine fibers significantly enhanced the inactivation of bacteria. The fibrous membrane was better than other wound dressing containing AgNPs in wound healing rate. Similarly, higher antibacterial activity was observed in the electrospun non-woven mats of AgNPs/ PVA/CS blends than in those of PVA/CS blends [93]. The as spun mats are also excellent wound dressing.

3.4. Tissue engineering

The development of bioinspired or biomimetic materials is essential and has formed one of the most important fields in today's tissue engineering research. Hydroxyapatite (HAp) is a well known biomimetic material. A biomimetic nanocomposite nanofibers of HAp/chitosan was prepared by combining an *in situ* co-precipitation synthesis approach with an electrospinning process [87]. Biological *in vitro* cell culture with human fetal osteoblast cells for up to 15 days demonstrated that the incorporation of HAp nanoparticles into chitosan nanofibrous scaffolds led to significant bone formation oriented outcomes compared to that of the pure electrospun chitosan scaffolds. The nanofibers are of potential interest for bone tissue engineering applications. Yang *et al.* [89] prepared chitosan/PVA/ HAp nanofibrous biocomposite scaffolds by electrospinning. The attachment and growth of mouse fibroblast on the Surface of the nanofibrous structure indicated that a combination of nanofibrous CS/PVA and HAp that mimics the nanoscale features of the extracellular matrix could be promising for application as scaffolds for tissue regeneration, especially in low or non load bearing areas. Another biomimetic chitosan/PVA/HAp nanofibrous scaffold prepared by using chitosan/PVA electrospun membranes as organic matrix and HAp being formed in supersaturated $CaCl_2$ and KH_2PO_4 solution is also of potential application in the field of biomedicine [90].

Based on a biomimetic approach, Mohammadi *et al.* [49] developed 3D nanofibrous hybrid scaffolds consisting of PCL, PVA and chitosan (PCL/PVA/CS scaffolds) via a multi-jet electrospinning method. Osteogenically induced cultures revealed that cells were well-attached, penetrated into the framework and were uniformly distributed. Besides, PCL nanofibers containing various amounts of chitosan (0, 3, 9, and 23%) were also prepared and evaluated for their osteogenic differentiation of preosteoblasts in 2D and 3D cultures [47]. The results revealed that incorporation of chitosan in PCL nanofibers not only improved the adhesion and proliferation of MC 3T3-E1 cells but also elevated calcium deposition, alkaline phosphatase activity, and the expression of osteopontin compared to PCL alone nanofibers. The nanofibers are superior to PCL nanofibers in promoting bone tissue formation. The chitosan/PLA micro/nanofibers prepared by electrospinning.are also expected to be used in the native extracellular matrix for tissue engineering [51].

Bridging of nerve gaps after injury is a major problem in peripheral nerve regeneration. Electrospun PCL/chitosan nanofibrous scaffolds were evaluated *in vitro* using rat Schwann cells (RT4-D6P2T) for nerve tissue engineering [109]. The Young's modulus and strain at break of the electrospun PCL/chitosan nanofibers were better than those of the chitosan nanofibers. PCL/chitosan scaffolds showed better cell proliferation than PCL scaffolds (48% more cell proliferation after 8 days of culture) and maintained their characteristic cell morphology, with spreading bipolar elongations to the nanofibrous substrates. This electrospun nanofibrous matrix was proved of specific interest in tissue engineering for peripheral nerve regeneration.

Electrospun chitosan nano/microfibrous tubes with a degree of deacetylation (DD) of 93% were examined the effects of their mechanical strength and permeability on nerve regeneration [110]. The study indicated that the chitosan nano/microfiber mesh tubes with a DD of 93% have sufficient mechanical properties to preserve tube space, provide a better scaffold for cell migration and attachment, and facilitate humoral permeation to enhance nerve regeneration. Afterwards, Wang *et al.* [111] constructed a chitosan nonwoven nanofiber mesh tube consisting of oriented fibers by the electrospinning method. The efficacy of oriented nanofibers on Schwann cell alignment and positive effect of this tube on peripheral nerve regeneration were confirmed. As a result of fiber orientation, the tensile strength along the axis of the sheet increased. Because Schwann cells aligned along the nanofibers, oriented fibrous sheets could exhibit a Schwann cell column. Functional recovery and electrophysiological recovery occurred in the oriented nanofibers and approximately matched those in the isograft. The oriented chitosan nanofiber mesh tube may be a promising substitute for autogenous nerve graft.

Liver tissue engineering requires a perfect extracellular matrix for primary hepatocytes culture to maintain high level of liver specific functions and desirable mechanical stability. Galactosylated chitosan (G-CS) nanofibrous scaffold was fabricated by electrospinning using formic acid as spinning solvent [80]. The G-CS nanofibrous scaffolds dis-

played slow degradation and suitable mechanical properties as an extracellular matrix for hepatocytes. Hepatocytes cultured on G-CS nanofibrous scaffold formed stably immobilized 3D flat aggregates and exhibited superior cell bioactivity with higher levels of liver-specific function maintenance in terms of albumin secretion, urea synthesis and cytochrome P-450 enzyme than 3D spheroid aggregates formed on G-CS films. Such G-CS-based nanofibrous scaffolds could be useful for various applications such as bioartificial liver-assist devices and tissue engineering for liver regeneration as primary hepatocytes culture substrates.

Ultra-fine fiber mats of hexanoyl chitosan (H-CS) for potential use as skin tissue scaffolds was fabricated [112]. The results showed that the fiber mats were non-toxic and did not release substances harmful to mouse fibroblasts (L929). The fibrous scaffolds could support the attachment and the proliferation of both human keratinocytes (HaCaT) and human foreskin fibroblasts (HFF), especially for HaCaT. In addition, the cells cultured on the fibrous scaffolds exhibited normal cell shapes and integrated well with surrounding fibers. The obtained results confirmed the potential for use of the fiber mats as scaffolds for skin tissue engineering.

Duan *et al.* [113, 114] prepared nanofibrous composite membranes of poly(lactide-co-glycolide) (PLGA)/chitosan/PVA by electrospinning. In their studies, PLGA and chitosan/PVA were simultaneously electrospun from two different syringes and mixed on the rotating drum. Then membrane was crosslinked by glutaraldehyde vapor. Cell culture indicated that the cells could not only favorably attach and grow well on the composite membranes, but were also able to migrate and infiltrate the membranes. Therefore, the results suggest that the composite membranes can positively mimic the structure of natural extracellular matrices and have the potential for application as three-dimensional tissue engineering scaffolds.

3.5. Drug delivery

Electrospun nanofibers are better drug delivery systems than the bulk materials due to the high specific surface area and short diffusion passage length. The drug release rate can be finely controlled by modulation of nanofiber morphology, porosity and composition. The blends of poly(ethylene glycol)-g-chitosan (PEG-g-CS) and ibuprofen-loaded poly(lactide-co-glycolide) (PLGA) were made into fiber mats by electrospinning [115]. It was found that the glass transition temperature of PLGA decreased with increasing PEG-g-CS content in the composite membranes, which results in decrease in tensile stress at break but increase in tensile strain of the membranes. The degree of shrinkage of these composite membranes decreased from 76 to only 3% when the PEG-g-CS content in the membranes increased from 10 to 30%. The presence of PEG-g-CS significantly moderated the burst release rate of ibuprofen from the electrospun PLGA membranes. Moreover, ibuprofen could be conjugated to the side chains of PEG-g-CS to prolong its release for more than two weeks. The sustained release capacity of the PLGA/PEG-g-CS composite membranes, together with their compliant and stable mechanical properties, renders them ideal matrices for atrial fibrillation.

Nanofibrous materials containing the antitumor drug doxorubicin hydrochloride (DOX) were prepared using a one-step method by electrospinning of DOX/quaternized chitosan (Q-CS)/poly(l-lactide-co-d,l-lactide)(coPLA) solutions [116]. The release rate of DOX from the prepared fibers increased with the increase in DOX content. The DOX release process was diffusion-controlled. The studies revealed that incorporation of DOX and Q-CS in the nanofibrous mats led to a significant reduction in the HeLa cells viability. It was found that the antitumor efficacy of the DOX-containing mats at 6 h was higher than that of the free DOX. Chitosan/hydroxybenzotriazole(HOBt)/PVA blend nanofibers may be suitable for drug delivery or tissue engineering applications too [117].

For effective cancer gene therapy, systemic administration of tumor-targeting adenoviral (Ad) complexes is critical for delivery to both primary and metastatic lesions. Electrospinning was used to generate nanocomplexes of Ad/chitosan/poly(ethylene glycol) (PEG)/folic acid (FA) for effective FA receptor-expressing tumor-specific transduction [118]. The transduction efficiency of Ad/chitosan–PEG–FA was increased as a function of FA ratio in FA receptor-expressing KB cells, but not in FA receptor-negative U343 cells, demonstrating FA receptor-targeted viral transduction. In addition, the transduction efficiency of Ad/chitosan/PEG/FA was

57.2% higher than chitosan-encapsulated Ad, showing the superiority of FA receptor-mediated endocytosis for viral transduction. The production of inflammatory cytokine, IL-6 from macrophages was significantly reduced by Ad/chitosan/PEG/FA nanocomplexes, implying the potential for use in systemic administration. These results clearly demonstrate that cancer cell-targeted viral transduction by Ad/chitosan/PEG/FA nanocomplexes can be used effectively for metastatic tumor treatment with reduced immune reaction against Ad.

3.6. Catalysis

A nanofibrous catalyst was fibricated by electrospinning of Chitosan grafting acrylic acid copolymer (CS-g-AA) supporting nano palladium [100]. The diameter of nanofiber was about 70–200 nm, the size of metal particles were in a range of 10–40 nm, and palladium particles dispersed on nanofibers homogeneously. The catalyst was applied to catalyze alpha-octene hydrogenation in normal temperature and pressure. The results showed that the conversion of alpha-octene was 99 percent , and the yield of octane was 65 percent by double-metal catalyst. This indicated the excellent catalysis efficiency of the nanofibrous catalyst. Another nanofibrous catalyst was also prepared by Shan *et al.* [119]. Chitosan nanofibers were used to modify indium tin oxide (ITO) electrode by electrospinning. Then, Prussian blue (PB) nanoparticles were electrodeposited on the nanofibers by potentiostatic technique in an acidic solution containing single ferricyanide. The modified electrode exhibited electrocatalytic activity towards reduction of H_2O_2.

4. Conclusions and perspectives

Chitosan is soluble in most of acid solutions. The protonation of the amino groups on the chitosan backbone inhibits the spinnability of pure chitosan. There are several ways to overcome the defect restricting the formation of continuous fibers. One is to use a special solvent (such as concentrated acetic acid solution) to reduce the surface tension of chitosan solution and increase the electrostatic charge density of the jet. The second is to change the amino groups of chitosan into salts directly in the solvent (e.g. TFA as solvent) to decrease the free amino groups of chitosan. The third is to mix chitosan with other substances (such as synthetic polymers, proteins, etc.), so that the free amino groups of chitosan are reduced by the intermolecular interactions between chitosan and the additives through some form, such as hydrogen bonds. The fourth is to change chitosan into its derivatives. The solubilities of chitosan derivatives have been greatly improved, thus the spinnabilities are also greatly improved. The nanofibers containing chitosan have potential use in the areas of enzyme immobilization, filtration, wound dressing, tissue engineering, drug delivery and catalysis not only because chitosan is a non-toxic, antibacterial, biodegradable and biocompatible biopolymer, but also because the nanofibers have large surface areas and high porosity (Table 1).

During the past few years, enormous progress has been made in the area of electrospinning to produce various nanofibres containing chitosan with unique shape and unique properties. However, there are many problems that need to be solved for large-scale manufacturing of chitosan based new nanofibers, such as: how to fabricate uniform nanofibers with same morphologies, mechanical and chemical properties repeatedly and massively. How to improve the mechanical properties of chitosan nanofibers and how to avoid the toxicity arised from the toxic spinning solvents which will limit the applications of as-spun nanofibrous products, etc. Designing mixtures containing chitosan and other substances as electrospinning materials, adjusting various parameters of the spinning process to control the fiber diameter, orientation and morphology of the electrospun nanofibers, searching for 'green solvents' without toxicity as electrospinning solvents and further modifying the as spun nanofiber products to improve the characteristics will perhaps be focused by researchers. With the applications of new electrospinning technologies (such as in-situ mixing electrospinning, two-phase electrospinning, wind assisted electrospinning and coaxial electrospinning, etc.), abundant novel nanofibrous pruducts based on chitosan would be designed and the applications of the products which are still at the laboratory level will became true in near future by the efforts of researchers.

Table 1. Chitosan based nanofibers and their applications

Polymer	Solvent	DD	Average fiber diameter (nanoparticle size) [nm]	Application	Reference
Chitosan	aq AA	54	130	–	[17]
Chitosan	aq AA	75–85	70±45	–	[18]
Chitosan	TFA/DCM	95	130±10	–	[15]
Chitosan	TFA/DCM	85	126±20	tissue engineering	[14]
Chitosan (neutralized with K_2CO_3 solution)	TFA	86.7	235	filtration	[16]
Chitosan/PVA (removing PVA with 0.5 M NaOH)	aq AA	90	80~150	enzyme immobilization	[30]
Chitosan/PVA	aq AA	90	99±21	wound dressings	[33]
Chitosan/PEO	aq AA	80	10–240	–	[39, 40]
Chitosan/PEO	aq AA	67-83	80±35	filtration	[105, 106]
Chitosan/ UHMWPEO(5%) Chitosan/ UHMWPEO(10%) Chitosan/ UHMWPEO(20%)	aq AA/DMSO	>85	114±19 138±15 102±14	–	[43]
Chitosan/PET	TFA	85	500–800	wound dressings	[45]
Chitosan/PCL	HFIP	75–85	450±110	bone tissue engineering	[47]
Chitosan/PCL	HFIP/TFA/DCM	–	190±26	nerve tissue engineering	[109]
Chitosan/nylon-6	HFIP/FA	85	80–310	filtration	[54, 107]
Chitosan/PVA-PCL (by multi-jet electrospinning method)	aq AA/$CHCl_3$	85	100–200	bone tissue engineering	[49]
Chitosan/PVA-PLGA (by multi-jet electrospinning method)	aq AA THF/DMF	90	275±175	tissue engineering	[113, 114]
Chitosan/collagen (crosslinked by GA vapor)	HFIP/TFA	85	434–691	tissue engineering	[61]
Chitosan/collagen/PEO (crosslinked by GA vapor)	aq AA	95	398±76	wound dressings	[62]
Chitosan/SF	FA	86	180–790	–	[67]
O-CMCS/PVA	water	84.7	130	–	[72]
N-CECS/PVA	water	82.5	131–456	wound dressings	[74]
H-CS	$CHCl_3$	88	640–3930	skin tissue engineering	[78, 112]
G-CS	FA	85	160	liver tissue engineering	[80]
Q-CS/PVA (crosslinked by UV irradiation)	aq AA	80	60–200	wound dressings	[81]
Q-CS/PVP (crosslinked by UV irradiation)	water	80	2400±640	wound dressings	[82]
Q-CS)/coPLA	DMF/DMSO	80	470	drug delivery	[116]
PCL-g-CS/PCL	DMF/$CHCl_3$	91	–	tissue engineering	[85]
PEG-g-CS/ PLGA	DMF	85	–	drug delivery	[115]
CS-HOBt/PVA	water	85	190–282	drug delivery	[117]
Chitosan/HAp/UHMWPEO	aq AA/DMSO	>85	214±25 (100×30)	bone tissue engineering	[87]
Chitosan/HAp/PVA	aq AA	91	49±10 (–)	bone tissue engineering	[88]
Chitosan/HAp/PVA	aq AA/DMSO	88	100–700 (–)	bone tissue engineering	[89]
Chitosan/PEO/AgNPs	aq AA	80	~100 (<5)	wound dressings	[91]
Chitosan/gelatin/AgNPs	aq AA	87	220–400 (2–10)	wound dressings	[94]
CS-g-AA/ PaNPs	aq AA	78	70–200 (10–40)	catalyst	[100]

Abbrevitions: THF, tetrahydrofuran, aq AA, aqueous acetic acid solution; DMSO: dimethyl sulfoxide. Other abbrevitions are in the text.

Acknowledgements

We are grateful to the Scientific & Technological Support Project of Sichuan Province (No. 2009GZ0167) for financial support of this work.

References

[1] Formhals A.: Process and apparatus for preparing artificial thread. U.S. Patent 1975504, USA (1934).

[2] Doshi J., Reneker D. H.: Electrospinning process and applications of electrospun fibers. Journal of Electrostatics, **35**, 151–160 (1995). DOI: 10.1109/IAS.1993.299067

[3] Deitzel J. M., Kleinmeyer J. D., Hirvonen J. K., Tan B. N. C.: Controlled deposition of electrospun poly(ethylene oxide) fibers. Polymer, **42**, 8163–8170 (2001). DOI: 10.1016/S0032-3861(01)00336-6

[4] Deitzel J. M., Kleinmeyer J., Harris D., Tan B. N. C.: The effect of processing variables on the morphology of electrospun nanofibers and textiles. Polymer, **42**, 261–272 (2001).
DOI: 10.1016/S0032-3861(00)00250-0

[5] Frenot A., Chronakis I. S.: Polymer nanofibers assembled by electrospinning. Current Opinion in Colloid and Interface Science, **8**, 64–75 (2003).
DOI: 10.1016/S1359-0294(03)00004-9

[6] Hunley M. T., Long T. E.: Electrospinning functional nanoscale fibers: A perspective for the future. Polymer International, **57**, 385–389 (2008).
DOI: 10.1002/pi.2320

[7] Mi F-L., Tan Y-C., Liang H-F., Sung H-S.: In vivo biocompatibility and degradability of a novel injectable- chitosan-based implant. Biomaterials, **23**, 181–191 (2002).
DOI: 10.1016/S0142-9612(01)00094-1

[8] Angelova N., Manolova N., Rashkov I., Maximova V., Bogdanova S., Domard A.: Preparation and properties of modified chitosan films for drug release. Journal of Bioactive and Compatible Polymers, **10**, 285–298 (1995).
DOI: 10.1177/088391159501000401

[9] Selmer-Olsen E., Ratnaweera H. C., Pehrson R.: A novel treatment process for dairy wastewater with chitosan produced from shrimp-shell waste. Water Science and Technology, **34**, 33–40 (1996).
DOI: 10.1016/S0273-1223(96)00818-9

[10] Min B. M., Lee S. W., Lim J. N., You Y., Lee T. S., Kang P. H., Park W. H.: Chitin and chitosan nanofibers: Electrospinning of chitin and deacetylation of chitin nanofibers. Polymer, **45**, 7137–7142 (2004).
DOI: 10.1016/j.polymer.2004.08.048

[11] Ohkawa K., Cha D., Kim H., Nishida A., Yamamoto H.: Electrospinning of chitosan. Macromolecular Rapid Communications, **25**, 1600–1605 (2004).
DOI: 10.1002/marc.200400253

[12] Hasegawa M., Isogai A., Onabe F., Usuda M.: Dissolving states of cellulose and chitosan in trifluoroacetic acid. Journal of Applied Polymer Science, **45**, 1857–1863 (1992).
DOI: 10.1002/app.1992.070451020

[13] Ohkawa K., Minato K-I., Kumagai G., Hayashi S., Yamamoto H.: Chitosan nanofiber. Biomacromolecules, **7**, 3291–3294 (2006).
DOI: 10.1021/bm0604395

[14] Sangsanoh P., Suwantong O., Neamnark A., Cheepsunthornc P., Pavasantd P., Supaphola P.: *In vitro* biocompatibility of electrospun and solvent-cast chitosan substrata towards Schwann, osteoblast, keratinocyte and fibroblast cells. European Polymer Journal, **46**, 428–440 (2010).
DOI: 10.1016/j.eurpolymj.2009.10.029

[15] Sangsanoh P., Supaphol P.: Stability improvement of electrospun chitosan nanofibrous membranes in neutral or weak basic aqueous solutions. Biomacromolecules, **7**, 2710–2714 (2006).
DOI: 10.1021/bm060286l

[16] Haider S., Park S-Y.: Preparation of the electrospun chitosan nanofibers and their applications to the adsorption of Cu(II) and Pb(II) ions from an aqueous solution. Journal of Membrane Science, **328**, 90–96 (2009).
DOI: 10.1016/j.memsci.2008.11.046

[17] Geng X., Kwon O-H., Jang J.: Electrospinning of chitosan dissolved in concentrated acetic acid solution. Biomaterials, **26**, 5427–5432 (2005).
DOI: 10.1016/j.biomaterials.2005.01.066

[18] Vrieze S. D., Westbroeak P., Camp T. V., Van Langenhove L.: Electrospinning of chitosan nanofibrous structures: Feasibility study. Journal of Materials Science, **42**, 8029–8034 (2007).
DOI: 10.1007/s10853-006-1485-6

[19] Homoyoni H., Ravandi S. A. H., Valizadeh M.: Electrospinning of chitosan nanofibers: Processing optimization. Carbohydrate Polymers, **77**, 656–661 (2009).
DOI: 10.1016/j.carbpol.2009.02.008

[20] Schiffman J. D., Schauer C. L.: Cross-linking chitosan nanofibers. Biomacromolecules, **8**, 594–601 (2007).
DOI: 10.1021/bm060804s

[21] Schiffman J. D., Schauer C. L.: One-step electrospinning of cross-linked chitosan fibers. Biomacromolecules, **8**, 2665–2667 (2007).
DOI: 10.1021/bm7006983

[22] Fong H., Chun I., Reneker D. H.: Beaded nanofibers formed during electrospinning. Polymer, **40**, 4585–4592 (1999).
DOI: 10.1016/S0032-3861(99)00068-3

[23] Lin T., Wang H., Wang H., Wang X.: The charge effect of cationic surfactants on the elimination of fibre beads in the electrospinning of polystyrene. Nanotechnology, **15**, 1375–1381 (2004).
DOI: 10.1088/0957-4484/15/9/044

[24] Son W. K., Youk J. H., Lee T. S., Park W. H.: The effects of solution properties and polyelectrolyte on electrospinning of ultrafine poly(ethylene oxide) fibers. Polymer, **45**, 2959–2966 (2004).
DOI: 10.1016/j.polymer.2004.03.006

[25] Jia Y-T., Gong J., Gu X-H., Kim H-Y., Dong J., Shen X-Y.: Fabrication and characterization of poly (vinyl alcohol)/chitosan blend nanofibers produced by electrospinning method. Carbohydrate Polymers, **67**, 403–409 (2007).
DOI: 10.1016/j.carbpol.2006.06.010

[26] Allen M. J., Schoonmaker J. E., Bauer T. W., Williams P. F., Higham P. A., Hansen Y.: Preclinical evaluation of a poly (vinyl alcohol) hydrogel implant as a replacement for the nucleus pulposus. Spine, **29**, 515–523 (2004).
DOI: 10.1097/01.BRS.0000113871.67305.38

[27] Chen D-H., Leu J-C., Huang T-C.: Transport and hydrolysis of urea in a reactor–separator combining an anion-exchange membrane and immobilized urease. Journal of Chemical Technology and Biotechnology, **61**, 351–357 (1994).
DOI: 10.1002/jctb.280610411

[28] Li L., Hsieh Y-L.: Chitosan bicomponent nanofibers and nanoporous fibers. Carbohydrate Research, **341**, 374–381(2006).
DOI: 10.1016/j.carres.2005.11.028

[29] Zhou Y. S., Yang D., Nie J.: Electrospinning of chitosan/poly(vinyl alcohol)/acrylic acid aqueous solutions. Journal of Applied Polymer Science, **102**, 5692–5697 (2006).
DOI: 10.1002/app.25068

[30] Huang X-J., Ge D., Xu Z-K.: Preparation and characterization of stable chitosan nanofibrous membrane for lipase immobilization. European Polymer Journal, **43**, 3710–3718 (2007).
DOI: 10.1016/j.eurpolymj.2007.06.010

[31] Zheng H., Du Y., Yu J., Huang R., Zhang L.: Preparation and characterization of chitosan/poly(vinyl alcohol) blend fibers. Journal of Applied Polymer Science, **80**, 2558–2565 (2001).
DOI: 10.1002/app.1365

[32] Lin T., Fang J., Wang H., Wang X.: Using chitosan as a thickener for electrospinning dilute PVA solutions to improve fibre uniformity. Nanotechnology, **17**, 3718–3723 (2006).
DOI: 10.1088/0957-4484/17/15/017

[33] Zhang Y., Huang X., Duan B., Wu B., Li S., Juan X.: Preparation of electrospun chitosan/poly(vinyl alcohol) membranes. Colloid and Polymer Science, **285**, 855–863 (2007).
DOI: 10.1007/s00396-006-1630-4

[34] Zhou Y. S., Yang D. Z., Nie J.: Preparation and characterization of crosslinked chitosan-based nanofibers. Chinese Chemical Letters, **18**, 118–120 (2007).
DOI: 10.1016/j.cclet.2006.11.035

[35] Sims C. D., Butler P. E., Casanova R., Lee B. T., Randolph M. A., Lee W. P., Vacanti C. A., Yaremchuk M. J.: Injectable cartilage using polyethylene oxide polymer substrates. Plastic and Reconstructive Surgery, **98**, 843–850 (1996).

[36] Yoshii F., Zhansahan Y., Isobe K., Shinozaki K., Makuuchi K.: Electron beam crosslinked PEO and PEO/PVA hydrogels for wound dressing. Radiation Physics and Chemistry, **55**, 133–138 (1999).
DOI: 10.1016/S0969-806X(98)00318-1

[37] Klossner R. R., Queen H. A., Coughlin A. J., Krause W. E.: Correlation of chitosan's rheological properties and its ability to electrospin. Biomacromolecules, **9**, 2947–2953 (2008).
DOI: 10.1021/bm800738u

[38] Bhattarai N., Edmondson D., Veiseh O., Matsenb F. A., Zhang M.: Electrospun chitosan-based nanofibers and their cellular compatibility. Biomaterials, **26**, 6176–6184 (2005).
DOI: 10.1016/j.biomaterials.2005.03.027

[39] Kriegel C., Kit K. M., McClements D. J., Weiss J.: Electrospinning of chitosan–poly(ethylene oxide) blend nanofibers in the presence of micellar surfactant solutions. Polymer, **50**, 189–200 (2009).
DOI: 10.1016/j.polymer.2008.09.041

[40] Kriegel C., Kit K. M., McClements D. J., Weiss J.: Influence of surfactant type and concentration on electrospinning of chitosan–poly(ethylene oxide) blend nanofibers. Food Biophysics, **4**, 213–228 (2009).
DOI: 10.1007/s11483-009-9119-6

[41] Zhang J-F., Yang D-Z., Xu F., Yin R-X., Nie J.: Electrospun core−shell structure nanofibers from homogeneous solution of poly(ethylene oxide)/chitosan. Macromolecules, **42**, 5278–5284 (2009).
DOI: 10.1021/ma900657y

[42] Duan B., Dong C., Yuan X., Yao K.: Electrospinning of chitosan solutions in acetic acid with poly(ethylene oxide). Journal of Biomaterials Science, Polymer Edition, **15**, 797–811 (2004).
DOI: 10.1163/156856204774196171

[43] Zhang Y. Z., Su B., Ramakrishna S., Lim C. T.: Chitosan nanofibers from an easily electrospinnable UHMWPEO-doped chitosan solution system. Biomacromolecules, **9**, 136–141 (2008).
DOI: 10.1021/bm701130e

[44] Yang M-R., Chen K-S., Tsai J-C., Tseng C-C., Lin S-F.: The antibacterial activities of hydrophilic modified nonwoven PET. Materials Science and Engineering: C, **20**, 167–173 (2002).
DOI: 10.1016/S0928-4931(02)00028-0

[45] Jung K-H., Huh M-W., Meng W., Yuan J., Hyun S. H., Bae J-S., Hudson S. M., Kang I-K.: Preparation and antibacterial activity of PET/chitosan nanofibrous mats using an electrospinning technique. Journal of Applied Polymer Science, **105**, 2816–2823 (2007).
DOI: 10.1002/app.25594

[46] Lopes-da-Silva J. A., Veleirinho B., Delgadillo I.: Preparation and characterization of electrospun mats made of PET/chitosan hybrid nanofibers. Journal of Nanoscience and Nanotechnology, **9**, 3798–3804 (2009).
DOI: 10.1166/jnn.2009.NS70

[47] Yang X. C., Chen X. N., Wang H. J.: Acceleration of osteogenic differentiation of preosteoblastic cells by chitosan containing nanofibrous scaffolds. Biomacromolecules, **10**, 2772–2778 (2009).
DOI: 10.1021/bm900623j

[48] Shalumon K. T., Anulekha K. H., Girish C. M., Prasantha R., Naira S. V., Jayakumar R.: Single step electrospinning of chitosan/poly(ε-caprolactone) nanofibers using formic acid/acetone solvent mixture. Carbohydrate Polymers, **80**, 413–419 (2010).
DOI: 10.1016/j.carbpol.2009.11.039

[49] Mohammadi Y., Soleimani M., Fallahi-Sichani M., Gazme A., Haddadi-Asl V., Arefian E., Kiani J., Moradi R., Atashi A., Ahmadbeigi N.: Nanofibrous poly(ε-caprolactone)/poly(vinyl alcohol)/chitosan hybrid scaffolds for bone tissue engineering using mesenchymal stem cells. The International Journal of Artificial Organs, **30**, 204–211 (2007).

[50] Oksman K., Skrifvars M., Selin J-F.: Natural fibres as reinforcement in polylactic acid (PLA) composites. Composites Science and Technology, **63**, 1317–1324 (2003).
DOI: 10.1016/S0266-3538(03)00103-9

[51] Xu J., Zhang J. H., Gao W. Q., Liang H., Wang H., Li J.: Preparation of chitosan/PLA blend micro/nanofibers by electrospinning. Materials Letters, **63**, 658–660 (2009).
DOI: 10.1016/j.matlet.2008.12.014

[52] Chen F., Li X. Q., Mo X. M., He C., Wang H., Ikada Y.: Electrospun chitosan-P(LLA-CL) nanofibers for biomimetic extracellular matrix. Journal of Biomaterials Science, Polymer Edition, **19**, 677–691 (2008).
DOI: 10.1163/156856208784089661

[53] Ryu Y. J., Kim H. Y., Lee K. H., Park H. C., Lee D. R.: Transport properties of electrospun nylon 6 nonwoven mats. European Polymer Journal, **39**, 1883–1889 (2003).
DOI: 10.1016/S0014-3057(03)00096-X

[54] Zhang H. T., Li S. B., Christopher J., Ning X., Nie H., Zhu L.: Studies on electrospun nylon-6/chitosan complex nanofiber interactions. Electrochimica Acta, **54**, 5739–5745 (2009).
DOI: 10.1016/j.electacta.2009.05.021

[55] Mohammed Z. H., Hember M. W. N., Richardson R. K., Morris E. R.: Application of polymer blending laws to composite gels of agarose and crosslinked waxy maize starch. Carbohydrate Polymers, **36**, 27–36 (1998).
DOI: 10.1016/S0144-8617(98)00012-5

[56] Teng S-H., Wang P., Kim H-E.: Blend fibers of chitosan–agarose by electrospinning. Materials Letters, **63**, 2510–2512 (2009).
DOI: 10.1016/j.matlet.2009.08.051

[57] Rho K. S., Jeong L., Lee G., Seod B-M., Park Y. J., Hong S-D., Roh S., Cho J. J., Park W. H., Min B-M.: Electrospinning of collagen nanofibers: Effects on the behavior of normal human keratinocytes and early-stage wound healing. Biomaterials, **27**, 1452–1461 (2006).
DOI: 10.1016/j.biomaterials.2005.08.004

[58] Chen Z. G., Mo X. M., Qing F. L.: Electrospinning of collagen–chitosan complex. Materials Letters, **61**, 3490–3494 (2007).
DOI: 10.1016/j.matlet.2006.11.104

[59] Chen Z. G., Mo X. M., He C. L., Wang H.: Intermolecular interactions in electrospun collagen–chitosan complex nanofibers. Carbohydrate Polymers, **72**, 410–418 (2008).
DOI: 10.1016/j.carbpol.2007.09.018

[60] Chen Z. G., Wei B., Mo X. M., Ramakrishna S., Cui F.: Mechanical properties of electrospun collagen–chitosan complex single fibers and membrane. Materials Science and Engineering: C, **29**, 2428–2435 (2009).
DOI: 10.1016/j.msec.2009.07.006

[61] Chen Z. G., Wang P. W., Wei B., Cui F. Z.: Electrospun collagen–chitosan nanofiber: A biomimetic extracellular matrix for endothelial cell and smooth muscle cell. Acta Biomaterialia, **6**, 372–382 (2010).
DOI: 10.1016/j.actbio.2009.07.024

[62] Chen J-P., Chang G-Y., Chen J-K.: Electrospun collagen/chitosan nanofibrous membrane as wound dressing. Colloids and Surfaces A: Physicochemical and Engineering Aspects, **313–314**, 183–188 (2008).
DOI: 10.1016/j.colsurfa.2007.04.129

[63] Santin M., Motta A., Freddi G., Cannas M.: In vitro evaluation of the inflammatory potential of the silk fibroin. Journal of Biomedical Materials Research, **46**, 382–389 (1999).
DOI: 10.1002/(SICI)1097-4636(19990905)46:3<382::AID-JBM11>3.0.CO;2-R

[64] Wang Y. Z., Kim H-J., Vunjak-Novakovic G., Kaplan D. L.: Stem cell-based tissue engineering with silk biomaterials. Biomaterials, **27**, 6064–6082 (2006).
DOI: 10.1016/j.biomaterials.2006.07.008

[65] Park W. H., Ha W. S., Ito H., Miyamoto T., Inagaki H., Noishiki Y.: Relationships between antithrombogenicity and surface free energy of regenerated silk fibroin films. Fibers and Polymers, **2**, 58–63 (2001).
DOI: 10.1007/BF02875259

[66] Sukigara S., Gandhi M., Ayutsede J., Micklus M., Ko F.: Regeneration of *Bombyx mori* silk by electrospinning – Part 1: Processing parameters and geometric properties. Polymer, **44**, 5721–5727 (2003).
DOI: 10.1016/S0032-3861(03)00532-9

[67] Park W. H., Jeong L., Yoo D., Hudson S.: Effect of chitosan on morphology and conformation of electrospun silk fibroin nanofibers. Polymer, **45**, 7151–7157 (2004).
DOI: 10.1016/j.polymer.2004.08.045

[68] Torres-Giner S., Gimenez E., Lagaron J. M.: Characterization of the morphology and thermal properties of Zein Prolamine nanostructures obtained by electrospinning. Food Hydrocolloids, **22**, 601–614 (2008).
DOI: 10.1016/j.foodhyd.2007.02.005

[69] Torres-Giner S., Ocio M. J., Lagaron J. M.: Novel antimicrobial ultrathin structures of zein/chitosan blends obtained by electrospinning. Carbohydrate Polymers, **77**, 261–266 (2009).
DOI: 10.1016/j.carbpol.2008.12.035

[70] Song T. Y., Yao C., Li X. S.: Electrospinning of zein/chitosan composite fibrous membranes. Chinese Journal of Polymer Science, **28**, 171–179 (2010).
DOI: 10.1007/s10118-010-8239-2

[71] Chen R-N., Wang G-M., Chen C-H., Ho H-O., Sheu M-T.: Development of N,O-(carboxymethyl)chitosan/collagen matrixes as a wound dressing. Biomacromolecules, **7**, 1058–1064 (2006).
DOI: 10.1021/bm050754b

[72] Du J., Hsieh Y-L.: Nanofibrous membranes from aqueous electrospinning of carboxymethyl chitosan. Nanotechnology, **19**, 125707/1–125707/9 (2008).
DOI: 10.1088/0957-4484/19/12/125707

[73] Mincheva R., Manolova N., Rashkov I.: Bicomponent aligned nanofibers of *N*-carboxyethylchitosan and poly(vinyl alcohol). European Polymer Journal, **43**, 2809–2818 (2007).
DOI: 10.1016/j.eurpolymj.2007.04.020

[74] Zhou Y. S., Yang D., Chen X., Xu Q., Lu F., Nie J.: Electrospun water-soluble carboxyethyl chitosan/poly(vinyl alcohol) nanofibrous membrane as potential wound dressing for skin regeneration. Biomacromolecules, **9**, 349–354 (2008).
DOI: 10.1021/bm7009015

[75] Mincheva R., Manolova N., Paneva D., Rashkov I.: Preparation of polyelectrolyte-containing nanofibers by electrospinning in the presence of a non-ionogenic water-soluble polymer. Journal of Bioactive and Compatible Polymers, **20**, 419–435 (2005).
DOI: 10.1177/0883911505057447

[76] Lee K. Y., Ha W. S., Park W. H.: Blood compatibility and biodegradability of partially *N*-acylated chitosan derivatives. Biomaterials, **16**, 1211–1216 (1995).
DOI: 10.1016/0142-9612(95)98126-Y

[77] Hirano S., Noishiki Y.: The blood compatibility of chitosan and *N*-acylchitosans. Journal of Biomedical Materials Research, **19**, 413–417 (1985).
DOI: 10.1002/jbm.820190406

[78] Neamnark A., Rujiravanit R., Supaphol P.: Electrospinning of hexanoyl chitosan. Carbohydrate Polymers, **66**, 298–305 (2006).
DOI: 10.1016/j.carbpol.2006.03.015

[79] Peesan M., Rujiravanit R., Supaphol P.: Electrospinning of hexanoyl chitosan/polylactide blends. Journal of Biomaterials Science, Polymer Edition, **17**, 547–565 (2006).
DOI: 10.1163/156856206776986251

[80] Feng Z. Q., Chu X., Huang N. P., Wang T., Wang Y., Shi X., Ding Y., Gu Z-Z.: The effect of nanofibrous galactosylated chitosan scaffolds on the formation of rat primary hepatocyte aggregates and the maintenance of liver function. Biomaterials, **30**, 2753–2763 (2009).
DOI: 10.1016/j.biomaterials.2009.01.053

[81] Ignatova M., Starbova K., Markova N., Manolova N., Rashkov I.: Electrospun nano-fibre mats with antibacterial properties from quaternised chitosan and poly (vinyl alcohol). Carbohydrate Research, **341**, 2098–2107 (2006).
DOI: 10.1016/j.carres.2006.05.006

[82] Ignatova M., Manolova N., Rashkov I.: Novel antibacterial fibers of quaternized chitosan and poly(vinyl pyrrolidone) prepared by electrospinning. European Polymer Journal, **43**, 1112–1122 (2007).
DOI: 10.1016/j.eurpolymj.2007.01.012

[83] Alipour S. M., Nouri M., Mokhtari J., Bahrami S. H.: Electrospinning of poly(vinyl alcohol)–water-soluble quaternized chitosan derivative blend. Carbohydrate Research, **344**, 2496–2501 (2009).
DOI: 10.1016/j.carres.2009.10.004

[84] Wan Y., Cao X. Y., Zhang S. M., Wang S., Wu Q.: Fibrous poly(chitosan-g-dl-lactic acid) scaffolds prepared via electro-wet-spinning. Acta Biomateriala, **4**, 876–886 (2008).
DOI: 10.1016/j.actbio.2008.01.001

[85] Duan K. R., Chen H. L., Huang J., Yu j., Liu S., Wang D., Li Y.: One-step synthesis of amino-reserved chitosan-graft-polycaprolactone as a promising substance of biomaterial. Carbohydrate Polymers, **80**, 498–503 (2010).
DOI: 10.1016/j.carbpol.2009.12.013

[86] Skotak M., Leonov A. P., Larsen G., Noriega S., Subramanian A.: Biocompatible and biodegradable ultrafine fibrillar scaffold materials for tissue engineering by facile grafting of l-lactide onto chitosan. Biomacromolecules, **9**, 1902–1908 (2008).
DOI: 10.1021/bm800158c

[87] Zhang Y. Z., Venugopal J. R., El-Turki A., Ramakrishna S., Su B., Lim C. T.: Electrospun biomimetic nanocomposite nanofibers of hydroxyapatite/chitosan for bone tissue engineering. Biomaterials, **29**, 4314–4322 (2008).
DOI: 10.1016/j.biomaterials.2008.07.038

[88] Shen K., Hu Q. L., Chen L., Shen J.: Preparation of chitosan bicomponent nanofibers filled with hydroxyapatite nanoparticles via electrospinning. Journal of Applied Polymer Science, **115**, 2683–2690 (2010).
DOI: 10.1002/app.29832

[89] Yang D. Z., Jin Y., Ma G. P., Chen X., Lu F., Nie J.: Fabrication and characterization of chitosan/PVA with hydroxyapatite biocomposite nanoscaffolds. Journal of Applied Polymer Science, **110**, 3328–3335 (2008).
DOI: 10.1002/app.28829

[90] Yang D. Z., Jin Y., Zhou Y. S., Ma G., Chen X., Lu F., Nie J.: In situ mineralization of hydroxyapatite on electrospun chitosan-based nanofibrous scaffolds. Macromolecular Bioscience, **8**, 239–246 (2008).
DOI: 10.1002/mabi.200700221

[91] An J., Zhang H., Zhang J. T., Zhao Y., Yuan X.: Preparation and antibacterial activity of electrospun chitosan/poly(ethylene oxide) membranes containing silver nanoparticles. Colloid and Polymer Science, **287**, 1425–1434 (2009).
DOI: 10.1007/s00396-009-2108-y

[92] Penchev H., Paneva D., Manolova N., Rashkov I.: Electrospun hybrid nanofibers based on chitosan or N-carboxyethylchitosan and silver nanoparticles. Macromolecular Bioscience, **9**, 884–894 (2009).
DOI: 10.1002/mabi.200900003

[93] Hang A. T., Tae B., Park J. S.: Non-woven mats of poly(vinyl alcohol)/chitosan blends containing silver nanoparticles: Fabrication and characterization. Carbohydrate Polymers, **82**, 472–479 (2010).
DOI: 10.1016/j.carbpol.2010.05.016

[94] Zhuang X. P., Cheng B. W., Kang W. M., Xu X.: Electrospun chitosan/gelatin nanofibers containing silver nanoparticles. Carbohydrate Polymers, **82**, 524–527 (2010).
DOI: 10.1016/j.carbpol.2010.04.085

[95] Wang L., Wang A. Q.: Adsorption characteristics of Congo Red onto the chitosan/montmorillonite nanocomposite. Journal of Hazardous Materials, **147**, 979–985 (2007).
DOI: 10.1016/j.jhazmat.2007.01.145

[96] Liu K-H., Liu T-Y., Chen S-Y., Liu D-M.: Drug release behavior of chitosan–montmorillonite nanocomposite hydrogels following electrostimulation. Acta Biomaterialia, **4**, 1038–1045 (2008).
DOI: 10.1016/j.actbio.2008.01.012

[97] Park J. H., Lee H. W., Chae D. K., Oh W., Yun J. D., Deng Y., Yeum J. H.: Electrospinning and characterization of poly(vinyl alcohol)/chitosan oligosaccharide/clay nanocomposite nanofibers in aqueous solutions. Colloid and Polymer Science, **287**, 943–950 (2009).
DOI: 10.1007/s00396-009-2050-z

[98] Feng W., Wu Z. G., Li Y., Feng Y., Yuan X.: The fabrication and electrochemical properties of electrospun nanofibers of a multiwalled carbon nanotube grafted by chitosan. Nanotechnology, **19**, 105707/1–105707/6 (2008).
DOI: 10.1088/0957-4484/19/10/105707

[99] Son B., Yeom B. Y., Song S. H., Lee C-S., Hwang T. S.: Antibacterial electrospun chitosan/poly(vinyl alcohol) nanofibers containing silver nitrate and titanium dioxide. Journal of Applied Polymer Science, **111**, 2892–2899 (2009).
DOI: 10.1002/app.29233

[100] Yu J. X., Liu T. Q.: Preparation of chitosan grafting acrylic acid supported palladium fibrous catalyst and its application in hydrogenation. Materials Science Forum, **620–622**, 537–540 (2009).
DOI: 10.4028/www.scientific.net/MSF.620-622.537

[101] Wang Z. G., Wan L. S., Liu Z. M., Huang X-J., Xu Z-K.: Enzyme immobilization on electrospun polymer nanofibers: An overview. Journal of Molecular Catalysis B: Enzymatic, **56**, 189–195 (2009).
DOI: 10.1016/j.molcatb.2008.05.005

[102] Desai K., Kit K.: Effect of spinning temperature and blend ratios on electrospun chitosan/poly(acrylamide) blends fibers. Polymer, **49**, 4046–4050 (2008).
DOI: 10.1016/j.polymer.2008.07.012

[103] Wan Ngah W. S., Endud C. S., Mayanar R.: Removal of copper(II) ions from aqueous solution onto chitosan and cross-linked chitosan beads. Reactive and Functional Polymers, **50**, 181–190 (2002).
DOI: 10.1016/S1381-5148(01)00113-4

[104] Huang C., Chung Y-C., Liou M-R.: Adsorption of Cu(II) and Ni(II) by pelletized biopolymer. Journal of Hazardous Materials, **45**, 265–277 (1996).
DOI: 10.1016/0304-3894(95)00096-8

[105] Desai K., Kit K., Li J. J., Davidson P. M., Zivanovic S., Meyer H.: Nanofibrous chitosan non-wovens for filtration applications. Polymer, **50**, 3661–3669 (2009).
DOI: 10.1016/j.polymer.2009.05.058

[106] Desai K., Kit K., Li J., Zivanovic S.: Morphological and surface properties of electrospun chitosan nanofibers. Biomacromolecules, **9**, 1000–1006 (2008).
DOI: 10.1021/bm701017z

[107] Zhang H. T., Wu C. Y., Zhang Y. L., White C. J. B., Xue Y., Nie H., Zhu L.: Elaboration, characterization and study of a novel affinity membrane made from electrospun hybrid chitosan/nylon-6 nanofibers for papain purification. Journal of Materials Science, **45**, 2296–2304 (2010).
DOI: 10.1007/s10853-009-4191-3

[108] Lu S. Y., Gao W. J., Gu H. Y.: Construction, application and biosafety of silver nanocrystalline chitosan wound dressing. Burns, **34**, 623–628 (2008).
DOI: 10.1016/j.burns.2007.08.020

[109] Prabhakaran M. P., Venugopal J. R., Chyan T. T., Hai L. B., Chan C. K., Lim A. Y., Ramakrishn S.: Electrospun biocomposite nanofibrous scaffolds for neural tissue engineering. Tissue Engineering Part A, **14**, 1787–1797 (2008).
DOI: 10.1089/ten.tea.2007.0393

[110] Wang W., Itoh S., Matsuda A., Ichinose S., Shinomiya K., Hata Y., Tanaka J.: Influences of mechanical properties and permeability on chitosan nano/microfiber mesh tubes as a scaffold for nerve regeneration. Journal of Biomedical Materials Research Part A, **84**, 557–566 (2008).
DOI: 10.1002/jbm.a.31536

[111] Wang W., Itoh S., Konno K., Kikkawa T., Ichinose S., Sakai K., Ohkuma T., Watabe K.: Effects of Schwann cell alignment along the oriented electrospun chitosan nanofibers on nerve regeneration. Journal of Biomedical Materials Research Part A, **91**, 994–1005 (2009).
DOI: 10.1002/jbm.a.32329

[112] Neamnark A., Sanchavanakit N., Pavasant P., Rujiravanita R., Supaphola P.: *In vitro* biocompatibility of electrospun hexanoyl chitosan fibrous scaffolds towards human keratinocytes and fibroblasts. European Polymer Journal, **44**, 2060–2067 (2008).
DOI: 10.1016/j.eurpolymj.2008.04.016

[113] Duan B., Yuan X., Zhu Y., Zhang Y., Li X., Zhang Y., Yao K.: A nanofibrous composite membrane of PLGA–chitosan/PVA prepared by electrospinning. European Polymer Journal, **42**, 2013–2022 (2006).
DOI: 10.1016/j.eurpolymj.2006.04.021

[114] Duan B., Wu L., Li X., Yuan X., Li X., Zhang Y., Yao K.: Degradation of electrospun PLGA-chitosan/PVA membranes and their cytocompatibility *in vitro*. Journal of Biomaterials Science, Polymer Edition, **18**, 95–115 (2007).
DOI: 10.1163/156856207779146105

[115] Jiang H., Fang D., Hsiao B., Chu B., Chen W.: Preparation and characterization of ibuprofen-loaded poly(lactide-*co*-glycolide)/poly(ethylene glycol)-*g*-chitosan electrospun membranes. Journal of Biomaterials Science, Polymer Edition, **15**, 279–296 (2004).
DOI: 10.1163/156856204322977184

[116] Ignatova M. G., Manolova N. E., Toshkova R. A., Rashkov I. B., Gardeva E. G., Yossifova L. S., Alexandrov M. T.: Electrospun nanofibrous mats containing quaternized chitosan and polylactide with in vitro antitumor activity against HeLa cells. Biomacromolecules, **11**, 1633–1645 (2010).
DOI: 10.1021/bm100285n

[117] Charernsriwilaiwat N., Opanasopit P., Rojanarata T., Ngawhirunpata T., Supaphol P.: Preparation and characterization of chitosan-hydroxybenzotriazole/polyvinyl alcohol blend nanofibers by the electrospinning technique. Carbohydrate Polymers, **81**, 675–680 (2010).
DOI: 10.1016/j.carbpol.2010.03.031

[118] Park Y., Kang E., Kwon O-J., Hwang T., Park H., Leed J. M., Kim J. H., Yun C-O.: Ionically crosslinked Ad/chitosan nanocomplexes processed by electrospinning for targeted cancer gene therapy. Journal of Controlled Release, **148**, 75–82 (2010).
DOI: 10.1016/j.jconrel.2010.06.027

[119] Shan Y. P., Yang G. C., Gong J., Zhang X., Zhu L., Qu L.: Prussian blue nanoparticles potentiostatically electrodeposited on indium tin oxide/chitosan nanofibers electrode and their electrocatalysis towards hydrogen peroxide. Electrochimica Acta, **53**, 7751–7755 (2008).
DOI: 10.1016/j.electacta.2008.05.035

eXPRESS Polymer Letters Vol.5, No.4 (2011) 362–373
Available online at www.expresspolymlett.com
DOI: 10.3144/expresspolymlett.2011.35

New waterborne polyurethane-based nanocomposites reinforced with low loading levels of chitin whisker

J. Huang[1,3,5], *J. W. Zou*[1], *P. R. Chang*[2*], *J. H. Yu*[3], *A. Dufresne*[4]

[1]College of Chemical Engineering, Wuhan University of Technology, Wuhan 430070, P.R. China
[2]Bioproducts and Bioprocesses National Science Program, Agriculture and Agri-Food Canada, 107 Science Place, Saskatoon, SK, S7N 0X2, Canada
[3]Interdisciplinary Science and Technology Institute for Advanced Study, East China Normal University, Shanghai 200062, P.R. China
[4]The International School of Paper, Print Media and Biomaterials (Pagora), Grenoble Institute of Technology, BP 65 - 38402 Saint Martin d'Hères Cedex, France
[5]State Key Laboratory of Pulp and Paper Engineering, South China University of Technology, Guangzhou 510640, P.R. China

Received 2 September 2010; accepted in revised form 17 November 2010

Abstract. New waterborne polyurethane (WPU)-based nanocomposites were prepared by incorporating low loading levels of chitin whiskers (ChWs) as the nanophase. The resultant WPU/ChW nanocomposites exhibited prominent enhancement in both strength and Young's modulus, and maintained an elongation of greater than ca. 500%. The ChW loading level of 3 wt% showed the maximum tensile strength (28.8 MPa) and enhanced Young's modulus (6.5 MPa), ca.1.8- and 2.2-fold over those of neat WPU. The active surface and rigidity of ChW facilitated formation of the interface for stress transferring and contributed to higher stress-endurance. As the ChW loading level increased, self-aggregation of ChWs resulted in a decrease in strength; however, the rigidity of ChW still supported the increase in Young's modulus, and the nanocomposites containing 5 wt% ChWs had the highest Young's modulus (9.6 MPa). This work enriches the research into achieving high mechanical performance of waterborne polyurethane-based nanocomposites by introducing a natural nanofiller, and this high performance 'green' bionanocomposites will likely have promising prospects.

Keywords: *nanocomposites, waterborne polyurethane, chitin whisker*

1. Introduction

Public concern over the environment, the depletion of fossil fuels, and climate change has promoted the development of bionanocomposites in the past decade. Compared to polymeric resources from petroleum, natural polymers from renewable resources have the advantages of biodegradability, biocompatibility, non-toxicity, high reactivity, low cost, ease of availability, and so forth [1–3]. Natural nanofillers are the crystalline residues after acidic or alkaline hydrolysis of natural polysaccharides, most notably the rod-like whiskers of cellulose [4] and chitin [5], and the platelet-like nanocrystal of starch [6, 7]. These nanofillers not only inherit all the advantages of the natural polymers, but also have a reinforcing function in composites, similar to traditional inorganic nanofillers [4, 5, 8–10], by virtue of their rigidity. Moreover, compared with inorganic nanofillers, the relatively active surface of natural nanofillers makes it easy to perform chemical derivation and grafting [11–13] or to form strong physical interactions.

*Corresponding author, e-mail: peter.chang@agr.gc.ca

Chitin, a natural polymer, is an abundant renewable resource [14]. Structurally, chitin is very similar to cellulose, except that its basic monosaccharide is 2-acetamido-2-deoxy-D-glucose (*N*-acetyl-D-glucosamine). Chitin and its derivatives have excellent biocompatibility and physiological non-toxicity, such that it may be used for drug delivery, cell culture anticoagulant, sutures and coagulant, etc. [15–17]. Chitin whiskers (ChWs), obtained by removing protein and other impurities from chitin, also possess excellent rigidity and intensity and are often used as a reinforcing agent in nanocomposites [18]. They are being widely used in aerospace flight vehicle elements and components, as well as in the chemical industry, machinery, motorcars, biomedicine and other industrial applications. Nair and Dufresne [19] reported significant improvement in the mechanical properties of natural rubber reinforced by ChWs. Lu *et al.* [20] incorporated ChWs into soy protein to prepare thermoplastic composites, further confirming the reinforcing role ChW nanofillers play in composites.

Due to increasing concerns about human health and environmental-friendliness, organic, solvent-free polyurethane (i.e. waterborne polyurethane, WPU) with its low volatile organic compound (VOC) levels and non-toxicity has been rapidly developed and applied [21, 22]. Environmentally-friendly WPU can be applied to leather and textile finishing, floor coverings, adhesives, pressure sensitive adhesives, and so on [23–27]. Starch [28], soy protein [29], lignin [30], and chitin derivative [31] have been incorporated into WPU for the purposes of reducing cost, improving biodegradability, and enhancing mechanical performance. Additionally, cellulose whisker has also been filled into a WPU matrix as a reinforcing nanophase, resulting in a significant increase in strength and Young's modulus [32].

In this work, we incorporated very low loading levels of ChWs into WPU to prepare WPU/ChW nanocomposites. Subsequently, the structure and mechanical properties of the resultant nanocomposite materials were investigated by attenuated total reflection-Fourier transform infrared spectroscopy (ATR-FTIR), X-ray diffraction (XRD), differential scanning calorimetry (DSC), dynamic mechanical analysis (DMA), scanning electron microscopy (SEM) and tensile tests.

2. Experimental part

2.1. Materials

Chitin (crab shell) was purchased from Yuhuan Ocean Biochemical Co. Ltd. (Zhejiang, China), and used as received. Polycaprolactone, with a number-average molecular weight (M_n) of 2000 (PCL_{2000}), was purchased from Sigma–Aldrich Chemical Co. (Saint Louis, MO, USA). Diphenyl-methane-diisocyanate (MDI-100) was purchased from Yantai Wanhua Polyurethanes Co. Ltd. (Shandong, China). Dimethylol propionic acid (DMPA) was donated by Huzhou Changsheng Chemical Co. Ltd. (Zhejiang, China), and dehydrated under vacuum at 60ºC for 12 h. Triethylamine (TEA) was purchased from Sinopharm Chemical Reagent Co. Ltd. (Shanghai, China), and redistilled before use. Analytical grade butanone solvent was purchased from Sinopharm Chemical Reagent Co. Ltd. (Shanghai, China) and dehydrated by adding CaH_2 and then distilling.

2.2. Preparation of chitin whiskers

According to the previous report [19], the procedure used for preparing a stable suspension of chitin whiskers is described as follows: Chitin was first boiled and mechanically stirred in a 5% KOH solution for 6 h to remove most of the proteins. It was then kept at room temperature overnight under constant stirring, followed by filtering and washing several times with distilled water. The resultant solid was bleached with 17 g of $NaClO_2$ in 1 l 0.3 M CH_3COONa for 6 h at 80°C, and the bleach solution changed every 2 h. After bleaching, the suspension was kept in a 5% KOH solution for 48 h to remove residual proteins and then centrifuged at 3600 rpm for 15 min. The purified chitin was hydrolyzed with boiling 3 N HCl for 90 min under mechanical stirring (30 ml HCl per 1 g chitin). Finally, the acid hydrolyzed suspension was diluted with distilled water, centrifuged (36 000 rpm for 15 min), and then dialyzed until the pH reached 4.0. The resultant chitin whiskers were completely dispersed using ultrasonic treatment or vigorous mechanical shearing, and stored at 6°C after adding sodium azide to inhibit bacterial growth.

2.3. Preparation of WPU/ChW nanocomposites

The synthesis of waterborne polyurethane (WPU) is depicted as follows: Both 4.98 g PCL_{2000} and 2.23 g

MDI were first dissolved in 10 g butanone and then placed into a three-necked round-bottomed flask equipped with a mechanical stirrer, a reflux condenser, and a dry nitrogen inlet. The reactant was then heated to ca.70ºC, and kept under a nitrogen atmosphere for 2 h with mechanical stirring. Thereafter, 0.46 g DMPA, a chain-extender, was dispersed in butanone and added to give a NCO/OH molar ratio of 1.6. The reaction temperature was elevated to 85ºC and held here for 1 h. During this period butanone was occasionally added in order to lower the viscidity of the reactant. Afterward, the resultant product was cooled to less than 40ºC, and then the –COOH of DMPA in the polyurethane chains was neutralized by adding 0.34 g TEA. Emulsification was subsequently carried out by adding icy water under severe shear to produce WPU latex with a solids content of 20 wt%. Finally, the desired amount of ChWs suspended in distilled water was added and the reaction was allowed to continue for another 0.5 h. The WPU latex was cast onto a Teflon mold after vacuum degassing, and allowed to solidify as a film at 60ºC via water evaporation. By changing the ChWs content over a range of 0, 1, 2, 3, 4, and 5 wt%, a series of nanocomposite films were obtained, and coded as WPU, WPU/ChW-1, WPU/ChW-2, WPU/ChW-3, WPU/ChW-4 and WPU/ChW-5, respectively. The resultant films were stored at room temperature in a desiccator containing P_2O_5 with 0% relative humidity (RH) for 5 days.

2.4. Characterization

2.4.1. FTIR analysis

Attenuated total reflectance-Fourier transform infrared (ATR-FTIR) spectra of all the films were recorded on a FTIR 5700 spectrometer (Nicolet, USA). The films were scanned in the range of 4000~700 cm^{-1} using Smart OMNT reflect accessories.

2.4.2. X-ray diffraction (XRD)

X-ray diffraction measurements were performed on a D/max-IIIA X-ray diffractometer (Rigaku Denki, Tokyo, Japan) using Cu K_α radiation ($\lambda = 0.154$ nm) at 40 kV and 60 mA with a scan rate of 12°·min^{-1}. The diffraction angle of 2θ ranged from 2 to 60°.

2.4.3. Atomic force microscopy (AFM)

Atomic force microscopy was performed on a Digital 3100 IIIa microscope (USA). A droplet of a dilute whisker suspension was coated onto a flake of mica, and the water was evaporated at room temperature.

2.4.4. Scanning electron microscope (SEM)

Scanning electron microscope observation was carried out on an S-4800 scanning electron microscope (Hitachi, Japan) with an accelerating voltage of 10 kV. The films were frozen in liquid nitrogen and then snapped immediately. The fracture surfaces were sputtered with Pt, and then observed and photographed.

2.4.5. Differential scanning calorimetry (DSC)

Differential scanning calorimetry analysis was carried out on a DSC-204 instrument (Netzsch, Germany) under a nitrogen atmosphere at a heating or cooling rate of 20ºC·min^{-1}. The specimen was scanned over the range of –150 to 100ºC after a pretreatment to eliminate thermal history and remove volatiles (heating from 20 to 100ºC and then cooling to –150ºC).

2.4.6. Dynamic mechanical analysis (DMA)

Dynamic mechanical analysis measurement was carried out on a DMA-242C dynamic mechanical analyzer (Netzsch, Germany) at a frequency of 1 Hz over the range of –150 to 100 C with a heating rate of 3ºC·min^{-1}. A dual cantilever device was used and the specimen size was 40×10×ca. 0.5 mm^3.

2.4.7. Tensile test

The tensile strength (σ_b), elongation at break (ε_b) and Young's modulus (E) were measured on a CMT6503 universal testing machine (SANS, Shenzhen, China) with a crosshead rate of 100 mm·min^{-1} according to method GB13022-91. The tested specimens were cut into quadrate strips 10 mm wide and the distance between testing marks was 30 mm. The average value of five replicates of each sample was taken.

3. Results and discussion

3.1. Chitin whiskers

The AFM image of a dilute suspension of chitin whiskers (ChWs) is shown in Figure 1. The suspen-

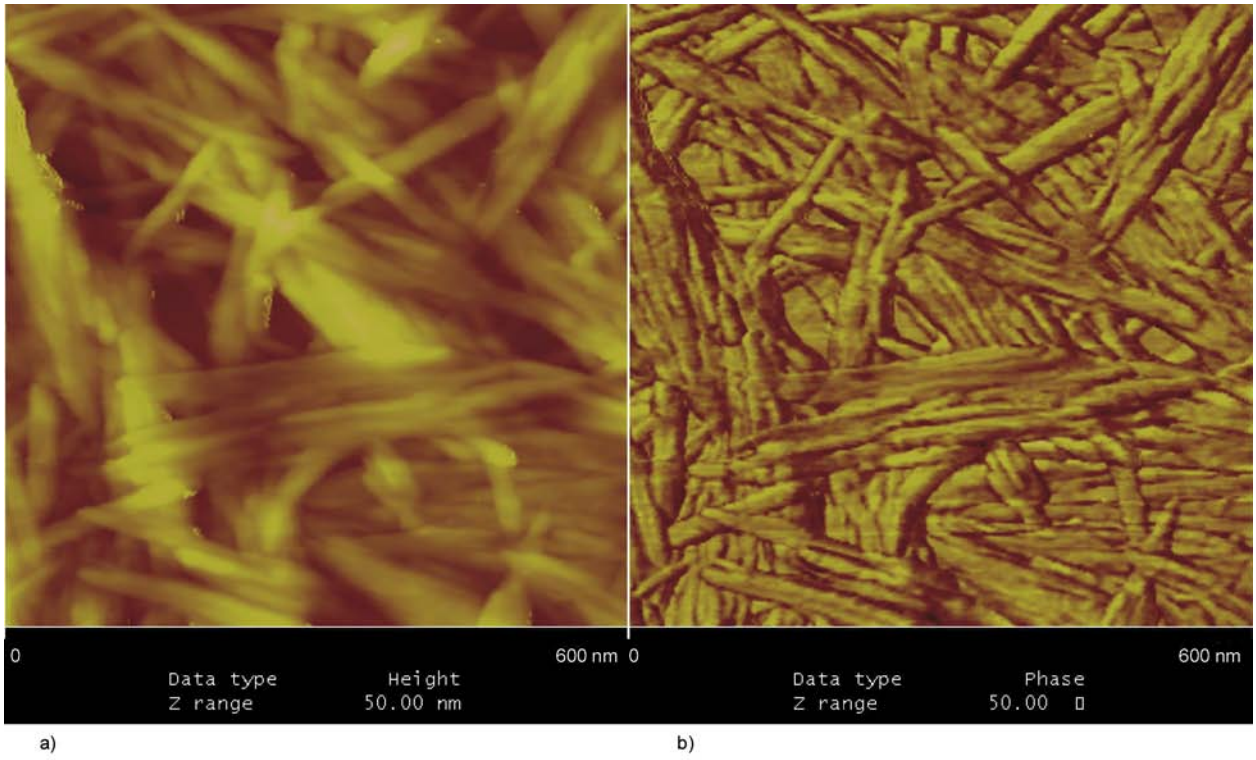

Figure 1. AFM images of a dilute suspension of chitin whiskers (a) height image; b) phase image)

sion consisted of individual chitin fragments having a spindle shape. These fragments had a broad distribution in length (L), ranging from 100 to 350 nm, and diameter (D), ranging from 5 to 35 nm. Exact determination of the latter was difficult because of both the tapering of the chitin fragments and the presence of narrow microcrystals. The average of length and diameter were estimated to be 250±50 and 20±10 nm, respectively; therefore, the average aspect ratio, i.e. L/D, was 12.5±5, which is very close to the dimensions of squid pen (L = 50~300 nm, D = 10 nm, L/D = 15) [5] but much lower than chitin from Riftia tubers (L = 0.5~10 μm, D = 18 nm, L/D = 120) [33]. For a three-dimensional network, the critical volume fraction (V_{Rc}) depends on the aspect ratio (L/D = 12.5) of the chitin whiskers since $V_{Rc} = 0.7\ (L/D)$ [19]. Substitution of the L/D value of chitin whiskers into that equation yields a value of V_{Rc} = 5.6 vol%, or ca. 8.4 wt%. The highest ChWs content in this work was 5 wt%, which is lower than the critical weight fraction, so a three-dimensional network of chitin whiskers was absent in the as-prepared nanocomposites.

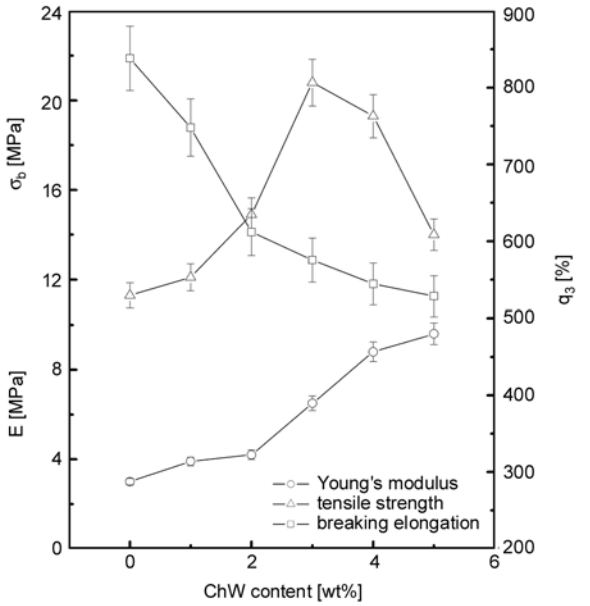

Figure 2. Effects of ChW loading level on tensile strength (σ_b), elongation at break (ε_b) and Young's modulus (E) of WPU/ChW nanocomposite films, with WPU film as reference

3.2. Mechanical properties of nanocomposites

Figure 2 shows the effects of the ChW loading level on the mechanical properties of the WPU/ChW nanocomposites, including tensile strength (σ_b), Young's modulus (E) and elongation at break (ε_b). As expected, the rigidity of ChW enhanced the strength of WPU significantly. Compared with σ_b of 11.3 MPa and E of 3.0 MPa for neat WPU, the σ_b and E values of the WPU/ChW nanocomposites

were both enhanced. When the ChW loading level was 3 wt%, σ_b reached a maximum value of 20.8 MPa, approximately 1.8-fold over that of neat WPU. Thereafter, the continuous increase in the ChW loading level resulted in a slight decrease in σb, but the value of *E* continued to increase. When the ChW loading level reached 5 wt%, *E* increased to 9.6 MPa, ca. 3.2-fold over that of neat WPU. On the other hand, the change in ε_b as the ChWs content increased was just opposite of *E*, and all the ε_b values of the WPU/ChW nanocomposites were lower than that of neat WPU. In other words, enhancement of the strength and Young's modulus occurred at the expense of elongation; however, compared with the obvious enhancement of σ_b and *E*, a certain level of decline in ε_b is acceptable. From the above results, we found that neat ChWs had an evident reinforcing role, furthermore, with a ChW content of 3 wt%, σ_b reached the maximum value and *E* reached 6.5 MPa, which were ca. 1.8 and 2.2-fold over those of neat WPU, respectively. At this time, the ε_b value of the nanocomposites remained at 575.4%. Enhancement of the nanocomposite mechanical properties by ChWs may be attributed to the uniform dispersion of ChWs at the nanoscale as well as to the physical interaction between the ChW nanofiller and the WPU matrix [34] for the transfer of stress to the rigid ChW nanofiller. However, with an increase in the loading level of ChWs, self-aggregation of ChWs may break the original structure and interaction in the WPU matrix, resulting in a decrease in strength and elongation. The rigid nature of ChW and its aggregate, however, maintained the continuous increase in Young modulus.

3.3. Hydrogen bonding in nanocomposites

ATR-FTIR spectra of the WPU/ChW nanocomposites and the neat WPU are shown in Figure 3a. As is well known, the hydrogen bond is an essential physical interaction in waterborne polyurethane affecting the microphase separation structure and mechanical properties of materials [35]. In this case, the –NH in the hard-segment was hydrogen-bonded with the –C=O of the hard-segments, the ester –C=O of the PCL_{2000} soft-segments and the –C=O on the ChW surface. In addition, –OH on the ChW surface also participated in hydrogen bonding with the –C=O in the soft- and hard- segments. All the nanocomposites showed the analogical –NH bands with the main peak located at ca. 3314 cm^{-1} despite the absorption of –OH in ChWs being embedded in them. As a result, absorptions in the range of 3450~3250 cm^{-1} for all the WPU/ChW nanocomposites and WPU were divided into two peaks by curve-fitting (Figure 3b), i.e. Peak I located at 3391–3394 cm^{-1} and Peak II located at 3320–3339 cm^{-1}. The former was the free –NH absorption while the latter was the absorption of hydrogen-bonded –NH for WPU, or included the additional –OH absorption for the WPU/ChW nanocomposites. Table 1 summarizes the detailed locations and fractions of Peaks I and II for all the WPU/ChW nanocomposites and for WPU. The increasing Peak II fraction was not proportional to the increment contributed by –OH absorption, indicating that the original hydrogen bonds associated with –NH in the WPU matrix cleaved. When the ChW loading level was lower than 2 wt%, the relatively prominent increase in the fraction for Peak II was attributed to less inhibition to the original –NH-based hydrogen bonding, and to the formation of hydrogen bonds associated with –OH, –NH- and –C=O on the ChW surface. The analogical –C=O bands of the WPU/ChW nanocomposites and WPU were also divided into three peaks (Figure 3c), namely Peak III from the free –C=O located at 1730–1732 cm^{-1}, Peak IV from the hydrogen-bonded –C=O in the amorphous region located at 1712–1713 cm^{-1} and Peak V from the hydrogen-bonded –C=O in the ordered domain located at 1697–1698 cm^{-1} [36]. The location and fraction of these three peaks in the WPU/ChW nanocomposites and WPU are also summarized in Table 1. Adding ChWs appeared to slightly decrease the fraction of the free –C=O peak (Peak III), indicating that the hydrogen bonding associated with –C=O of hard-segments and PCL_{2000} soft-segments was improved. This was attributed to the newly formed hydrogen bonds between the –C=O of the WPU component and the –OH or –NH- on the ChW surface. Although hydrogen bonding associated –C=O was improved as a whole, the effect of adding ChW on the region of hydrogen bonding in the nanocomposites was distinctly different. With an increase in the ChW loading level, the increasing fraction of Peak IV suggested that the improvement of hydrogen bonding occurred mainly in the amor-

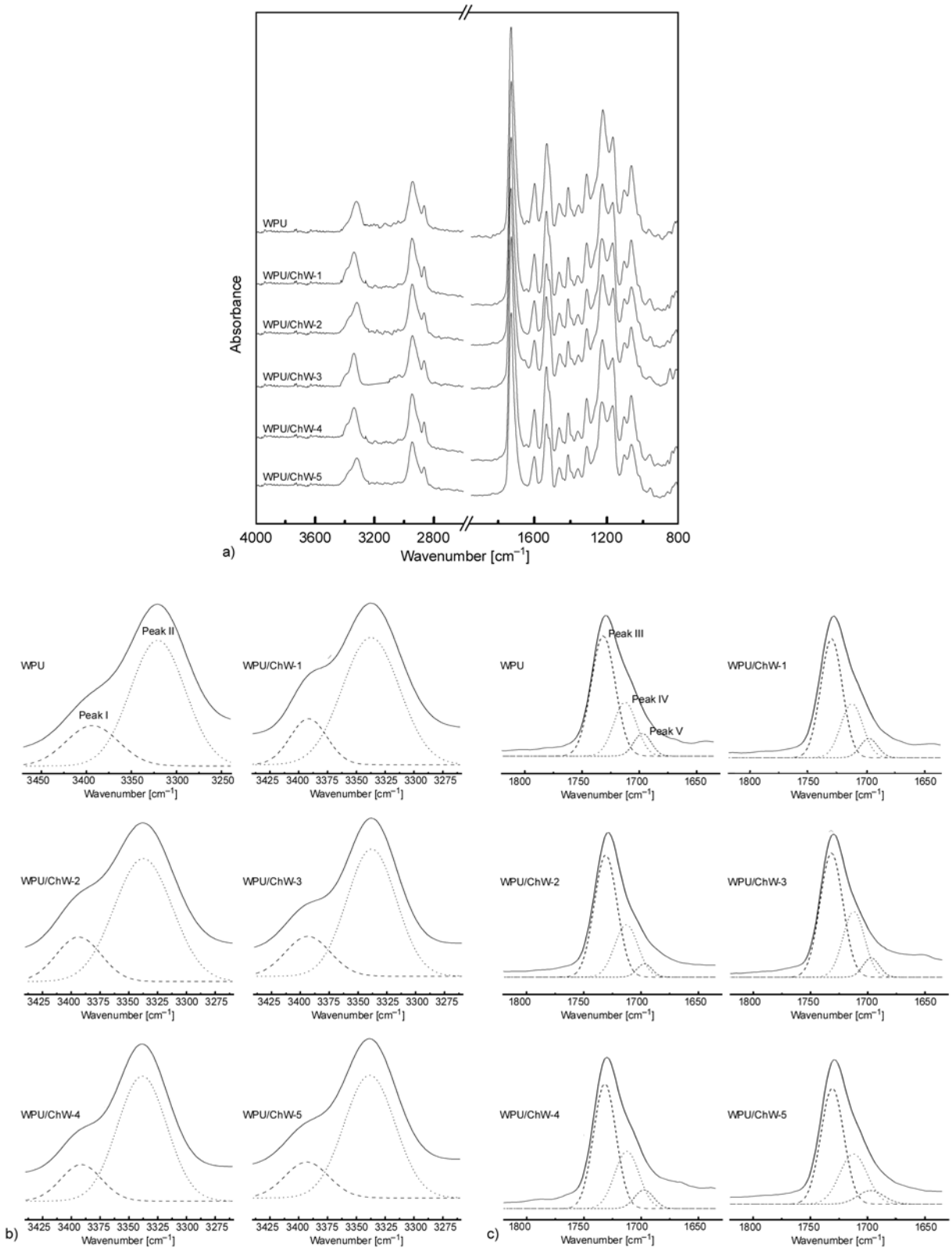

Figure 3. FTIR spectra of the WPU/ChW nanocomposite films and WPU film as reference ((a): full spectra; (b): the curve-fitting for the –NH absorption of WPU/ChW nanocomposites as representive (——) experimental curve, (– – –) free –NH, (· · · ·) hydrogen-bonded –NH; (c): the curve-fitting for the –C=O absorption of WPU/ChW nanocomposites as representive (——) experimental curve, (– – –) free –C=O, (· · · ·) hydrogen-bonded –C=O in amorphous region, (- - -) hydrogen-bonded –C=O in ordered domain)

Table 1. Location and Fraction of Curve-Fitting Peaks for the –NH and –C=O Bands in the FTIR Spectra of WPU/ChW Nanocomposites and WPU (Peak I: Free –NH; Peak II: Hydrogen-Bonded –NH; Peak III: Free –C=O; Peak IV: Hydrogen-Bonded –C=O in Amorphous Region; Peak V: Hydrogen-Bonded –C=O in Ordered Domain).

Sample code	–NH band				–C=O band					
	Peak I		Peak II		Peak III		Peak IV		Peak V	
	Location [cm^{-1}]	Fraction [%]	Location [cm^{-1}]	Fraction [%]	Location [cm^{-1}]	Fraction [%]	Location [cm^{-1}]	Fraction [%]	Location [cm^{-1}]	Fraction [%]
WPU	3393.6	23.5	3320.8	76.5	1731.5	64.1	1712.4	27.2	1697.3	8.7
WPU/ChW-1	3393.1	19.6	3337.4	80.4	1730.2	62.8	1712.4	29.1	1697.5	8.1
WPU/ChW-2	3393.6	21.8	3337.4	78.2	1730.8	63.6	1712.9	29.8	1697.1	6.6
WPU/ChW-3	3393.6	21.1	3338.9	78.9	1731.7	62.1	1712.2	31.1	1697.1	6.8
WPU/ChW-4	3391.5	19.3	3338.9	80.7	1731.7	61.4	1712.4	30.8	1697.5	7.8
WPU/ChW-5	3393.1	18.9	3338.4	81.1	1730.8	60.4	1712.4	31.5	1697.3	8.1

phous region, while the slight decrease in the fraction of Peak V proved the cleavage of hydrogen bonding in the ordered domain. Usually, hydrogen bonding in the ordered domain was constructed by hard-segments in the WPU matrix, which suggested that adding ChW drew down the original ordered alignment among hard-segments.

3.4. Crystalline character of nanocomposites

Figure 4 shows the XRD patterns of the WPU/ChW nanocomposites with various ChW loading levels, as well as neat WPU and ChWs. When the ChWs loading level was lower than 2 wt%, the WPU/ChW nanocomposites inherited the amorphous nature of neat WPU, shown as a diffuse peak located at 20.06° of 2θ, in spite of the fact that –C=O-based hydrogen bonds constructed a small scale ordered domain in the WPU matrix, as mentioned above. Although the ChWs had a semi-crystalline character, at low loading levels and with relatively uniform dispersion, the well-defined diffraction peaks were absent in the nanocomposites. When the ChW loading level increased to 3 wt%, a weak diffraction peak appeared at 19.47° of 2θ, which corresponded to the strongest diffraction of semi-crystalline ChWs located at 19.69° of 2θ. When the ChW loading level increased to 4 wt%, a diffraction peak appeared at 9.04° of 2θ. Furthermore, when the ChWs content reached 5 wt%, two other obvious diffraction peaks appeared at 21.18 and 23.44° of 2θ, which corresponded to the diffraction of ChW located at 21.37 and 23.61° of 2θ respectively. This proved that the ChWs existed in the nanocomposites and tended to self-aggregate with an increase in the ChW loading level.

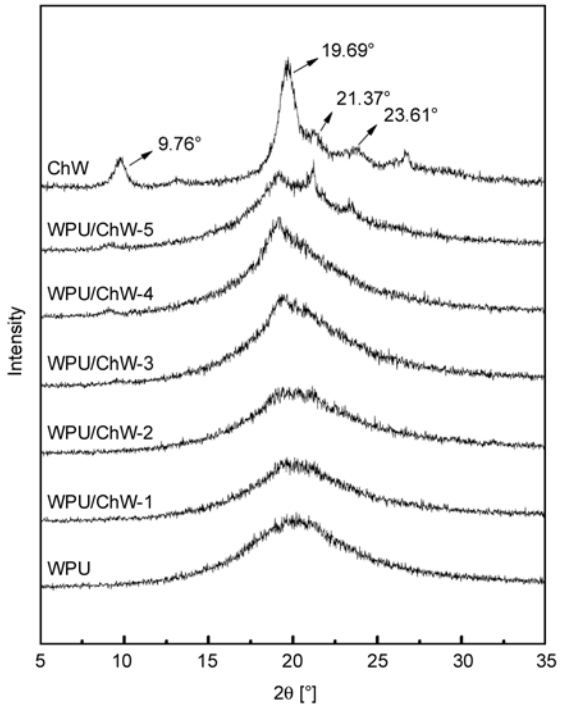

Figure 4. XRD patterns of WPU/ChW nanocomposites as well as WPU and freeze-dried ChW powder

3.5. Thermal behaviour of nanocomposites

DSC and DMA were used to further understand the interaction between the ChW nanofiller and the WPU matrix, as well as the structural changes to the WPU matrix and the distribution of ChWs, by observing the variances in the domain-scale glass transition and the molecular-level α-relaxation assigned to the PCL_{2000} soft-segment, respectively. Table 2 summarizes the glass transition temperature at midpoint ($T_{g,mid}$), the heat-capacity increment (ΔC_p), the melting temperature (T_m) and the heat enthalpy (ΔH_m) of the WPU/ChW nanocomposites and the neat WPU. In the WPU/ChW nanocomposites, the temperatures of glass transition (T_g) and α-relaxation (T_α) of the PCL_{2000} soft-segment can be affected by ChWs in two opposite ways. First, the motion of the soft-segment may be suppressed by

Table 2. DSC data for WPU/ChW nanocomposites and WPU reference

Sample	$T_{g,mid}$ [°C]	ΔC_p [J/g·K]	$T_{m,PCL}$ [°C]	$\Delta H_{m,PCL}$ [J/g]
WPU	–47.5	0.19	45.2	2.34
WPU/ChW-1	–46.7	0.24	45.2	2.75
WPU/ChW-2	–45.9	0.24	46.4	4.15
WPU/ChW-3	–44.3	0.28	47.2	4.44
WPU/ChW-4	–45.4	0.32	48.9	6.24
WPU/ChW-5	–45.9	0.28	47.4	6.59

the steric hindrance of the rigid ChW nanophase and by hydrogen bonding onto the active ChW surface. This could result in a shift of T_g and T_α to a higher temperature. In the opposite way, incorporating ChWs may cleave the original interaction between the hard- and soft-segments and hence change the microphase structure in the WPU matrix. In other words, the soft-segment could escape from the binding of the hard-segment, leading to decreased T_g and T_α. The $T_{g,mids}$ of all the WPU/ChW nanocomposites were higher than that of neat WPU, suggesting that the restriction of ChWs to the mobility of soft-segments was dominant in spite of the inevitable cleavage of the original interaction between the hard- and soft-segments in the WPU matrix. When the ChW loading level was less than 2 wt%, the rigid ChWs homogeneously dispersed into the WPU matrix, and then

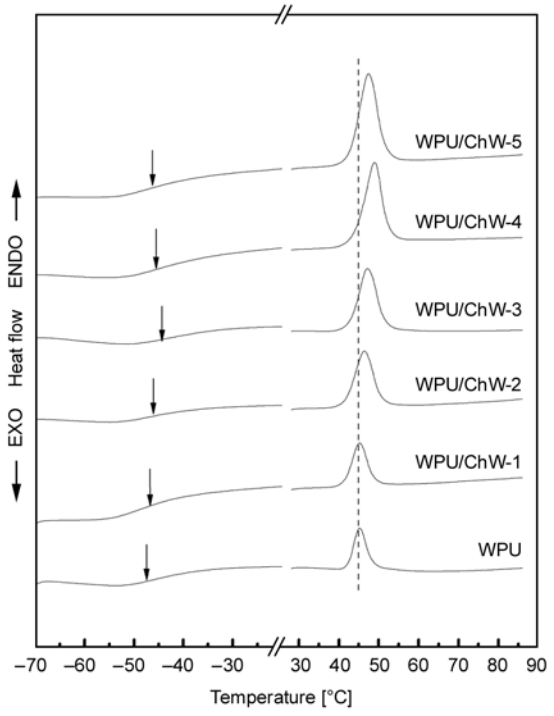

Figure 5. DSC thermograms of WPU/ChW nanocomposites and WPU as reference

inhibited the motion of the soft-segment, mediated by the newly formed interaction with the WPU component. At this time, the $T_{g,mids}$ increased with an increase in ChW loading level. When the ChW content reached 3 wt%, $T_{g,mid}$ of the nanocomposites showed the maximum value; however, increasing the ChW loading level caused the $T_{g,mids}$ to gradually decrease because the increasing loading level of ChW induced self-aggregation of the ChWs and hence weakened the restriction to motion of the soft-segment. This was proven by the obvious diffraction peaks that corresponded to the semi-crystalline character of ChW in the XRD pattern. On the other hand, compared with the ΔH_m value for the neat WPU of 2.34 J·g^{-1}, all the WPU/ChW nanocomposites showed dramatically higher ΔH_m values, suggesting that increasing the ChW loading level improved the crystallinity of the PCL component in the WPU matrix due to the nucleation effect of the ChW (Figure 5).

DMA is a powerful technique that reflects the mobility of the soft-segment through α-relaxation at the molecular-level, for which the specific heat increment of the domain-scale glass transition as measured by DSC is generally ill-defined. Figure 6 shows the logarithm of the storage modulus (logE') and the tangent of the loss angle (tanδ) as a function of temperature The α-relaxation temperature at onset ($T_{\alpha\ onset}$) and the corresponding storage modulus (logE'), α-relaxation temperature of loss peak ($T_{\alpha\ max}$), and the tangent of loss angle (tanδ) are summarized in Table 3. Obviously, the $T_{\alpha\ max}$s of all the WPU/ChW nanocomposites were higher than that of neat WPU. Considering the improved hydrogen bonding associated with –C=O in the amorphous region of the WPU matrix (seen in Table 1), the increase in $T_{\alpha\ max}$s was attributed to the formation of interaction between the polar groups on the ChW surface and the WPU matrix. In this case, the suppression of ChWs to the mobility of soft-segments was proportional to the effective surface of ChWs. When the ChWs were homogeneously dispersed in the WPU matrix (the ChW loading level <2 wt%), the increasing interfacial area between the ChW nanofiller and the WPU matrix resulted in an increase in $T_{\alpha\ max}$s and $T_{\alpha\ onset}$s with an increase of the ChW loading level. This is in good agreement with the DSC results. Thereafter, with a continuous increase in the loading level of ChW, the ChWs

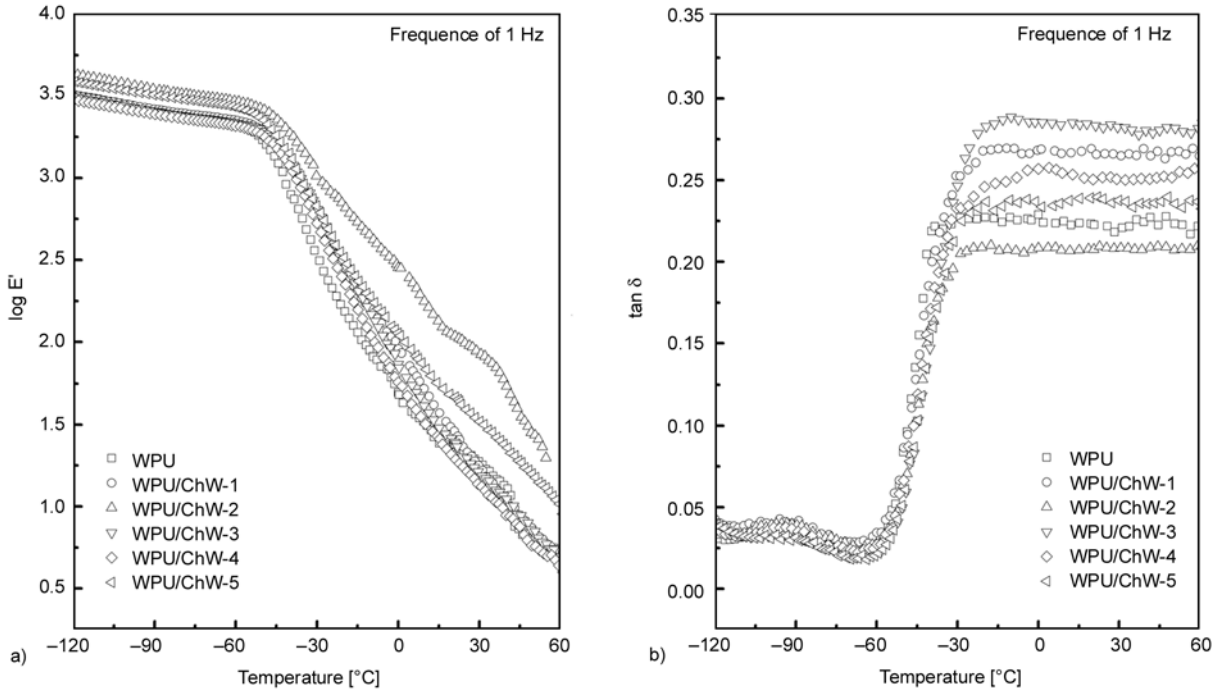

Figure 6. Logarithm of storage modulus (logE') and tangent of loss angle (tanδ) vs. temperature measured at 1 Hz for WPU/ChW nanocomposites with various ChW loading levels, and WPU as reference

Table 3. DMA data for WPU/ChW nanocomposites and WPU reference

Sample	$T_{\alpha\ onset}$ [°C]	logE [MPa]	$T_{\alpha\ max}$ [°C]	tanδ
WPU	–49.5	3.16	–30.4	0.22
WPU/ChW-1	–48.1	3.20	–30.0	0.26
WPU/ChW-2	–45.7	3.37	–29.8	0.20
WPU/ChW-3	–43.3	3.18	–24.5	0.28
WPU/ChW-4	–44.6	3.21	–28.9	0.24
WPU/ChW-5	–45.5	3.26	–29.5	0.21

gradually self-aggregated, resulting in the decrease of $T_{\alpha\ max}$s and $T_{\alpha\ onset}$s for the WPU/ChW nanocomposites. In the WPU/ChW nanocomposites, the rigidity was mainly contributed by the ChWs nanophase as filler [37] and the ordered hard-segment domain of WPU matrix. Although the ordered hard-segment domain of WPU matrix partly cleaved after adding ChW (seen in the discussion on the hydrogen bonding associated with –C=O in ordered domain), the logE' of all the WPU/ChW nanocomposites were still higher than that of neat WPU due to the reinforcing function of rigid ChW. This was in positive correlation with the Young's modulus (E) of the nanocomposites.

3.6. Fracture morphologies of nanocomposites

Figure 7 shows the SEM images of fractured surfaces of the WPU/ChW nanocomposites and neat WPU. When the ChW loading level was lower than 2 wt%, the WPU/ChW nanocomposites (Figure 7b and 7c) showed a fluctuant fractured surface similar to that of neat WPU (Figure 7a). This was attributed to the fact that at a lower loading level ChW uniformly dispersed in the WPU matrix and had almost no effect on the original structure and fractured behaviour of the WPU matrix. However, with an increase in the ChW loading level, the fracture morphologies gradually became smooth surfaces with regular and compact thin stripes. This brittle-fracture characteristic was in agreement with the decrease in strength and elongation at break, and was attributed to breakage of the original structure of the WPU matrix after adding higher levels of ChWs. In addition, with an increase in the loading level of ChW, the ChW nanophase in the WPU matrix could be observed, showing many white dots dispersed on the fracture surface. The SEM images seemed to verify the effects of increasing the ChW loading level on the increasing number and expanded size of the ChW nanophase in the nanocomposites.

4. Conclusions

New nanocomposite materials were prepared by casting and evaporating a mixture with waterborne

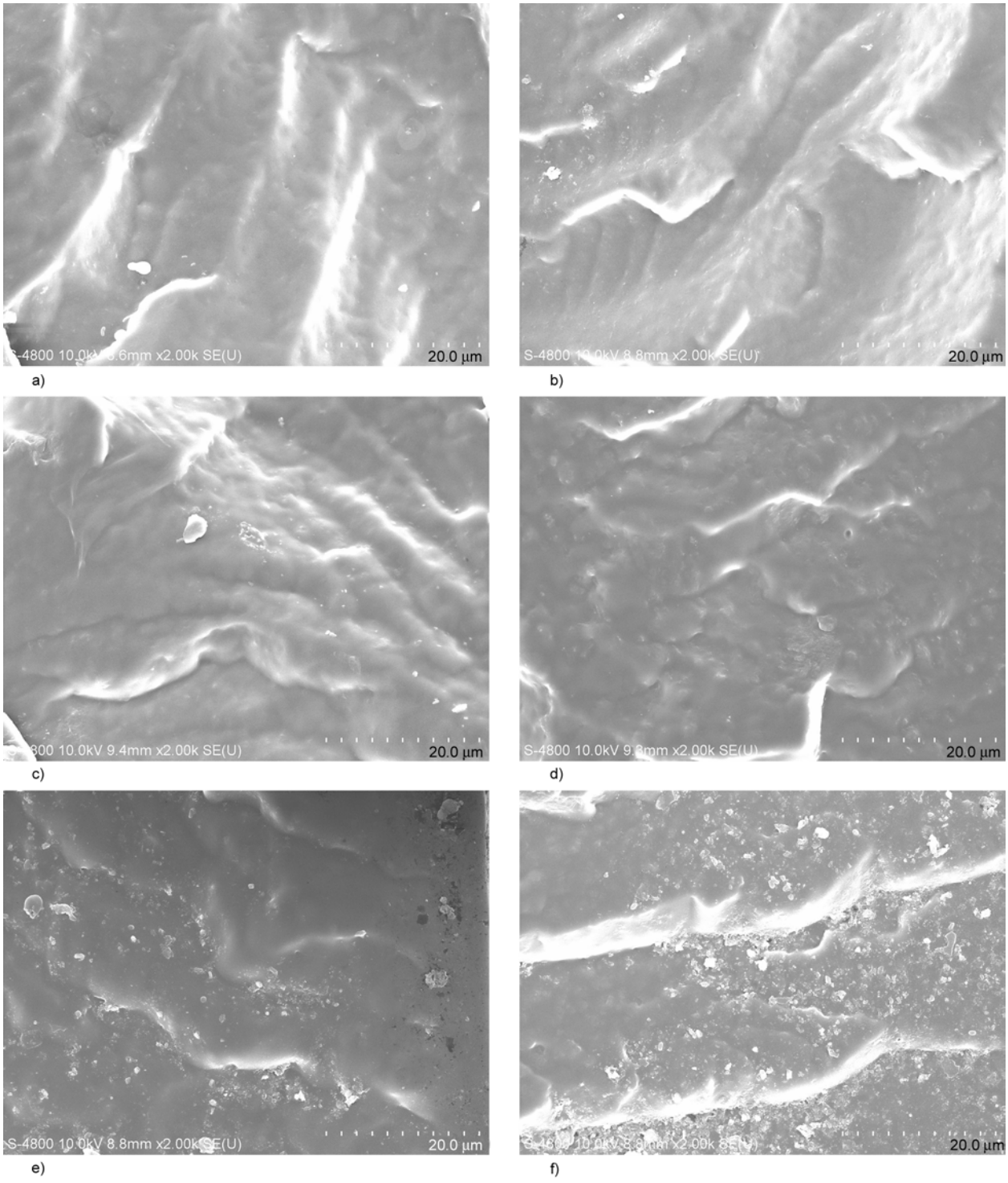

Figure 7. SEM images of fractured surfaces of WPU/ChW nanocomposites with various ChW loading levels and WPU as reference. ((a): WPU; (b): WPU/ChW-1; (c): WPU/ChW-2; (d): WPU/ChW-3; (e): WPU/ChW-4; (f): WPU/ChW-5)

polyurethane (WPU) as matrix and chitin whiskers (ChW) as nanofiller. The strength and Young's modulus of the nanocomposites were simultaneously enhanced and maintained ca. 500% elongation. Herein, the WPU/ChW-3 containing only 3 wt% ChWs had the maximum tensile strength (28.8 MPa) and enhanced Young's modulus (6.5 MPa) that were ca. 1.8- and 2.2-fold over those of neat WPU, respectively. The WPU/ChW-5 containing 5 wt% ChWs had the highest Young's modulus (9.6 MPa), which was enhanced by ca. 220%. The prominent improvement of mechanical performance was attributed to the enduring stress of rigid ChW and stress transfer mediated by strong

interactions between the ChW nanofiller and the WPU matrix. This work rendered a strategy for achieving high mechanical performance of waterborne polyurethane-based nanocomposites by a simple method, and the novel bionanocomposites developed could have great potential applications.

Acknowledgements

The research work was financially supported by the National Natural Science Foundation of China (50873080); Program of Energy Research and Development (PERD) of Canada; Agricultural Bio-products Innovation Program (ABIP) of Canada via the Pulse Research Network (PURENET); State Key Laboratory of Pulp and Paper Engineering (200906); and Fundamental Research Funds for the Central Universities (Self-Determined and Innovative Research Funds of WUT 2010-II-022).

References

[1] Mecking S.: Nature or petrochemistry? – Biologically degradable materials. Angewandte Chemie International Edition, **43**, 1078–1085 (2004).
DOI: 10.1002/anie.200301655

[2] Smith R.: Biodegradable polymers for industrial applications. CRC Press, London (2005).

[3] Wool R., Sun X. S.: Bio-based polymers and composites. Elsevier, London (2005).

[4] Azizi Samir M. A. S., Alloin F., Dufresne A.: Review of recent research into cellulosic whiskers, their properties and their application in nanocomposite field. Biomacromolecules, **6**, 612–626 (2005).
DOI: 10.1021/bm0493685

[5] Paillet M., Dufresne A.: Chitin whisker reinforced thermoplastic nanocomposites. Macromolecules, **34**, 6527–6530 (2001).
DOI: 10.1021/ma002049v

[6] Putaux J-L., Molina-Boisseau S., Momaur T., Dufresne A.: Platelet nanocrystals resulting from the disruption of waxy maize starch granules by acid hydrolysis. Biomacromolecules, **4**, 1198–1202 (2003).
DOI: 10.1021/bm0340422

[7] Angellier H., Choisnard L., Molina-Boisseau S., Ozil P., Dufresne A.: Optimization of the preparation of aqueous suspensions of waxy maize starch nanocrystals using a response surface methodology. Biomacromolecules, **5**, 1545–1551 (2004).
DOI: 10.1021/bm049914u

[8] Angellier H., Molina-Boisseau S., Dole P., Dufresne A.: Thermoplastic starch- waxy maize starch nanocrystals nanocomposites. Biomacromolecules, **7**, 531–539 (2006).
DOI: 10.1021/bm050797s

[9] Angellier H., Molina-Boisseau S., Dufresne A.: Mechanical properties of waxy maize starch nanocrystal reinforced natural rubber. Macromolecules, **38**, 9161–9170 (2005).
DOI: 10.1021/ma0512399

[10] Yuan H., Nishiyama Y., Wada M., Kuga S.: Surface acylation of cellulose whiskers by drying aqueous emulsion. Biomacromolecules, **7**, 696–700 (2006).
DOI: 10.1021/bm050828j

[11] Angellier H., Molina-Boisseau S., Belgacem M. N., Dufresne A.: Surface chemical modification of waxy maize starch nanocrystals. Langmuir, **21**, 2425–2433 (2005).
DOI: 10.1021/la047530j

[12] Thielemans W., Belgacem M. N., Dufresne A.: Starch nanocrystals with large chain surface modifications. Langmuir, **22**, 4804–4810 (2006).
DOI: 10.1021/la053394m

[13] Labet M., Thielemans W., Dufresne A.: Polymer grafting onto starch nanocrystals. Biomacromolecules, **8**, 2916–2927 (2007).
DOI: 10.1021/bm700468f

[14] Rinaudo M.: Chitin and chitosan: Properties and applications. Progress in Polymer Science, **31**, 603–632 (2006).
DOI: 10.1016/j.progpolymsci.2006.06.001

[15] Martina M., Hutmacher D. W.: Biodegradable polymers applied in tissue engineering research: A review. Polymer International, **56**, 145–157 (2007).
DOI: 10.1002/pi.2108

[16] Senda T., He Y., Inoue Y.: Biodegradable blends of poly(ε-caprolactone) with α-chitin and chitosan: Specific interactions, thermal properties and crystallization behavior. Polymer International, **51**, 33–39 (2002).
DOI: 10.1002/pi.793

[17] He Y., Inoue Y.: Novel FTIR method for determining the crystallinity of poly(ε-caprolactone). Polymer International, **49**, 623–626 (2000).
DOI: 10.1002/1097-0126(200006)49:6<623::AID-PI435>3.0.CO;2-8

[18] Zeng M., Gao H. N., Wu Y. Q., Fan L. R., Li A. P.: Preparation and characterization of nanocomposite films from chitin whisker and waterborne poly(ester-urethane) with or without ultra-sonification treatment. Journal of Macromolecular Science Part A: Pure and Applied Chemistry, **47**, 867–876 (2010).
DOI: 10.1080/10601325.2010.492277

[19] Nair K. G., Dufresne A.: Crab shell chitin whisker reinforced natural rubber nanocomposites. 2. Mechanical behavior. Biomacromolecules, **4**, 666–674 (2003).
DOI: 10.1021/bm0201284

[20] Lu Y. S., Weng L. H., Zhang L. N.: Morphology and properties of soy protein isolate thermoplastics reinforced with chitin whiskers. Biomacromolecules, **5**, 1046–1051 (2004).
DOI: 10.1021/bm034516x

[21] Wicks Z. W., Wicks D. A., Rosthauser J. W.: Two package waterborne urethane systems. Progress in Organic Coatings, **44**, 161–183 (2002).
DOI: 10.1016/S0300-9440(02)00002-4

[22] Noble K-L.: Waterborne polyurethanes. Progress in Organic Coatings, **32**, 131–136 (1997).
DOI: 10.1016/S0300-9440(97)00071-4

[23] Lin Y., Hsieh F., Huff H. E.: Water-blown flexible polyurethane foam extended with biomass materials. Journal of Applied Polymer Science, **65**, 695–703 (1997).
DOI: 10.1002/(SICI)1097-4628(19970725)65:4<695::AID-APP8>3.0.CO;2-F

[24] Coogan R. G.: Post-crosslinking of waterborne urethanes. Progress in Organic Coatings, **32**, 51–63 (1997).
DOI: 10.1016/S0300-9440(97)00010-6

[25] Kim B. K., Kim T. K., Jeong H. M.: Aqueous dispersion of polyurethane anionomers from H12MDI/IPDI, PCL, BD, and DMPA. Journal of Applied Polymer Science, **53**, 371–378 (1994).
DOI: 10.1002/app.1994.070530315

[26] Duecoffre V., Diener W., Flosbach C., Schubert W.: Emulsifiers with high chemical resistance: A key to high performance waterborne coatings. Progress in Organic Coatings, **34**, 200–205 (1997).
DOI: 10.1016/S0300-9440(98)00032-0

[27] Brinkman E., Vandevoorde P.: Waterborne two-pack isocyanate-free systems for industrial coatings. Progress in Organic Coatings, **34**, 21–25 (1997).
DOI: 10.1016/S0300-9440(98)00030-7

[28] Wu Q. X., Zhang L. N.: Structure and properties of casting films blended with starch and waterborne polyurethane. Journal of Applied Polymer Science, **79**, 2006–2013 (2001).
DOI: 10.1002/1097-4628(20010314)79:11<2006::AID-APP1009>3.0.CO;2-F

[29] Wang N. G., Zhang L. N.: Preparation and characterization of soy protein plastics plasticized with waterborne polyurethane. Polymer International, **54**, 233–239 (2005).
DOI: 10.1002/pi.1696

[30] Cui G., Xia W., Chen G., Wei M., Huang J.: Enhanced mechanical performances of waterborne polyurethane loaded with lignosulfonate and its supramolecular complexes. Journal of Applied Polymer Science, **106**, 4257–4263 (2007).
DOI: 10.1002/app.27077

[31] Zeng M., Zhang L. N., Wang N. G., Zhu Z. C.: Miscibility and properties of blend membranes of waterborne polyurethane and carboxymethylchitin. Journal of Applied Polymer Science, **90**, 1233–1241 (2003).
DOI: 10.1002/app.12660

[32] Cao X., Dong H., Li C. M.: New nanocomposite materials reinforced with flax cellulose nanocrystals in waterborne polyurethane. Biomacromolecules, **8**, 899–904 (2007).
DOI: 10.1021/bm0610368

[33] Morin A., Dufresne A.: Nanocomposites of chitin whiskers from *riftia* tubes and poly(caprolactone). Macromolecules, **35**, 2190–2199 (2002).
DOI: 10.1021/ma011493a

[34] Kim D. H., Fasulo P. D., Rodgers W. R., Paul D. R.: Effect of the ratio of maleated polypropylene to organoclay on the structure and properties of TPO-based nanocomposites. Part I: Morphology and mechanical properties. Polymer, **48**, 5960–5978 (2007).
DOI: 10.1016/j.polymer.2007.08.010

[35] Chen G. J., Wei M., Chen J. H., Huang J., Dufresne A., Chang P. R.: Simultaneous reinforcing and toughening: New nanocomposites of waterborne polyurethane filled with low loading level of starch nanocrystals. Polymer, **49**, 1860–1870 (2008).
DOI: 10.1016/j.polymer.2008.02.020

[36] Huang J., Zhang L. N.: Effects of NCO/OH molar ratio on structure and properties of graft-interpenetrating polymer networks from polyurethane and nitrolignin. Polymer, **43**, 2287–2294 (2002).
DOI: 10.1016/S0032-3861(02)00028-9

[37] Cui L., Ma X., Paul D. R.: Morphology and properties of nanocomposites formed from ethylene-vinyl acetate copolymers and organoclays. Polymer, **48**, 6325–6339 (2007).
DOI: 10.1016/j.polymer.2007.08.040

eXPRESS Polymer Letters Vol.5, No.4 (2011) 374–383
Available online at www.expresspolymlett.com
DOI: 10.3144/expresspolymlett.2011.36

Position transitions of polymer-grafted nanoparticles in diblock-copolymer nanocomposites

*G. K. Xu, X. Q. Feng**

Institute of Biomechanics and Medical Engineering, Department of Engineering Mechanics, Tsinghua University, Beijing 100084, China

Received 10 September 2010; accepted in revised form 17 November 2010

Abstract. Self-assembly of block copolymer/nanoparticle blends has promising applications in the design and fabrication of novel functional nanomaterials. Precise control of the spatial positions of nanoparticles within block copolymer-based nanomaterials is crucial to achieve some special physical properties and functions. Here, we employ the self-consistent field method to theoretically investigate the self-assembly of polymer grafted-nanoparticles in a diblock copolymer. It is found that by varying the size and selectivity of nanoparticles, one can not only produce various self-assembled nanostructures but also modulate the spatial positions of the nanoparticles, either at the copolymer interfaces or in the center of one copolymer phase, within the nanostructures. A denser grafted polymer brush plays a role of shielding effect on nanoparticles and can position them into the center of one copolymer phase. The nanostructural transition we observed is dictated by the competition between entropy and enthalpy. On the basis of a number of simulations, two phase diagrams of self-assembled nanostructures are constructed. This study may be helpful for optimal design of advanced materials with desired nanostructures and enhanced performance.

Keywords: *nanocomposites, self-assembly, diblock copolymer, polymer-grafted nanoparticle, modeling and simulation*

1. Introduction

Incorporation of inorganic nanoparticles into a polymeric host has been explored as a highly promising area devoted to improving mechanical, catalytic, magnetic, electrical, and optical properties of nanocomposites [1–8]. The high performance of such nanocomposites makes them attractive for many technologically important applications in, for instance, nanostructured solar cells, photonic band gap materials, optical filters, highly efficient catalysts, and high-density magnetic storage media.

Owing to their rich assortment of ordered morphologies, block copolymers are found to be particularly effective to control the spatial distribution of nanoparticles [9–19], which is crucial to achieve the required properties of nanocomposites. The dispersion of nanoparticles within block copolymer domains is affected by many factors, e.g., the size, shape and selectivity of nanoparticles [5, 9, 17, 20]. Among these factors, the chemical interaction between the particles and block copolymers plays the most important role in the self-assembly of nanocomposites. To elaborately adjust this interaction and to prevent macrophase separation, nanoparticles are often grafted by a brush of short polymers which are chemically identical to one component of the block copolymer [10, 12–14, 16]. Recent experiments evidence that various self-assembled nanostructures can be created by incorporating the polymer-grafted nanoparticles into a block copolymer film [10]. Kim *et al.* [13] reported that in a poly (styrene-b-2-vinylpyridine) (PS-b-P2VP) lamellar morphology, a high grafting PS chain density can drive nanoparticles to move towards the center of

*Corresponding author, e-mail: fengxq@tsinghua.edu.cn

PS domains, while a low grafting density results in the concentration of nanoparticles at the PS/P2VP interfaces. These findings suggest a facile and versatile means to control self-organization of functionalized nanoparticles and block copolymer blends [10, 12–14, 16].

Various techniques (e.g., mean-field theory [21], strong segregation theory [22], Monte Carlo [23, 24], dissipative particle dynamics [25, 26], and molecular dynamics [27] methods) have also been developed to investigate the spatial and temporal evolution of complex polymer-nanoparticle systems. Among them, self-consistent field theory (SCFT) has proven to be a powerful method for exploring complex morphologies of block copolymers and blends [28–32]. Small bare nanoparticles can be regarded as large solvent molecules, and their distribution in ordered triblock copolymers has been evaluated by using SCFT [33]. For large nanoparticles in block copolymers, the effect of excluded volume of particles should be taken into account by such methods as a combination of SCFT with density functional theory (DFT) [34–36] and hybrid particle-field method [37]. Very recently, SCFT was further extended to study the self-assembly behavior of polymer-grafted particles in block copolymers. Reister and Fredrickson proposed a novel approach to investigate the phase behavior of a mixture of diblock copolymers and nanoparticles with polymer chains tethered to their surfaces by modeling the grafted particles as star polymers [38]. By regarding particles as an ideal gas, Kim and Matsen explored how to position a single grafted particle in a block copolymer [39].

To date, however, there is still a lack of theoretical study on the spatial distribution of polymer-grafted nanoparticles in a diblock-copolymer lamellar matrix via self-assembly. In particular, it is crucial to quantitatively examine the effect of the grafted polymer brushes and to exploit their role in tuning the nanostructures. In this paper, therefore, we theoretically investigate the self-assembly behavior of polymer-grafted nanoparticle/diblock copolymer blends and the spatial position of nanoparticles within lamellar copolymer phases by employing the self-consistent field theory. The grafted nanoparticles are assumed to be sufficiently small so that they can be approximated as solvent molecules in the system [33]. The interactions among the nanoparticles, grafted polymers and copolymer matrix are all taken into account in our simulations because of their important roles in the self-assembling progress. Since the performance of a nanocomposite relies strongly on the spatial arrangement of nanoparticles, our attention is focused on how to precisely control the particle position in the nanocomposites. We find that by varying the size and selectivity of nanoparticles as well as the density of the grafted polymer brushes, one can not only obtain different self-assembled nanostructures but also control the spatial positions of the nanoparticles within the nanostructures. Therefore, these factors can be utilized to design nanostructures with a desired particle array, which may endow the material with specific physical properties and functions.

2. Theoretical model and computational method

We consider a system containing AB diblock copolymers and polymer-grafted nanoparticles. Each diblock chain consists of N_D segments, while each grafted chain is composed of $N_G = \beta N_D$ A-type segments. All polymer chains are modeled as flexible Gaussian chains. The volume fraction of A segments in each diblock chain is denoted as f. For simplicity, assume that A and B segments have the identical volume ρ_0^{-1} and statistical length α. The particle (P) has a radius R_P, and let $\alpha = 4\pi\rho_0 R_P^3/3N_D$ denote the volume ratio of a particle to a diblock chain. In this paper, α is taken in the range of 0.01–0.1 to ensure that the nanoparticles are small enough to be approximated as solvent molecules in the system, as assumed by Spontak *et al.* [33]. For larger particles with a size comparable to the diblock radius of gyration, $R_g = a\sqrt{N_D/6}$, one should account for the effects of their excluded volume by employing, for instance, the SCFT/DFT approach [34–36]. The number of polymer chains grafted on each particle is denoted as σ. The volume fractions of diblock copolymers and polymer-grafted particles in the blend are φ_D and $\varphi_{GP} = 1 - \varphi_D$, respectively. In the SCFT method, the pair interactions between different components are determined by a set of effective chemical potential fields, $W_I(\mathbf{r})$, denoting the intensity of the mean field felt by the species I at position $\mathbf{r}$. The dimensionless free energy of the system is given by Equation (1):

$$F = \frac{N_D F_0}{\rho_0 k_B T V} = -\varphi_D \ln\left(\frac{Q_D}{V\varphi_D}\right) - \frac{\varphi_{GP}}{(\alpha + \sigma\beta)} \ln\left(\frac{Q_{GP}}{V\varphi_{GP}}\right) - \frac{1}{V}\int d\mathbf{r} \sum_I W_I\phi_I + \frac{1}{2V}\int d\mathbf{r} \sum_I \sum_{J\neq I} N_D \chi_{IJ}\phi_I\phi_J \quad (1)$$

where F_0 is the free energy of the system, V the volume of the system, k_B the Boltzmann constant, T the temperature, $\phi_I(\mathbf{r})$ the local volume fraction of species I, and χ_{IJ} the Flory-Huggins interaction parameter between species I and J. Q_D and Q_{GP} are the partition functions of a single diblock chain and a polymer-grafted nanoparticle, respectively.

For a diblock chain, the contour variable s increases continuously from 0 at the free end of A-blocks to 1 at the free end of B-blocks. The spatial coordinate $\mathbf{r}$ is normalized by the diblock radius of gyration, R_g. The propagator $q_D(\mathbf{r},s)$ represents the probability of finding the sN_D segment of the diblock chain at position $\mathbf{r}$, which satisfies the modified diffusion equation (see Eqtions (2) and (3)):

$$\frac{\partial q_D(\mathbf{r},s)}{\partial s} = \nabla^2 q_D(\mathbf{r},s) - W_I(\mathbf{r}) q_D(\mathbf{r},s) \quad (2)$$

$$W_I(\mathbf{r}) = \begin{cases} W_A(\mathbf{r}), & 0 < s < f \\ W_B(\mathbf{r}), & f < s < 1 \end{cases} \quad (3)$$

subject to the initial condition $q_D(\mathbf{r},0) = 1$. The complementary propagator $q_D^+(\mathbf{r},s)$ satisfies an equation similar to Equation (2) except that its right-hand side is multiplied by –1 and the initial condition becomes $q_D^+(\mathbf{r},1) = 1$. The grafted polymer chain propagator $q_G(\mathbf{r},s)$ is given by Equation (4) [40, 41]:

$$\frac{\partial q_G(\mathbf{r},s)}{\partial s} = \beta\nabla^2 q_G(\mathbf{r},s) - \beta W_A(\mathbf{r}) q_G(\mathbf{r},s) \quad (4)$$

with the initial condition $q_G(\mathbf{r},0) = 1$ for the free end of the grafted chain at $s = 0$. The complementary propagators $q_G^+(\mathbf{r},s)$ obeys an equation similar to Equation (4) except that its right-hand sides is multiplied by –1 with the initial condition being given by Equation (5):

$$q_G^+(\mathbf{r},s) = \exp[-\alpha W_P(\mathbf{r})] q_G(\mathbf{r},1)^{\sigma-1} \quad (5)$$

In terms of these propagators, the partition functions Q_D and Q_{GP} are calculated by Equations (6) and (7):

$$Q_D = \int d\mathbf{r} q_D(\mathbf{r},1) \quad (6)$$

$$Q_{GP} = \int d\mathbf{r} \exp[-\alpha W_P(\mathbf{r})] q_G(\mathbf{r},1)^{\sigma} \quad (7)$$

The SCFT method is to find the equilibrium structure of a system by obtaining the minimization of its free energy F as a function of the local densities $\phi_I(\mathbf{r})$ and the mean fields $W_I(\mathbf{r})$ of all components. By minimizing the free energy F with respect to $\phi_I(\mathbf{r})$, one has the following Equations (8)–(10):

$$W_A(\mathbf{r}) = N_D\chi_{AB}\phi_B(\mathbf{r}) + N_D\chi_{AP}\phi_P(\mathbf{r}) + \xi(\mathbf{r}) \quad (8)$$

$$W_B(\mathbf{r}) = N_D\chi_{AB}\phi_A(\mathbf{r}) + N_D\chi_{BP}\phi_P(\mathbf{r}) + \xi(\mathbf{r}) \quad (9)$$

$$W_P(\mathbf{r}) = N_D\chi_{AP}\phi_A(\mathbf{r}) + N_D\chi_{BP}\phi_B(\mathbf{r}) + \xi(\mathbf{r}) \quad (10)$$

where ξ is a Lagrange multiplier enhancing the incompressible condition (see Equation (11)):

$$\phi_A(\mathbf{r}) + \phi_B(\mathbf{r}) + \phi_P(\mathbf{r}) = 1 \quad (11)$$

Using the propagators $q_D(\mathbf{r},s)$, $q_D^+(\mathbf{r},s)$, $q_G(\mathbf{r},s)$ and $q_G^+(\mathbf{r},s)$, the local densities of different components are calculated respectively by Eqtions (12)–(14):

$$\phi_A(\mathbf{r}) = \frac{\varphi_D V}{Q_D}\int_0^f ds\, q_D(\mathbf{r},s) q_D^+(\mathbf{r},s) + \frac{\varphi_{GP}\sigma\beta V}{(\alpha+\sigma\beta)Q_{GP}}\int_0^1 ds\, q_G(\mathbf{r},s) q_G^+(\mathbf{r},s) \quad (12)$$

$$\phi_B(\mathbf{r}) = \frac{\varphi_D V}{Q_D}\int_f^1 ds\, q_D(\mathbf{r},s) q_D^+(\mathbf{r},s) \quad (13)$$

$$\phi_P(\mathbf{r}) = \frac{\varphi_{GP}\alpha V}{(\alpha+\sigma\beta)Q_{GP}} \exp[-\alpha W_P(\mathbf{r})] q_G(\mathbf{r},1)^{\sigma} \quad (14)$$

Equations (8)–(14) form a closed set of equations that can be solved self-consistently in real space. To obtain the equilibrium nanostructure, we solve these equations by using the combinatorial screening technique of Drolet and Fredrickson [30, 42] implemented with a highly stable and accurate numerical algorithm [43, 44]. All the simulations are performed in a two-dimensional square lattice with periodic boundary conditions. Since the equilibrium morphology is somewhat influenced by the simulation box size [45], two methods have been often adopted to minimize the free energy with respect to the box size. One is to fix the simulation cell shape and to gradually adjust the cell size [46,

47], while in the other, both the shape and size of the cell are adjusted [48]. In our simulations, we use the former method to achieve an equilibrium structure by changing the square cell size, a, such that $\partial F(a_{min})/\partial a = 0$. The system is thought to have reached equilibrium when the relative difference between the free energies of the system at two neighboring iteration steps has been smaller than 0.0001%. More details on the numerical implementation of SCFT can be found in the literature [30, 42–44].

3. Results and discussion

In this study, the incompatibility between A- and B-blocks is set as $N_D\chi_{AB}$. The interaction parameters of A- and B-blocks with the particle are respectively characterized by $N_D\chi_{AP} = \varepsilon N_D\chi_{AB}$ and $N_D\chi_{BP} = (1-\varepsilon)N_D\chi_{AB}$, in which ε denotes the particle selectivity [33]. If $\varepsilon > 0.5$, the particle has a preferable interaction to B-blocks (i.e., B-selective). $\varepsilon < 0.5$ indicates an attraction interaction between the particle and A-blocks (i.e., A-selective). For a neutral particle, one has $\varepsilon = 0.5$. Unless specified otherwise, the following representative values are used: f=0.5, $\sigma = 3$, $\Delta s = 0.01$, $\alpha = 0.08$ and $\varepsilon = 0.5$. We have carried out a large number of simulations by changing the number σ of polymer chains tethered on each particle in the range from 2 to 6. The results demonstrate that $\sigma = 3$ can well describe the effect of grafted polymers and shorten the calculation time. The formation of various patterns depends on the volume fraction of polymer-grafted nanoparticles [10]. In our previous work [49], it has been demonstrated that a transition from the lamellar ($\varphi_{GP} = 0.15$, Figure 1a) to hexagonally packed ($\varphi_{GP} = 0.4$, Figure 1b) pattern occurs as the grafted particle concentration φ_{GP} increases. In this paper, our attention is focused on how to control the spatial distribution of nanoparticles in a diblock-copolymer lamellar morphology, because of its wide applications in nanocomposites [2, 5, 9, 12–14]. In what follows, we will take $\varphi_{GP} = 0.15$.

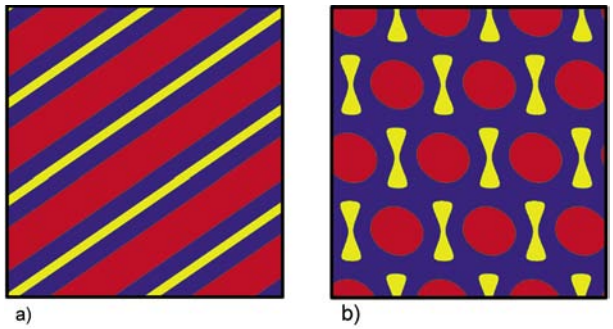

Figure 1. Aggregation morphologies of polymer-grafted nanoparticle and diblock copolymer blends under different concentrations of polymer-grafted nanoparticles: (a) lamellar pattern under $\varphi_{GP} = 0.15$ and (b) hexagonally packed pattern under $\varphi_{GP} = 0.4$. The concentration of grafted polymers is taken as $\varphi_G = 2\varphi_{GP}/3$ in these two cases. The blue, red, and yellow colors represent A-blocks, B-blocks, and particles, respectively.

3.1. Effect of nanoparticle size

We first examine the size effect of nanoparticles on the equilibrium structure. The concentration of grafted A-type polymers is fixed at $\varphi_G = 0.075$ in this subsection. The tethered A-type polymers will prevent the presence of the nanoparticles in B domains because of the repulsive interaction between the grafted A chains and the B segments. The self-assembled nanostructures of the blends are shown in Figure 2a, 2c, 2e under three representative sizes of nanoparticles. It is seen from Figure 2a that when the particles (yellow) are very small (e.g., $\alpha = 0.01$), they will have a concentration at the copolymer interfaces. Particles with mediate sizes (e.g., $\alpha = 0.02$) can be observed both at the copolymer interfaces and in the center of A domains (Figure 2c). Bigger particles will mainly reside in the center of A domains, as illustrated in Figure 2e, where we take $\alpha = 0.08$. To reveal the structures more clearly, the density profiles of different components (nanoparticles, A- and B-blocks) with two periods are plotted along the direction perpendicular to the interfaces in the lamellar structure (Figure 2b, 2d, 2f). A period refers to the region between the centers of two neighboring B domains. In Figure 2b, the particle density profile in each period has two peaks, located at the A/B interfaces, indicating that the nanoparticles are mainly distributed in A domains with a concentration at the copolymer interfaces. In Figure 2d, the particle density profile has three peaks in each period, which are located at the copolymer interfaces and in the center of A domains, respectively, but the spatial distribution within A domains is relatively even. In the case of the largest particles we study, the particle density profile has only one peak in the center of each period (Figure 2f), representing the aggregation of particles in the center of A domains.

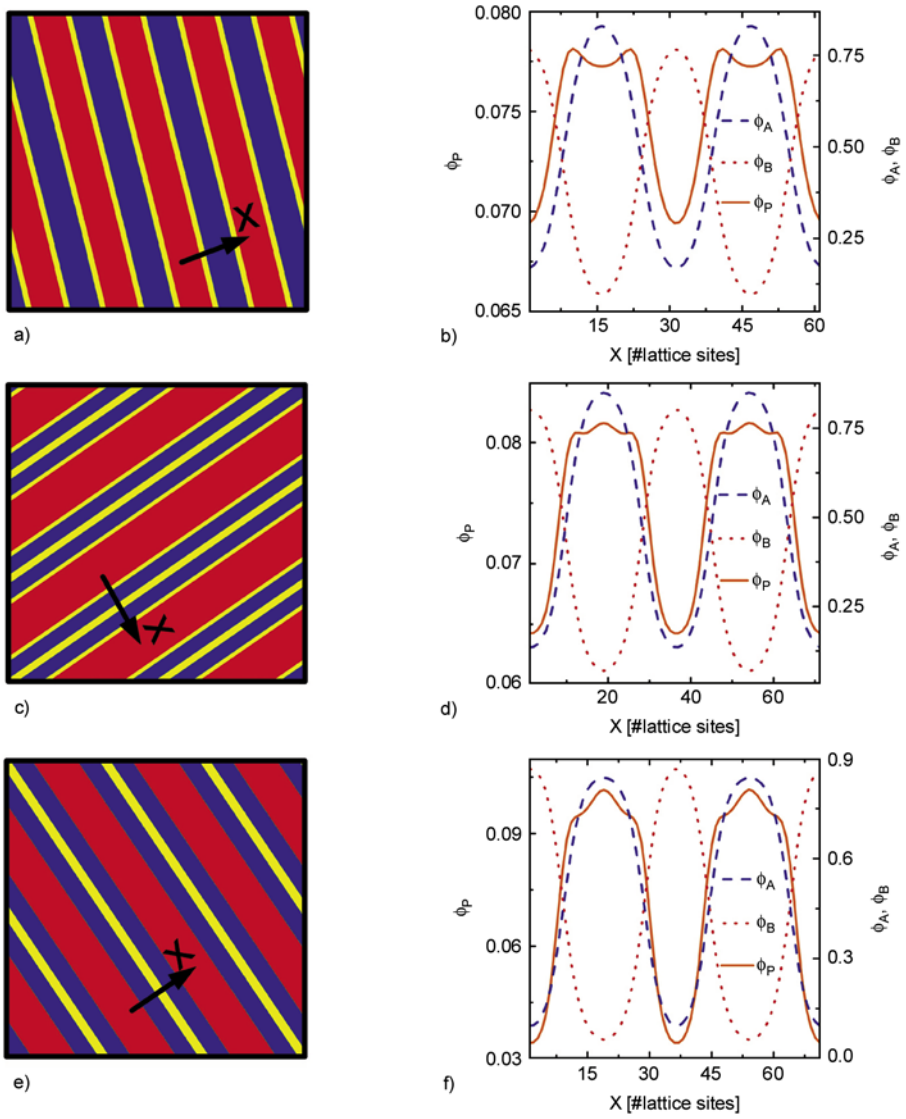

Figure 2. Influence of the particle size α on the self-assembled nanostructures of polymer-grafted nanoparticle and diblock copolymer blends: (a) $\alpha = 0.01$, (c) $\alpha = 0.02$ and (e) $\alpha = 0.08$. The blue, red and yellow colors represent A-blocks, B-blocks, and nanoparticles, respectively. The corresponding two period-density profiles of A-blocks (ϕ_A), B-blocks (ϕ_B) and particles (ϕ_P) are plotted in (b), (d) and (f) as the arrows pointed in the (a), (c) and (e), respectively.

The size-induced particle position transitions are more clearly schematized in Figure 3. This transition can be understood by considering the competition between the translational entropy of nanoparticles and the conformational entropy of copolymers. For large particles, the copolymers push them towards the center of A domains to gain more conformational entropy, which overcomes the loss of particle translational entropy. Under a fixed volume fraction, the number of particles increases as their size reduces. Therefore, small particles are mainly dispersed in the preferred domains and their translational entropy dominates the final nanostructure. This morphological transition with the variation of the particle size is consistent with recent experimental observations [9]. In addition, Balazs *et al.* [34] drawn a similar conclusion in their study of the structures of bare particle/diblock copolymer blends.

3.2. Effect of grafted polymer brush

In this subsection, we quantitatively investigate the effect of grafted polymer brushes, which serve as a shield on nanoparticles and play a significant role in the self-assembling process of the blends. The concentration of grafted polymers, φ_G, is a function of the grafted chain length β and the number σ of grafted polymers on each particle. Under a fixed

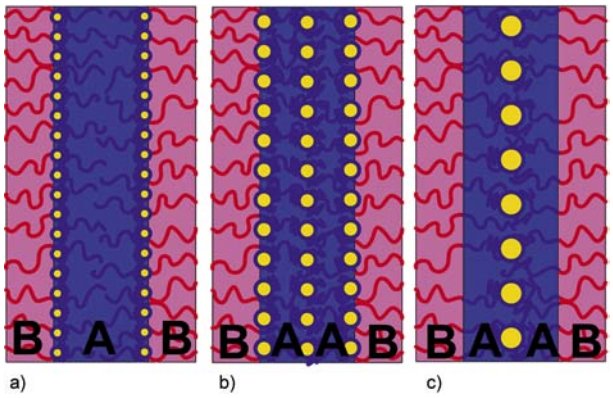

Figure 3. Schematic diagrams showing the major positions of nanoparticles under different conditions. Small nanoparticles segregate to the copolymer interfaces (a), while large nanoparticles locate in the center of A domains (c). A combination of the two particle positions occurs at the mediate particle size (b). The blue, red and yellow colors represent A-blocks, B-blocks, and particles, respectively.

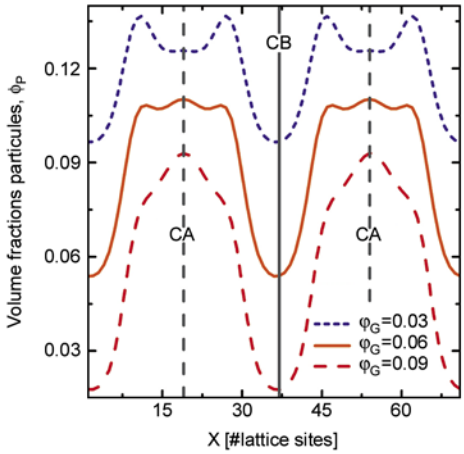

Figure 4. Two period-density profiles of particles are plotted with various grafted polymer concentrations: φ_G = 0.03, 0.06 and 0.09. The gray dashed line represents the center of A domains (CA), and the gray solid line shows the center of B domains (CB).

value of $\sigma = 3$, therefore, φ_G depends mainly on the attached chain length β. A larger value of φ_G stands for a denser grafted polymer brush and a stronger shielding effect. For several representative values of φ_G, the density profiles of particles are compared in Figure 4, where the notations CA and CB respectively represent the centers of A and B domains. It is seen that in the case of a sparse polymer brush (e.g., $\varphi_G = 0.03$), most nanoparticles mainly reside in the A domains but, simultaneously, there is an enrichment at the copolymer interfaces, which weakens the enthalpic interaction between A- and B-blocks. When the polymer brushes are denser (e.g., $\varphi_G = 0.09$), particles are mainly embedded in the center of A domains. A combination of the above two distributions of nanoparticles occurs at the mediate range of the grafted polymer concentration (e.g., $\varphi_G = 0.06$). At a small value of φ_G, the particles move towards the copolymer interfaces, effectively reducing the interfacial interaction between A- and B-blocks at A/B interfaces. However, under a larger concentration of grafted polymers, the particles are almost completely shielded by the denser polymer brushes. As a result, the nanoparticles migrate into the center of A domains, inducing a decrease of enthalpic interaction between the grafted A brushes and B-blocks and also an increase of the entropy of copolymers. Recently, Chiu *et al.* [16] experimentally observed that A-grafted nanoparticles locate only in the center of A domains, irrespective of the particle size. This finding can be interpreted by the shielding effect of the denser grafted polymer brushes used in their experiments, as observed in our simulations. Therefore, it is conclusive that by appropriate design of the grafted polymer brush and the particle size, nanoparticles can be precisely positioned in a nanostructure, either in the required domains or interfaces, depending on the need for specific physical properties and functions.

3.3. Effect of selectivity

Enthalpy often dominates the self-assembly and microphase segregation of a system, especially at the nanoscale. Therefore, we here investigate the effect of enthalpic interactions between nanoparticles and different components of copolymers on the equilibrium structure. The particle selectivity ε is varied to study this effect under a fixed polymer brush concentration, $\varphi_G = 0.075$. Figure 5 shows the density profiles of nanoparticles under several representative values of ε. It is seen from Figure 2f that neutral particles ($\varepsilon = 0.5$) segregate to the center of A domains. When the particles are highly B-selective (e.g., $\varepsilon = 0.875$), they tend to reside in B domains because of their preferable interaction, whereas the incompatibility between grafted A brushes and B-blocks excludes the presence on nanoparticles in B domains. The competition of these two factors induces the enrichment of particles at A/B inter-

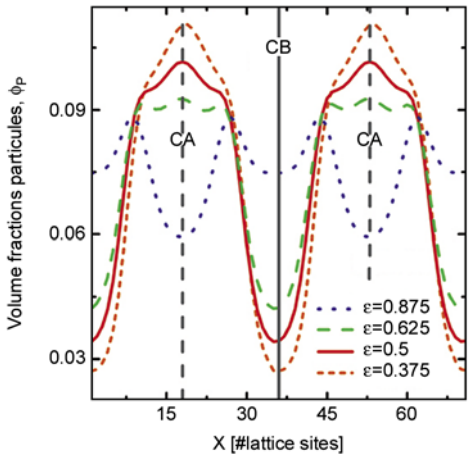

Figure 5. Two period-density profiles of particles under various particle selectivities: $\varepsilon = 0.875$, 0.625, 0.5, and 0.375. $\varepsilon > 0.5$ and $\varepsilon < 0.5$ indicate that the particles are B-selective and A-selective, respectively, while $\varepsilon = 0.5$ indicates neutral particles. The gray dashed line represents the center of A domains (CA), and the gray solid line shows the center of B domains (CB).

faces. In the case of $\varepsilon = 0.625$, there are three peaks in each period of the particle density profile, indicating that particles reside both in the center of A domains and at the A/B interfaces. For A-selective particles (e.g., $\varepsilon = 0.375$), they mainly locate in the center of A domains owing to the favorable interaction between the particles and A-blocks in spite of the loss in the particle translational entropy.

To quantitatively explore the physical mechanisms underlying the formation of the above-described nanostructures, we calculate the contributions of entropy and enthalpy to the total free energy. In Equation (1), the first three terms of the right-hand side represent the energy associated with entropy while the last term corresponds to enthalpy. The dimensionless total free energy of the system (F), the contribution of entropy (F_S) and enthalpy (F_E) are compared in Table 1 for under several representative values of the selectivity coefficient ε. As ε decreases, the entropic contribution to the total free energy increases because the concentration of nanoparticles at the centre of A domains leads to a partial loss of their translational entropy. However, the enthalpic interaction decreases since the total contact area between copolymers and particles reduces as the particles migrate from the A/B interfaces to the center of A domains. For instance, the difference of the entropic contribution to the free energy between two situations of $\varepsilon = 0.875$ and $\varepsilon = 0.375$ is 0.248, whereas the corresponding enthalpic contribution to the free energy has a difference of –0.377. In comparison with the entropic contribution, the enthalpy dominates the particle distribution within the self-assembled nanostructures.

Table 1. Comparison of the dimensionless free energy F of the system at equilibrium under several representative values of the selectivity coefficient, ε. F_S and F_E stand for the entropic and enthalpic contributions to the free energy, respectively.

Selectivity ε	Entropic contribution F_S	Enthalpic contribution F_E	Total free energy F
0.875	1.151	2.791	3.942
0.625	1.241	2.654	3.895
0.500	1.309	2.547	3.856
0.375	1.399	2.414	3.813

3.4. Phase diagrams of self-assembled nanostructures

To further reveal the dependence of the particle location upon the particle size, particle selectivity and grafted polymer concentration, two phase diagrams of the self-assembled lamellar structures are provided in Figure 6 based on a number of simulations. The gray lines represent the transition boundaries, and the insets delineate particle positions. Corresponding to distinctly different particle positions within the lamellar morphology, each diagram is divided into three regions, marked by I, (I+CA) and CA, respectively. The notation I stands for the preferential segregation of nanoparticles to A/B interfaces, while the notation CA stands for the concentration of particles in the center of A domains. It is clearly seen from Figure 6a that the particle position transitions in the order of I → (I+CA) → CA can be achieved by increasing either the particle size or the concentration of grafted polymer brushes. With increasing ε, the morphological transitions take place in the order of CA → (I+CA) → I, as shown in Figure 6b, as a result of the increased preferential interaction between the nanoparticles and B segments. Such phase diagrams provide a facile tool to predict the particle distribution in a block-copolymer lamellar morphology under specified conditions.

4. Conclusions

In summary, we report a theoretical investigation of the spatial distribution of polymer-tethered nano-

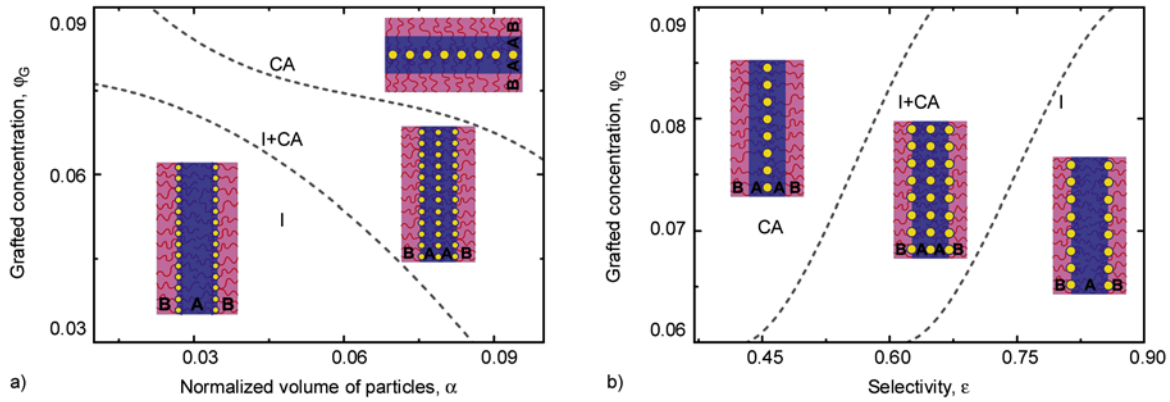

Figure 6. Phase diagrams illustrating the dependence of particle position on the particle size α, particle selectivity ε, and grafted polymer concentration φ_G. (a) Particle size-grafted concentration phase diagram. (b) Particle selectivity-grafted concentration phase diagram. The insets show the preferable positions of particles. The notations I and CA stand for particles mainly locating at the copolymer interfaces and in the center of A domains, respectively.

particles within the lamellar diblock-copolymer matrix. Our study suggests that by appropriate design of the grafted polymer brush, the nanoparticle size and surface treatment (i.e., selectivity), nanoparticles can be precisely positioned in nanocomposites with a desired array for specific properties and applications. Through systematic SCFT simulations, we constructed two phase diagrams describing the dependence of the spatial distribution of nanoparticles on their size and selectivity and the concentration of the grafted polymers. The observed position transition of particles is dictated by the competition between entropy and enthalpy in the system. The present method can also account for other factors (e.g., the composition of copolymers [50], shape [20] and concentration [10, 51] of nanoparticles) that can be utilized to fabricate more delicate nanostructures. This study is helpful for optimal design of self-assembled composites with desired nanostructures and enhanced properties.

Acknowledgements

The supports from the National Natural Science Foundation of China (Grants Nos. 10972121, 10732050 and 10772093), the Ministry of Education (SRFDP 20090002110047), and the 973 program of MOST (2010CB631005) are acknowledged.

References

[1] Balazs A. C., Emrick T., Russell T. P.: Nanoparticle polymer composites: Where two small worlds meet. Science, **314**, 1107–1110 (2006).
DOI: 10.1126/science.1130557

[2] Bockstaller M. R., Thomas E. L.: Proximity effects in self-organized binary particle–block copolymer blends. Physical Review Letters, **47**, 166106/1–166106/4 (2004).
DOI: 10.1103/PhysRevLett.93.166106

[3] Liff S. M., Kumar N., McKinley G. H.: High-performance elastomeric nanocomposites via solvent-exchange processing. Nature Materials, **6**, 76-83 (2007).
DOI: 10.1038/nmat1798

[4] Warren S. C., Messina L. C., Slaughter L. S., Kamperman M., Zhou Q., Gruner S. M., DiSalvo F. J., Wiesner U.: Ordered mesoporous materials from metal nanoparticle-block copolymer self-assembly. Science, **320**, 1748–1752 (2008).
DOI: 10.1126/science.1159950

[5] Bockstaller M. R., Mickiewicz R. A., Thomas E. L.: Block copolymer nanocomposites: Perspectives for tailored functional materials. Advanced Materials, **17**, 1331–1349 (2005).
DOI: 10.1002/adma.200500167

[6] Thompson R. B., Rasmussen K. Ø., Lookman T.: Origins of elastic properties in ordered block copolymer/nanoparticle composites. Nano Letters, **6**, 2455–2459 (2006).
DOI: 10.1021/nl048407f

[7] Meli L., Green P. F.: Aggregation and coarsening of ligand-stabilized gold nanoparticles in poly(methl methacrylate) thin films. ACS Nano, **2**, 1305–1312 (2008).
DOI: 10.1021/nn800045s

[8] Akcora P., Liu H., Kumar S. K., Moll J., Li Y., Benicewicz B. C., Schadler L. S., Acehan D., Panagiotopoulos A. Z., Pryamitsyn V., Ganesan V., Ilavsky J., Thiyagarajan P., Colby R. H., Douglas J. F.: Anisotropic self-assembly of spherical polymer-grafted nanoparticles. Nature Materials, **8**, 354–359 (2009).
DOI: 10.1038/NMAT2404

[9] Bockstaller M. R., Lapetnikov Y., Margel S., Thomas E. L.: Size-selective organization of enthalpic compatibilized nanocrystals in ternary block copolymer/particle mixture. Journal of the American Chemical Society, **125**, 5276–5277 (2003).
DOI: 10.1021/ja034523t

[10] Kim B. J., Chiu J. J., Yi G-R., Pine D. J., Kramer E. J.: Nanoparticle-induced phase transitions in diblock-copolymer films. Advanced Materials, **17**, 2618–2622 (2005).
DOI: 10.1002/adma.200500502

[11] Lin Y., Böker A., He J., Sill K., Xiang H., Abetz C., Li X., Wang J., Emrick T., Long S., Wang Q., Balazs A., Russell T. P.: Self-directed self-assembly of nanoparticle/copolymer mixtures. Nature, **434**, 55–59 (2005).
DOI: 10.1038/nature03310

[12] Chiu J. J., Kim B. J., Kramer E. J., Pine D. J.: Control of nanoparticle location in block copolymers. Journal of the American Chemical Society, **127**, 5036–5037 (2005).
DOI: 10.1021/ja050376i

[13] Kim B. J., Bang J., Hawker C. J., Kramer E. J.: Effect of areal chain density on the location of polymer-modified gold nanoparticles in a block copolymer template. Macromolecules, **39**, 4108–4114 (2006).
DOI: 10.1021/ma060308w

[14] Kim B. J., Fredrickson G. H., Kramer E. J.: Effect of polymer ligand molecular weight on polymer-coated nanoparticle location in block copolymers. Macromolecules, **41**, 436–447 (2008).
DOI: 10.1021/ma701931z

[15] Kang H., Detcheverry F. A., Mangham A. N., Stoykovich M. P., Daoulas K. C., Hamers R. J., Müller M., de Pablo J. J., Nealey P. F.: Hierarchical assembly of nanoparticle superstructures from block copolymer-nanoparticle composites. Physical Review Letters, **100**, 148303/1–148303/4 (2008).
DOI: 10.1103/PhysRevLett.100.148303

[16] Chiu J. J., Kim B. J., Yi G-R., Bang J., Kramer E. J., Pine D. J.: Distribution of nanoparticles in lamellar domains of block copolymers. Macromolecules, **40**, 3361–3365 (2007).
DOI: 10.1021/ma061503d

[17] Warren S. C., DiSalvo F. J., Wiesner U.: Nanoparticle-tuned assembly and disassembly of mesostructured silica hybrids. Nature Materials, **6**, 156–161 (2007).
DOI: 10.1038/nmat1819

[18] Hickey R. J., Sanchez-Gaytan B. L., Cui W., Composto R. J., Fryd M., Wayland B. B., Park S-J.: Morphological transitions of block-copolymer bilayers via nanoparticle clustering. Small, **6**, 48–51 (2010).
DOI: 10.1002/smll.200901266

[19] Darling S. B.: Directing the self-assembly of block copolymers. Progress in Polymer Science, **32**, 1152–1204 (2007).
DOI: 10.1016/j.progpolymsci.2007.05.004

[20] Kim J. U., O'Shaughnessy B.: Morphology selection of nanoparticle dispersions by polymer media. Physical Review Letters, **89**, 238301/1–238301/4 (2002).
DOI: 10.1103/PhysRevLett.89.238301

[21] Pryamtisyn V., Ganesan V., Panagiotopoulos A. Z., Liu H., Kumar S. K.: Modeling the anisotropic self-assembly of spherical polymer-grafted nanoparticles. Journal of Chemical Physics, **131**, 221102/1–221102/4 (2009).
DOI: 10.1063/1.3267729

[22] Pryamitsyn V., Ganesan V.: Strong segregation theory of block copolymer−nanoparticle composites. Macromolecules, **39**, 8499–8510 (2006).
DOI: 10.1021/ma0613382

[23] Wang Q., Nealey P. F., de Pablo J. J.: Behavior of single nanoparticle/homopolymer chain in ordered structures of diblock copolymers. Journal of Chemical Physics, **118**, 11278–11285 (2003).
DOI: 10.1063/1.1575207

[24] Huh J., Ginzburg V. V., Balazs A. C.: Thermodynamic behavior of particle/diblock copolymer mixtures: Simulation and theory. Macromolecules, **33**, 8085–8096 (2000).
DOI: 10.1021/ma000708y

[25] Huang J., Wang Y.: Control of aggregation of nanoparticles by double-hydrophilic block copolymers: A dissipative particle dynamics study. The Journal of Physical Chemistry B, **111**, 7735–7741 (2007).
DOI: 10.1021/jp070160y

[26] Huang J., Luo M., Wang Y.: Dissipative particle dynamics simulation on a ternary system with nanoparticles, double-hydrophilic block copolymers, and solvent. The Journal of Physical Chemistry B, **112**, 6735–6741 (2008).
DOI: 10.1021/jp710567f

[27] Schultz A. J., Hall C. K., Genzer J.: Computer simulation of block copolymer/nanoparticle composites. Macromolecules, **38**, 3007–3016 (2005).
DOI: 10.1021/ma0496910

[28] Matsen M. W.: The standard Gaussian model for block copolymer melts. Journal of Physics: Condensed Matter, **14**, R21–R47 (2002).
DOI: 10.1088/0953-8984/14/2/201

[29] Matsen M. W.: Stabilizing new morphologies by blending homopolymer with block copolymer. Physical Review Letters, **74**, 4225–4228 (1995).
DOI: 10.1103/PhysRevLett.74.4225

[30] Drolet F., Fredrickson G. H.: Combinatorial screening of complex block copolymer assembly with self-consistent field theory. Physical Review Letters, **83**, 4317–4320 (1999).
DOI: 10.1103/PhysRevLett.83.4317

[31] Xu G. K., Li Y., Li B., Feng X. Q., Gao H.: Self-assembled lipid nanostructures encapsulating nanoparticles in aqueous solution. Soft Matter, **5**, 3977–3983 (2009).
DOI: 10.1039/b906918f

[32] Xu G. K., Feng X. Q., Li Y.: Self-assembled nanostructures of homopolymer and diblock copolymer blends in a selective solvent. The Journal of Physical Chemistry **B**, 114, 1257–1263 (2010).
DOI: 10.1021/jp908823h

[33] Spontak R. J., Shankar R., Bowman M. K., Krishnan A. S., Hamersky M. W., Samseth J., Bockstaller M. R., Rasmussen K. Ø.: Selectivity- and size-induced segregation of molecular and nanoscale species in microphase-ordered triblock copolymers. Nano Letters, **6**, 2115–2120 (2006).
DOI: 10.1021/nl061205u

[34] Thompson R. B., Ginzburg V. V., Matsen M. W., Balazs A. C.: Predicting the mesophases of copolymer-nanoparticle composites. Science, **292**, 2469–2472 (2001).
DOI: 10.1126/science.1060585

[35] Thompson R. B., Ginzburg V. V., Matsen M. W., Balazs A. C.: Block copolymer-directed assembly of nanoparticles: Forming mesoscopically ordered hybrid materials. Macromolecules, **35**, 1060–1071 (2002).
DOI: 10.1021/ma011563d

[36] Lee J. Y., Shou Z., Balazs A. C.: Modeling the self-assembly of copolymer-nanoparticle mixtures confined between solid surfaces. Physical Review Letters, **91**, 136103/1–136103/4 (2003).
DOI: 10.1103/PhysRevLett.91.136103

[37] Sides S. W., Kim B. J., Kramer E. J., Fredrickson G. H.: Hybrid particle-field simulations of polymer nanocomposites. Physical Review Letters, **96**, 250601/1–250601/4 (2006).
DOI: 10.1103/PhysRevLett.96.250601

[38] Reister E., Fredrickson G. H.: Phase behavior of a blend of polymer-tethered nanoparticles with diblock copolymers. Journal of Chemical Physics, **123**, 214903/1–214903/13 (2005).
DOI: 10.1063/1.2117008

[39] Kim J. U., Matsen M. W.: Positioning Janus nanoparticles in block copolymer scaffolds. Physical Review Letters, **102**, 078303/1–078303/4 (2009).
DOI: 10.1103/PhysRevLett.102.078303

[40] Patel D. M., Fredrickson G. H.: Quenched and annealed disorder in randomly grafted copolymer melts. Physical Review E, **68**, 051802/1–051802/4 (2003).
DOI: 10.1103/PhysRevE.68.051802

[41] Zhang L., Lin J., Lin S.: Aggregate morphologies of amphiphilic graft copolymers in dilute solution studied by self-consistent field theory. The Journal of Physical Chemistry B, **111**, 9209–9217 (2007).
DOI: 10.1021/jp068429l

[42] Drolet F., Fredrickson G. H.: Optimizing chain bridging in complex block copolymers. Macromolecules, **34**, 5317–5324 (2001).
DOI: 10.1021/ma0100753

[43] Tzeremes G., Rasmussen K. Ø., Lookman T., Saxena A.: Efficient computation of the structural phase behavior of block copolymers. Physical Review E, **65**, 041806/1–041806/5 (2002).
DOI: 10.1103/PhysRevE.65.041806

[44] Sides S. W., Fredrickson G. H.: Parallel algorithm for numerical self-consistent field theory simulations of block copolymer structure. Polymer, **44**, 5859–5866 (2003).
DOI: 10.1016/S0032-3861(03)00606-2

[45] Bohbot-Raviv Y., Wang Z-G.: Discovering new ordered phases of block copolymers. Physical Review Letters, **85**, 3428–3431 (2000).
DOI: 10.1103/PhysRevLett.85.3428

[46] Jiang Y., Yan X., Liang H., Shi A-C.: Effect of polydispersity on the phase diagrams of linear ABC triblock copolymers in two dimensions. The Journal of Physical Chemistry B, **109**, 21047–21055 (2005).
DOI: 10.1021/jp052902y

[47] Kou D., Jiang Y., Liang H.: Microstructures from a mixture of ABC 3-miktoarm star terpolymers and homopolymers in two-dimensional space. The Journal of Physical Chemistry B, **110**, 23557–23563 (2006).
DOI: 10.1021/jp063695k

[48] Tyler C. A., Morse D. C.: Stress in self-consistent-field theory. Macromolecules, **36**, 8184–8188 (2003).
DOI: 10.1021/ma034601x

[49] Xu G. K., Feng X. Q., Yu S. W.: Controllable nanostructural transitions in grafted nanoparticle-block copolymer composites. Nano Research, **3**, 356–362 (2010).
DOI: 10.1007/s12274-010-1039-8

[50] Lo C-T., Lee B., Pol V. G., Dietz Rago N. L., Seifert S., Winans R. E., Thiyagarajan P.: Effect of molecular properties of block copolymers and nanoparticles on the morphology of self-assembled bulk nanocomposites. Macromolecules, **40**, 8302–8310 (2007).
DOI: 10.1021/ma070835v

[51] Kim B. J., Fredrickson G. H., Bang J., Hawker C. J., Kramer E. J.: Tailoring core−shell polymer-coated nanoparticles as block copolymer surfactants. Macromolecules, **42**, 6193–6201 (2009).
DOI: 10.1021/ma9009406